THE ANALYSIS OF A NIP IMPINGED, THREE DIMENSIONAL WOUND ROLL

By

PAUL HOFFECKER

Bachelor of Science
University of Colorado, Boulder
Boulder, Colorado
1994

Master of Science
Oklahoma State University
Stillwater, Oklahoma
1997

Submitted to the Faculty of the
Graduate College of the
Oklahoma State University
in partial fulfillment of
the requirements for
the Degree of
DOCTOR OF PHILOSOPHY
May, 2006

THE ANALYSIS OF A NIP IMPINGED, THREE

DIMENSIONAL WOUND ROLL

Thesis Approved:

Dr. J. K. Good
Thesis Advisor

Dr. G. Steven Gipson

Dr. Hongbing Lu

Dr. C. E. Price

Dr. A. Gordon Emslie
Dean of the Graduate College

ACKNOWLEDGMENTS

I extend my sincere appreciation to my advisor Dr. James K. Good for his support and guidance during this investigation. Without his instruction and experience, this would have been an exercise in futility. I am also grateful for his friendship, character, and consideration. His direction has given me confidence and maturity, and encouraged me to pursue deeper understanding.

Many others also deserve my appreciation. I would like to thank my committee for their vision and insight. It has been a rewarding experience getting to know and learn from them. Thanks also to the Department of Mechanical and Aerospace Engineering, the endowed graduate fellowship, the Web Handling Research Center, and the consortium sponsors for their direction and financial assistance during this research. To Ron Markum I extend a special appreciation for the material testing and experimentation he conducted on my behalf. To Joe Beisel and Balaji Kandadai, thanks for your friendship; and to all of the other “webbies”, keep up the good work! All of the above helped make it possible for me to pursue this dream.

To my lovely wife Heather, I owe you so much. Your patience, encouragement, belief, respect, and love are so evident and so greatly appreciated. You inspired me and gave me motivation when I had none, and helped me see the big picture when I lost sight. May this be a stepping stone for wonderful things to come, and a stop along the way to remember with great fondness. With you, I can celebrate this accomplishment, and move on to our next great adventure.

My sincere hope is that someone else will also benefit from the labor and the product of this research. The project certainly had a dynamic all its own. There were times it seemed impossible. Many times it was highly unlikely. There were even a few, rare occasions when the solution appeared obvious. But, all of these instances together created an endeavor worthy of attempt, challenging to continue, humbling in nature, and victorious in completion. My effort brings to light the true source of accomplishments…

"You are worthy, O Lord,
To receive glory and honor and power;
For You created all things,
And by Your will they exist and were created."
Rev. 4:1

TABLE OF CONTENTS

LIST OF TABLES

LIST OF FIGURES

LIST OF EQUATIONS

NOMENCLATURE

0	index modifier which corresponds to an initial or a relaxed state
A	Coefficient in Radial Modulus representation
ARSG	Acoustic Roll Structure Gage
$\overline{\mathbf{A}}_{nip}$	Nip Lagrange Multiplier link vector
$\overline{\mathbf{A}}_{roll}$	Roll Lagrange Multiplier link vector
a	Altmann [1] material expansion variable
a	Hertzian [18] half-width of contact
α	Altmann [1] material expansion variable
B	Coefficient in Radial Modulus representation
$\overline{\mathbf{B}}$	FEM transformation matrix
b	Altmann [1] material expansion variable
β	Altmann [1] material expansion variable
$\beta_1, \beta_2, \beta_0$	Multi-point Constraint multipliers
C	Coefficient in Radial Modulus representation
$C_0 \ldots C_4$	Coefficients in Radial Modulus representations
CMD	Cross Machine Direction; the transverse or z direction
C_n	Altmann's [1] tension power series coefficients
$\bar{c}$	Altmann's [1] core radius
c	generic left beam node identifier
$\overline{\mathbf{D}}$	FEM Material stiffness matrix

$D_1 \ldots D_9$	Core dimension variables
Δ	delta; indicates a change in a value it precedes
ΔWOT_j	inter-segment Wound On Tension differential
$\delta\bar{\boldsymbol{\varepsilon}}$	incremental global strains
δP	incremental pressure
$\delta\bar{\mathbf{Q}}$	incremental global deformations
$\delta\bar{\boldsymbol{\sigma}}$	incremental global stresses
d	generic right beam node identifier
E	Modulus of Elasticity
E_r	Radial Modulus of Elasticity
$E_{r,net}$	net Radial Modulus of Elasticity in a nipped roll segment from nip and axisymmetric contributions
$E_{r,eff}$	Effective Radial Modulus of Elasticity
E_θ	Circumferential Modulus of Elasticity
E_Z	CMD Modulus of Elasticity
ESM	Element Stiffness Matrix
$\bar{\boldsymbol{\varepsilon}}$	strain vector
ε_{rr}	Polar radial strain
$\varepsilon_{r,eff}$	Effective radial strain
$\varepsilon_{r,nip}$	Nip Compression induced radial strain
$\varepsilon_{\theta\theta}$	Polar circumferential or tangential strain
e	finite element index
F	applied force in Hookes' law
$\bar{\mathbf{F}}$	FEM Global Force Vector
FEM	Finite Element Model

FSR	Force Sensing Resistor
$\bar{\mathbf{f}}$	FEM Body force vector
G	Modulus of Rigidity; Shear Modulus
GPa	GigaPascals, common unit of pressure ($1x10^9$ Newtons/meter)
GSM	Global Stiffness Matrix
g^2	Hakiel [14] modulus ratio
γ	Altmann [1] material expansion variable
H_1, H_2	Altmann [1] general solution constants
η	FEM natural coordinate
I	Moment of Inertia
I_A	motor armature current
i	index modifier which corresponds to lap
in	inch
$\bar{\mathbf{J}}$	Jacobian matrix
j	index modifier which corresponds to CMD sector or region
$\bar{\varphi}$	Shape functions matrix
φ	Shape functions, numbered 1 – 4, used to interpolate nodal values
$\bar{\mathbf{K}}$	FEM Global Stiffness Matrix
K_1	Pfeiffer's [24] Compressive Modulus Expression coefficient; rest pressure
K_2	Pfeiffer's [24] Compressive Modulus Expression coefficient; basic springiness factor
k	spring stiffness in Hooke's law
k_{eff}	effective spring stiffness
k_2	Pfeiffer's [24] Dynamic Modulus Expression coefficient; the dynamic springiness factor
κ	curvature of contacting body

$\overline{\mathbf{L}}$, L	FEM Point Load
L_{MD}	unsupported MD free-span length
LPW	Hertzian [18] Contact Load per CMD Width
LUD	Lower Upper Decomposition pivoting method
l	node to node length of an element's side
l_e	element length
Λ	Altmann's [1] tension power series function
λ	Lagrange Multiplier link
M	Maximum number of any index especially in a summation
M_X	Bending moment about the X coordinate axis
MD	Machine Direction; the direction of web travel
MPa	MegaPascals
mil	milli-inch, common unit of thickness measurement ($1x10^{-3}$ inch)
mm	millimeter
m_{eff}	drive motor electrical energy conversion efficiency
μ_s	static coefficient of friction
μ_k	kinetic coefficient of friction
N	Normal Force exerted by the nip
NIT	Nip Induced Tension; a layer's tension above T_W caused by the nip
n	index modifier which corresponds to terms in tension power series
ν	Poisson's Ratio
$\nu_{r\theta}$	Poisson's Ratio where a strain from the radial direction is transferred to the tangential direction
$\nu_{\theta r}$	Poisson's Ratio where a strain from the tangential direction is transferred to the radial direction

$\nu_{r\,Z}$	Poisson's Ratio where a strain from the radial direction is transferred to the CMD direction
$\nu_{Z\,r}$	Poisson's Ratio where a strain from the CMD direction is transferred to the radial direction
$\nu_{Z\,\theta}$	Poisson's Ratio where a strain from the CMD direction is transferred to the tangential direction
$\nu_{\theta\,Z}$	Poisson's Ratio where a strain from the tangential direction is transferred to the CMD direction
P	Radial pressure
P_{In}, P_{Ex}	Inside pressure, External pressure
PET	PolyEthylene Terephthalate
p	distributed beam load, load per length
pli	pounds per linear inch; a common web line tension unit
psi	pounds per square inch
ϕ	Nip Wrap Angle
ϕ_n	Altmann's [1] tension power series exponent terms
$\overline{\mathbf{Q}}$	FEM Global Deformation vector
$\overline{\mathbf{Q}}_{nip}$	Nip Global Deformation sub-vector
$\overline{\mathbf{Q}}_{roll}$	Roll Global Deformation sub-vector
Q_{P1}, Q_{P2}	Multi-point Constraint Degrees of Freedom to be constrained
$\overline{\mathbf{q}}$	FEM master element Deformation vector
R_0	Hakiel's [15] relaxation radius
R_{eff}	Hertzian [18] effective radius
r, R	indicates radius or the radial direction in a roll
R_{In}, R_{Ex}	Roisum's [31] Internal Radius, External Radius
ρ	Material Density

S	Elastic Foundation stiffness per unit width
s	radial integration variable
$\bar{\boldsymbol{\sigma}}$	stress vector
σ_{rr}	Polar radial stress
σ_{rz}	Shear stress in the CMD due to the Radial Direction
$\sigma_{\theta\theta}$	Polar circumferential or tangential stress
σ_{y}	Material yield stress
σ_{zz}	CMD stress
T	tension in a roll
$\bar{\mathbf{T}}$	FEM Surface traction vector
$T_{C.R.}$	Tension entering the nip to roll contact region after wrapping the nip
T_{fb}	tension force needed to bend web
T_{fI}	tension force due to inertia
T_{W}	Web line winding tension given as force/area, force/width or just force
t	web thickness for 2D roll, or average thickness for 3D roll
t.o.f.	time of flight
θ	indicates the circumferential or tangential direction in a roll
U	Strain Energy
UCB	Un-Coated Bond paper
u	radially directed deflection
V_0	web's incoming velocity
V_A	motor armature voltage
v	laterally (CMD) directed deflection
ϖ	beam element rotational degree of freedom

WHRC	Web Handling Research Center; a consortium sponsored research lab at OSU dedicated to the study of wound roll behavior
WOT	Wound On Tension; the total tension actually wound into a web layer
WP	Work Potential Energy
w	CMD width of web
ω	roll rotational rate in radians per time
X	indicates the axial direction in a beam
x	spring deformation in Hooke's law
x_{total}	total deformation of a spring system
ξ	FEM natural coordinate
Y	indicates the lateral direction in a beam
ψ	Square root of E_θ/E_r for Lekhnitskii [22] formulation
z, Z	indicates the CMD direction in a roll
$\measuredangle$	Wound Roll circumferential rotational angle

CHAPTER ONE

INTRODUCTION

Wound Rolls

Wound rolls are made of long, thin, continuous materials called webs, coiled onto a central core. Their shape accommodates the web's length, and when "wound" onto the core, usually a cylinder made of card board, aluminum, plastic or steel, the rolls support the web, making it more manageable (see Figure #I-1). The webs come in various

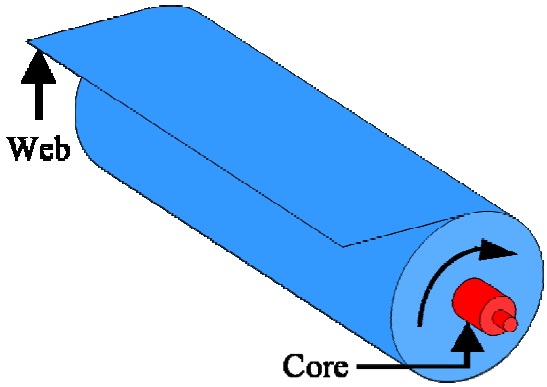

Figure #I-1: Sheet-like materials called webs often are wound and stored in "wound" rolls.

widths, thicknesses, and materials, and common examples include newspaper before it is cut into individual sheets, audio and video tape, camera film, aluminum foil, and toilet paper. Wound rolls often contain thousands of layers and measure many feet in width, which makes them complex structures that are anything but easy to manage.

For example, unlike most “solids”, wound rolls have exponentially increasing stress-strain diagrams, non-uniform pressure and radius distributions across their width, and can contain unstable, internal voids. All of these stem from the interactions between the roll’s layers.

The terminology used in referring to wound rolls is shown in Figure #I-2. The wound roll’s radius (R), refers to the distance from the core’s axis outward to the roll’s top layer. The Machine Direction (MD), (θ), corresponds to the direction the web travels

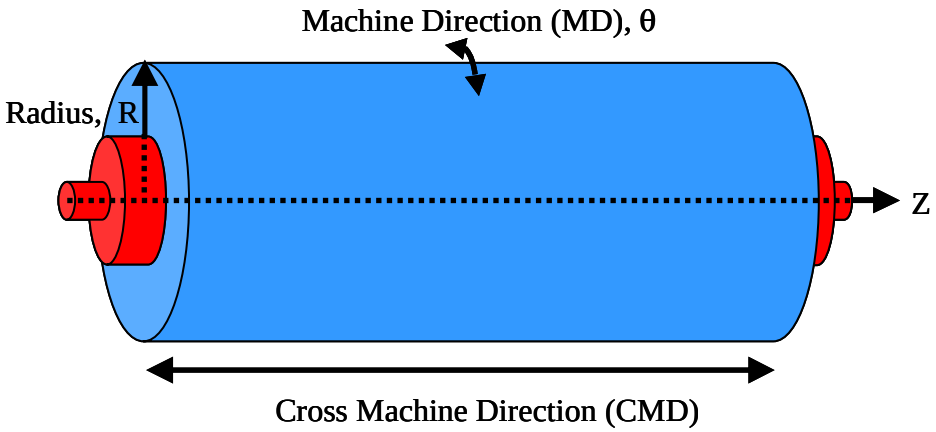

Figure #I-2: Three coordinates define wound roll geometry: radius(R), an angle aligned with circumference (θ), and width (Z).

during winding. The web’s total MD distance therefore is also its length. The width of a web (and its corresponding wound roll) is known as the Cross Machine Direction (CMD), (Z), or sometimes Cross Direction (CD). Often the distance from the outside of the core to the roll’s top layer is referred to as the stack, or pile height.

Wound Roll Stresses

A wound roll is in a state of tri-axial stress. The two most studied and understood stresses are the radial pressure, and the circumferential stress. The impact of the CMD

stresses, and the shearing stresses on the web before it enters the wound roll have been carefully studied. But, the web's CMD stresses after the web is inside the wound roll have been comparatively ignored to this point. They have been assumed to be negligible and as a result their importance is not yet known.

As shown in Figure #I-3, the quality of a wound roll directly relates to its stresses.

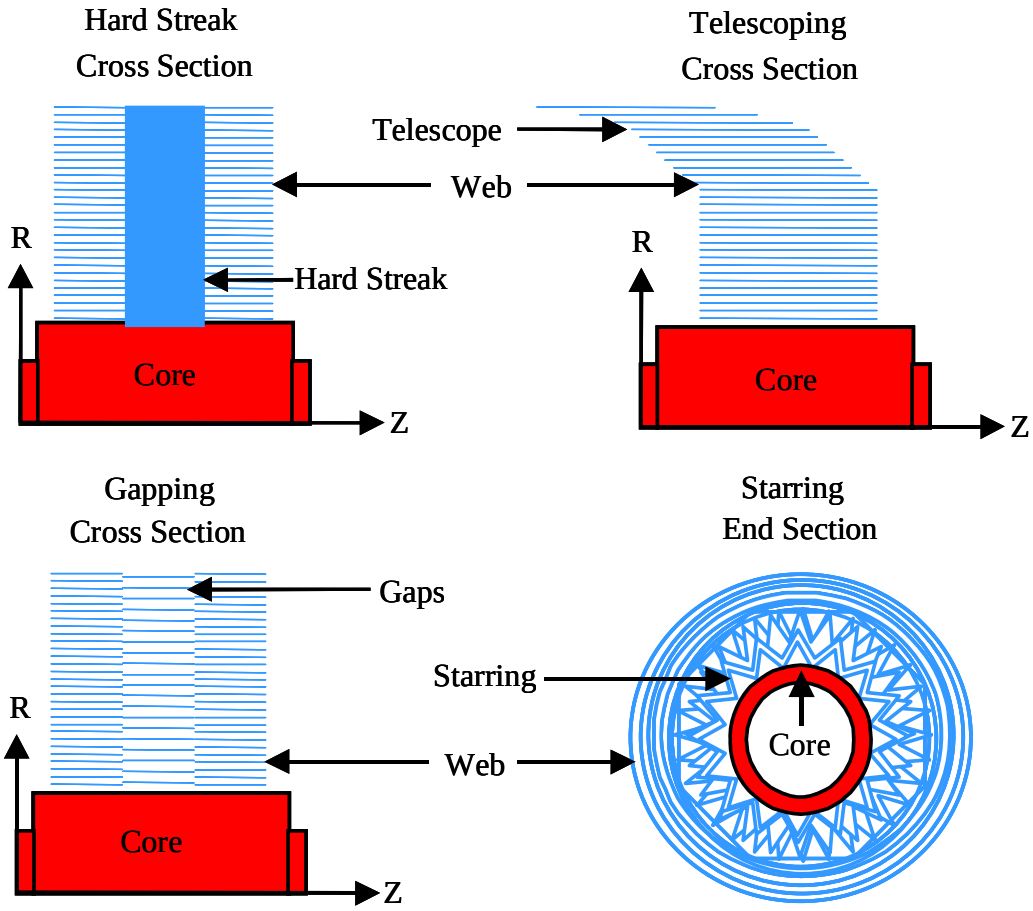

Figure #I-3: In a wound roll, very high or very low stresses can cause defects such as hard streaks, telescoping, gapping, or starring.

Small radial pressure translates into small, interlayer normal forces and consequently low frictional forces. The result may be a defect known as telescoping, where layers slip past each other in the CMD direction. Conversely, excessive radial pressure may induce inelastic deformations or permanently adhere layers together into a solid. Since these

layers typically persist around the roll's circumference, they become a near rigid band in a defect known as a hard streak. Another stress related defect is a soft area caused by gapping. Gapping occurs when successive layers in a region do not contact each other due to a low, local circumferential stress. This can result in creases in the material. The opposite extreme occurs when large circumferential stresses cinch upper layers tight around lower layers causing them to buckle or fold. This defect is called starring because when the roll is examined from its end, down the Z axis, it looks geometrically like a star. In some extreme cases, high pressures and stresses could even collapse the core inward.

The stresses in a wound roll trace back to either winding or storage. During the winding process, the tension applied to a web being wound into a roll ends up as stress inside the roll. For webs that spend little time wound up as a roll, the winding induced stresses are the only ones of concern. However, when a web is stored as a wound roll for any significant period of time, after-winding variables such as viscoelasticity, losing entrained air, and temperature also become possible stress sources. These variables generally reallocate the stresses wound into the roll creating stress differentials, which can damage a previously acceptable roll. The time required for defects to occur depends on the mechanism driving the changes. Whether they occur during or after winding, the correlation between wound roll stress and quality justifies further study.

Radial Modulus

The stress versus strain curves for web stacks characterize wound roll behavior. Most continuous substances have linear stress versus strain curves up to some yield point. But, in a landmark publication, Pfeiffer [24] showed that stress-versus-strain profiles for

web stacks are nonlinear. He proposed an expression with coefficients that essentially become material constants. Of greater practical use was his radial modulus (E_r) expression, which is the slope of the radial pressure versus strain curve. Pfeiffer determined a web's radial modulus depends on the pressure applied to it.

Many variations of Pfeiffer's radial modulus expression are in use today. Despite their differences, they all maintain a dependence on the radial pressure. Table #I-1 lists the radial modulus expressions for an aluminum block, and four example web materials. For comparison, Figure #I-4 plots the expressions used for the different materials.

Material	Radial Modulus Expression	Unit	Reference
Aluminum Block	1.0 E 7	psi	[16]
Pfeiffer; CATALOG Paper	41.4*P	psi	[24]
Hakiel; Polyester Film	$1060*P - 0.513*P^2$	psi	[14]
Cole/ Hakiel; PET Film	$361840.1*(1-e^{(-P / 1254.47)})$	psi	[4]
Good; NEWS Paper	$50.6*P - 0.664*P^2 + 0.005*P^3$	psi	[11]

Table #I-1: Contrasting the constant radial modulus for continuous solids (like a block of aluminum), radial moduli for web stacks depend on applied pressure.

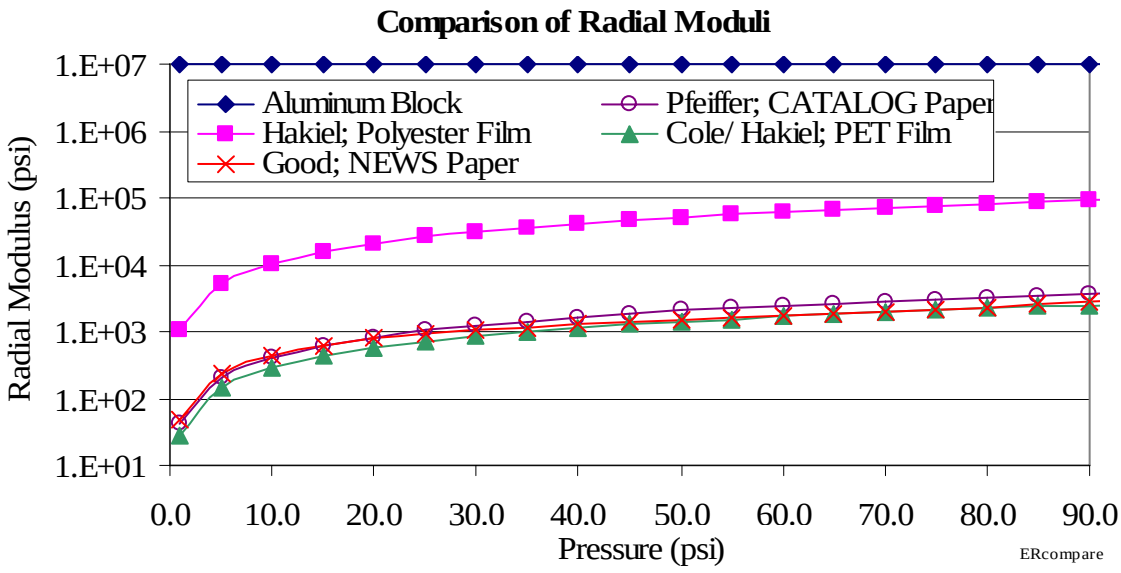

Figure #I-4: At low pressures, most web stacks have a low radial modulus, and therefore are initially quite compressible. Continuous solids, such as an aluminum block, have much higher, constant moduli, with no compressibility change.

In a wound roll, the radial modulus' pressure dependence makes it vary with radius. As mentioned, a web wound into a roll is under tension. As it wraps the roll, the web is in the shape of a spiral and acts like a tensioned hoop. It exerts radial pressure inward in proportion to its tension. So as a roll winds, each new layer exerts pressure on all the layers below it. This also means each layer receives some amount of pressure from every layer wound above it. Those layers closer to the core have more layers above them and consequently have more total pressure exerted on them. Thus, in a wound roll the radial pressure and its corresponding radial modulus are highest at the core and diminish toward the outside. The diminishing radial pressure with radius can be seen graphically in a copy of Pfeiffer's [27, Fig. #4] pressure versus radius plot shown as Figure #I-5.

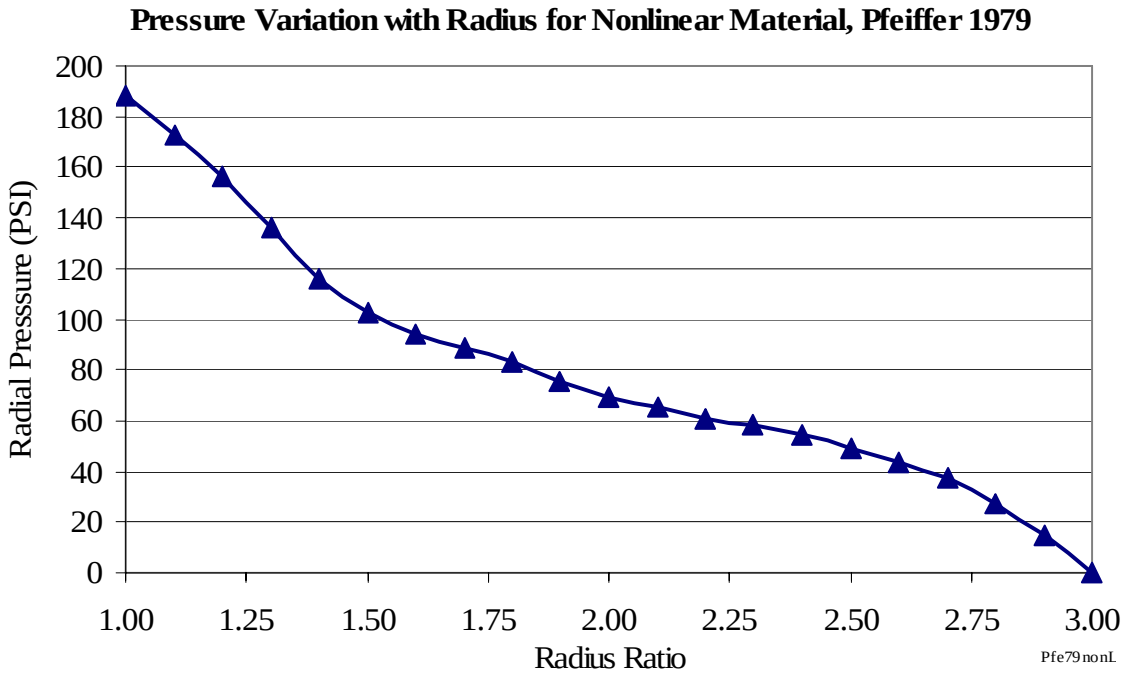

Figure #I-5: During winding the radial pressure in a wound roll builds up near the core and falls to zero at the outside edge.

Thickness Variations

In addition to varying with the radius in a wound roll, thickness variations cause the pressure to vary also with CMD location. Thickness variations are non-uniformities in the web's thickness with respect to the CMD direction. They tend to persist in the web's length dimension because whatever creates the variations during the manufacturing process tends to remain in the manufacturing process. For this reason they are sometimes referred to as lengthwise persistent thickness variations. Figure #I-6 shows a CMD thickness profile for a PolyEthylene Terephthalate (PET) web with a varying thickness as presented by Cole and Hakiel [4, Fig. #7].

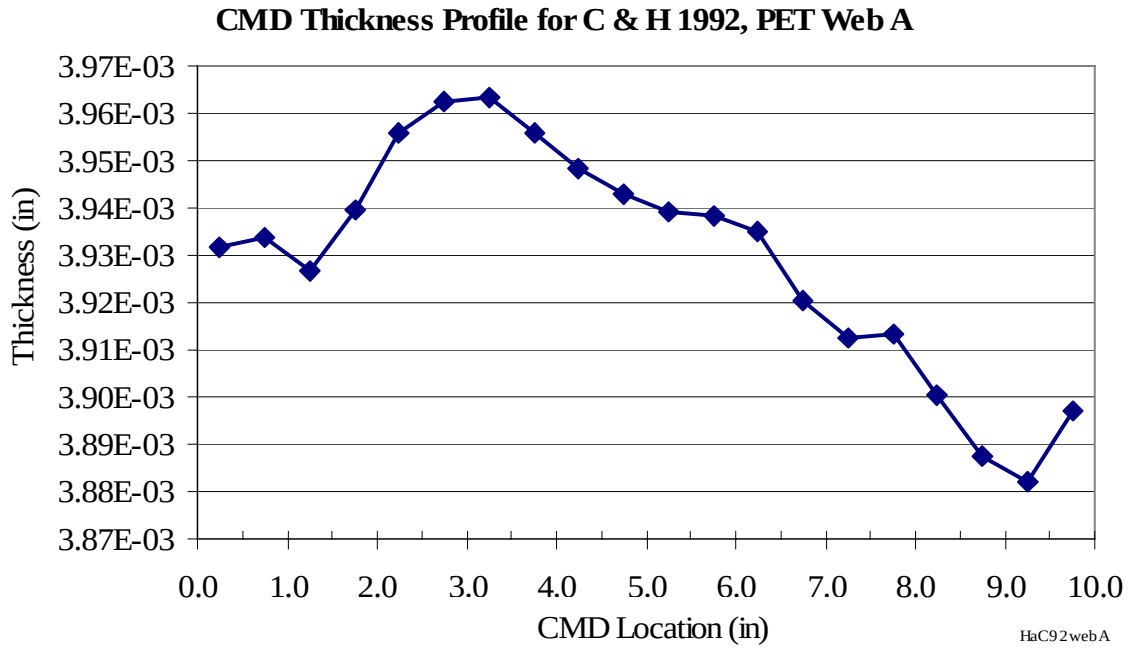

Figure #I-6: Webs often vary in thickness across their width, and this variation tends to persist along their length.

Figure #I-7 presents the resulting wound roll radial pressure variation Cole and Hakiel measured when they wound this web.

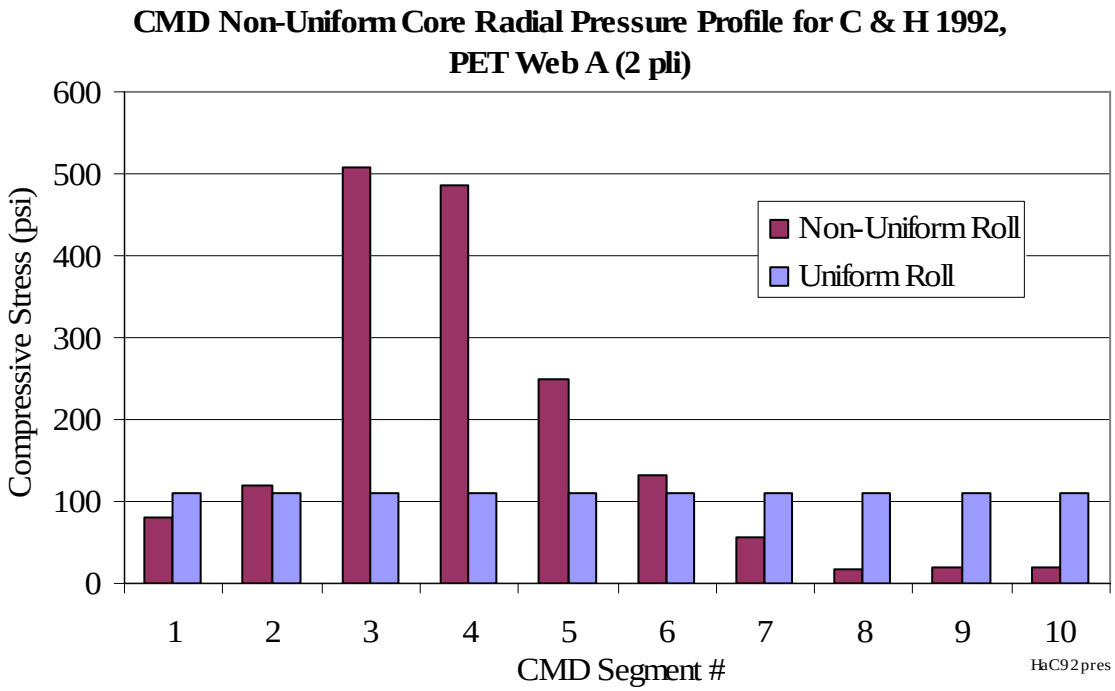

Figure #I-7: A web with a non-uniform CMD thickness profile produces a radial pressure profile with increased pressures in locations corresponding to increased thicknesses.

The lengthwise persistence of the thickness variations significantly impacts the winding. When many layers are wound on top of each other, the thickness variations are amplified. This fact is illustrated by the simple example web profile in Figure #I-8.

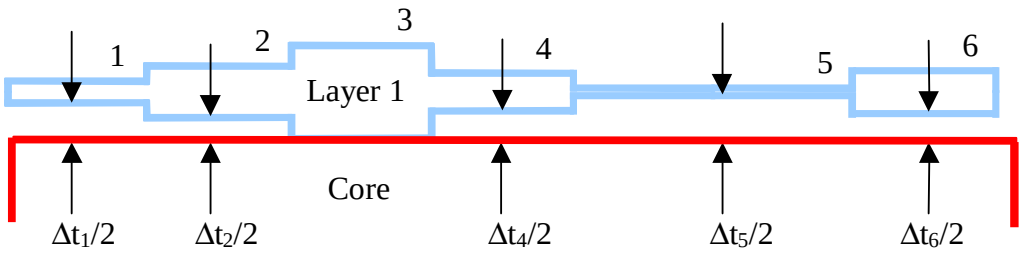

Figure #I-8: A non-uniform layer suspended above a core leaves gaps equivalent to half the difference (Δ) in segment thicknesses.

As the web winds, the thickest area (also called a segment), area three (3), builds in height faster than the other thinner areas. For example, for each layer added, segment one (1) falls behind by the amount $2*(\Delta t_1/2) = \Delta t_1$ as shown in Figure #I-9.

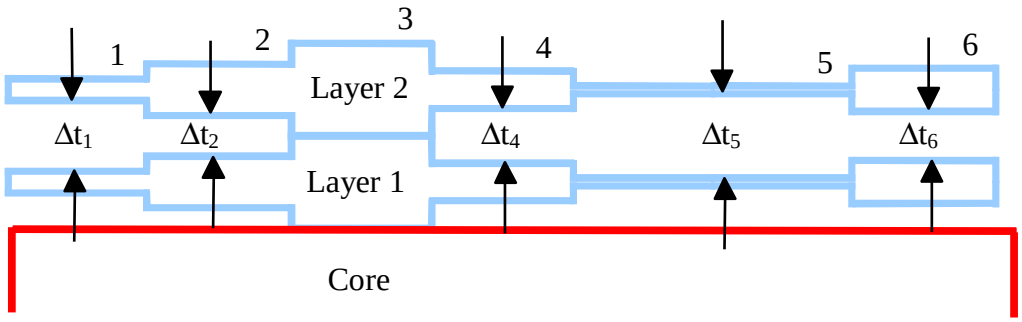

Figure #I-9: As non-uniform layers are wound onto one another, thinner segments must overcome gaps equal to the difference in segment thicknesses before they will contact adjoining layers.

If there were no tensions or bending involved, each successive layer would remain suspended above the others as shown. However as seen in Figure #I-10, the tensions and bending move the layers in toward the core until they rest in equilibrium.

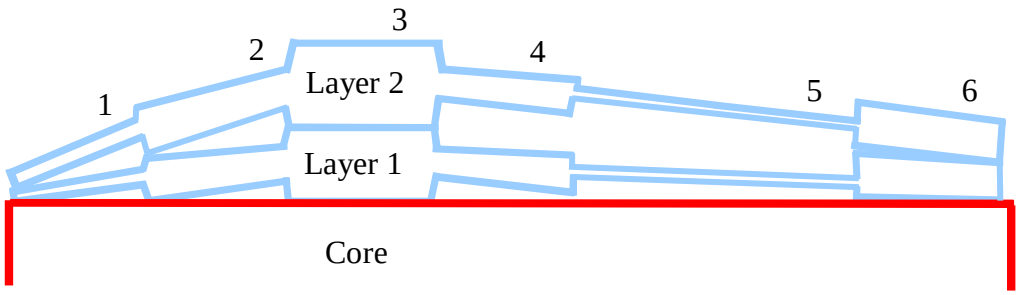

Figure #I-10: In the presence of tension and bending, layers move inward and compress until equilibrium is reached.

At segment three (3), the outer layer always contacts the layers beneath it, so the layer's movement toward the core compresses the segment more, and thereby gives it a higher radial pressure. At the same time, since segment five (5) receives little or no contact, the radial movement creates no pressure. For this reason, a perfectly uniform thickness roll

won't have either the high or the low pressures, nor the possible resulting defects associated with a non-uniform roll.

Nip Rollers

The presence of a nip roller during winding can also cause a CMD pressure variation. A nip roller (sometimes referred to as a rider roller) is a roller that rests on the outside surface of a wound roll during winding. As seen in Figure #I-11, forces applied

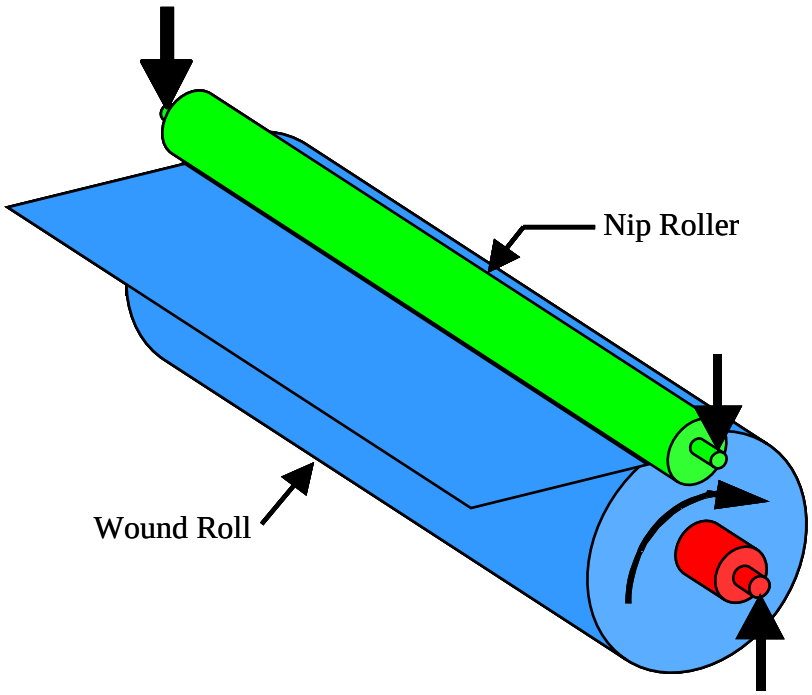

Figure #I-11: Nip rollers are placed on the outsides of wound rolls to make them more uniform by compressing them.

to the nip roller's stub shafts push it toward the wound roll. This compresses the wound roll anywhere the nip roller contacts it. The amount of nip induced compression varies across the wound roll width in response to the nip roller's loading, its bending stiffness, and the wound roll's radial modulus. The result of a nip roller on a uniform roll is a varying radius across the width as depicted in Figure #I-12.

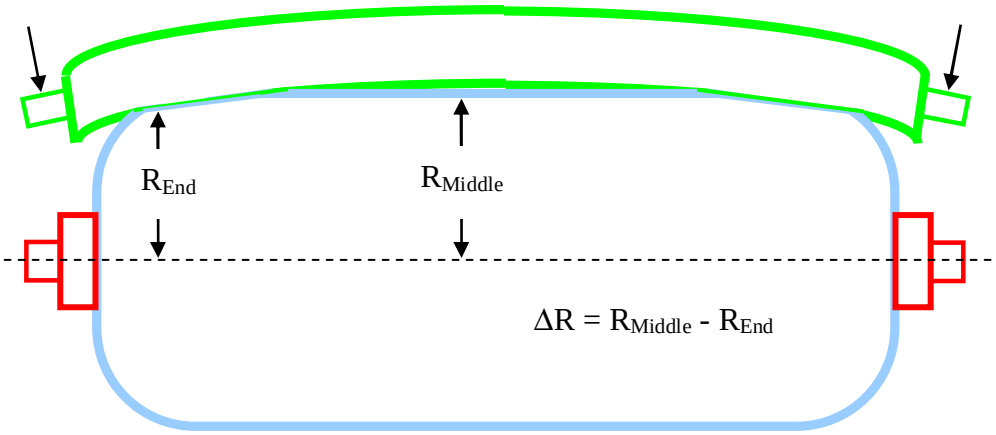

Figure #I-12: Due to their loading and bending, nip rollers compress a uniform wound roll more at the edges then in the center.

The wound roll pressures are higher in the areas of greater wound roll compression. Hoffecker [17] correlates the nip's load, to the compression it induces across the width, using a static finite element model (FEM) analysis.

Nip rollers are commonly used to flatten out non-uniform wound rolls. If a nip roller is brought down into contact with a non-uniform roll, it contacts the roll's highest segments first. By increasing the load applied to the nip, the highest segments are compressed until the nip contacts some of the lower segments. With the additional applied load, the nip contacts more segments. Thus, the non-uniform roll is forced to conform to the nip's shape. As mentioned before, this occurs at the expense of increased radial pressure in the thicker segments. The nip however is generally not brought into contact with a non-uniform roll with large radial variations across its width, because it instead starts out contacting the roll before many layers are wound. As a result, it may be in nearly full contact across the width of the roll throughout the entire wind. Even so, the radial pressures will still be highest for the thickest segments. Each segment will be

compressed by the nip immediately as it enters the wound roll in proportion to its thickness as the nip works to maintain the roll to its shape.

The overall contact between the nip and a non-uniform roll during winding is a complex combination of four local contact possibilities as depicted in Figure #I-13.

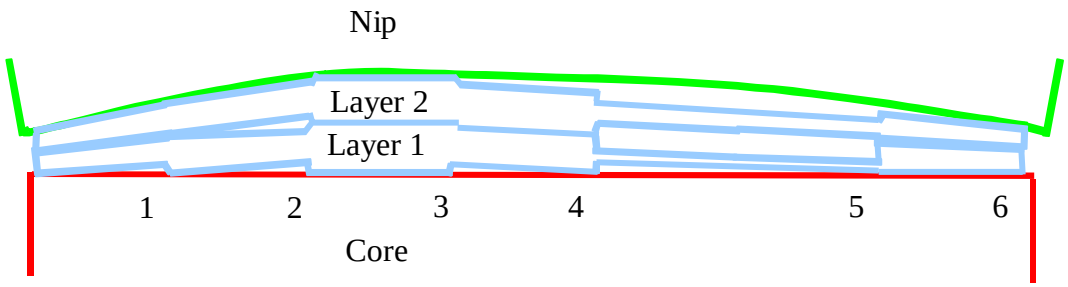

Figure #I-13: The overall contact between a nip roller and a non-uniform wound roll is a combination of: contact with a higher radius segment (segment 3), contact with a lower radius segment (segment 1), non-contact with a higher radius segment (segment 4), and non-contact with a lower radius segment (segment 5).

The nip roll may contact a location with a higher radius. Or, the nip roll may contact a location with a lower radius. A location may have a higher radius, but no nip roll contact. Finally, the location may have a lower radius and no nip roll contact. Since the overall contact can contain any number or combination of the four possibilities, it depends not only on their individual effects, but also how they combine. Their combination must satisfy constraining conditions resulting from equilibrium, the angle the web wraps the nip, nip gapping, web wrinkling, and the thickness variations.

Project Goals

In industries that deal with wound rolls (generally known as web handlers), roll quality is of paramount importance. Web and wound roll defects are estimated to

account for millions of dollars worth of product losses annually. As a result, wound roll quality prediction has been a major concern in the industry for many years. It is the reason that a number of web handling companies formed a consortium in partnership with the Web Handling Research Center (WHRC) at Oklahoma State University. Wound roll quality prediction and improvement is the underlying theme from the already mentioned Pfeiffer [24] publication from 1966. Another early publication, from Altmann [1] in 1968, also cites the importance of quality prediction and even mentions government sponsored funding conducted by Gutterman [13], dating back to 1959. More recent publications also address how to improve and predict wound roll quality. It is therefore certain that the web handling industry would benefit greatly if it was able to accurately estimate the quality of a roll, before the roll was even wound. It is also certain that, since the need still exists after 40 years of effort, accurately predicting and improving wound roll quality is a difficult task.

This project's primary goal is the development of an accurate three dimensional, nip contacting, wound roll model. It requires both a theoretical analysis, and an experimental validation. The resulting model, in the form of an executable computer code, should accommodate various roll, core, and nip configurations. Additional, secondary goals include searching for dominating and constraining mechanisms and characterizing the equilibrium, wrap angle, nip gapping, wrinkling, and thickness variations present in a nip impinged, three dimensional roll. The intention is to provide a tool that determines wound roll stresses well enough that it can be used to improve a wound roll's quality.

CHAPTER TWO

LITERATURE SURVEY

The groundwork needed to construct a nip impinged, three dimensional wound roll model includes three categories: two dimensional rolls, three dimensional rolls, and nip roller mechanics. Two dimensional focused investigations are concerned only with the radial and circumferential directions in a wound roll. Effects due to CMD variations in properties like thickness (also called caliper), and tension are not included. All properties remain uniform across the entire web width. Three dimensional investigations specifically examine how non-uniform properties across the width affect a wound roll. Many of them extend existing two dimensional works by adding a CMD caliper variation. The investigations into nip roller mechanics attempt to characterize the role nip rollers play in winding. They analyze both the roll's resulting compression and the redistribution of the web's tension. Some works do address more than one category, but none produce a comprehensive package.

Two Dimensional Investigations

Two dimensional investigations focus on determining a relationship between the web's tension before it is wound onto a roll (known as the web line tension, T_W), and the roll's resulting stresses. Pfeiffer [24] addresses stresses throughout a roll, but lacks a qualitative procedure to predict them. It shows that the radial stack modulus is not a

constant by quantifying an experimentally found, non-linear dependence between a roll's compressive pressure and its strain. Conversely, Altmann's [1] publication predicts a roll's stresses from its web line tension, but its solution is a function of a constant radial modulus. Yagoda [33] shows that the core's stiffness and deformation also impacts the roll's stresses. Then, Hakiel [14] combines the energy input from the web line tension, the core dependence, and the variable modulus into the first widely accepted center-winding model. Finally, Good and Pfeiffer [10] show that web line tension can be lost through radial deformation of the wound roll.

Pfeiffer [24] is a broad publication addressing many wound roll issues. It considers winding with and without a nip roller. It explores ways to experimentally measure pressures in a roll. It proposes an expression that models the intrinsic relationship between the stress and strain in a web stack. It also suggests explicit correlations between in-roll stresses and wound roll defects.

Pfeiffer's investigation began by looking for a device to gauge wound roll hardness. An accelerometer mounted on a striker produced repeatable data with output amplitudes proportional to roll hardness. He concluded that the speed a sound wave traveled through a paper stack or roll was related to its pressure, so in further tests he instrumented finished wound rolls with a sound generator and receiver combination. The resulting data facilitated calculations and plots of the radial pressure and circumferential tension versus each roll's radius. These plots helped explain physical phenomena in the rolls like the causes of some defects. Stress versus radius plots are still widely used today to appraise a wound roll's stress state.

Of great significance is the investigation's treatment of the compressive and dynamic moduli. Figure #II-1 (taken directly from Pfeiffer's publication) shows the compressive pressure versus compressive strain in both linear and semilogarithmic plots. The relaxation curves on the right side of each plot were found to be independent of the strain rate. On the other hand, the minor loop in the semilog plot came from a dynamic loading and is strain rate dependent.

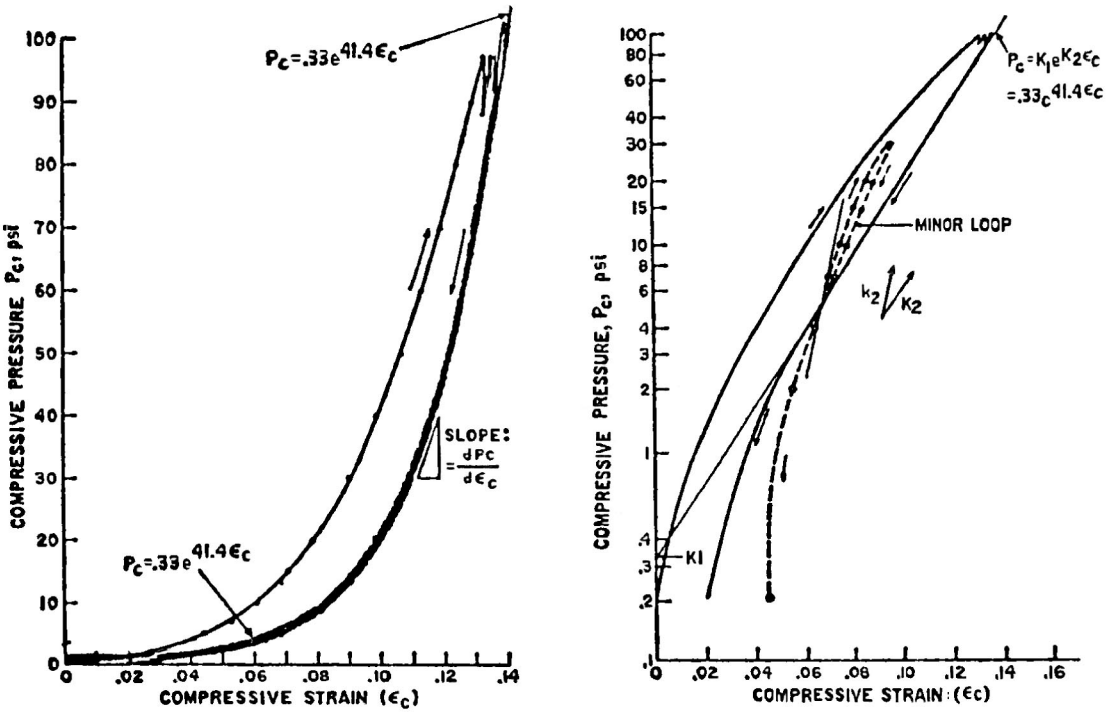

Figure #II-1: Pfeiffer's [24, Figs. #7 & #8] compressive stress versus strain plots for catalog paper show the exponential behavior associated with web stacks.

Since the slope of a material's stress versus strain plot is equivalent to its tangential modulus, Pfeiffer sought out an expression for the slope. The linearity in the semilog plot prompted him to curve fit to an exponential function, given here as equation #II-1.

$$P_c = K_1 e^{K_2 \varepsilon_c} = 0.33 e^{41.4 \varepsilon_c} \qquad \text{(II-1.}$$

The compressive pressure and compressive strain are represented by P_c (psi), and ε_c (in/in) respectively. The coefficients K_1 and K_2 hold little meaning at this point, but become valuable in the next step: expressing the elastic modulus E. It is found by taking the derivative of P_c (see equation #II-2). Pfeiffer also wanted the modulus to be in terms of the compressive pressure, so the P_c expression (equation #II-1) is substituted back in.

$$\text{elastic compressive tangential radial modulus} = E = \frac{dP_c}{d\varepsilon_c} = K_2 K_1 e^{K_2 \varepsilon_c} = K_2 P_c \quad \text{(II-2.}$$

The elastic modulus E (psi) ends up being linearly dependent on P_c by the factor K_2. In other words, K_2 is the basic springiness factor of the material (as well as the slope of the semilog plot). Likewise, K_1 is the rest pressure in psi (also the y-intercept on the plot). The dynamic modulus is similarly found to be $k_2 P_c$, with k_2 referred to as the dynamic springiness factor. At the origination pressure of the minor loop, the slope is consistent above and below the pressure point, and equals k_2. However, at a different origination pressure, k_2 would take on a different value, and therefore it is a function of pressure. By inserting the dynamic modulus expression into an equation for the velocity of sound traveling through a medium, and comparing that to the earlier mentioned relationship between the speed of sound and the compressive pressure in a web stack, k_2 is found to be equal to the expression shown in equation #II-3.

$$k_2 = P^{-0.275} \quad \text{(II-3.}$$

Equation #II-4 then expresses the dynamic modulus in terms of pressure only.

$$\text{dynamic modulus} = k_2 P = P^{0.725} \quad \text{(II-4.}$$

In this way, Pfeiffer expressed both the elastic and dynamic moduli in terms of the pressure applied to the web stack.

In another significant publication, Altmann [1] takes an analytical approach to find expressions for the radial pressure and circumferential tension in a center-wound roll. To simplify the endeavor, he assumes the roll has a uniform core, web profile, and circumferential stress, has no slipping, and most notably is a homogenous cylinder with constant moduli and Poisson's ratios.

He first utilizes governing equations to find a general solution. Altmann begins with the two dimensional, radial and circumferential constitutive equations, equations #II-5 and #II-6 (which have been modified here to maintain consistent nomenclature).

$$\varepsilon_{rr} = \frac{\sigma_{rr}}{E_r} - \nu_{\theta r}\frac{\sigma_{\theta\theta}}{E_\theta} \qquad \text{(II-5.}$$

$$\varepsilon_{\theta\theta} = \frac{\sigma_{\theta\theta}}{E_\theta} - \nu_{r\theta}\frac{\sigma_{rr}}{E_r} \qquad \text{(II-6.}$$

The ε_{rr} and $\varepsilon_{\theta\theta}$ are radial and tangential strains, $\nu_{\theta r}$ is the Poisson's ratio that transfers strain from the tangential direction to the radial direction, and $\nu_{r\theta}$ is the Poisson's Ratio that transfers strain from the radial direction to the tangential direction. Also, σ_{rr} and $\sigma_{\theta\theta}$ are the radial and tangential stresses, while E_r and E_θ are the radial and tangential moduli. By substituting polar strains (equations #II-7 and #II-8) into equations #II-5 and #II-6,

$$\varepsilon_{rr} = \frac{du}{dr} \qquad \text{(II-7.}$$

$$\varepsilon_{\theta\theta} = \frac{u}{r} \qquad \text{(II-8.}$$

simultaneously solving for the stresses, (equations #II-9 and #II-10)

$$\sigma_{rr} = \left(\frac{E_r}{1-\nu_{r\theta}\nu_{\theta r}}\right)\left(\nu_{\theta r}\frac{u}{r} + \frac{du}{dr}\right) \qquad \text{(II-9.}$$

$$\sigma_{\theta\theta} = \left(\frac{E_\theta}{1 - \nu_{r\theta}\nu_{\theta r}} \right) \left(\frac{u}{r} + \nu_{r\theta} \frac{du}{dr} \right) \qquad \text{(II-10.}$$

and then substituting them into the polar equilibrium equation (equation #II-11),

$$r \frac{d\sigma_{rr}}{dr} + \sigma_{rr} - \sigma_{\theta\theta} = 0 \qquad \text{(II-11.}$$

he finds a second-order differential equation in terms of radial deformation u, and radius r, whose general solution is equation #II-12 (modified for consistent nomenclature).

$$u = \left(H_1 \left[\frac{r}{\bar{c}} \right]^{\alpha} + H_2 \left[\frac{r}{\bar{c}} \right]^{-\beta} \right) \bar{c} \qquad \text{(II-12.}$$

The solution is presented in terms of two unknown constants H_1 and H_2, the core's radius $\bar{c}$, and two variables α and β which contain material properties. Equations #II-13 and #II-14 show the explicit expansions of variables α and β.

$$\alpha = \frac{1}{2E_r} \left[\sqrt{\nu_{\theta r}^2 E_r^2 - 2\nu_{\theta r} E_r E_\theta \nu_{r\theta} + \nu_{r\theta}^2 E_\theta^2 + 4E_\theta E_r} + E_\theta \nu_{r\theta} - E_r \nu_{\theta r} \right] \qquad \text{(II-13.}$$

$$\beta = \frac{1}{2E_r} \left[\sqrt{\nu_{\theta r}^2 E_r^2 - 2\nu_{\theta r} E_r E_\theta \nu_{r\theta} + \nu_{r\theta}^2 E_\theta^2 + 4E_\theta E_r} - E_\theta \nu_{r\theta} + E_r \nu_{\theta r} \right] \qquad \text{(II-14.}$$

To solve for the pressure and tension, Altmann applies a boundary condition which matches the radial pressure of the core and the wound roll at the core's outer contact surface. To express the core's radial pressure, he uses the core's elasticity constant E_C (defined as the pressure required to strain the core's outside surface radially inward one inch/ inch) to set up a relationship between radial pressure and displacement. Solving this relationship explicitly for deformation (modified here as equation #II-15),

$$u = \left(\frac{\sigma_{rr}}{E_c} \right) \bar{c} \qquad \text{(II-15.}$$

setting it equal to equation #II-12 evaluated at r = $\bar{c}$, and then multiplying through by E_C yields equation #II-16 for the core radial pressure in terms of the constants H_1 and H_2.

$$\sigma_{rr} = E_c\left(H_1 + H_2\right) \qquad \text{(II-16.}$$

Now, setting equation #II-16 equal to equation #II-9 (with again both u, via equation #II-12, and r evaluated at the core) enforces the core pressure boundary condition, and establishes the first equation necessary to solve for H_1 and H_2.

A second boundary condition assumes a particular applied pressure at the outside of the wound roll. This pressure depends on the winding tension and changes with each layer wound onto the roll in proportion to the current outside radius. In this way, each outside web layer itself serves as a boundary layer imposing a different boundary pressure. Each new boundary layer's pressure contributes incrementally to the pressures and tensions of all the web layers beneath it. The relationship between the boundary pressure, the web line tension, and the radius also depends on the thickness of the web layer (t), and is referred to as the hoop stress formula. It is given here as equation #II-17.

$$\sigma_{rr} = \frac{T_W}{r} t \qquad \text{(II-17.}$$

Inserting equation #II-12 (evaluated at the current radius r) and an incremental thickness version of equation #II-17 into equation #II-9 yields the necessary second equation to solve for H_1 and H_2.

The equations are now combined to create the overall pressure and tension in the roll. H_1 and H_2 substitute directly back into equation #II-12. In turn, this goes into equations #II-9 and #II-10 to produce the incremental pressure and tension in a wound roll resulting from adding on a layer at tension T_W. The roll's pressure and tension at a radius r are found by integrating these two equations from that radius outward to the final

radius R. The variable s is used as the integration term for r. The resulting integrals (modified here for consistent nomenclature) are equations #II-18 and #II-19.

$$P[r] = \left(\frac{1 + a\left(\frac{r}{\bar{c}}\right)^{-2\gamma}}{\left(\frac{r}{\bar{c}}\right)^{b}} \right) \int_{\left(\frac{r}{\bar{c}}\right)}^{\left(\frac{R}{\bar{c}}\right)} \left(\frac{\left(\frac{s}{\bar{c}}\right)^{b}}{1 + a\left(\frac{s}{\bar{c}}\right)^{-2\gamma}} \right) \left(\frac{T_W}{s} \right) ds \qquad \text{(II-18.}$$

$$T[r] = T_W - \left(\frac{\alpha - a\beta\left(\frac{r}{\bar{c}}\right)^{-2\gamma}}{\left(\frac{r}{\bar{c}}\right)^{b}} \right) \int_{\left(\frac{r}{\bar{c}}\right)}^{\left(\frac{R}{\bar{c}}\right)} \left(\frac{\left(\frac{s}{\bar{c}}\right)^{b}}{1 + a\left(\frac{s}{\bar{c}}\right)^{-2\gamma}} \right) \left(\frac{T_W}{s} \right) ds \qquad \text{(II-19.}$$

Here, P and T are the total pressure and tension in the roll respectively. For reference the expressions for variables a, b and γ are given collectively as equation #II-20.

$$a = \frac{\gamma 2E_c E_r - E_r E_c \nu_{\theta r} + E_\theta E_c \nu_{r\theta} - 2E_\theta E_r}{\gamma 2E_c E_r + E_r E_c \nu_{\theta r} + E_\theta E_c \nu_{r\theta} + 2E_\theta E_r}$$

$$\gamma = \frac{1}{2E_r} \left| \sqrt{\left(E_r \nu_{\theta r} - E_\theta \nu_{r\theta}\right)^2 + 4E_r E_\theta} \right| \qquad \text{(II-20.}$$

$$b = \frac{1}{2E_r} \left(2E_r - \left| \sqrt{\left(E_r \nu_{\theta r} - E_\theta \nu_{r\theta}\right)^2 + 4E_r E_\theta} \right| - E_r \nu_{\theta r} - E_\theta \nu_{r\theta} \right)$$

The resulting Altmann algorithm compares well with Pfeiffer's experimental results in constant-pressure rolls. In varying-pressure rolls, equations #II-18 and #II-19 bracket Pfeiffer's results giving a range for comparison. This is evident in Figure #II-2, taken directly from Altmann [1]. Altmann states the bracketing is necessary because his derivation assumes E_r to be a constant throughout the roll, not a pressure dependent variable as in Pfeiffer's [24] E_r function (equation #II-2). He concludes that with good knowledge of the input variables (especially T_W), the algorithm predicts pressure and tension in two-dimensional wound rolls quite well.

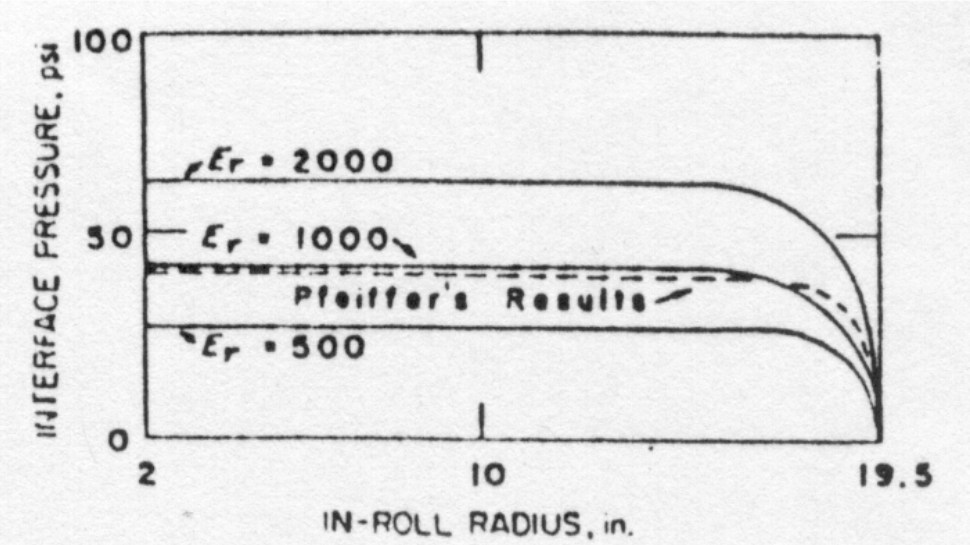

Fig. 1. Measured and computed interface pressures for Pfeiffer's 33-lb newsprint roll.

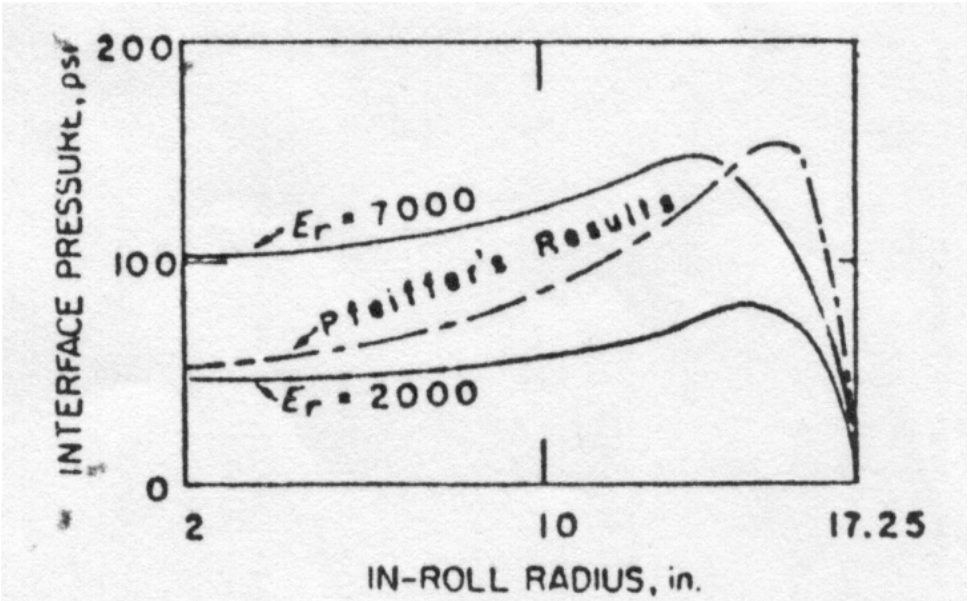

Fig. 3. Measured and computed interface pressures for Pfeiffer's 22-lb catalog grade roll.

Figure #II-2: Altmann's [1, Figs. #1 & #3] roll model resembles Pfeiffer's experimental results when predicting radial interface pressures in constant-pressure 33-lb newsprint, but not in the variable-pressure 22-lb catalog paper.

Yagoda [33] focuses on the effect a core has on a wound roll. He believes previous formulations underestimate the core's impact because they exhibit constant radial pressure for nearly the entire roll. Yagoda explains there should instead be a variation in radial pressure near the core that indicates the transition to a comparatively compressible roll. He states that the core is crucial in supporting the rest of the roll.

His model builds off of Altmann's [1] formulation, but then makes two distinct departures. The underlying framework established by equations #II-18, and #II-19 is the same with the minor exception of a P_W term (an applied radial pressure) added to equation #II-18 to make it more general. But then, the core boundary condition goes beyond matching the interface pressure, as Altmann did, by additionally equating its strains. This is significant because mathematically equating pressure alone does not guarantee the core and first layer's deflections are physically synchronized. In other words, layers inside the roll are subject to bi-axial (or even tri-axial) loading and thus behave according to equation #II-6 and equation #II-11, not just the pressure matching equation #II-17. Yagoda's second departure from Altmann's formulation is to solve the closed form solution integrals by using hypergeometric functions. This approach requires T_W to be expressed as a power series summation dependent on the roll radius and as a result, the solutions (given here as equation #II-21 and #II-22) are series expansions whose accuracy depends on the number of terms used.

$$\frac{P}{T_0} = \frac{P_W}{T_0} + \left(1 + a\left(\frac{r}{\bar{c}}\right)^{-2\gamma}\right)\sum_{n=0}^{M} \Lambda\left(\frac{r}{\bar{c}}, \frac{R}{\bar{c}}, \phi_n\right) C_n \left(\frac{r}{\bar{c}}\right)^{\phi_n} \qquad \text{(II-21.}$$

$$\frac{T}{T_0} = \frac{T_W}{T_0} - \left(\alpha - a\beta\left(\frac{r}{\bar{c}}\right)^{-2\gamma}\right)\sum_{n=0}^{M} \Lambda\left(\frac{r}{\bar{c}}, \frac{R}{\bar{c}}, \phi_n\right) C_n \left(\frac{r}{\bar{c}}\right)^{\phi_n} \qquad \text{(II-22.}$$

In these equations, the T_0 variable represents initial web line tension. The terms C_n, and ϕ_n from inside the summation are respectively the coefficients and exponent terms of the tension power series. They number up to M terms. The function $\Lambda(r/\bar{c}, R/\bar{c}, \phi_n)$ depends on the physical radii of the roll and the power series exponents. The full expansion is available in Yagoda [33, eq. #39].

Ultimately, Yagoda's solution results in a more realistic model. The core boundary condition allows him to develop a relation between core pressure and the wound roll's circumferential stress. This facilitates parametric analyses to determine if cores have adequate elastic stiffness, E_C, to support their rolls. The proper selection of E_C, and the additional accuracy offered through the hypergeometric functions combine to produce a model better suited to the changing stresses in the roll. Yagoda's solution captures the roll's large, radial pressure transition in the vicinity of the core as is readily apparent in its radial pressure and circumferential stress plots, shown as Figure #II-3. Although, in the figure, the transition region for a continuous linear scale on the abscissa would be quite narrow, the behavior is widely accepted today as a trademark of wound rolls near the core. More recent investigations, especially Hakiel [14], find the region is larger and that its shape even serves as a way to identify the type and hardness of the web material. They determine that compressible webs transition more rapidly and drastically than nearly incompressible webs.

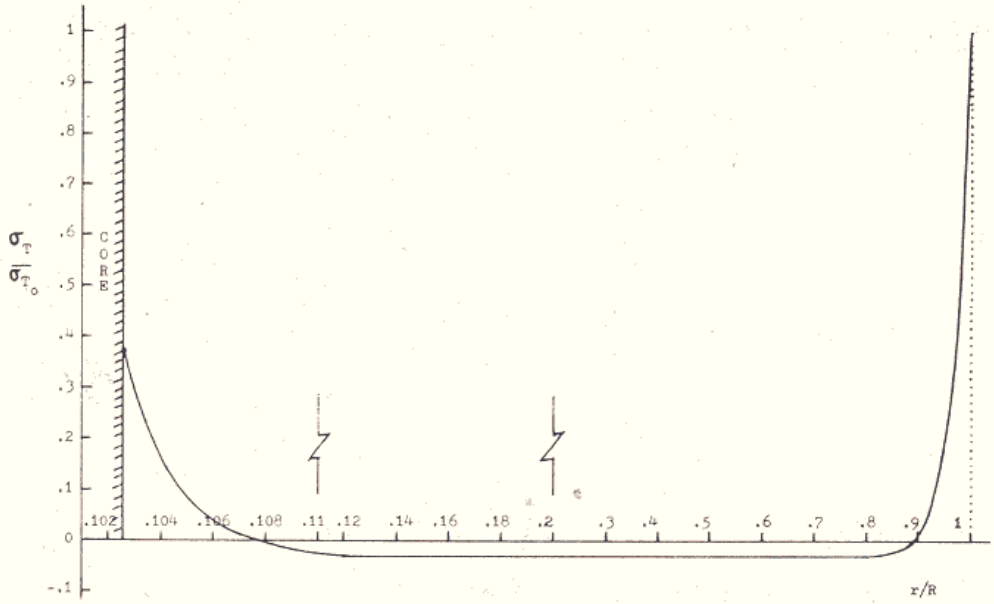

Fig. 3(*a*) Circumferential stress profile for the 33-lb newsprint roll, e.g., equation (43)

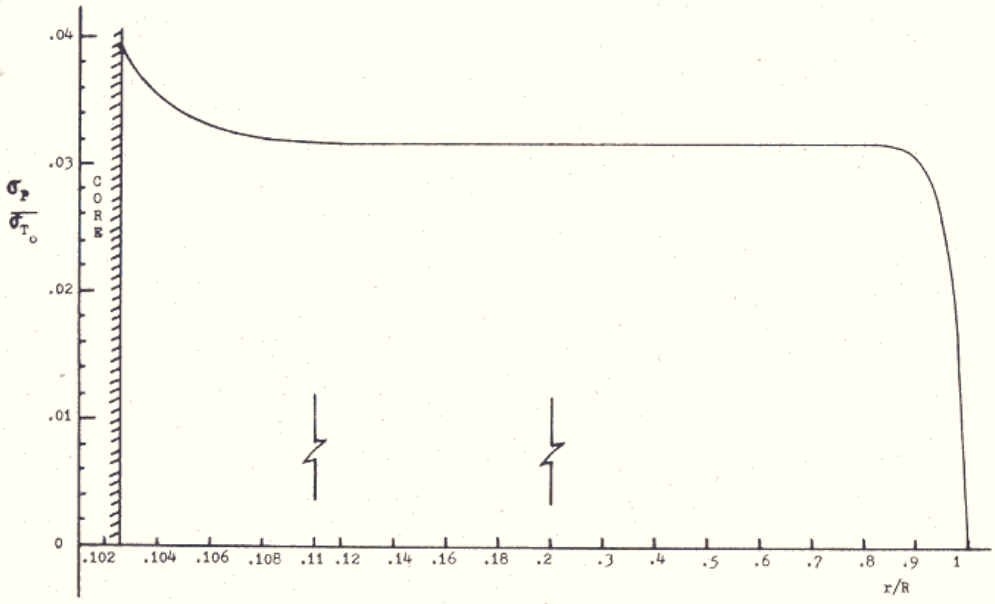

Fig. 3(*b*) Pressure profile for the 33-lb newsprint roll, e.g., equation (43)

Figure #II-3: Yagoda's [33, Fig. #3(a) and #3(b)] roll model radial pressure and circumferential stress results plotted on a non-linear, radius-ratio abscissa show a definite transition region near the comparatively incompressible core.

Hakiel [14] successfully incorporates the three previous works into a cohesive stress predicting model for center-wound rolls. He continues the assumptions of constant web and roll properties across the width and throughout each layer, and constrains all the stresses to a cross sectional plane, making it a plane stress model. But in the plane he combines the linear circumferential modulus with Pfeiffer's [24] nonlinear radial modulus to produce orthotropic behavior. Hakiel then uses much of Altmann's [1] roll derivations to produce a non-analytical boundary value problem that conforms to the core boundary condition given by Yagoda [33].

Hakiel first develops an expression to model wound roll radial pressure behavior. Utilizing Maxwell's energy conservation relationship (modified here as equation #II-23),

$$\frac{\nu_{r\theta}}{E_r} = \frac{\nu_{\theta r}}{E_\theta} \qquad \text{(II-23.}$$

he establishes the interdependence of the material parameters. A variable substitution for the ratio of the two moduli (equation #II-24),

$$g^2 = \frac{E_\theta}{E_r} \qquad \text{(II-24.}$$

simplifies the expansion. Then, he uses the strain compatibility equation in polar coordinates (equation #II-25),

$$r\frac{d\varepsilon_{\theta\theta}}{dr} + \varepsilon_{\theta\theta} - \varepsilon_{rr} = 0 \qquad \text{(II-25.}$$

in conjunction with equations #II-5, #II-6 and #II-11 to establish a second order, linear, differential equation of radial pressure dependent on roll radius. This is given here as equation #II-26.

$$r^2\left(\frac{d^2\sigma_r}{dr^2}\right)+3r\left(\frac{d\sigma_r}{dr}\right)-\left(g^2-1\right)\sigma_r=0 \qquad \text{(II-26.}$$

The pressure resulting from winding on a single lap, at a radius r, is called the incremental pressure δP. Substituting δP into equation #II-26 to replace σ_r makes the equation a representation of incremental pressure in the roll.

To apply the radial pressure expression to an actual wound roll, Hakiel converts it into a numerical system. Both of the derivatives in the incremental version of equation #II-26 are replaced with central difference approximations and then rearranged. This produces an expression of the incremental radial pressure in a lap in terms of the incremental pressures of the laps above and below it, its material constants, and the lap's radius. The expression (given here as equation #II-27, where i denotes a single arbitrary lap),

$$\delta P_{i+1}\left[1+\left(\frac{3t}{2r_i}\right)\right]+\delta P_i\left[\left(\frac{t^2}{r_i^2}\right)\left(1-g_i^2\right)-2\right]+\delta P_{i-1}\left[1-\left(\frac{3t}{2r_i}\right)\right]=0 \qquad \text{(II-27.}$$

applies directly to every lap in the roll except the first and last. At these two laps the previous lap is the core and the next lap is the free span web respectively. To determine their pressures, Hakiel utilizes the previously mentioned boundary conditions. At the core, he matches the radial strains by setting equation #II-6 (modified by equation #II-23) equal to equation #II-8, and at the outside the free span incremental pressure is set by equation #II-17. This produces a system with a matching number of algebraic equations and unknowns.

Solving the system and summing the incremental contributions for each lap yields the entire roll's radial pressure state. The circumferential stresses throughout the roll are then easily determined via the equilibrium equation, equation #II-11. Figure #II-4

displays an example of the output Hakiel obtained from his model. The model's in-roll stresses compare fairly well with Pfeiffer's experimental data. With its nonlinear radial modulus, the model represents a significant step towards simulating the stresses in wound rolls. However, the assumptions restrict its application and necessitate the development of more sophisticated models.

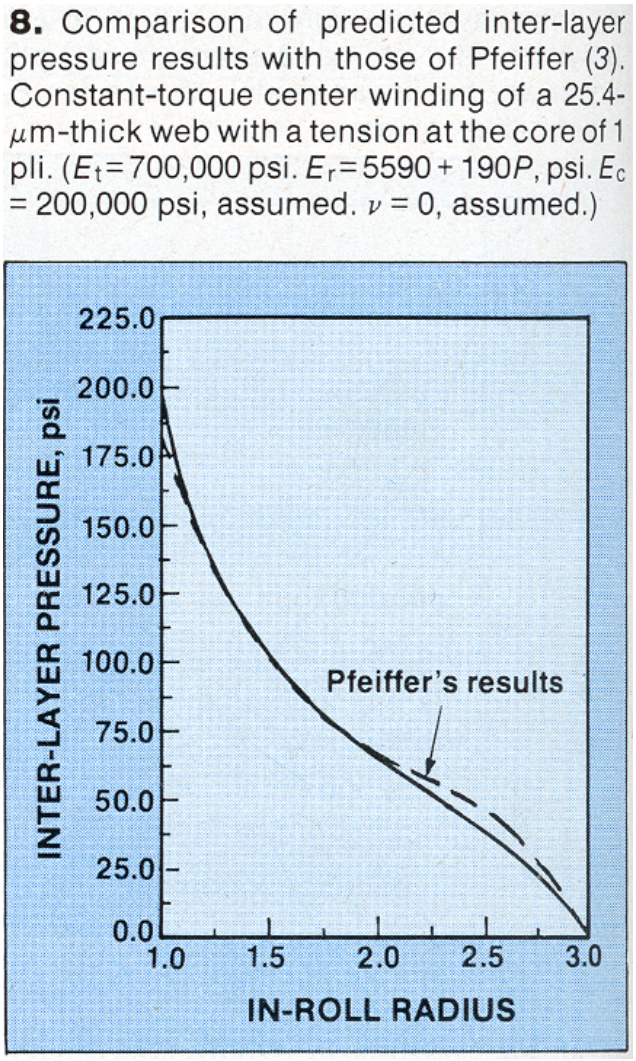

Figure #II-4: Hakiel's [14, Fig. #8] roll model radial pressure compares closely to Pfeiffer's experimental results for a 25.4 μm polyester film despite its non-linear nature.

Good and Pfeiffer [10] notice significant discrepancies between two dimensional pressure profiles predicted by models such as Hakiel [14] and their own experimental results. In some cases a constant radial pressure outboard of the core, known as the plateau pressure, measures half the predicted value as shown in Figure #II-5. This is especially true for compressible material rolls (and explains why Hakiel's pressures were not far off for the nearly incompressible film in Figure #II-4 above).

Through a process of elimination, they determine that insufficient radial pressure resistance at the outside of the roll results in tension loss. The only winding parameter capable of causing such pressure variances from the predicted values is T_W. Contrary to prior theory, they find the tension actually wound into the roll (referred to as Wound On Tension, WOT) is not the full web line tension. Some of it is lost.

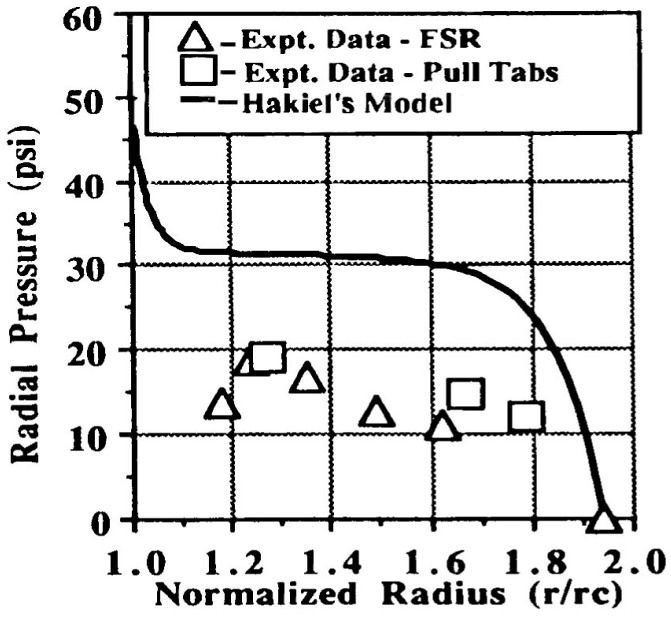

Figure #II-5: For compressible materials like 3.5 mil bond paper center wound at 750 psi, Good and Pfeiffer [10, Fig. #3] found radial pressures throughout the roll were distinctly less than from Hakiel's theory.

Through a process of elimination, they determine that insufficient radial pressure resistance at the outside of the roll results in tension loss. Since wound roll geometry and loading is similar to that of thin wall pressure vessels, they both use the same equilibrium equation, the hoop stress formula of equation #II-17. The formula identifies a direct relationship between the outer lap's radial pressure and its T_W. As the outermost layer is wound on, this relationship must be constantly satisfied. Therefore, for smaller radial pressures to exist, the tension actually wound into the roll must be smaller than T_W. From another point of view, the roll simply has insufficient radial pressure in its outside layer to keep the WOT equal to T_W. In fact, before the outermost lap is wound on, the radial pressure at the outside of the previous layer is zero. As the outermost lap winds on, the pressure must increase to maintain the equilibrium. This is accomplished via the mechanism mentioned in Pfeiffer [24] if the wound roll radially deforms inward.

The inward radial deformation caused by the addition of the outer layer reduces the circumferential strain and tension in the layers below. Circumferential strains in wound rolls follow the polar, biaxial, strain-stress relationship for orthotropic materials, equation #II-6. But, because both $\nu_{r\theta}$ and σ_{rr} for the outer layer are small, it simplifies to a uni-axial, direct dependence between tangential stress and strain. Good and Pfeiffer found that the tangential strain in the outermost layer has two contributing components, as shown in equation #II-28.

$$\varepsilon_t = \varepsilon_{t1} + \varepsilon_{t2} = \frac{T_W}{E_\theta} + \varepsilon_{\theta\theta} = \frac{T_W}{E_\theta} + \frac{u}{r} \qquad \text{(II-28.}$$

The first component is due to T_W and the second is due to radial deformation, with u positive outward. Any inward radial deformation is a negative u that serves to subtract away from T_W / E_θ and results in a reduced ε_t. So, when the uni-axial, simplified version

of equation #II-6 is solved for WOT (with WOT used in place of $\sigma_{\theta\theta}$), and equation #II-28 is substituted into it for the strain, the resulting equation #II-29 is an expression of the WOT in the outermost lap caused by T_W and accounting for radial deformation. It is referred to as the tension loss expression.

$$WOT = T_W + E_\theta \frac{u}{r} \qquad \text{(II-29.}$$

The resulting deformation and corresponding tension loss is greatest in the uncompressed layers directly beneath the new outside layer, and drops off drastically for the inboard layers.

Calculating the amount of tension loss is involved, but Good and Pfeiffer's results prove it must be included. The WOT clearly depends on the radial deformation, but also the deformation depends on the WOT. This interdependence demands an iterative scheme. Good and Pfeiffer use the previous lap's calculated deformation as a first approximation for the outermost lap's deformation. It inserts into the tension loss expression to estimate WOT, which in turn substitutes into the hoop stress formula to estimate the radial pressure. From here, a wound roll boundary value solution scheme, like Hakiel [14], solves for the roll stresses, and deformations. When the outer layer's calculated deformation successfully inserts back into the solution algorithm and reproduces itself, the solution is converged on the radial deformation and WOT of the outermost lap. Good and Pfeiffer [10] reported Figure #II-6 below to show how well the tension loss algorithm matches experimental data.

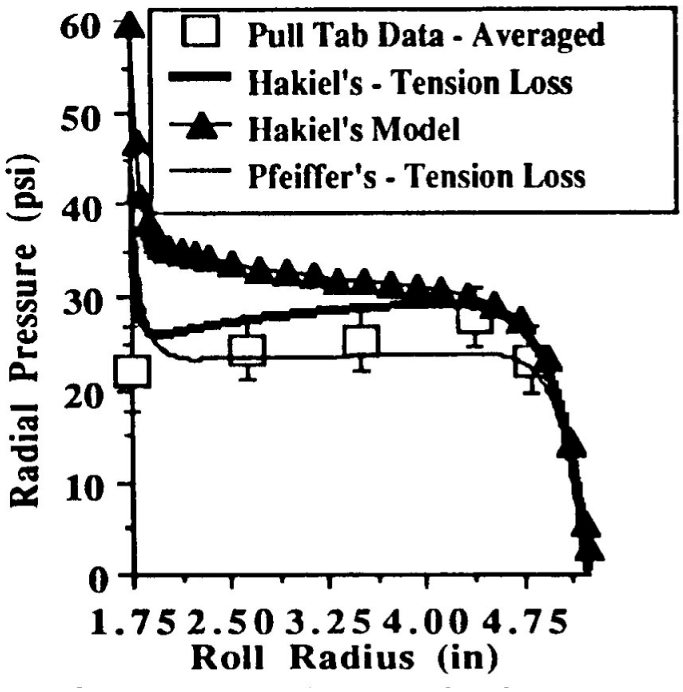

Figure #II-6: Good and Pfeiffer's [10, Fig. #13] tension loss models match up well to their 750 psi, center wound radial pressures for 2.8 mil newsprint.

Three Dimensional Investigations

Three dimensional investigations go one step further than two dimensional investigations by dealing with how CMD variations affect the stresses throughout a wound roll. Collectively, their focus includes the compounding effects of web thickness variations which persist in the length direction, non-uniformities in the core's radius, and changes in the core's stiffness. Kedl [19] addresses the web thickness and core radius variations by maintaining the outer layer's material compatibility when distributing the web line tension across the roll's width. The investigations of Hakiel in [15], and Cole and Hakiel in [4] accommodate CMD web thickness and core radius variations by ensuring each layer's allocated tensions sum to match the web line tension. The more recent investigations by Lee and Wickert [20 and 21] focus on the impact of core

stiffness variations under uniformly and non-uniformly applied web line tension respectively. None of these three dimensional investigations address CMD variations in the web's in-roll tension distribution, or its properties (other than radial modulus).

Kedl [19] divides a three dimensional roll into two dimensional (2D) rolls with each roll's tension dependent on its circumference. Their radii are first made equal to a numerical average of the web in the corresponding region. The model then winds each one by stacking orthotropic thick walled cylinders on top of one another until the outer radius is reached. Web material is conserved during winding, so each 2D roll's circumferential strain (and therefore its tension) is linked to the incoming web line strain. Kedl assigns the strains by scaling its circumferential velocity to the web's overall surface velocity in equation #II-30 (Kedl's equation #4).

$$\varepsilon_{\theta\theta,j} = 1 - \frac{V_0\left(1-\varepsilon_{\theta\theta,0}\right)}{R_j\omega} \qquad \text{(II-30.}$$

Here $\varepsilon_{\theta\theta,j}$ and $\varepsilon_{\theta\theta,0}$ denote individual 2D roll strains versus the incoming web strain respectively. Likewise, R_j is the individual roll's radius while V_0 is the incoming web's velocity. The variable ω represents the rotational rate and is the same for all the 2D rolls.

As the rolls accrete (wind), their radii change and so their portion of the web line tension is altered. Each layer's resulting tension and pressure compresses the layers below it, alters its stresses, and changes the radius of the roll. Kedl believes webs have an inherently low bending stiffness that isolates each roll, so the radius change will not depend on the tension present in the other rolls. Still, the model must iterate each 2D roll to find what tension produces the radial compression necessary to achieve the radius of the roll. For each 2D roll, radial dependent tension is made into an expression

proportional to the initial tension, radius, and a parameter referred to as its tension taper. The tension taper indicates how the 2D roll's tension changed during the wind.

Each 2D roll's tension taper is then inserted into another model (like Hakiel [14]) to calculate the final pressures in the roll. The compression of each roll was handled during the iteration using the thick walled cylinder model, and is thereby imbedded in the tension tapers. Any non-uniformities of the core were also addressed at that time through the R_j term in equation #II-30, and are incorporated. The results then, are stresses versus radii across the width, which collectively represent the three dimensional wound roll. Figure # II-7, compares the average radial pressure from the model and experiments. Unfortunately, limitations in the model make it unable to predict the radii across the width of a three dimensional wound roll.

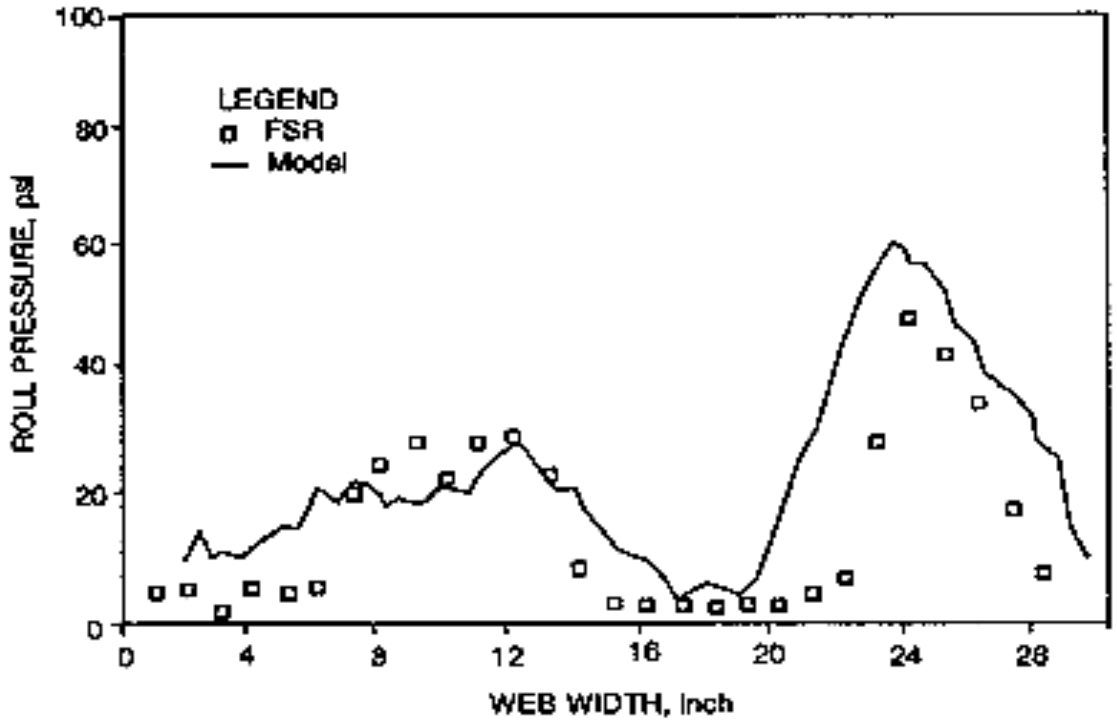

Figure # II-7: Using material compatibility to allocate tension, provided Kedl [19, Fig. #6] with radially averaged roll pressures that fit well with experimental data taken on a 29 inch wide polyester web.

Hakiel [15] separates three dimensional rolls into 2D rolls as well, but the tension is allocated using each 2D roll's radius. The radii start out equal to the sum of the core and web values which correspond to the roll's CMD location. As layers are added, regions with greater core radii and/ or thicker web build up faster than the lesser regions. The difference in radii from one 2D roll to another can become so large that layers in the lesser regions suspend above each other without contact. Such regions are said to be "gapped" and are not allowed to carry tension. Their tension is doled away from them and concentrated into the greater radius regions.

Each layer's radii are iterated until the sum of the 2D tensions converges to the web line tension. This is done by first estimating a radius where that layer's lesser regions will gap. This is called the relaxation radius, R_0. Each 2D roll's radius, r, is compared against R_0, via the polar circumferential strain equation (equation #II-8), to obtain that 2D roll's individual tension stress, $\sigma_{\theta\theta,j}$. Then these 2D roll tensions are converted to tension forces, and summed across the width to verify that they maintain equilibrium with the web line tension. The summation across the M 2D regions is shown here as equation #II-31 which modifies and combines Hakiel's equations [15, eq. #5-#6].

$$\sum_{j=1}^{M}\left(\frac{E_\theta}{(1-\nu^2)}\frac{r_j-R_0}{R_0}\frac{wt}{M}\right)=\sum_{j=1}^{M}\left(\sigma_{\theta\theta,j}\frac{wt}{M}\right)=T_W \qquad \text{(II-31.}$$

Here, j is the reference index for the 2D regions. The web's width is w, so w/M is the average region's width. The web's average CMD thickness is t. The isotropic Poisson's ratio is ν, and the circumferential modulus is E_θ. If the sum of the 2D tensions does not equal T_W, the initial guess for R_0 is altered. The tensions are then recalculated, compared, and adjusted until equilibrium is obtained. This is done for each layer.

After all the tensions converge, the in-roll stresses are ascertained and compared with experimental data. The converged tensions at each layer in the 2D rolls represent a loading versus radius profile. Sending the profiles to a 2D model such as Hakiel [14] produces the final radial and circumferential stresses in the 2D roll. When the data from all the 2D rolls are put together, the result is a full 3D roll. Validation comes from comparisons to data obtained from a core with one inch wide, independent segments across its width which are instrumented with strain gauges. The model predicts the qualitative stress and radius behavior present in a 3D roll, but misses their actual values. A likely source for the discrepancies is the fact that the 2D rolls are not linked in the CMD; they are not allowed to influence neighboring rolls. Another possibility comes from not addressing the radial compression caused when layers are added on (as Kedl [19] did). This isolates the allocated tension away from its effects, and is the reason the model is later referred to as "uncoupled".

Another landmark publication, Cole and Hakiel [4] refines Hakiel [15] by radially compressing the roll during tension allocation. As each layer winds on, an additional deformation term, tracks the resulting compression in each 2D roll. The term is assumed to be linearly dependent on the applied tension, and is used in a ratio to alter the roll's radius while R_0 iterates. The deformation term, u, appears in the tension sum expression, equation #II-32, (which is a modification of Cole and Hakiel's equations [4, eq. #7-#10]).

$$\sum_{j=1}^{M}\left(\frac{r_j+\frac{t_j}{2}-R_0}{\frac{1-\nu^2}{Ew_jt_j}R_0-\frac{u_j}{T_j}}\right)=T_W \qquad \text{(II-32.}$$

Here T_j refers to the tension allocated to a 2D roll. After the allocated tensions sum to the web line tension, each 2D roll is solved for its stress distributions. Unlike in Hakiel [15], the rolls are solved after every lap at some fraction of their final radius. Thus, the stresses are then scaled and summed into the final roll package.

The radii throughout the roll and the pressure at the core in Cole and Hakiel [4] match quite well to their experimental results. To measure the radii across the width, Cole and Hakiel mounted an LVDT on a traversing carriage. As it moves in the CMD the LVDT produces a radial profile snapshot of the outside of a roll. Stacking the radius profiles on top of each other gives a depiction of the roll throughout its wind. Figure #II-8 presents the profiles of one test roll at 4 pli, and shows how it compares to the profiles predicted by both the coupled model [4] and the uncoupled model [15].

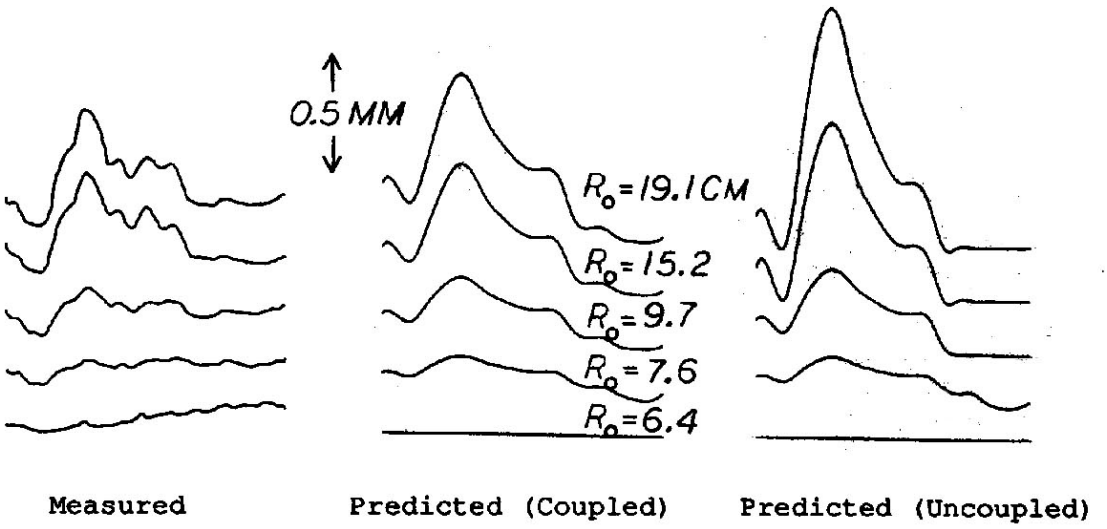

Figure #II-8: Cole and Hakiel [4, Fig. #10] capture the radial profiles throughout the 0.102 mm average web thickness PET roll with their model which couples the tension allocated across the width to the radial deformation it produces.

The Hakiel [15] instrumented core measured the pressures across the test roll's width. Its resulting profile is plotted against the coupled and uncoupled model in Figure #II-9.

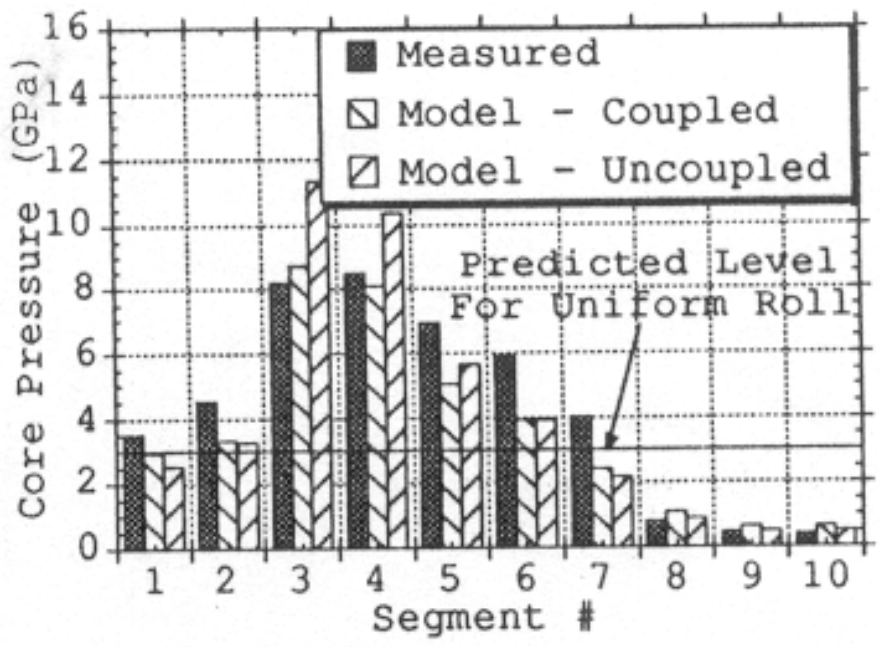

Figure #II-9: Cole and Hakiel's [4, Fig. #14] coupled model shows good agreement with the core pressures for the 25.4 cm wide PET web "A" wound at 7.0 N/ cm.

(Note that the pressure units should be MPa not GPa as shown.) Both figures show the marked improvement produced by the coupled model over the uncoupled model.

Lee and Wickert [20] use an accretive FEM that accommodates a CMD varying core stiffness. The model uses two dimensional, quadrilateral, axisymmetric finite elements attached across the width to simulate the web and the core. (See chapter III for greater detail on this modeling approach.) The elements in the CMD link together into a cohesive shell with continuous properties. Thus, CMD variations and interactions are captured and visible via stresses σ_{ZZ} and σ_{RZ}. The model first establishes a stiffness matrix for one of their two desired, isotropic, plastic cores. This is coupled to a non-linear, orthotropic stiffness matrix of the web's first layer. Tension is applied by shrink-fitting the web onto the core, and iterated until the displacements and resulting coupled stiffness matrices converge. Then another layer is added and the iteration restarts.

Lee and Wickert investigate the stress profiles in a few rolls. First, their results compare well to the two dimensional, uniform stress results from Hakiel [14]. Next, they simulate two rolls wound onto cores with varying stiffness across their width. One roll's core is hollow, while the other is cantilevered as it has a support on only one end. Both rolls show three dimensional stress variations across the width at the core. Also, both rolls show the stress variations become more uniform towards the outside of the roll, as the core's influence diminishes. Figure #II-10 is an example of the radial stress variation for the core with one end supported.

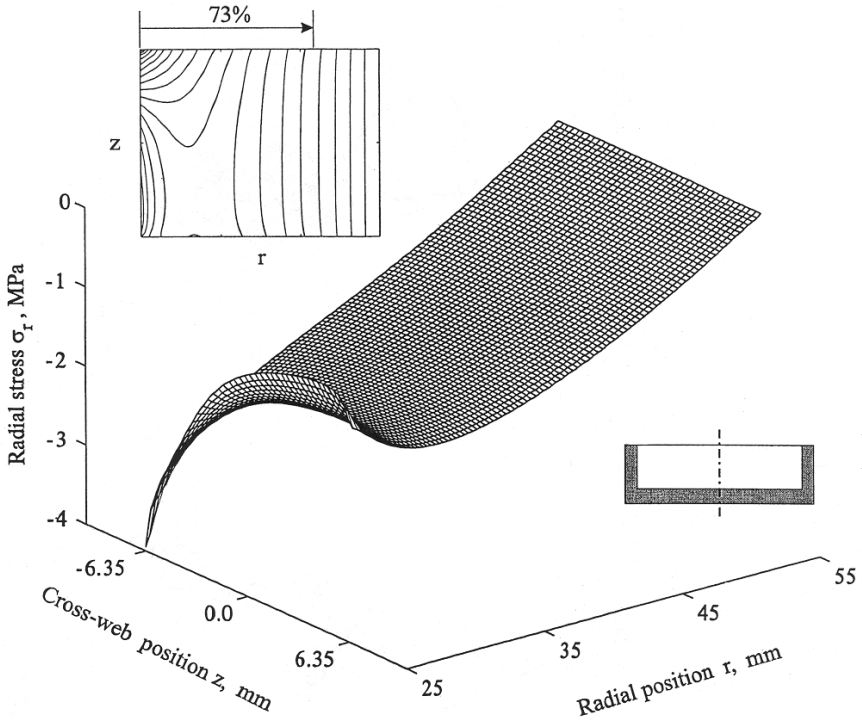

Figure #II-10: Lee and Wickert's [20, Fig. #10] model illustrates the role core stiffness plays in varying the wound roll's radial pressure across the width for even a uniform thickness web.

In [21], Lee and Wickert explore the effects two other plastic core geometries, and CMD varying winding tension have on the stresses in magnetic tape rolls. One core is symmetric in the CMD with a single radial support in the center, while the other is

asymmetric and is a reinforced facsimile of their previous cantilevered core. Their results show a direct correlation between the core's compliance, and the stress build up in the rolls. Lee and Wickert wind the roll by shrink-fitting uniform CMD thickness web layers onto it in proportion to the pre-specified web line tension. When they use a non-uniform web line tension across the width, both linearly and quadratically varying, it produces stress concentrations on the sides with higher tension. The impact of both the core's stiffness, and the web's tension profile can be seen in Figure #II-11. In addition, they derive a unique form for the stack's radial modulus by combining a linear spring stiffness for the substrate, with a non-linear asperity stiffness for the interfaces. They also briefly mention the width change the web undergoes during winding.

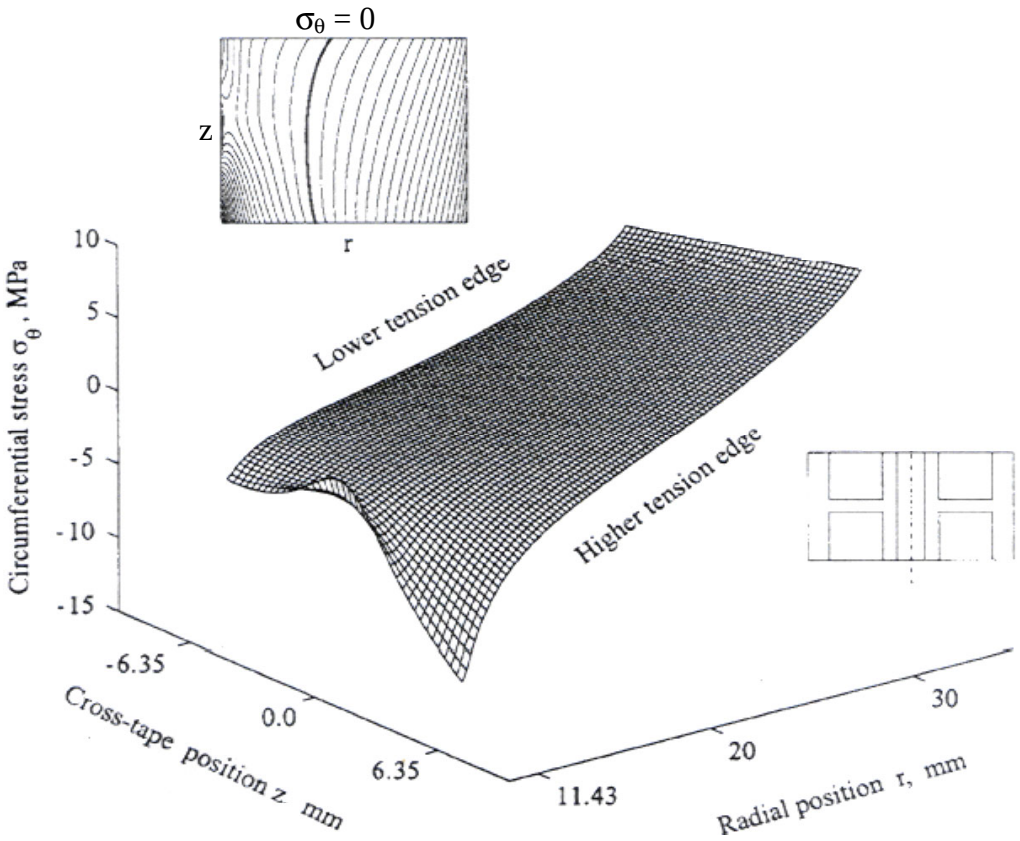

Figure #II-11: Lee and Wickert [21, Fig. #12] show a non-uniform core stiffness, and a linearly varying T_W, impact the circumferential stress in a wound roll.

Nip Roller Investigations

Nip investigations address the impact an external nip roller has on a wound roll. Good, Wu, and Fikes [11] determined a nip roller increases the tension wound into a roll in proportion to the nip's loading. They established a relationship to express the tension increase. Hoffecker [17] addresses the variation in nip impingement across a stationary wound roll. The impingement depth varies with roll material stiffness, the nip roller's bending stiffness, and the nip roller's constraints.

Good, Wu, and Fikes [11] examine the effect a nip roller has on wound roll tension. Various combinations of nip roll diameter and loading produced axial stress increases in a uniform thickness, aluminum strip. The total stress in the strip behaved consistently, and instead of continuing to increase with load, it always had a saturation value. This prompted further investigation into the nip mechanics. They loaded a two dimensional, plane strain, finite element model of the strip with a moving Hertzian contact pressure distribution. This model found all the resulting pre-saturation stresses were compressive, and therein identified the nip induced tension mechanism. As the nip progresses, its load and resulting compressions elongate the web out ahead of the nip and frictionally trap the constrained material behind the nip until its total tension saturates and exceeds the frictional force.

Nip induced tension builds up quite rapidly, and so most of the winding done with a nip roller is saturated. The value of the saturated stress derives from the WOT which is dependent on both the web line tension and a nip load term, as shown in equation #II-33.

$$WOT = T_w + \frac{\mu_k \, N/w}{t} \qquad \text{(II-33.}$$

Here, μ_k is the coefficient of kinetic friction, N is the nip's normal force, and the product $\mu_k(N/w)/t$ is collectively referred to as the Nip Induced Tension, NIT. Figure #II-12

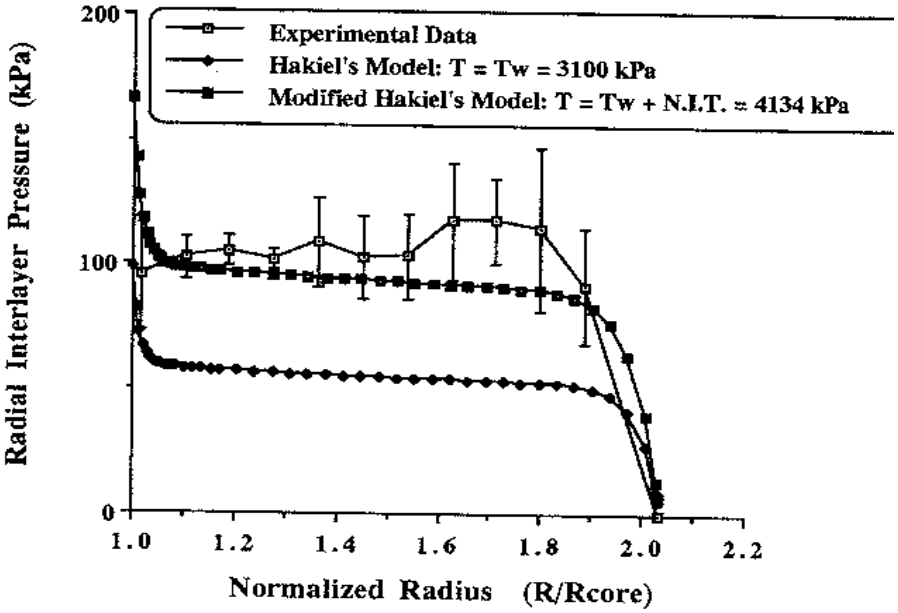

Fig. 5 Results for lightweight coated paper, nip load = 1.75 N/cm

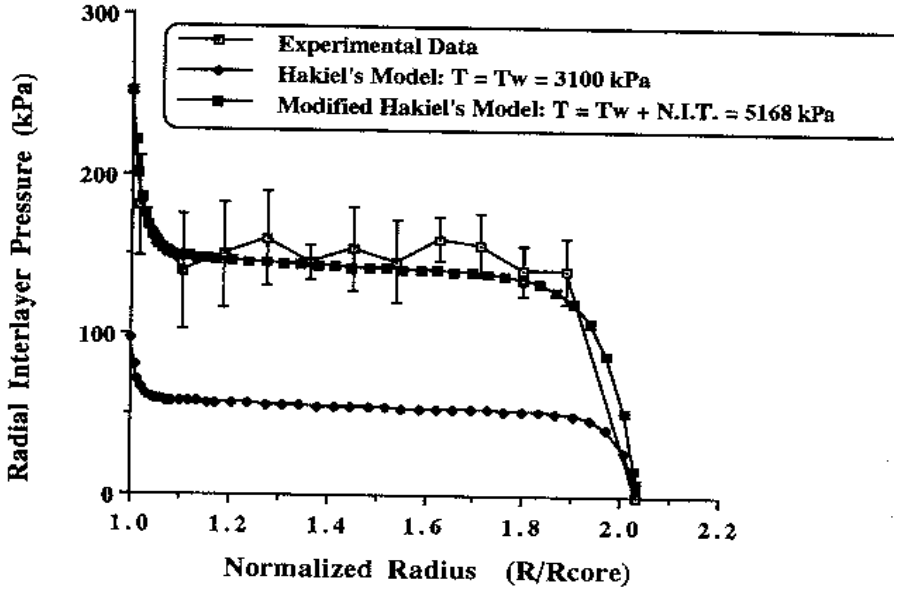

Fig. 6 Results for lightweight coated paper, nip load = 3.5 N/cm

Figure #II-12: Good, Wu, and Fikes' [11, Fig. #5 & #6] Nip Induced Tension modifier produces radial pressure results which match closely to experimental data collected on materials such as light weight coated paper.

plots the stresses from a modified center winding model, which uses the NIT to alter the outer boundary condition. By including the nip's influence, through the NIT, the model's modified tension matched nicely to numerous nip impinged wound roll experiments.

Hoffecker [17] addresses the effects of impinging a stationary nip into a wound roll. A FEM elastic foundation with a non-linear radial compressive modulus represents the wound roll. The nip roller becomes a beam pressed down into the foundation at specified loads. The model calculates the radial deformation corresponding to the applied nip load, at the initial elastic modulus value. The deformation then feeds back into an elastic modulus calculation, producing a new value. The process repeats until the deformation converges. The final amount of compression seen by the roll depends on the radial stiffness of the web, and as demonstrated in Figure #II-13 the compression also depends on the total load applied to the nip.

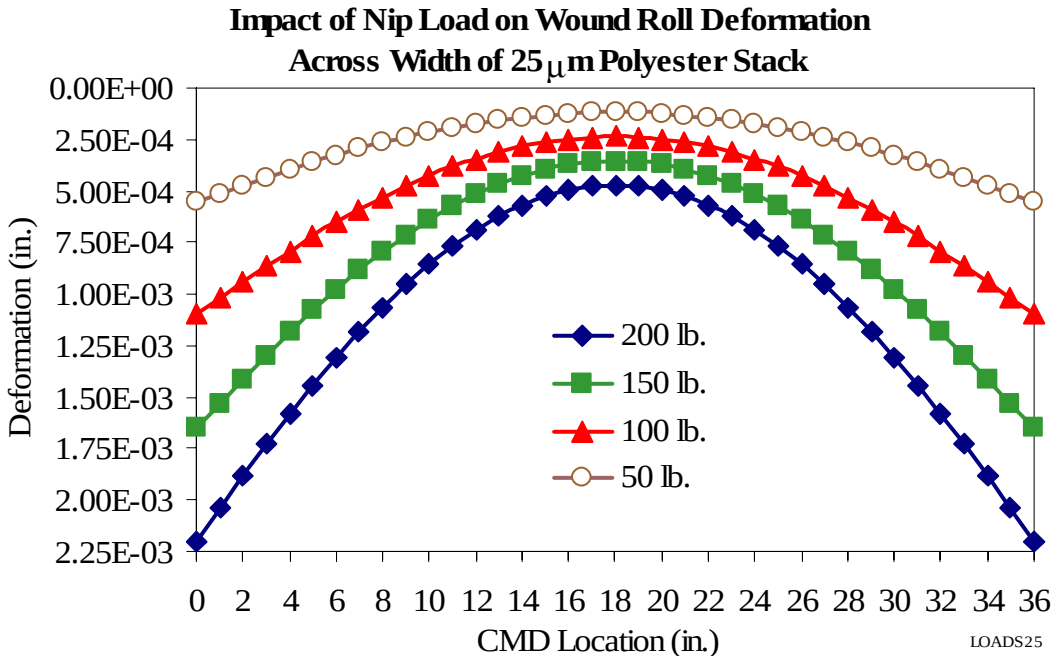

Figure #II-13: In Hoffecker [17, Fig. #37] the nip induced deformation of the wound roll is clearly proportional to the magnitude of the load applied to the nip.

The nip's impingement also depends on its rotational constraints, and its physical and material properties. Whenever its supports are constrained against rotation, the nip's shaft must maintain a zero degree angle of incidence. Without these constraints, the nip bows more freely in the center. This causes the nip's loading to vary more across the width of the roll. The radius, configuration, and type of material also impact the loading across the width. The stiffer the nip is, the less it will bend, and the more uniform will be its loading. Figure #II-14 displays the varying load across the width of a wound roll.

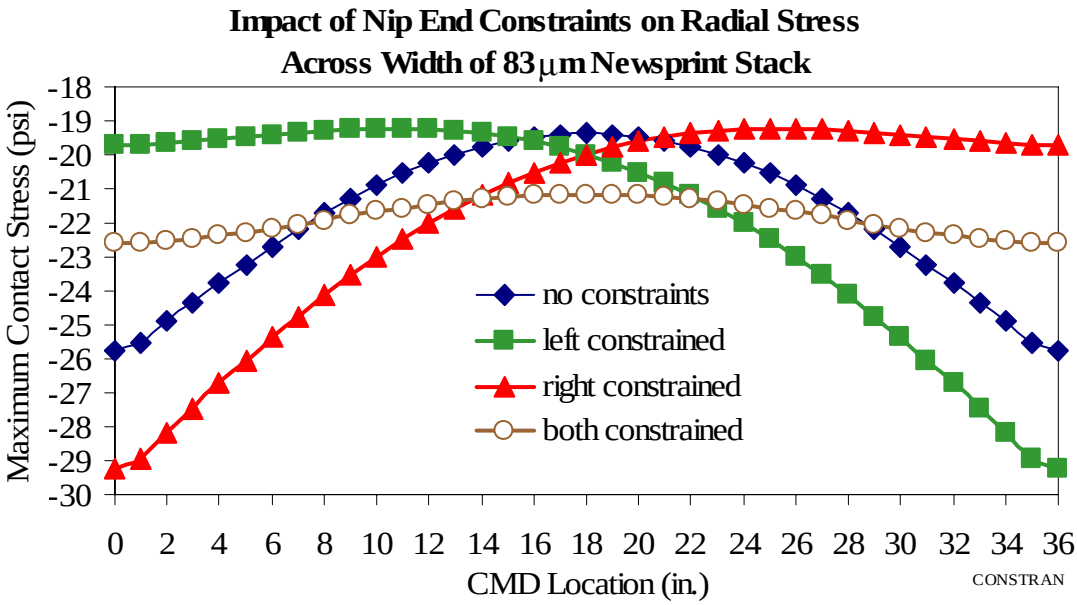

Figure #II-14: The radial stress across the roll's width is shown in Hoffecker [17, Fig. #45] to depend on the nip's constraints.

Project Method

The two dimensional, three dimensional, and nip roller intricacies dictate a three phased approach to meet the goal of developing an accurate three dimensional, nip impinging, wound roll model. First, a wound roll's state must be known at any point

throughout the wind and at any location through its depth, or across its width, before a nip can even be added. This is satisfied through the development of a three dimensional wound roll model. Second, the nip roller's performance is analyzed. The ensuing nip roller impingement model calculates the nip induced compression and the effects on the tension across the wound roll's width. Finally, the third phase ties the two models together into a cohesive and interacting package. Each phase then, addresses specific complexities presented in the literature.

The three dimensional roll model predicts the stresses inside of a wound roll with CMD variations. These rolls are more complex then they appear, due in a large part to their pressure dependent, non-linear radial modulus. In addition, their coiled, cylindrical geometry, when subjected to loading, constricts radially resulting in a circumferential tension reduction. In the past, numerous models attempted to capture this behavior, but it became apparent that CMD variations, including thickness, were not sufficiently represented. Since high radius areas collect larger amounts of tension, become stiffer and magnify the CMD variability, the models were also unable to accurately predict the radius of the outer layer. This project first attempted to address these concerns with a three dimensional version of the tension loss model. But, that model lacked CMD continuity and therefore also lacked the corresponding CMD interactions. This prompted an entirely new venture into a spatially formulated, three dimensional model, which utilizes axisymmetric quadrilateral finite elements. The result is a model with an accurate representation of the stresses and the positions throughout and across, the wound roll.

The nip impingement model determines the nip's influence on the wound roll. Past studies consolidated its influence with the addition of a single nip induced tension

parameter to the roll's winding tension. But, this is only effective on two dimensional rolls. The nip induced tension is neither uniform across three dimensional rolls, nor on uniform rolls of significant width. For non-uniform rolls, the induced tension's variation across the roll depends on numerous geometrical parameters not the least of which is the outer layer's radial profile. This project addresses the regions of contact and gap, and the varying stiffnesses present in the roll and nip across the width. The resulting model impinges the nip into the roll and iteratively determines the amount of compression seen across the roll and also the corresponding tensions the nip induces.

The combined model interlaces the three dimensional model with the nip impingement model. It accounts for the nip roller, and the non-uniform roll, through an essential iterative process. The model begins by utilizing the thickness variation profile and the amount of loading to estimate a layer's contact across the wound roll. Then it winds layers onto the roll, up to a prescribed average radius, to determine the radii and radial moduli across the width. Next, the nip is iteratively pressed into the wound roll while the moduli, and the CMD contact, are adjusted until all the constraining conditions like equilibrium and wrap angle are satisfied. The model then determines each segment's individual nip induced tension, and compression. These are used during the winding on of the next layers, and the process repeats until the entire roll is wound and all the resulting stresses are calculated.

Since the intention is to provide a tool that determines wound roll stresses well enough that it can be used to improve a wound roll's quality, the final state of the nip impinged roll is compared with experimental data. Discrepancies are discussed and recommendations are made on improvements to make the model more closely match the

experimental data. Some experimental comparison is done along the way to improve the results. This paper investigates and presents the complexity involved in the project. It outlines the current state of essential project building blocks by detailing their development, explores what was required experimentally, presents results, and discusses the obstacles encountered and their remedies.

CHAPTER THREE

COMPREHENSIVE THREE DIMENSIONAL WOUND ROLL MODEL

The three dimensional wound roll model generates an accurate radial profile across the roll's entire width. This profile is essential to predicting when a nip will come into contact with the roll. The model's development began with a three dimensional tension loss model, and then proceeded through three successive versions of an axisymmetric finite element model. The tension loss model used the tension allocation and deformation coupling of Cole and Hakiel [4] in conjunction with Good and Pfeiffer's [10] tension loss inside the wound roll. The results were promising, but the model lacked the proper interaction between neighboring 2D regions. The first axisymmetric finite element model represented each layer and the core as a separate cylinder. This model was a tension allocating, accretive, finite element model and was continuous in the CMD. The next version expanded the cylinder version's accuracy and usability to include extensive core modeling. Further additions such as variable width regions in the CMD, and an improved boundary condition representation necessitated the current working version. Since each model built on the models before it, the current version is the most complete and accurate three dimensional winding model known to exist. In addition, its flexibility means that it can be extended to include other winding aspects.

Three Dimensional Tension Loss

The three dimensional, tension loss model was designed to investigate the effects of CMD variations in caliper. Cole and Hakiel [4] had shown that the CMD variations accumulate during winding, causing bands of increased radial pressure. Their model provided the algorithm used by the 3D tension loss model to partition web line tension to the segments in proportion to their individual radii. It also provided the method to account for the core's radial deformation caused by the core-to-wound roll interface pressure. But, Good and Pfeiffer's [10] tension loss model showed that significant tension is lost in the roll due to that deformation. Using their tension loss algorithm, the 3D tension loss model updates the segment thicknesses after each lap is added which forces the roll's circumferential tension to readjust.

At first glance, the results from the three dimensional, tension loss model looked quite accurate. Simulations were conducted on Cole and Hakiel's case A, 2 pli roll. The radial profile at the roll's outer edge shown in Figure #III-1 captured the behavior rather well, but the radial variation was nearly twice the amount measured by Cole and Hakiel. The same was true for the radial pressures shown in Figure #III-2. They generally followed the desired shape, but were noticeably higher in magnitude. The 3D tension loss code and the 3D Cole and Hakiel code on which it was based shared a peculiarity. Whenever the segment thicknesses were mixed around, the pressures moved with them, but stayed the same in magnitude. This could only happen with segments independent of their neighbors. Unfortunately, the segments remain nearly autonomous, and thus do not interact with adjoining segments directly. Obviously, the model lacked the accuracy necessary to represent a three dimensional roll to be impinged by a nip roller.

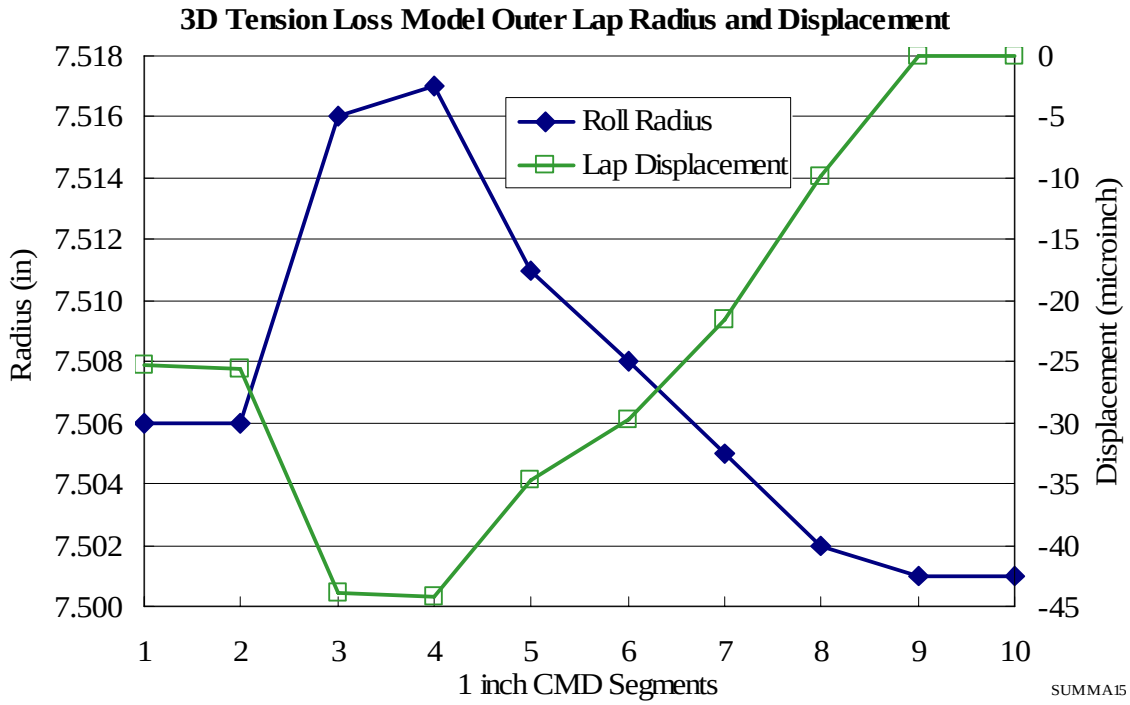

Figure #III-1: The three dimensional tension loss model's radial profile for the Cole and Hakiel [4] web A, at 2 pli, has the same general trend they reported (refer back to Figure #II-8).

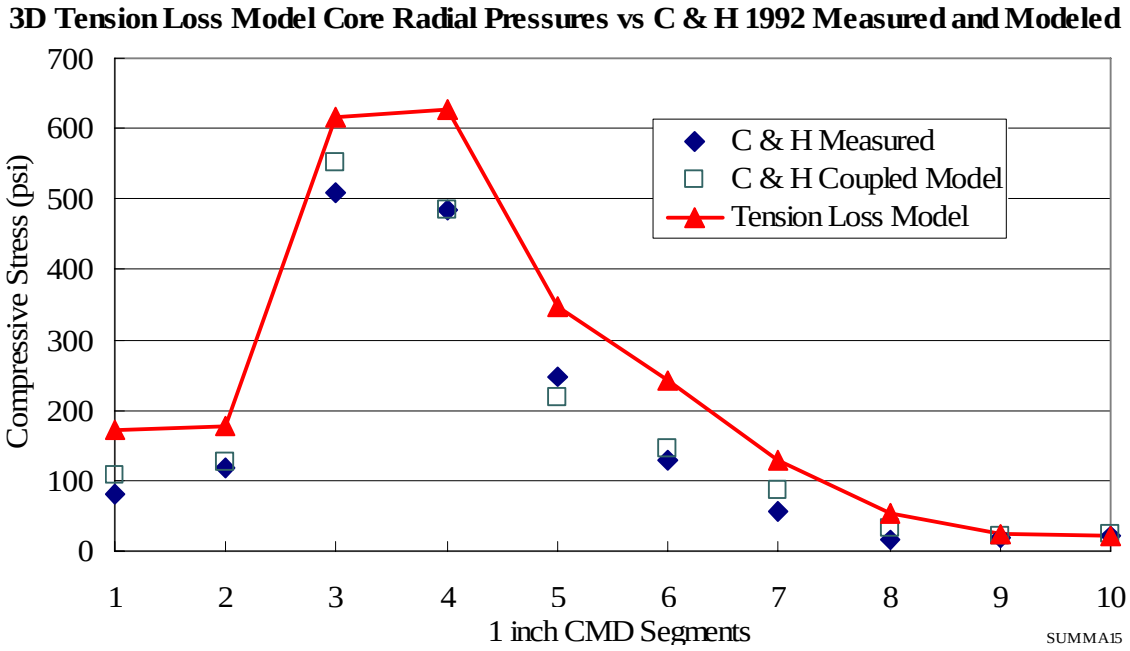

Figure #III-2: The core pressure from the three dimensional tension loss model's simulation of Cole and Hakiel [4] web A, at 2 pli, overshoots their measured peak value of approximately 500 psi.

Axisymmetric Cylinder

Overcoming the cross width continuity deficiency demands a new model. As mentioned, nearly all roll models up to this point were either two dimensional models, or three dimensional composites of two dimensional models. None adequately represent three dimensional rolls. Since nearly every roll has some three dimensional characteristic, there is a need for a model to accommodate it.

An axisymmetric FEM solves the cross width continuity problem. In general, a finite element is a mathematical representation of a physical, geometric object. Axisymmetric finite elements represent materials in the two dimensional RZ plane, and then spin them around the Z axis in the θ direction to form a three dimensional shell (see Figure #III-3).

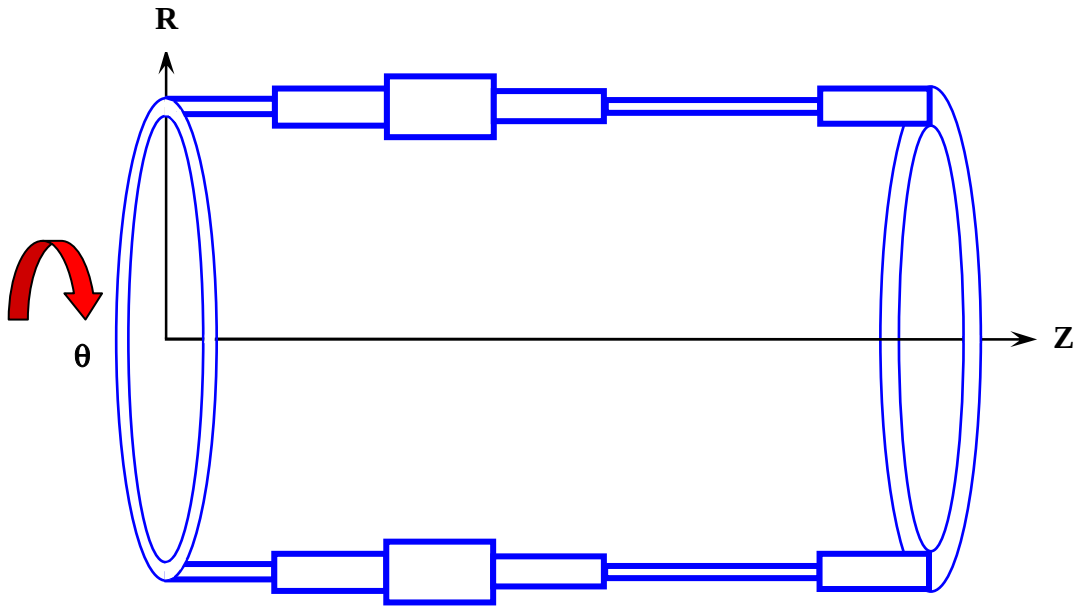

Figure #III-3: The axisymmetric Finite Element Model uses two dimensional quadrilateral elements rotated around a central axis to form a three dimensional material shell.

In this model, the axisymmetric elements are quadrilaterals. Their movement is defined by the motion of their four corners. These corner nodes, as they are called, have a degree of freedom in both the R and Z direction that allow them to deform anywhere in the plane. It is the relative deformation between an element's nodes that produces its strain. In addition to the deformations and strains, the corresponding stresses, and the material properties, can all vary in the R and Z directions, but can not vary in the θ direction. The invariance in the θ direction makes the representation symmetric about the Z axis, and is the source for the name axisymmetric. Physical variations in a wound roll are handled by placing multiple elements across the variation and thus subdividing it into smaller, well behaved portions. Adjacent finite elements share nodes, thereby passing deformations to each other. This provides continuity across the roll.

The quadrilateral elements are conducive to representing a web's cross section. The element's four corner nodes bracket the web layer's thickness, thereby following its profile across the width. Behaviors such as strain and stress are allowed to change linearly between the nodes. At the same time, properties like moduli and Poisson's ratios remain uniform in an element. This trait makes adjacent elements handle the necessary variations in the cross machine and radial directions and provides for a different material stiffness in each element.

Representing the web cross section's thickness variation across its width is deceptively complex. It is ambiguous to measure CMD thicknesses at a few points along the machine direction and average them to represent an "elemental thickness profile". What amount of deviation existed in the values that were averaged? Did the CMD thickness profiles persist in the MD? Were the thicknesses sampled sufficiently across

the width? Ultimately, the model cannot address these issues, so the user must exercise due diligence to properly represent the profile. This is because certainly, while it is difficult to ascertain what constitutes a significant departure from the true web profile, it will affect the model's ability to predict the roll.

To make the most of the input elemental thickness profiles, they must be processed into meaningful representations. They are input into the model as thickness values corresponding to a pre-specified number of equal cross width segments. Instead of looking like a web cross section, they therefore resemble a "bar chart" of CMD thicknesses. First, each segment's value is halved to establish its dimension about a thickness centerline. This is indeed an assumption, as the true profiles might not even be symmetric about a centerline. But, the complexity involved in characterizing profiles without a centerline would render the model unwieldy. Next, the average of each half segment value and its neighbor becomes a node on their boundary. Each end node's location comes from averaging the element's thickness with its already established node immediately inboard of the end. The resulting collection of nodes is hereafter referred to as a linearly varying thickness profile. The largest of these nodal locations is then added back to all of the nodes to create the top of the profile. Finally, the profile's bottom is created by placing nodes below the centerline at a distance equivalent to the linearly varying profile's values. Graphically, the thickness "bar chart" has been transformed into a profile called the bi-linearly varying thickness profile (see Figure #III-4).

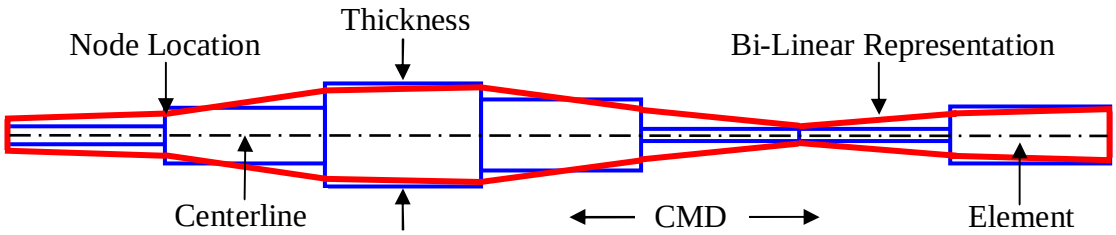

Figure #III-4: The input web layer's thickness profile is made into a bi-linearly varying representation in order to best capture its behavior across the width.

FEMs derive from a minimum potential energy formulation. The potential energy in a conservative system is the summation of its strain energy and its work potential. At its minimum, the potential energy formulation represents a unique, stable configuration. Taking the derivative of the formulation with respect to the deformations, and setting the result to zero, yields this minimum configuration. The deformations that satisfy the minimum configuration give the deformed state of the system.

The strain energy contribution to the potential energy comes from a material's inherent behavior. Linear elastic materials develop a strain energy per unit volume equal to $1/2\,\bar{\boldsymbol{\sigma}}^T\bar{\boldsymbol{\varepsilon}}$. Thus, the total strain energy results from integrating over the volume, as depicted in Equation #III-1.

$$U = \frac{1}{2}\int_V \bar{\boldsymbol{\sigma}}^T\bar{\boldsymbol{\varepsilon}}\,dV \qquad \text{(III-1.}$$

To simplify this expression, we utilize the fact that each material (and necessarily each element representing that material) abides by constitutive equations relating its stress and strain. The fully three dimensional, orthotropic, polar constitutive equations are given in Equation #III-2 (modified from [5, Eq. #ζ.1]).

$$\begin{bmatrix} \varepsilon_{rr} \\ \varepsilon_{\theta\theta} \\ \varepsilon_{zz} \\ \varepsilon_{r\theta} \\ \varepsilon_{rz} \\ \varepsilon_{\theta z} \end{bmatrix} = \begin{bmatrix} 1/E_r & -\nu_{\theta r}/E_\theta & -\nu_{zr}/E_z & 0 & 0 & 0 \\ -\nu_{r\theta}/E_r & 1/E_\theta & -\nu_{z\theta}/E_z & 0 & 0 & 0 \\ -\nu_{rz}/E_r & -\nu_{\theta z}/E_\theta & 1/E_z & 0 & 0 & 0 \\ 0 & 0 & 0 & 2/G_{r\theta} & 0 & 0 \\ 0 & 0 & 0 & 0 & 2/G_{rz} & 0 \\ 0 & 0 & 0 & 0 & 0 & 2/G_{\theta z} \end{bmatrix} \begin{bmatrix} \sigma_{rr} \\ \sigma_{\theta\theta} \\ \sigma_{zz} \\ \sigma_{r\theta} \\ \sigma_{rz} \\ \sigma_{\theta z} \end{bmatrix} \quad \text{(III-2.}$$

Note that these equations expand the two dimensional versions given in Equations #II-5, and #II-6. Also, this expansion introduces the modulus of rigidity (or shear modulus), G, in three different coordinate orientations. The matrix in Equation #III-2 is referred to as the compliance matrix [5]. Its inverse is the material stiffness matrix $\overline{\mathbf{D}}$, Equation #III-3.

$$\overline{\mathbf{D}} = N \begin{bmatrix} E_r(1-\nu_{z\theta}\nu_{\theta z}) & E_r(\nu_{\theta r}+\nu_{zr}\nu_{\theta z}) & E_r(\nu_{zr}+\nu_{\theta r}\nu_{z\theta}) & 0 & 0 & 0 \\ E_\theta(\nu_{r\theta}+\nu_{rz}\nu_{z\theta}) & E_\theta(1-\nu_{zr}\nu_{rz}) & E_\theta(\nu_{z\theta}+\nu_{r\theta}\nu_{zr}) & 0 & 0 & 0 \\ E_z(\nu_{rz}+\nu_{r\theta}\nu_{\theta z}) & E_z(\nu_{\theta z}+\nu_{\theta r}\nu_{rz}) & E_z(1-\nu_{r\theta}\nu_{\theta r}) & 0 & 0 & 0 \\ 0 & 0 & 0 & G_{r\theta}/2 & 0 & 0 \\ 0 & 0 & 0 & 0 & G_{rz}/2 & 0 \\ 0 & 0 & 0 & 0 & 0 & G_{\theta z}/2 \end{bmatrix}$$

$$\textit{with} \quad N = (1-\nu_{r\theta}\nu_{\theta r}-\nu_{rz}\nu_{zr}-\nu_{\theta z}\nu_{z\theta}-2\nu_{rz}\nu_{z\theta}\nu_{\theta r}) \quad \text{(III-3.}$$

Using #III-3 to substitute $\overline{\boldsymbol{\sigma}}$ out of #III-1, via $\overline{\mathbf{D}}\overline{\boldsymbol{\varepsilon}}$, yields Equation #III-4.

$$U = \frac{1}{2}\int_V \overline{\boldsymbol{\varepsilon}}^T \overline{\mathbf{D}}^T \overline{\boldsymbol{\varepsilon}}\, dV \quad \text{(III-4.}$$

All of the finite elements set up in the physical wound roll, are systematically linked onto an undeformed, representative, quadrilateral element in a model space. This element is referred to as the master element. Just like the physical RZ plane, the model space is a two dimensional plane, but it uses a different set of orthogonal coordinates referred to as the natural coordinates, ξ and η. The master element is sized in the model space so that both natural coordinates range from -1 to 1. Any value in the master

element's interior, or on its perimeter, can be represented as a combination of the values at its nodes. This is accomplished by using interpolation functions called shape functions. Each of the element's nodes has its own function, as seen in Equation #III-5

$$\begin{aligned}\varphi_1 &= \tfrac{1}{4}(1-\xi)(1-\eta)\\ \varphi_2 &= \tfrac{1}{4}(1+\xi)(1-\eta)\\ \varphi_3 &= \tfrac{1}{4}(1+\xi)(1+\eta)\\ \varphi_4 &= \tfrac{1}{4}(1-\xi)(1+\eta)\end{aligned} \qquad \text{(III-5.}$$

By inserting the natural coordinates of the value desired into the shape functions, they become weights that apply to their nodes. At the center of the master element for example, the radial and lateral deformations, u and v respectively, receive equal contributions from the deformations of all four nodes as shown in Equation #III-6.

$$\begin{aligned}u(\xi,\eta) = u(0,0) &= \varphi_1 q_1 + \varphi_2 q_3 + \varphi_3 q_5 + \varphi_4 q_7 = \tfrac{1}{4}(q_1 + q_3 + q_5 + q_7)\\ v(\xi,\eta) = v(0,0) &= \varphi_1 q_2 + \varphi_2 q_4 + \varphi_3 q_6 + \varphi_4 q_8 = \tfrac{1}{4}(q_2 + q_4 + q_6 + q_8)\end{aligned} \qquad \text{(III-6.}$$

The odd numbered q values are the radial deformations of the master element's four nodes, while the even numbered q values represent the lateral deformations. Altogether they make up the master element's deformation vector $\overline{\mathbf{q}}$.

Once the master element is set up, the finite element model transforms values back and forth from it to the physical space. The shape functions can handle the transformation for constant values, but derivatives like strain, require the use of the Jacobian matrix $\overline{\mathbf{J}}$, and its determinant. As seen in Equation #III-7, the Jacobian directly relates a change in the finite element's R and Z axes, to a change in the master element's ξ and η axes.

$$\bar{\mathbf{J}} = \begin{bmatrix} \dfrac{\delta R}{\delta \xi} & \dfrac{\delta Z}{\delta \xi} \\ \dfrac{\delta R}{\delta \eta} & \dfrac{\delta Z}{\delta \eta} \end{bmatrix} \qquad \text{(III-7.}$$

The Jacobian's determinant acts as a scale factor between the elemental areas in the two coordinate systems.

The strain in the RZ plane can now be calculated. Because the quadrilateral is a plane element, the out of plane strains are zero. The remaining in-plane strains are calculated from the derivatives of the deformations in the natural coordinate system as shown in Equation #III-8).

$$\bar{\boldsymbol{\varepsilon}} = \begin{bmatrix} \varepsilon_{rr} \\ \varepsilon_{zz} \\ \varepsilon_{rz} \end{bmatrix} = \frac{1}{\det \bar{\mathbf{J}}} \begin{bmatrix} J_{22} & -J_{12} & 0 & 0 \\ 0 & 0 & -J_{21} & J_{11} \\ -J_{21} & J_{11} & J_{22} & -J_{12} \end{bmatrix} \begin{bmatrix} \dfrac{\delta u}{\delta \xi} \\ \dfrac{\delta u}{\delta \eta} \\ \dfrac{\delta v}{\delta \xi} \\ \dfrac{\delta v}{\delta \eta} \end{bmatrix} \qquad \text{(III-8.}$$

The vector of derivatives is in turn found from the $u(\xi,\eta)$, and $v(\xi,\eta)$ expressions above, and can be expressed as the product of a matrix $\bar{\mathbf{G}}$, and the master element's deformation vector $\bar{\mathbf{q}}$. Equation #III-9 gives the $\bar{\mathbf{G}}$ matrix.

$$\bar{\mathbf{G}} = \frac{1}{4} \begin{bmatrix} -(1-\eta) & 0 & (1-\eta) & 0 & (1+\eta) & 0 & -(1+\eta) & 0 \\ -(1-\xi) & 0 & -(1+\xi) & 0 & (1+\xi) & 0 & (1-\xi) & 0 \\ 0 & -(1-\eta) & 0 & (1-\eta) & 0 & (1+\eta) & 0 & -(1+\eta) \\ 0 & -(1-\xi) & 0 & -(1+\xi) & 0 & (1+\xi) & 0 & (1-\xi) \end{bmatrix}$$

(III-9.

When $\overline{\mathbf{G}}\overline{\mathbf{q}}$ is put into the strain expression, Equation #III-8, the product of the $\overline{\mathbf{J}}$ terms and the $\overline{\mathbf{G}}$ matrix are collectively referred to as the transformation matrix, $\overline{\mathbf{B}}$. This leaves the succinct expression for strain shown in Equation #III-10.

$$\overline{\boldsymbol{\varepsilon}} = \overline{\mathbf{B}}\overline{\mathbf{q}} \qquad \text{(III-10.}$$

Equation #III-10 is the expression necessary to proceed on with the axisymmetric derivation. Substituting it into Equation #III-4, performing the transpose on the leading $\overline{\mathbf{B}}\overline{\mathbf{q}}$ term, and moving the $\overline{\mathbf{q}}$ out of the integral produces Equation #III-11.

$$U = \frac{1}{2}\overline{\mathbf{q}}^T \int_V \overline{\mathbf{B}}^T \overline{\mathbf{D}}^T \overline{\mathbf{B}}\, dV\ \overline{\mathbf{q}} \qquad \text{(III-11.}$$

Further specializations develop this generic strain energy expression into an axisymmetric formulation. The integral over the volume splits into three, one dimensional integrals over the R, Θ, and Z directions. The R and Z integrals cover the area in the quadrilateral's plane. The Θ integral provides the axisymmetry through the full 0 to 2π revolution about the Z axis. The circumference of the revolution depends on the radius of the quadrilateral, so the integral results in a 2πr factor. To make the integrals consistent with the $\overline{\mathbf{B}}^T\overline{\mathbf{D}}^T\overline{\mathbf{B}}$ matrices, they are converted to natural coordinates via the substitution $dr\ dz = det\,\overline{\mathbf{J}}\ d\xi\, d\eta$. Equation #III-12 shows the updated expression.

$$U = \frac{1}{2}\overline{\mathbf{q}}^T 2\pi \int_{-1}^{1}\int_{-1}^{1} \overline{\mathbf{B}}^T \overline{\mathbf{D}}^T \overline{\mathbf{B}}\ r \det \overline{\mathbf{J}}\ d\xi\, d\eta\ \overline{\mathbf{q}} \qquad \text{(III-12.}$$

With the out of plane strain terms removed for the two dimensional quadrilateral, $\overline{\boldsymbol{\varepsilon}}$ and therefore $\overline{\mathbf{D}}$, and $\overline{\mathbf{B}}$ all have only three rows. But, the axisymmetric formulation restores the third dimension by using the circumferential strain expression, #II-8 ($e_{\theta\theta} = u/r$), converted into a vector form. From Equation #III-6, the shape function expression for u

contains components of $\overline{\mathbf{q}}$, and therefore can be expressed as a product of it, as shown in Equation #III-13.

$$\varepsilon_{\theta\theta} = \left[\frac{\varphi_1}{r} \quad 0 \quad \frac{\varphi_2}{r} \quad 0 \quad \frac{\varphi_3}{r} \quad 0 \quad \frac{\varphi_4}{r} \quad 0 \right] \overline{\mathbf{q}} \qquad \text{(III-13.}$$

The row vector simply becomes the fourth row in a four by eight, expanded $\overline{\mathbf{B}}$ matrix.

A few adjustments are needed on the $\overline{\mathbf{D}}$ matrix. To maintain the necessary dimensionality, the formulation requires it be a four by four matrix. This comes by eliminating rows and columns 4, and 6 from Equation #III-2. In addition, Maxwell's relations (Equation #II-23) are imposed on cross diagonal terms thereby making it symmetric ($\overline{\mathbf{D}}^T = \overline{\mathbf{D}}$). This leaves seven independent material properties. However, Cheng and Cheng [3, Eq. #6] show the shear modulus can be represented as a function of the other material properties. Their expression (modified to the RZ plane, and applying Maxwell's relation) is Equation #III-14.

$$G_{rz} = \frac{E_r E_z}{E_r (1 + 2\nu_{zr}) + E_z} \qquad \text{(III-14.}$$

Thus, the total number of independent material properties can be reduced to six, if G_{rz} is not measured experimentally.

In practice, the strain energy is captured through the use of an element stiffness matrix (ESM). The ESM is the eight by eight matrix which results from the term in brackets in Equation #III-15.

$$U = \sum_e \frac{1}{2} \overline{\mathbf{q}}^T \left[2\pi \int_{-1}^{1} \int_{-1}^{1} \overline{\mathbf{B}}^T \overline{\mathbf{D}} \overline{\mathbf{B}} \det \overline{\mathbf{J}}\, r \, d\xi \, d\eta \right] \overline{\mathbf{q}} \qquad \text{(III-15.}$$

For practical implementation, the model uses two-point Gaussian Quadrature to approximate the two integrals. It would be unwieldy to find a closed form solution, since the direct expansion of the bracketed term is quite complex.

Assembling together all the element stiffness matrices produces a Global Stiffness Matrix (GSM), denoted $\overline{\mathbf{K}}$. This is done, as indicated in Equation #III-15, by summing the ESMs together to produce the total strain energy. The model collects the ESMs, and places them into $\overline{\mathbf{K}}$ according to their corresponding degrees of freedom. Because they share nodes across the width, the adjacent elements representing a wound roll layer (or the core) form a sub-structure, and are thus physically and mathematically linked. The GSM for the entire wound roll consists of elements for both the core and the web layers.

The work potential contribution to the potential energy arises from any of three general load categories applied to the system. Concentrated point loads ($\overline{\mathbf{L}}$) are forces that act on a single point. Body forces ($\bar{\mathbf{f}}$), like gravity, are loads distributed throughout a volume. Traction forces ($\overline{\mathbf{T}}$) are loads distributed over a surface area, and are the most significant and common loadings found in wound rolls. A process similar to that used for Equation #III-15 establishes the contributions of all three load categories in the axisymmetric formulation. This is evident in Equation #III-16.

$$WP = -\sum \bar{\mathbf{q}}^T \left[2\pi \int_{-1}^{1}\int_{-1}^{1} \bar{\varphi}^T \bar{\mathbf{f}}\, r \det \bar{\mathbf{J}}\, d\xi\, d\eta + 2\pi \bar{\varphi}^T \int_l \overline{\mathbf{T}}\, r\, dl + \bar{\varphi}^T \overline{\mathbf{L}} \right] \qquad \text{(III-16.}$$

If there is more than one load of a particular category, the equation must be expanded to include a formulation for each one. Therefore there can be multiple $\overline{\mathbf{T}}$ entries, for example. As a side note, the concentrated loads, $\overline{\mathbf{L}}$, become ring loads in the

axisymmetric formulation. They persist around the entire circumference at the radius of the node on which they are applied. Their magnitude is the total over that circumference.

Equation #III-16 also introduces the shape function matrix $\overline{\varphi}$. For the quadrilateral element, $\overline{\varphi}$ is as seen in Equation #III-17.

$$\overline{\varphi} = \begin{bmatrix} \varphi_1 & 0 & \varphi_2 & 0 & \varphi_3 & 0 & \varphi_4 & 0 \\ 0 & \varphi_1 & 0 & \varphi_2 & 0 & \varphi_3 & 0 & \varphi_4 \end{bmatrix} \qquad \text{(III-17.}$$

In the body force component of the *WP*, the shape function matrix is evaluated at the natural coordinates, during the Gaussian Quadrature numerical integration. For the traction force component, the natural coordinates are first substituted into the shape function matrix. The coordinates correspond to the element's side on which the traction acts. For any given side, two of the shape functions will be zero, and the other two will allocate the traction between them. The traction is then integrated over the length (*l*) of that side. Multiplying the integrated traction by the shape function matrix, results in the traction load being sent to the desired degrees of freedom. The shape function matrix similarly directs the application of the point loads, when a load's coordinates are inserted.

In the same way the strain energy was contained in $\overline{\mathbf{K}}$, the work potential from the applied loads is contained by a global force vector $\overline{\mathbf{F}}$. And, just like for $\overline{\mathbf{K}}$, the global force vector merges the contributions of all the elements in the roll. Each element's contribution is contained in its own local, elemental force vector. It is the eight by one vector arising out of the bracketed term in Equation #III-16. As such, it contains all the loads applied to a single element from all of the load categories. When the local loads are combined to produce $\overline{\mathbf{F}}$, each entry corresponds to a particular degree of freedom in the wound roll.

The primary load source in a center wound roll, its web line tension, is not directly compatible with an axisymmetric formulation. It is indeed a traction force distributed over the web surface, but all the load categories in Equation #III-16 must be in the plane of the element as established in Figure #III-3. The web line tension, however, is perpendicular to the element's RZ plane. One way around this difficulty would be to use the hoop stress equation (Equation #II-17) to convert T_W into an equivalent σ_{rr} that would satisfy the *WP* equation. But, this is not a practicable possibility for a number of reasons. First, the radial pressure varies dramatically through the depth of the outer web layer. The outside has no radial pressure at all. The radial pressure on the inside surface however, is the definite, tangible amount that satisfies the hoop stress. Since an element has one, distinct radial modulus, and radial pressure determines that radial modulus (Equation #II-2), every element must have only one pressure. This would be accomplished by averaging the pressures in the element, and using that value to calculate the radial modulus. But, because the pressure would be an average, it would be only valid at the center of the element, not at the hoop stress's lower surface. Thus, the element's average pressure is not the same physical entity as the hoop stress pressure. A second reason against converting T_W using the hoop stress formula, is that the expression uses t and r. Both the thickness and the radius will vary with the pressure applied! A third and final reason is that converting it back and forth this way is tedious, and introduces additional machine error.

Multi-point constraints are needed to construct the final wound roll model. In the actual wound roll, each layer connects to layers above or below it through physical contact. But in the model, elements that do not share nodes are not inherently linked.

Tying them together is accomplished by populating the GSM with a multi-point constraint equation like Equation #III-18.

$$\beta_1 Q_{P1} + \beta_2 Q_{P2} = \beta_0 \qquad \text{(III-18.}$$

Multi-point equations work by setting up a relationship between two previously independent points in the roll. The expression's *Q* terms refer to the degrees of freedom associated with the two points (1 and 2). The terms reference nodes numbered in the entire (global) wound roll, instead of in the master element's local four nodes. They are from the global deformation vector $\overline{\mathbf{Q}}$. The β terms are constants which ratio their corresponding degrees of freedom against each other. For example, if two layers' nodes are in contact, and are to move in concert, β_1 is set to -1, β_2 to 1, and β_0 to 0. This reduces Equation #III-18 to $Q_{P2} = Q_{P1}$, and locks the two degrees of freedom together. In a multi-point constraint, each contacting node's degrees of freedom are mathematically proportional to the other causing them to physically maintain their relative positions.

The multi-point constraint equation is a modification of the potential energy formulation. It does not actually contribute to either the system's strain energy, or its work potential, but its components conveniently fit into their formulations. This is evident in Equation #III-18 which shows β_1 and β_2 pre-multiplying $\overline{\mathbf{Q}}$ values (just as the ESM does in Equation #III-15), while β_0 does not. In practice, the multi-point constraints equation is enforced by placing its constants into the global matrices. Since the β values are ratios, they are cross multiplied, and then multiplied by a penalty constant (CNST) before being placed in $\overline{\mathbf{K}}$ or $\overline{\mathbf{F}}$. The CNST*β_1^2 and the CNST*β_2^2 are placed at the $Q_{P1(2)}$ row and column in $\overline{\mathbf{K}}$, respectively. The cross term CNST*$\beta_1\beta_2$ is placed at two

locations: Q_{P1} row with Q_{P2} column, and vice versa. Finally, $CNST*\beta_0\beta_1$ and $CNST*\beta_0\beta_2$ add into $\overline{\mathbf{F}}$ at the Q_{P1} and Q_{P2} rows respectively.

The web line tension is enforced indirectly by using a multi-point constraint to "interfere" a new layer into the roll. Like a compression fit, the interference acts to compress the roll, while the roll reacts and expands the new layer. The sum total of the inward compression and the outward expansion equals the imposed interference, and leaves the new layer's inner surface stretched over the roll's outer surface. The greater the layer's interference, the larger the resulting tension will be. The model does this with the multi-point constraints from Equation #III-18. To impose the interference, β_1 is -1, and β_2 is still 1, while β_0 is now equal to the interference. Just as they did for the multi-point constraint links between the layers, the β_1, and β_2 values populate $\overline{\mathbf{K}}$, while the β_0 terms insert into $\overline{\mathbf{F}}$. A physical depiction of the interference can be seen in Figure #III-5.

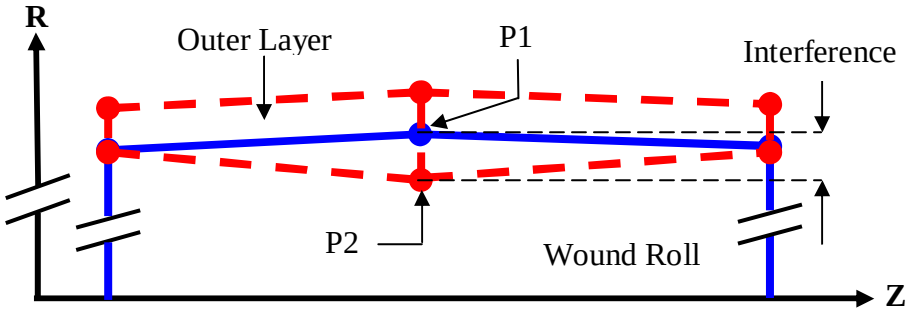

Figure #III-5: The model enforces the web line tension by placing the nodes on the new layer's inside surface (P2), inside of the roll's nodes (P1), and resolving the interference.

The amount of tension partitioned out to the nodes is based on conserving circumferential material. Since each web layer remains continuous across the roll width, the amount of material passing onto the roll must be the same at all CMD node locations. Otherwise, part of the web cross section would advance ahead of the rest, leaving the

web's center dangling in the free-span while the edges were on the roll, for example! For an unstrained material, the amount that passes onto the roll, in one revolution, equals the circumference of the roll at that moment. For less than one revolution, the amount is the arc length $r \cong \alpha$. Where r is the radius, and α is the angle of rotation. The rotational angle encountered by all the nodes across the width is, by definition, the same. Thus, for each node across the width to have the same $r \cong \alpha$, means that all the radii would have to be the same too! And, such would be the case in the absence of strain. However, the strains across the width are not equal. They circumferentially stretch the web in proportion to the local tension. Web that is wound on a larger local radius will have a greater arc length, and a corresponding lag behind its neighboring material. This will cause the web to stretch locally, in an effort to maintain material compatibility with the surrounding web layer. The local stretch is a local strain and a corresponding stress. Thus, each CMD node's radius provides the means to determine how much web line tension it should receive. This is the same method used by Kedl [19].

Each node's radial position establishes its relative tension portion while the layer's total tension iterates to match web line tension. Using the arc length calculation, the tension and then the strain needed at each node across the width are first determined. Then, from the circumferential strain expression, Equation #II-8, the initial interferences of the new layer's nodes are estimated. Next, the model is solved. If the resulting sum of the tensions across the width does not equal the web line tension, all the interferences are equally scaled up or down. The roll and new layer are reset, and the scaled interference is imposed. This process repeats until the tension summation converges to the web line tension. The radial moduli are adjusted during the interference iteration as well. After

finding each potential solution set, the radial moduli are recalculated throughout the wound roll. The flowchart in Figure #III-6 lays out the model's general progression.

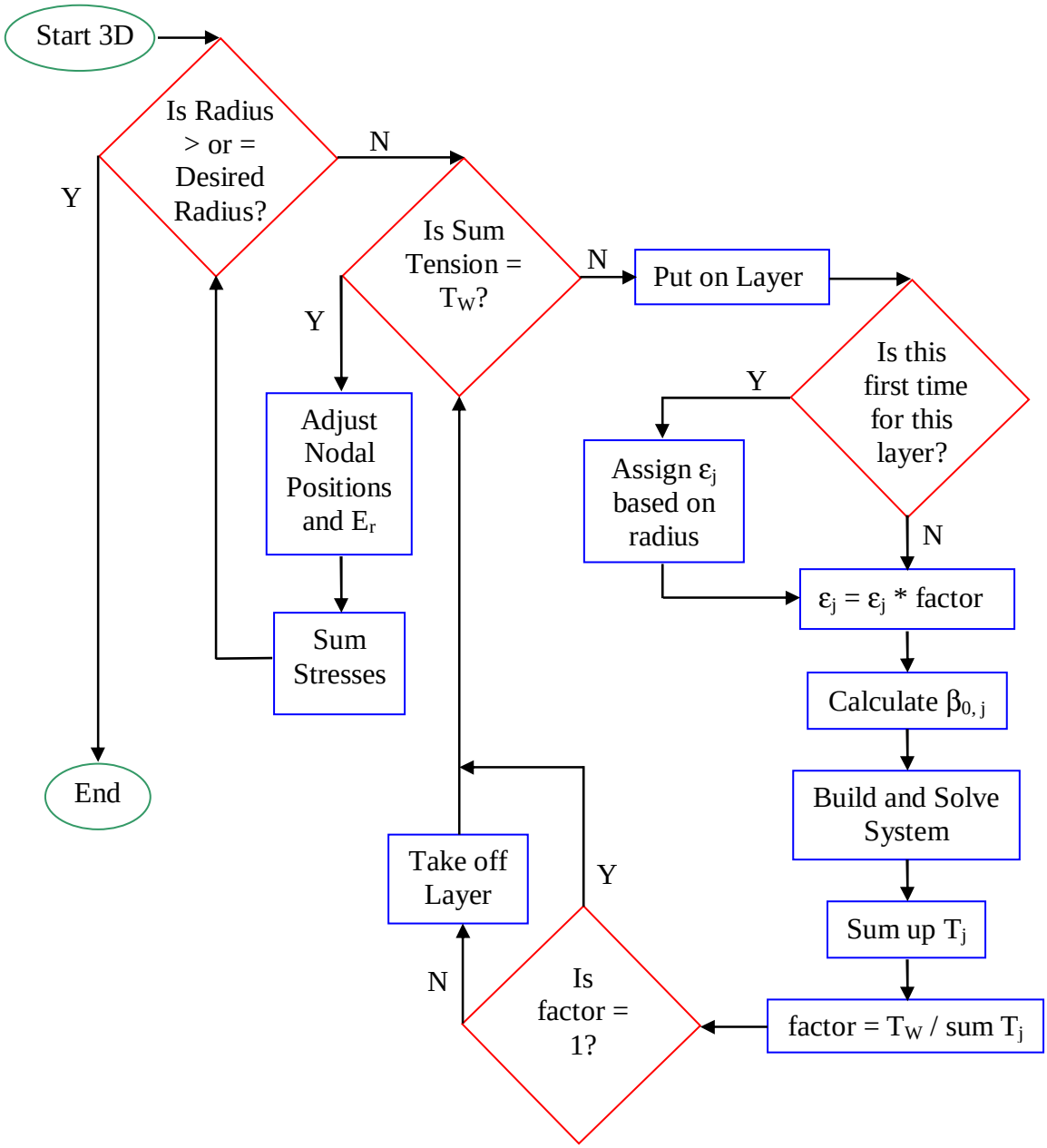

Figure #III-6: The model iterates until the outer layer's calculated tension sums up to the web line tension thereby ensuring the correct amount of energy is put into the roll.

The tension summation is much the same as that mentioned in the chapter II discussions of Hakiel [15], and Cole and Hakiel [4], and represented in Equation #II-31.

Determining the stable energy configuration or "solving the model", calculates the deformations throughout the roll in its current configuration. With the roll's layers, core, and connections combined into $\overline{\mathbf{K}}$, the external loads and interferences taken care of by $\overline{\mathbf{F}}$, and the unknown deformations represented as $\overline{\mathbf{Q}}$, the roll's configuration becomes a finite element system, Equation #III-19.

$$\overline{\mathbf{F}} = \overline{\mathbf{K}}\,\overline{\mathbf{Q}} \qquad \text{(III-19.}$$

In solving the model, the global stiffness matrix theoretically is inverted and multiplied by the force vector. Practically however, inverting $\overline{\mathbf{K}}$ is unmanageable, so the model instead uses the Lower Upper Decomposition (LUD) pivoting method. The result is the $\overline{\mathbf{Q}}$ vector of R and Z directed deformations of every node throughout the roll model.

Every new layer accreted onto the roll incrementally reconfigures the entire roll. This is because the new layer squeezes the previous outside layer, which in turn deforms into the layers beneath it. Thus, the deformations found by solving system #III-19 are a cascading reaction to the interference of only the outer layer. They are not the total deformations seen by the nodes when the entire roll is finished, but rather a snapshot of an intermediate state. In the comprehensive sense of the wound roll, they are better thought of as $\delta\overline{\mathbf{Q}}$.

The sum total of a node's $\delta\overline{\mathbf{Q}}$, from every time the system is solved, is that node's true total deformation. The model does not explicitly track the sum total delta deformations, but rather is concerned with the products from them. Each $\delta\overline{\mathbf{Q}}$ converts to a $\delta\overline{\boldsymbol{\varepsilon}}$, and a corresponding $\delta\overline{\boldsymbol{\sigma}}$. The $\delta\overline{\boldsymbol{\sigma}}$ are summed instead to produce the roll's comprehensive stress components σ_{rr}, σ_{zz}, σ_{rz}, and $\sigma_{\theta\theta}$. In that sense, the constitutive

equations (#III-2) for any one solution set of the accreting wound roll, are better represented as seen in Equation #III-20.

$$\begin{bmatrix} \delta\varepsilon_{rr} \\ \delta\varepsilon_{\theta\theta} \\ \delta\varepsilon_{zz} \\ \delta\varepsilon_{rz} \end{bmatrix} = \begin{bmatrix} 1/E_r & -\nu_{\theta r}/E_\theta & -\nu_{zr}/E_z & 0 \\ -\nu_{\theta r}/E_\theta & 1/E_\theta & -\nu_{z\theta}/E_z & 0 \\ -\nu_{zr}/E_z & -\nu_{z\theta}/E_z & 1/E_z & 0 \\ 0 & 0 & 0 & \dfrac{2\{E_r(1+2\nu_{zr})+E_z\}}{E_r E_z} \end{bmatrix} \begin{bmatrix} \delta\sigma_{rr} \\ \delta\sigma_{\theta\theta} \\ \delta\sigma_{zz} \\ \delta\sigma_{rz} \end{bmatrix} \quad \text{(III-20.}$$

Summing the stresses instead of the deformations was not a random choice. The total σ_{rr} values are needed to determine an element's current E_r.

The model is designed to accommodate various wound roll configurations so it can be used as a design tool. The core is represented as a hollow, uniform thickness cylinder. The radial thickness can be adjusted to match the wall thickness of the roll's actual core. The model divides the thickness into two radially stacked layers to facilitate radial variations in its stresses. The core's width can be made larger than the web's width, as is common in winding (see Figure #III-7).

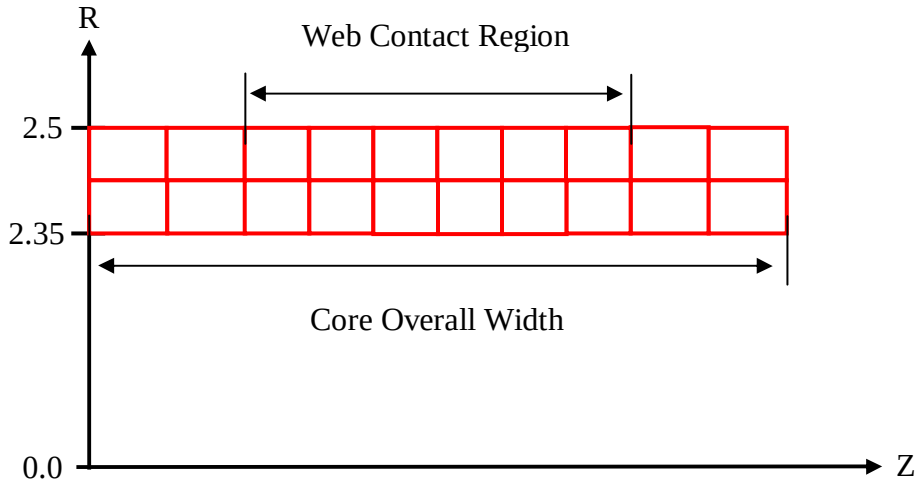

Figure #III-7: The axisymmetric model's core is a cylinder with a flexible wall thickness, and the capability to extended beyond the web's width.

This makes the model more realistic, and permits axial behavior, such as plane strain to plane stress transitions. It also provides a way to distance the web material away from the core supports. Many models simply represent the core as a composite stiffness value or as an isotropic shell. The axisymmetric formulation will allow it to be orthotropic if desired.

There are a number of inputs necessary in addition to those previously mentioned for the core, and for the thickness profile. The desired roll radius is the radius the model uses as a target to stop the wind. Note that the model automatically accounts for the compression in the roll, during winding. Thus, a highly compressible material will wind on more layers to reach the same target radius as a less compressible material. Of course, the web's material properties, especially its radial modulus must be given. They are incorporated directly into the ESMs. The model accommodates four popular representations of E_r given in Equation #III-21.

$$\begin{aligned} E_r &= K_1 K_2 + K_2 P \\ E_r &= C_1 + C_2 P + C_3 P^2 + C_4 P^3 \\ E_r &= C_0 \left(1 - e^{\frac{-P}{C_1}} \right) \\ E_r &= (A + BP)^C \end{aligned} \qquad \text{(III-21.}$$

Some of these representations are depicted in Table #I-1, and Figure #I-4.

There are limitations to this model. The core is modeled as a uniform cylinder without any stub shafts, vertical supports or thickness variations. Also, it is represented by only two radial element layers. Initial representations used eight radial layers, but because it was a uniform cylinder, two layers were deemed sufficient to model its stresses. Reducing the layers reduces the computation time. Another limitation is the

equal element widths. Regions with quick thickness changes require a sufficient number of small elements to capture their behavior. Regions with no thickness variation could instead be represented by two, wide elements. This results in more total elements across the width than necessary, but seemed tolerable, since the segments were equal in width in the only readily available experimental comparison data (Cole and Hakiel [4]). Along the same line as the elements, there is no provision for one composite model layer to represent multiple actual layers. This means every single web layer must be modeled and wound individually. Finally, there are no inter-layer voids, no lateral slipping constraints, and the center of each web and core layer cannot move in the z direction.

During the model development, results were compared to known sources for accuracy. The cylindrical core was developed first and checked against the Lekhnitskii [22] classical expressions that have been modified for consistent nomenclature and given in Equations #III-22, 23, and 24.

$$\sigma_{rr} = \left[\frac{P_{In}\left(\frac{R_{In}}{R_{Ex}}\right)^{\psi+1} - P_{Ex}}{1-\left(\frac{R_{In}}{R_{Ex}}\right)^{2\psi}} \right]\left(\frac{r}{R_{Ex}}\right)^{\psi-1} - \left[\frac{P_{In} - P_{Ex}\left(\frac{R_{In}}{R_{Ex}}\right)^{\psi-1}}{1-\left(\frac{R_{In}}{R_{Ex}}\right)^{2\psi}} \right]\left(\frac{R_{In}}{R_{Ex}}\right)^{\psi+1}\left(\frac{R_{Ex}}{r}\right)^{\psi+1} \quad \text{(III-22.}$$

$$\sigma_{\theta\theta} = \left[\frac{P_{In}\left(\frac{R_{In}}{R_{Ex}}\right)^{\psi+1} - P_{Ex}}{1-\left(\frac{R_{In}}{R_{Ex}}\right)^{2\psi}} \right]\psi\left(\frac{r}{R_{Ex}}\right)^{\psi-1} + \left[\frac{P_{In} - P_{Ex}\left(\frac{R_{In}}{R_{Ex}}\right)^{\psi-1}}{1-\left(\frac{R_{In}}{R_{Ex}}\right)^{2\psi}} \right]\psi\left(\frac{R_{In}}{R_{Ex}}\right)^{\psi+1}\left(\frac{R_{Ex}}{r}\right)^{\psi+1} \quad \text{(III-23.}$$

$$u = \frac{R_{Ex}}{1-\left(\frac{R_{In}}{R_{Ex}}\right)^{2\psi}}\left[\begin{array}{l}\left(P_{In}\left(\frac{R_{In}}{R_{Ex}}\right)^{\psi+1} - P_{Ex}\right)\left(\psi - \nu_{\theta r}\right)\left(\frac{r}{R_{Ex}}\right)^{\psi} + \\ \left(P_{In} - P_{Ex}\left(\frac{R_{In}}{R_{Ex}}\right)^{\psi-1}\right)\left(\psi + \nu_{\theta r}\right)\left(\frac{R_{In}}{R_{Ex}}\right)^{\psi+1}\left(\frac{R_{Ex}}{r}\right)^{\psi}\end{array}\right] \quad \text{(III-24.}$$

$$\text{with } \psi = \sqrt{\frac{E_\theta}{E_r}}$$

The core's inside radius and pressure are given as R_{In} and P_{In}, while the external values are R_{Ex}, and P_{Ex}. The variable r is the radius (between R_{In} and R_{Ex}) at which the equations are being evaluated. The square root of the modulus ratio is represented by ψ for simplification. Equations #III-22, 23, and 24 apply specifically to orthotropic, thick walled cylinders like the wound roll core. As seen in Figure #III-8, with P_{Ex} = 1 N/mm^2, the axisymmetric cylinder model's results matched the classical expressions closely.

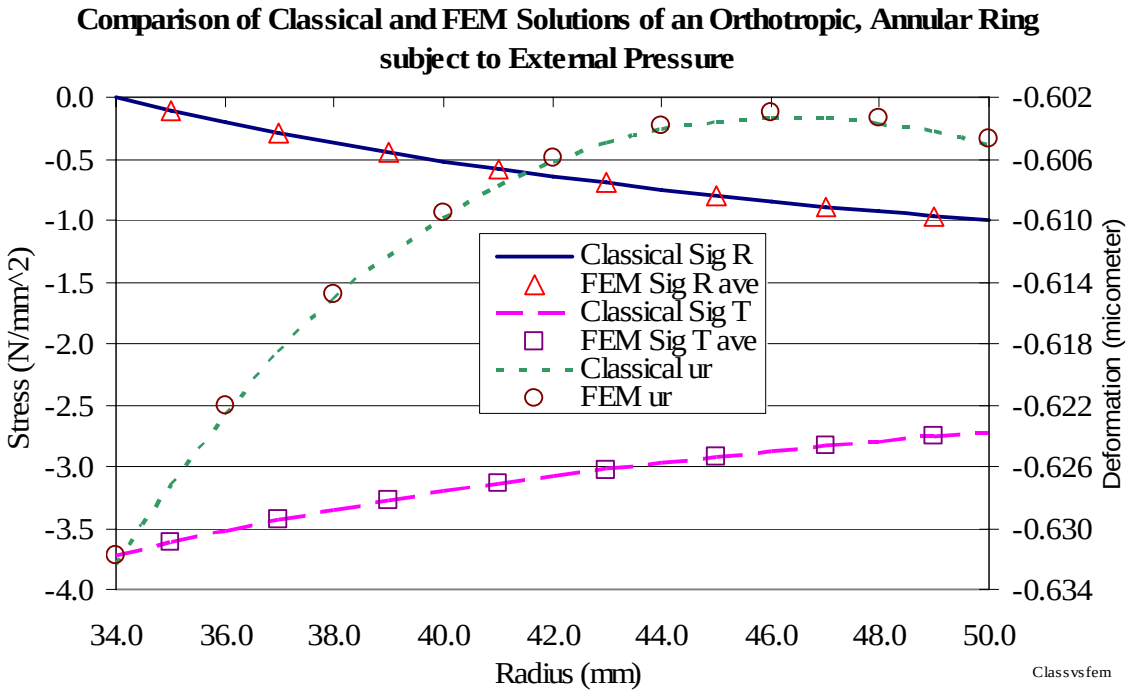

Figure #III-8: The axisymmetric model's radial pressure, circumferential stress, and deformation are nearly identical to the classical, orthotropic, Lekhnitskii [22] solution for an externally pressured annular ring.

The next developmental step added the ability to accrete a roll. Two dimensional test runs compared well with results reported in the literature. Among them was the 76 µm polyester film from Hakiel [14]. Figures #III-9, and #III-10 display the axisymmetric FEM's radial pressures and circumferential stresses against Hakiel's 2D model results. Throughout the roll's depth, especially at the core, the axisymmetric model's radial pressures are lower then Hakiel's, but the behavior is very similar. The circumferential stress magnitudes at the outside of the roll match closely, but differ in the middle.

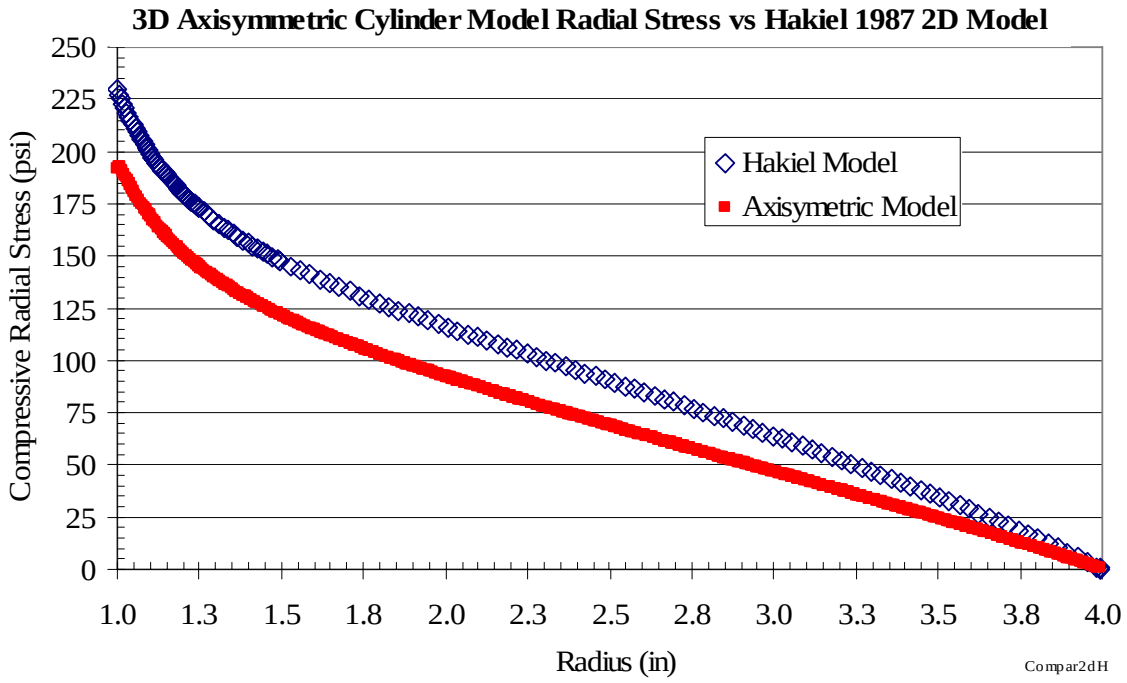

Figure #III-9: The axisymmetric model's radial pressure, for a two dimensional wound roll, compares well to Hakiel's [14] model, and additionally shows the effects of tension loss.

Simulations of other materials, using the axisymmetric model, similarly produced lower pressures at the core and in the plateaus, then Hakiel's model. This is acceptable and even desirable, because it is in accord with tension loss. The axisymmetric model automatically accounts for it while Hakiel's model does not.

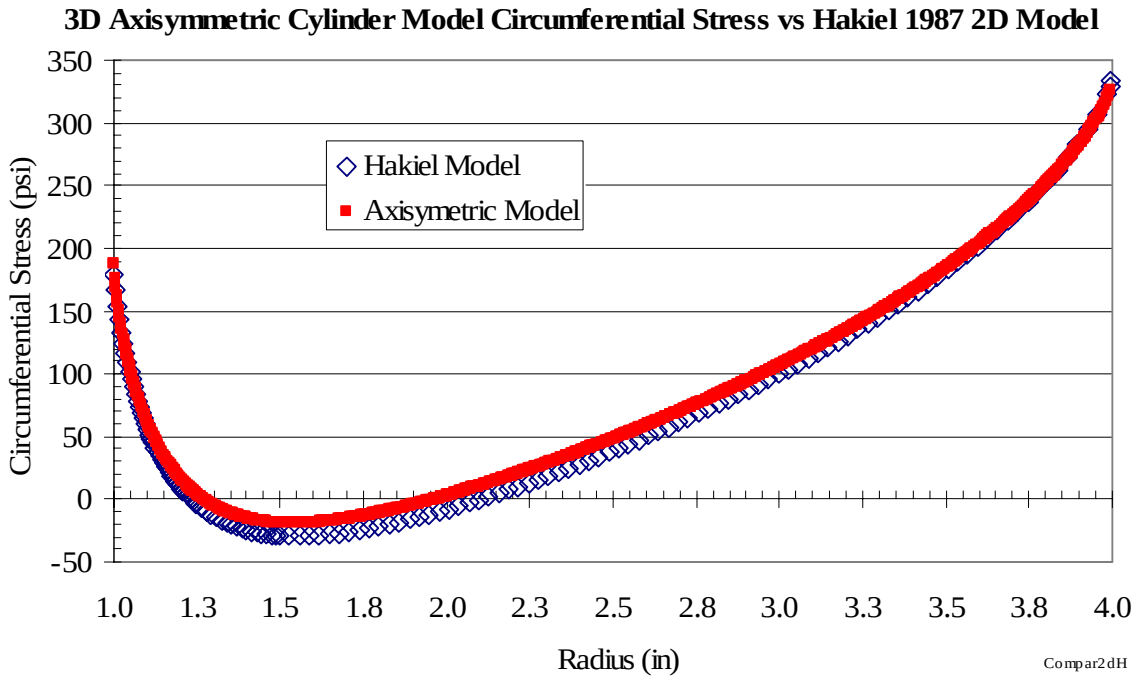

Figure #III-10: The circumferential stresses generated by the axisymmetric model are nearly identical to Hakiel's [14] two dimensional model, and clearly show a loss of tension for much of the radius.

Finally, a full three dimensional example was conducted. It used the web thickness profile referred to by Cole and Hakiel [4] as "case A" (shown in Figure #I-6). The web was a ten inch wide PET, with an average thickness of 0.0039 inches. The core they used was aluminum, with an outer radius of 2.5 inches, and a radial stiffness just over 512 ksi. From Roisum's [31] isotropic core stiffness relation (Equation #III-25), this made the wall thickness to be used in the axisymmetric model equal to 0.125 inches.

$$Stiffness = \frac{E\left(R_{Ex}^2 - R_{In}^2\right)}{\left(R_{Ex}^2 + R_{In}^2 - \nu\left(R_{Ex}^2 - R_{In}^2\right)\right)} \qquad \text{(III-25.}$$

Cole and Hakiel tried two different, constant web line tensions in their runs. The example run used their 2 pli tension. The results of the axisymmetric model are plotted in Figure #III-11 against values they measured at the core, and the results of their model.

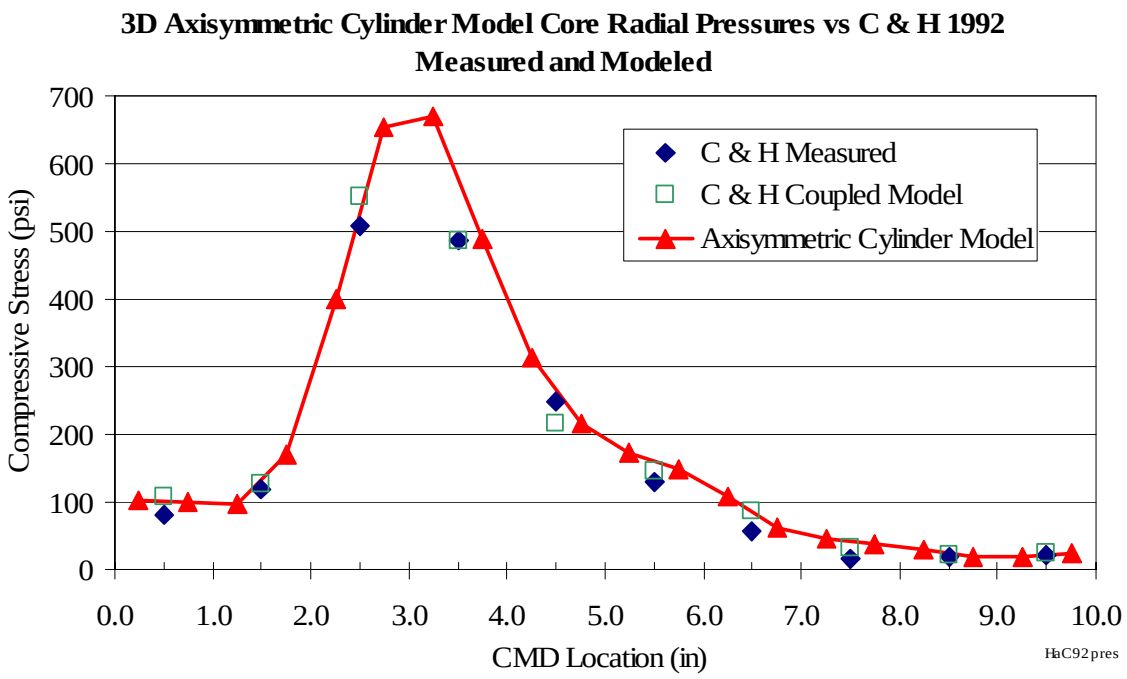

Figure #III-11: The axisymmetric model's predicted radial core pressures match favorably to Cole and Hakiel's [4] measured pressures at 2 pli.

It is apparent that the axisymmetric model did well in predicting the radial pressure behavior across the entire width. The peak values do exceed the measured values around the three inch CMD location, but this is partly because the measured values apply to one inch wide segments. The axisymmetric model results are for half inch wide segments, and when the two adjacent segments in each inch are averaged, the pressures compare almost exactly to the measured values.

Since it is important to accurately predict a wound roll's outside radius across its width, Figure #III-12 plots the model's CMD radial profile. Included in the plot are Cole and Hakiel's measured values, and the values predicted by their "coupled" model. (Note: the Cole and Hakiel values have been modified to English unit equivalents of their [4, Fig. #9].) The axisymmetric model comes closer to matching the magnitude displayed in the measured radial profile. Neither model captures all the nuances though.

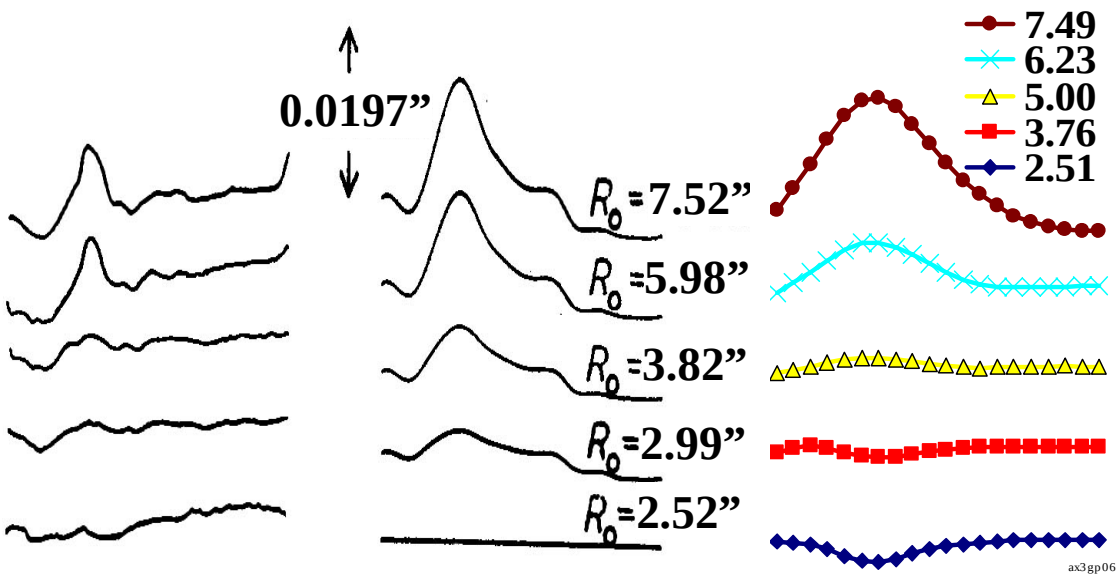

Figure #III-12: The CMD radial profiles from the axisymmetric model have magnitudes very close to Cole and Hakiel’s [4] measured values at 2 pli.

Overall, the three dimensional, axisymmetric, finite element model displays promising results. It utilizes the non-linear radial modulus, and captures the stress behavior seen in experiments and other models. It produces a realistic radial profile across a non-uniform wound roll. The formulation is also expandable making it an attractive foundation for further research. In this form, it is somewhat limited however. This version’s accuracy and utility are insufficient for it to be used as the three dimensional model in the nip impinged, 3D model.

Axisymmetric Expanded Core

The expanded core version of the three dimensional, axisymmetric model addresses many of the limitations present in the previous version. The most significant enhancement relates to the core. This version accommodates a variety of core materials and support conditions. Another improvement reduces computational time by representing multiple web layers as one model layer. The thicker model layers accrete more material in a winding pass, therefore fewer passes are needed. Also, the model looks at the interlayer contact in the R and Z plane. Voids between layers and CMD friction effects are newly added options.

The model divides the core into three separate components: the contact surface, the stub shafts, and the inserts. The cylindrical shell, that was the entire core in the earlier version, is referred to as the contact surface. It is not just the outer surface that comes into contact with the web material, but also includes the layers radially beneath it. In the previous version, two layers always simulated the surface's thickness. This version accommodates between one and eight layers. The material properties and the overall CMD width must be the same for all the layers in the contact surface. The other two core structure components together make up the newly added radial supports referred to collectively as end caps. The stub shaft is the component that connects the core to the winder. It is supported by the winder, it generally takes the shape and function of a shaft extending into the core, and it transmits rotation (and torque when applicable) between the core and the winder. The core insert is the component linking the stub shaft to the contact surface. All three components are shown in the right hand side of Figure #III-13.

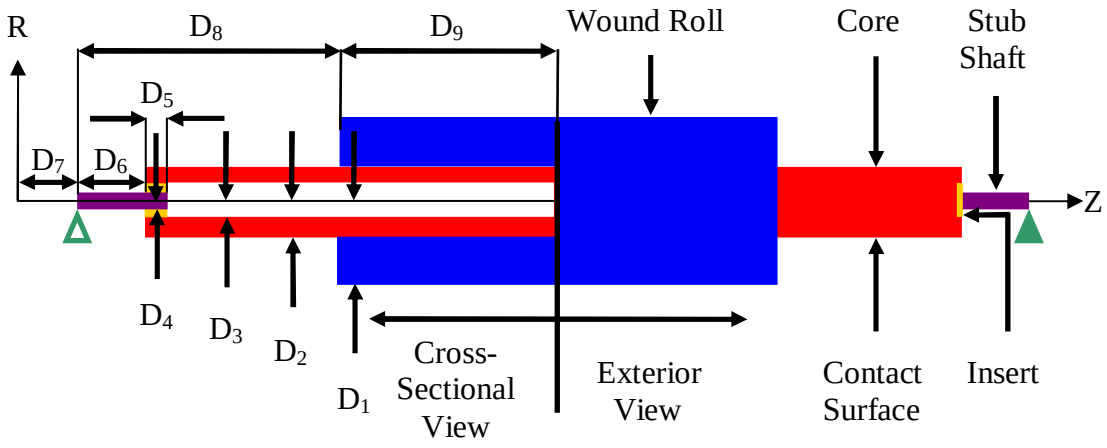

Figure #III-13: The numerous wound roll and core parameters provide the control necessary to make this configuration quite flexible.

The core's three components are defined by numerous dimensions. The contact surface's outer radius (which is also the inside radius of the roll), the inner radius, and its CMD width are key parameters. They are labeled in the cross-sectional view on the left hand side of Figure #III-13 as D_2, D_3, and $2*(D_8 + D_9 – D_6)$ respectively. The stub shaft's dimensions include its radius, D_4, and its width, D_5+D_6. Finally, the insert is defined by its width, D_5, and its boundaries with the already mentioned radii of the contact surface and the stub shaft.

Not all the components need be present in a winding simulation. While the contact surface must be present, the insert and stub shaft on the right side can be eliminated to make the core cantilever off the left side, for example. But, since the model is not side specific, the left insert and stub shaft can just as easily be removed. Removing both at the same time leaves a cylindrical core, as it was in the first version. Either insert can be removed by itself, but unless the radius of the stub shaft matches the inside radius of the contact surface, the stub shaft will not be linked to the contact surface. Thus, removing an insert effectively eliminates the stub shaft on that side too. The predominant

reason for having the different components is so they can be assigned separate material properties. For example, the stub shaft can be made of steel while the contact surface is aluminum.

Figure #III-14 shows a cantilevered core to better illustrate the possible core configurations. By setting their thicknesses to zero, the right insert and stub shaft are

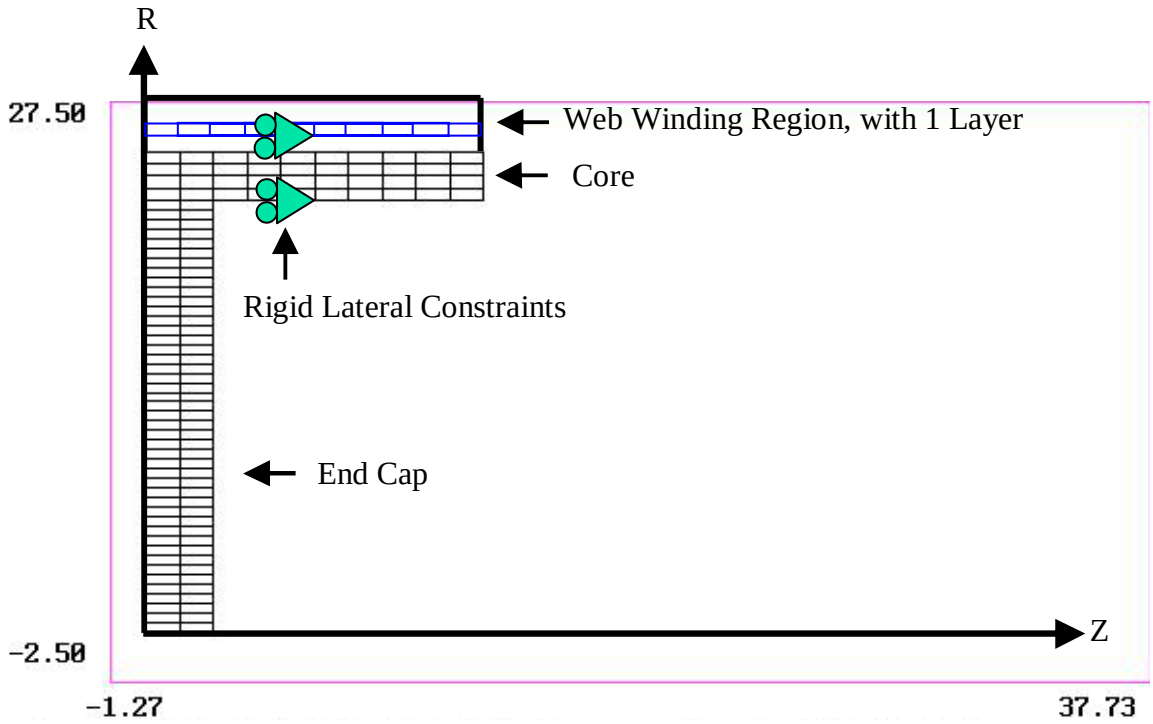

Figure #III-14: The cantilevered core's left end cap is underneath the edge of the web winding region making the core's left side much stiffer than the right.

eliminated. Also, the left end cap is moved in directly beneath the region on the contact surface where the web will accrete. This is done through a number of other input parameters. The model requires them (and a few others) for proper execution, but they are inconsequential to the discussion here.

The cantilevered core example also shows how the model constrains rigid body motions in the Z direction. The core, and each web layer, is fixed in the Z direction at the

node closest to center of the web winding width. This is a tie over from the modeling used for the cylindrical core version. The constraint is enforced through a degenerate form of the multi-point equation. When the β_2 and β_0 constants in Equation #III-18 are set to zero, and β_1 is set to one, the equation becomes $Q_{P1} = 0$. This results in the term CNST*β_1^2 (now equal to just CNST) being placed at row and column Q_{P1} in $\overline{\mathbf{K}}$.

The cantilevered core is for a winding simulation of ½" wide, magnetic film wound onto a plastic hub. The configuration comes from the work presented in Lee and Wickert [20]. Table #III-1 below summarizes the parameters used for the simulation, as they were reported in [20]. Note their web's ν value was the same for all three directions (θz, θr, zr), making it non-direction specific.

Parameter	**Web**	**Core**
Thick	10 μm	2.54 mm
Width	12.7 mm	12.7 mm
E_R	$7+590P-120P^2+10P^3$ Mpa	3.5 GPa
E_T	7 Gpa	3.5 GPa
E_Z	9 Gpa	3.5 GPa
ν	0.3	0.43
G_{RZ}	100 MPa	1.75 GPa
Layers	30 / model layer	4
Radius		25 mm

Table #III-1: The cantilevered core example had a ½" wide magnetic tape and a plastic core with the above parameters.

The results of the simulation, at 1 Newton of T_W, appear in the next four figures, Figures #III-15 through #III-18. In order, they show the radial pressure, circumferential stress, the shear stress, and the lateral stress throughout the wound roll, respectively.

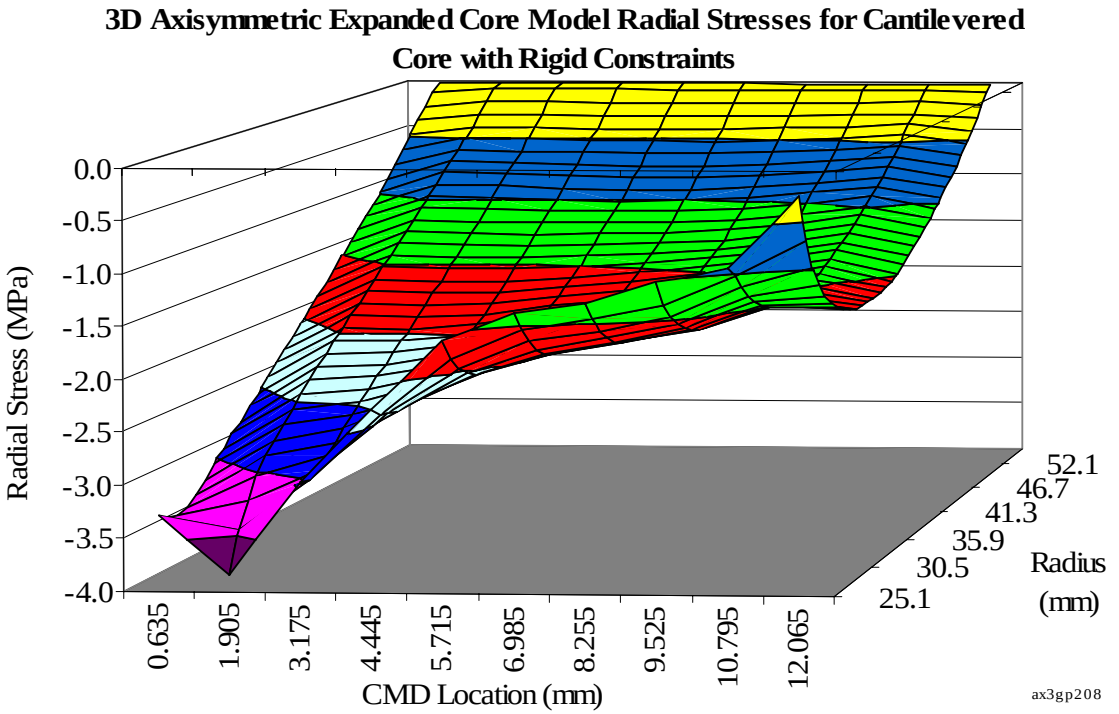

Figure #III-15: The radial pressure throughout the roll on the cantilevered core clearly shows the core is stiffer on the left.

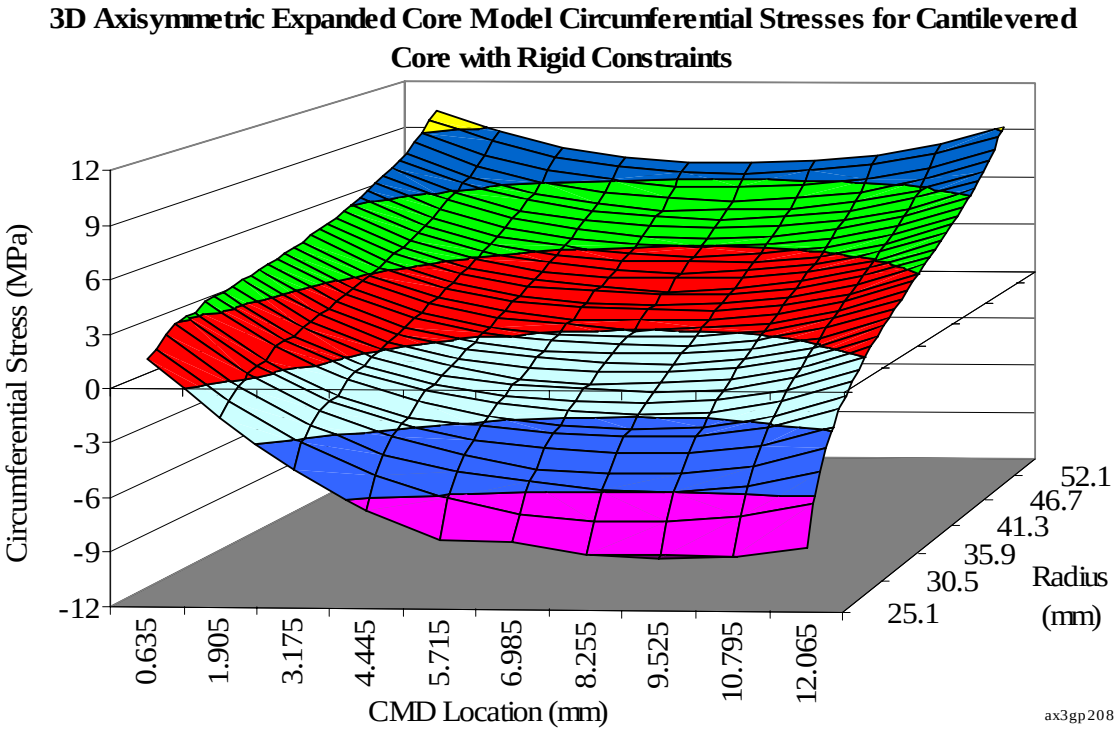

Figure #III-16: The circumferential stress in the roll shows a loss of tension on the right side where the cantilevered core cannot provide as much support.

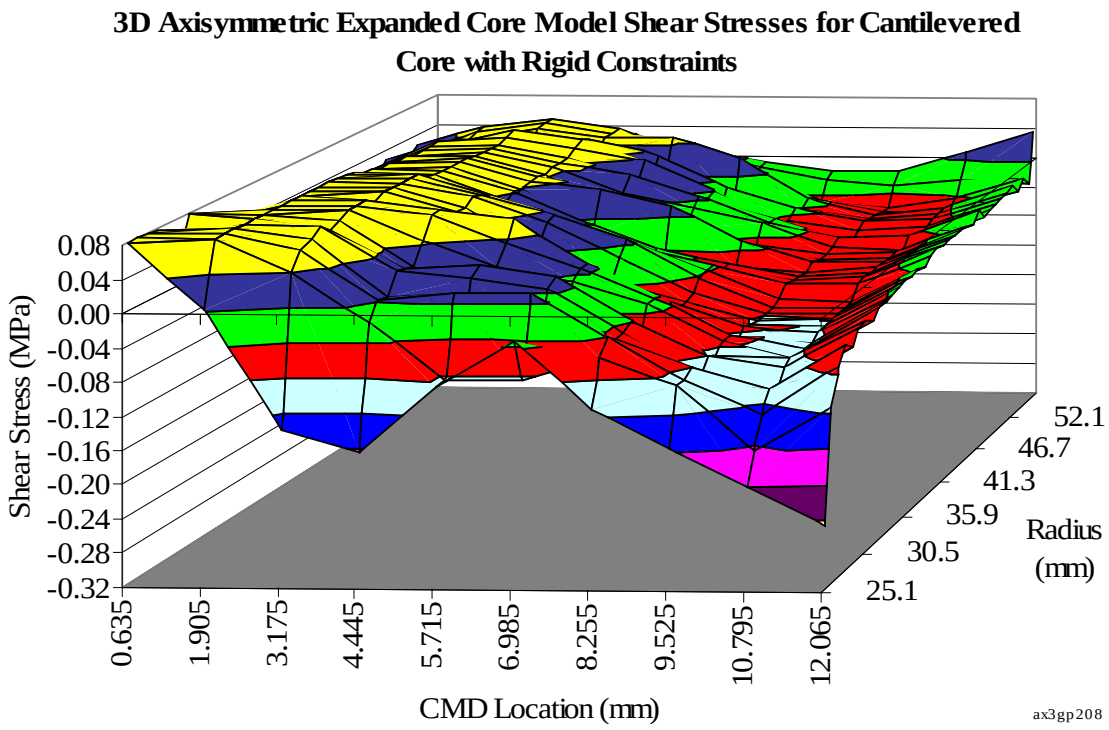

Figure #III-17: The model's shearing stresses show the layers shearing away from the roll's centerline as the core's compliance spreads them laterally.

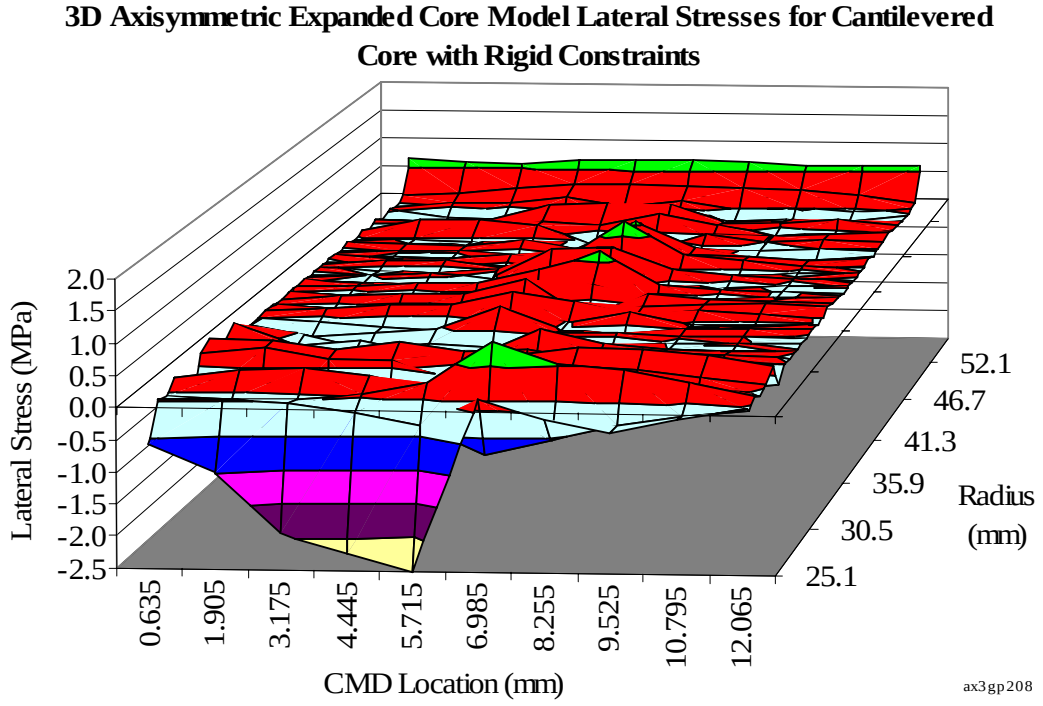

Figure #III-18: The cantilevered core's lateral stresses are quite unpredictable and random, and need further attention.

Representing multiple actual web layers with one composite model layer is another improvement. The number of web layers to group together is a parameter input by the user. The thickness profile for the model layer comes directly from multiplying the web's thickness profile by the layer parameter. Thus, the model layer becomes a radially exaggerated version of the web layer, as shown in Figure #III-19.

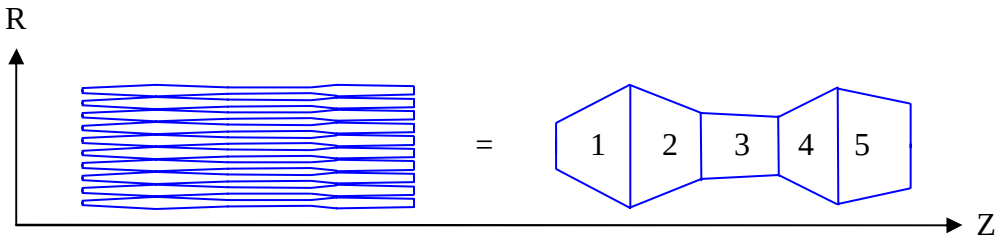

Figure #III-19: Multiple actual layers can be represented by one model layer in order to reduce computation time.

Placing multiple web layers into a model layer reduces the model's accuracy. This is because the model layer imposes the assumption that the thinner parts of the web's thickness profile will draw down together. Using Figure #III-19 as an example, this could only occur if the material on the border of sections 1, 2 and 4, 5 slipped laterally toward section 3, or underwent lateral, or shear strains. Since neither the slip, nor the strains, is accounted for in the model layer, it is not a true representation. The amount of error present will depend on the radial stiffness of the web, the degree of cross width thickness variation, and the number of web layers used in the model layer.

It is best for the user to pick some number of layers to put into a model layer, run the model at that value, and then also run it at about a third or half as many layers. If there is no appreciable difference in the results, the number of layers per model layer is sufficient. If not, they should make further reductions in the number of layers until

successive runs converge or every layer is being modeled. For softer materials (those with lower Er), the necessary number of layers is often around 5 to 10, while harder materials seem fine at 30 layers. But, utilizing this process should keep the number of actual layers per model layer as large as possible to help minimize run times, without compromising accuracy.

This version of the model also addresses the issue of void formation inside the roll. Whenever two layers pull radially apart from one another, and thereby are no longer in contact, a void forms. Cole and Hakiel [4] attribute this to an absence of local circumferential tension, and refer to it as a gap in the roll. They reach this conclusion by reasoning that a segment with no supporting contact beneath it, is free to displace radially inward until either all of its circumferential tension is lost (via Equation #II-8), or it attains contact. However, this overlooks the fact (just as the model layer representation does) that the layer is continuous across the width. Any inward, radial displacement simultaneously increases the CMD strain between the segment and its neighbors. As a result, it is more likely that if the support beneath a segment is removed, the segment will gap and suspend from its neighbors, and it will retain some circumferential tension.

When the model places a new layer across a roll, and encounters a gapped region or segment, it will assume that in that region, the new layer will form a cylindrical shell above the existing layer. This shell will span between the closest neighboring nodes that have contact. As the neighboring, contacting nodes interfere, and are then driven outward by the layer beneath, the suspended, gapped cylinder will be drawn outward as well. The amount of outward radial movement seen by any particular gapped segment will be directly based on the movement of its neighbors.

The next two figures demonstrate the procedure for gapping segments. The roll's existing outer layer represents its radial profile. It (and the new layer being added on) has twenty elements with twenty one nodes across the width. In Figure #III-20, the new layer accretes onto the roll with suspensions over it in a limited number of CMD gaps.

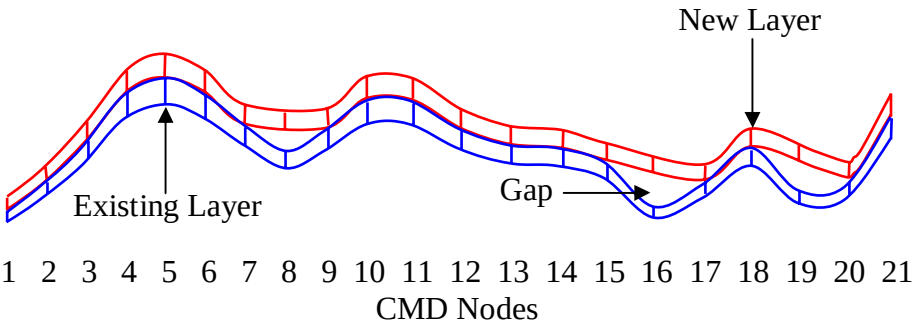

Figure #III-20: As the new layer is added onto the existing roll, some elements will form gaps suspended above the roll in a cylindrical shell.

The new layer will gap at nodes 8, 16, and 19. Node 8 will be placed at the same radial height as its contacting neighbors, nodes 7 and 9, because they are at equal radii. Nodes 16 and 19 will be on sloped lines which connect nodes 15 to 17, and nodes 18 to 20 respectively. Next, Figure #III-21 shows the same new layer accreting onto the wound roll, except that the web line tension is reduced, so the gapping is more extreme. Now nodes 8, and 13 through 20 are gapped, making a large right hand region suspend above the roll. Note also that node 1 is gapped (which can happen when segment 1 is gapped in the existing layer). This brings to light an added complexity encountered in placing the suspended elements. Technically, all of the "CMD nodes" are actually a vertically spaced pair of nodes on the side of a quadrilateral element. As the web's thickness varies in the CMD, the fundamental assumption was that it varies about a common centerline.

The elements suspended between two contacting nodes are thus not on a line between two neighboring nodes, but rather spaced relative to their common center.

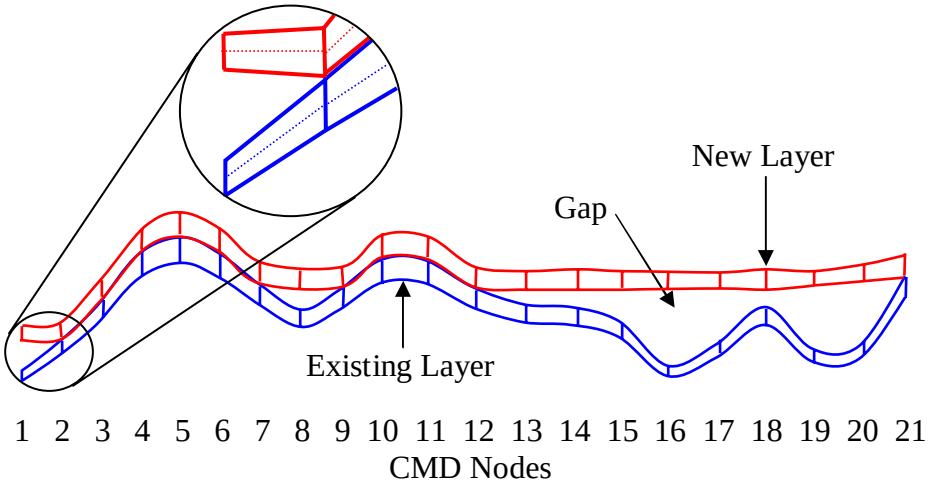

Figure #III-21: Cylindrical gap shells form by extending the centerlines of adjacent contacting elements, and bracketing the thickness variation by adjusting the nodes around it.

The zoomed in window in Figure #III-21 shows both how the centerline is maintained, and how the thicknesses are preserved. The model first finds the slope from the centerlines of the two neighboring elements, and then places the element above and below the centerline. In the case of an end node gap, the centerline is extended out horizontally as shown.

Although this discussion has focused on gaps formed in a new layer as it accretes onto the roll, it is possible that gaps form inside the roll as well. While the wound roll builds, its stresses and its radial profile change. This is witnessed by the in-roll radial profiles shown previously in Figure #III-12. Their shapes are not the same throughout the height of the roll. The change in the profile may cause one layer to pull away from another. The model looks for this by analyzing the multi-point constraints in the roll. If the links go into tension, it indicates a gap is forming. The model then removes the link

and allows the two layers to move independently at the gapped nodes. If their radii ever cross over, the link will be reestablished. Allowing the gaps in the roll helps rebalance the stresses at that location, and should increase the model's accuracy. Of course, the gaps are most likely to form in a region such as node 8 in the above examples, because it is a thin location surrounded by thicker ones. One final note regarding the gapping is that the process of opening and closing the gaps also alters the wound roll stresses and radial profiles. The effect can be so pronounced that it impacts the tension summation iteration occurring in the outer layer. Unfortunately, this can cause the model to enter a recursive loop where the tension allocation causes a gap to open, which causes the tension to be redirected, which in turn causes the gap to close, and the tension to be allocated back again. For this reason the model currently turns off the gapping possibility whenever the tension allocation is being iterated.

The final improvement warranting mention is the addition of lateral frictional constraints between the layers. Up to this point, all layers were free to slip past each other in the CMD. The only exception was the rigid constraint of the middle node, as shown back in Figure #III-14. Now, the model offers the option to let layers slip, or to constrain them with lateral friction. In terms of implementation the friction is handled in much the same way that gapping in the roll was. Individual nodes are examined to verify if they exceed the lateral static friction force. If so, their constraint links are replaced with kinetic friction loads directed against their motion. The coefficients of friction between the web and itself, and the web and the core must be input. This is for both static and kinetic friction.

Axisymmetric Lateral Movement

The lateral movement version of the three dimensional, axisymmetric wound roll model is the most current and realistic. It improves the representation of the cross width thickness variation by allowing the segment widths to be variable. Thus, narrower elements can be used in locations with rapid thickness change. Another change is the web line tension is no longer required to be constant across the width. In order to accommodate variations present in the free-span, each segment can have its own. This version also allows the wound roll to be less constricted in its lateral motion. The rigid constraints, at the center of each layer, have been replaced with relative ones. Each layer's motion is thereby dependent on its adjacent layers, not an absolute coordinate. The resulting model appears to better predict an actual wound roll.

Because accurately representing the web's thickness across the width is so critical, the model implements variable element widths to refine the thickness profile. This allows more elements to be placed at rapidly varying thickness locations, and fewer elements to be placed at locations that are nearly uniform. The resulting advantage is a better representation of trouble spots across the width, as is seen in Figure #III-22.

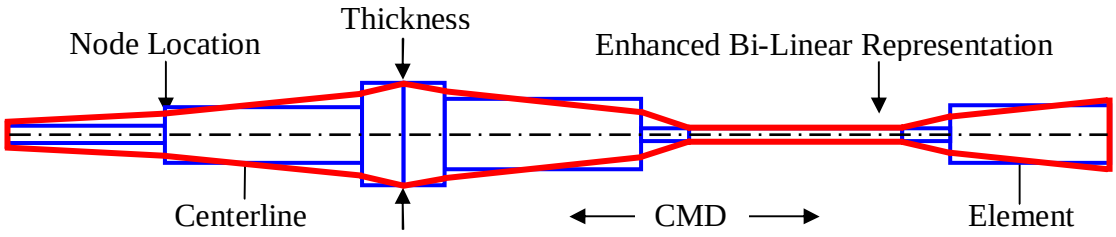

Figure #III-22: Varying the elements' widths across the layer produces an enhanced thickness representation, especially in the profile's thickest and thinnest regions.

Figure #III-22 is a revised representation of the thickness profile presented in Figure #III-4. Both the thickest and thinnest regions were modeled by more elements, with an increase from one to two, and one to three, respectively. This is a net gain of three elements across the width. But, the earlier scheme would have required double the original elements to capture the profile this well. This would have been a net gain of six elements. Thus, the variable width scheme produces a better representation at a reduced execution time. The previous versions traded off between the refinement and the execution time. An example where the variable widths lend themselves especially well is, to the rapid thickness change usually present at the web's edge, after a slitting process. Most of the cross section is relatively flat and will fit into two or three wide elements. This allows the modeling effort to focus on the edge where it is needed.

The model addresses a web handling industry desire to allow for a varying CMD web line tension. They have observed webs coming out of the free span, and entering the roll, with slack portions in the middle or on an edge. Slack in the web is a direct result of variations in web line tension across the width. Tension variations across the width are usually attributed to issues including: misalignments in the rollers leading up to the wound roll, lengthwise camber in the web, and plastic deformations. It is a possibility also, that the shape of the wound roll itself transmits back up the free span, and the tension variation is a result not a cause. The true source of the free span web line tension variation is beyond the focus of this investigation, but it has been added to allow for further research. The variation is entered by assigning each cross width element its own tension value. Thus, any T_W function of CMD position can be represented, within the confines of the resolution established by the number of elements across the width.

The previous versions rigidly constrained the core and web layers at the center of their width. This worked well for the cylindrical cores, and even for the expanded cores, as long as they were symmetric left to right. But, the runs made with the asymmetric cantilevered core showed randomness and instability. This was especially true for the stress values with a lateral component. For example, the lateral stresses in Figure #III-18 appear to reverse direction for every other layer. Careful investigation of the lateral displacements, and the shear stresses, showed this was caused by the manner in which the core and layers were constrained. As the cantilevered core was loaded, its stiffer left side deformed far less than its right. While the load near the left side radially compressed the end cap, the load towards the right used the width of the contact surface as a moment arm. This should have displaced the right edge radially downward, and also laterally, back to the left. But, the lateral motion was not present. In addition, all of the shear stresses change sign at the CMD center, and are zero there. Only rigid constraints can produce this behavior.

Some rigid constraint is necessary in the wound roll model. Without it, the whole roll could undergo a rigid body motion. Finite element models are designed for motions, or deformations, of a body relative to some stationary part of the body. Mathematically, rigid body motions occur when $\overline{\mathbf{K}}$ is singular and therefore unsolvable. The rigid constraints guarantee that there will be a sufficient number of equations to solve all of the displacements. The key to maintaining the roll's natural behavior is in the constraint's placement.

In an axisymmetric formulation, the only possible rigid body motion is along the Z axis. Because of the symmetry, motions in the circumferential direction do not exist.

Radially directed motions are countered by shell stiffness, and the fact that in the axisymmetric formulation, there is no negative radial coordinate. In other words, if an R-Z cross section was placed in an X-Y coordinate system, the rigid body could move unimpeded in either the positive, or negative, X direction. But, in the R-Z coordinate, a rigid body motion in the R direction means one half of the cross section would be moving inward in R, while the other would have to move outward. Thus the only possible rigid body motion is along the Z axis.

Thus to satisfy the formulation, each core modeled in the code must have a rigid, Z constraint somewhere. Since the model will accommodate essentially three different core configurations (cylindrical, cantilevered, and fully supported on each end), there is no one location that will always be available, and appropriate, to constrain. The model allowed only the cylindrical configurations at first, and it was fine to place the rigid constraints at their center. In this version, if the model is used on a cylindrical core, it will still place the constraint in the middle. Whenever a stub shaft is present however, the model will rigidly constrain it, on its outside edge, where it meets the Z axis. If there is a stub shaft on both the left and right, the model will choose the left one to constrain.

To further expand its usability and accuracy, the model also utilizes relative web layer constraints. After the core is properly constrained, the relative constraints couple each layer to what is beneath it. Thus, if the core moves down and to the left, the first layer will follow it, and the second will follow the first, and so on. Relative constraints are implemented in the model using multi-point constraints once again. But, instead of coupling radial motions together, the constraints act only on the CMD motions, just like the friction links did. Figure #III-23 shows the new location for the core's rigid

constraint, and the relative constraint between it and the first web layer. This eliminates rigid body motion, while allowing lateral flexure.

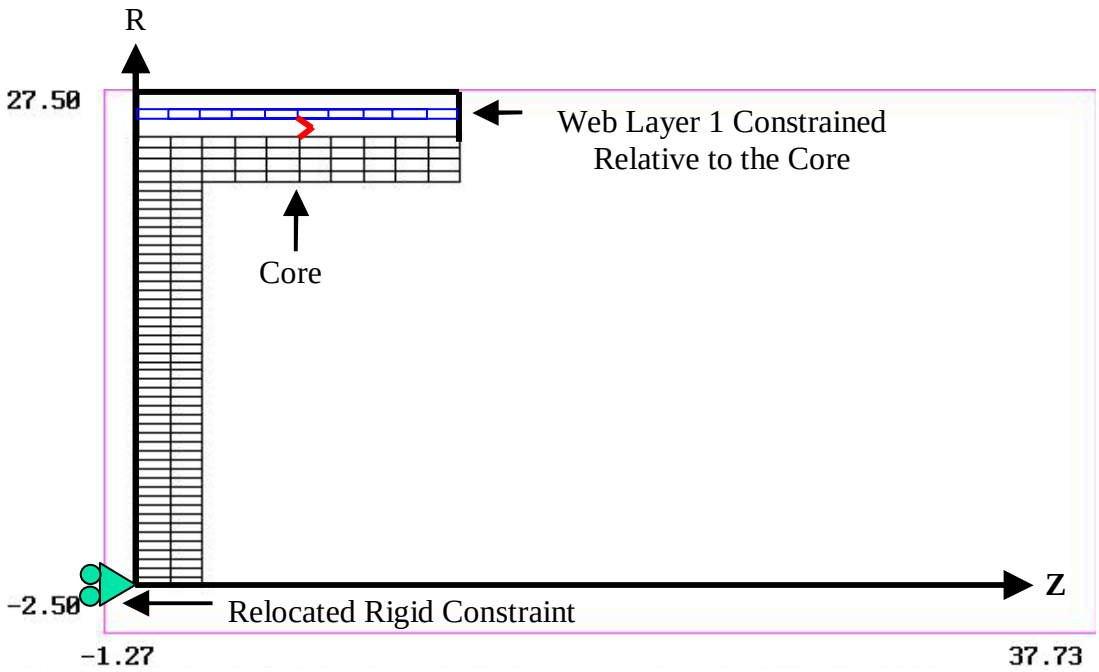

Figure #III-23: The core's rigid constraint is moved as close to the Z axis as possible, while the web layers are now linked to the layers beneath them.

The location of the relative constraints across the web width depends on its properties. Through them, the model goes through a series of checks to identify which node would be the most likely to stay fixed to the layer beneath. Since the roll's thickest region concentrates the web line tension, and thus produces the maximum CMD radial pressure, and corresponding friction, the thickest node is chosen first as the least likely to move. If the web is uniform across the width, then the model picks the one designated to receive the most T_W. If they are all equally tensioned, the widest element gets the constraint. Finally, in the absence of another distinguishing characteristic, the one closest to the center is constrained.

Resolving the cantilevered core example with the lateral web constraints greatly improves its behavior. The radial pressures in Figure #III-24 are smoother across the width, especially at the core. This is also true for the circumferential stresses at the core in Figure #III-25, and at the outside edge. It is interesting to note from Figure #III-26, which is from the early part of the wind (at about 17% of the final stack height), the $\sigma_{\Theta\Theta}$ stresses vary quite a bit across the width in response to the core's compliance. The variation diminishes with additional material wound onto the roll. The shear stresses in Figure #III-27 are also smoother throughout the radius. They show two behavior transitions: one -/+ combination near the core that switches within ten layers; and the other is the left to right anti-symmetry. The most notably improved are the σ_{ZZ} stresses in Figure #III-28. They indicate the roll stretches laterally over the left edge.

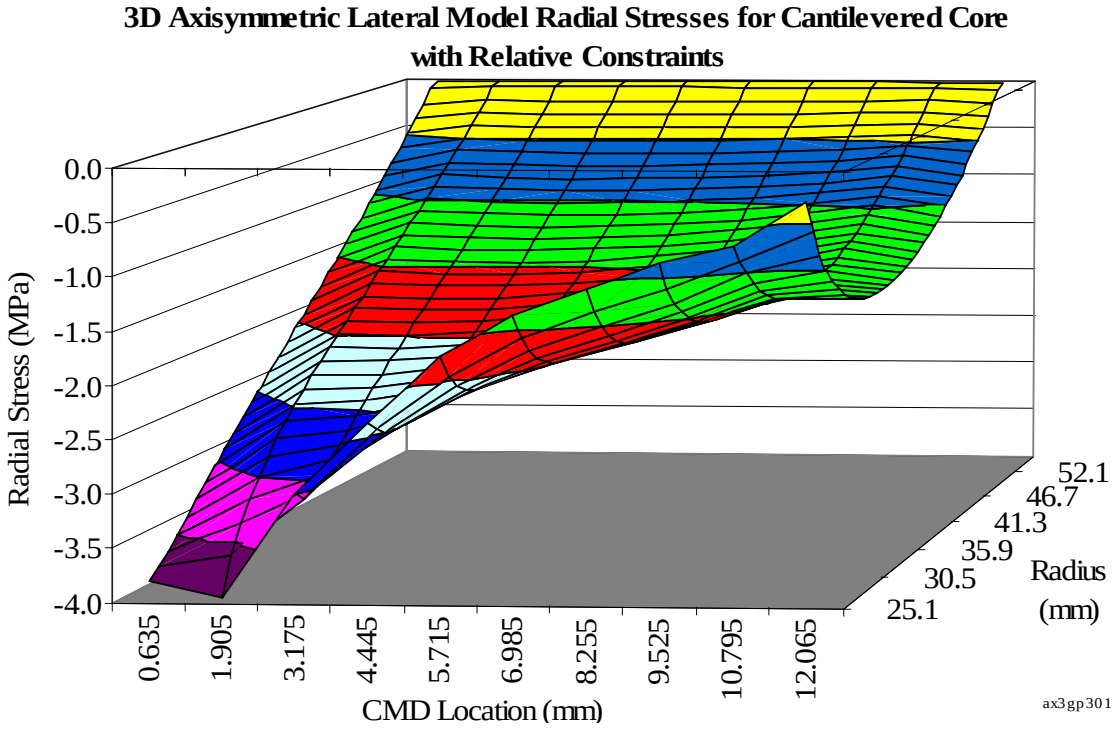

Figure #III-24: The relative constraints allow the radial pressures to smoothly transition from the peak values at the stiff part of the core to the much reduced values at the outside and at the soft part of the core.

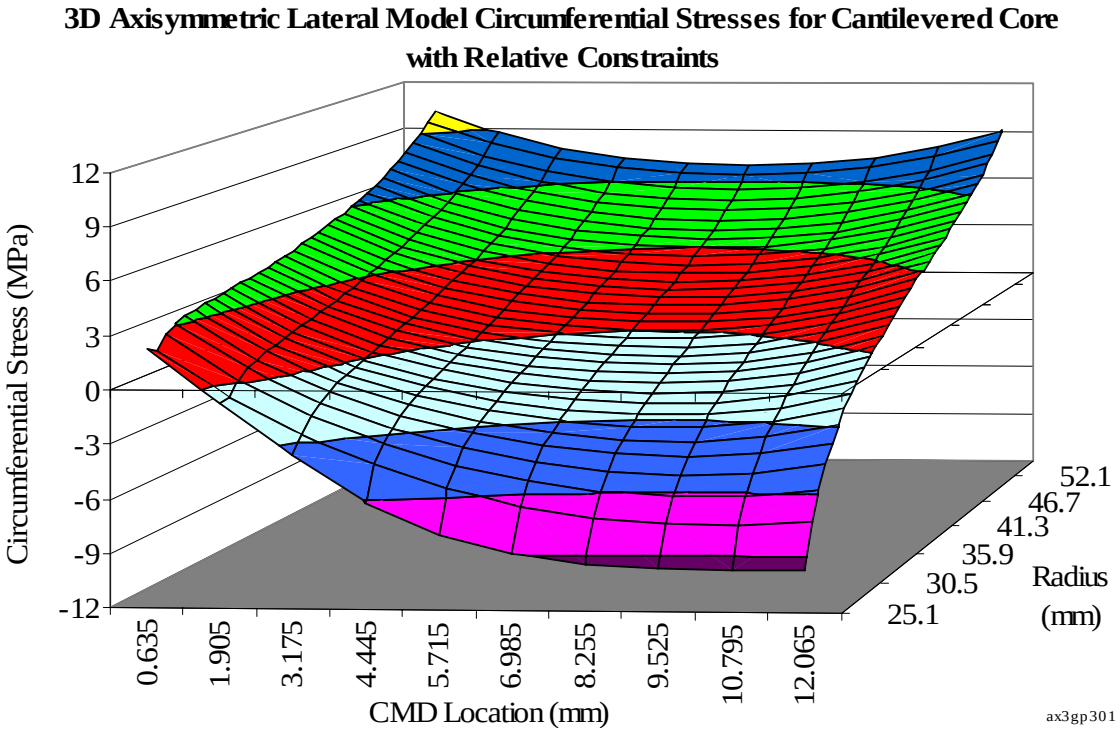

Figure #III-25: The circumferential stresses drop to zero wherever the core gives way, and are quite uniform across the width by the end of the wind.

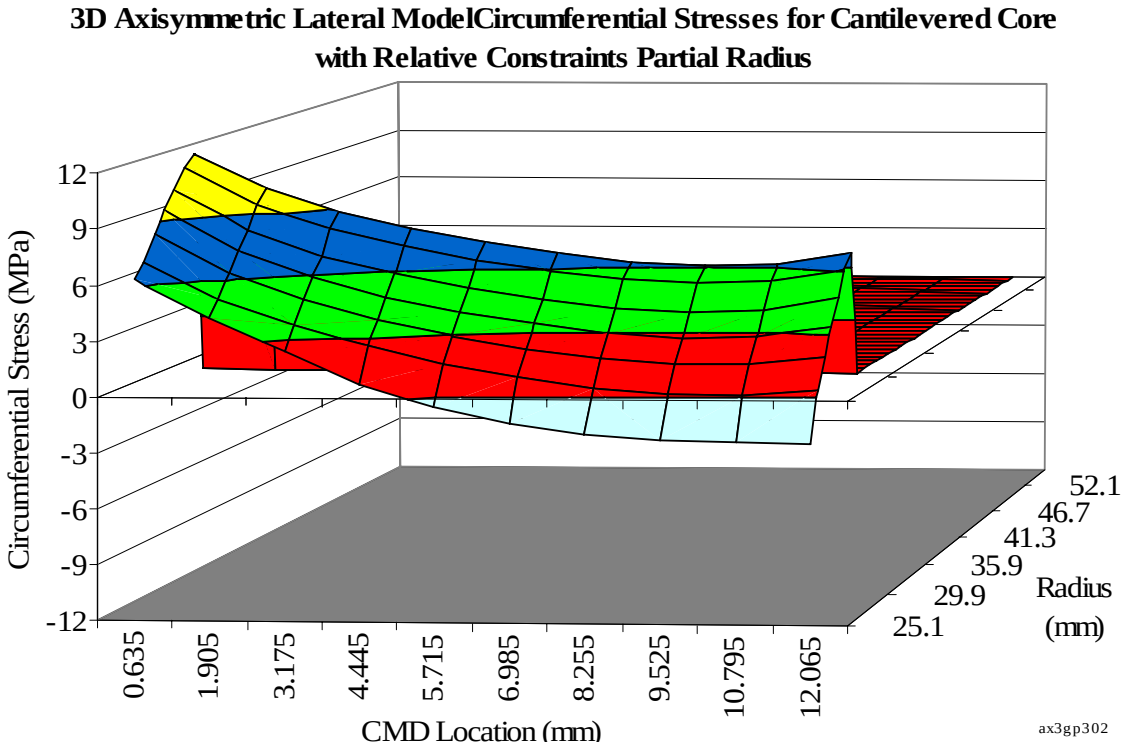

Figure #III-26: The circumferential stresses vary quite a bit across the width in this snapshot of the roll when it reached 30 mm in radius.

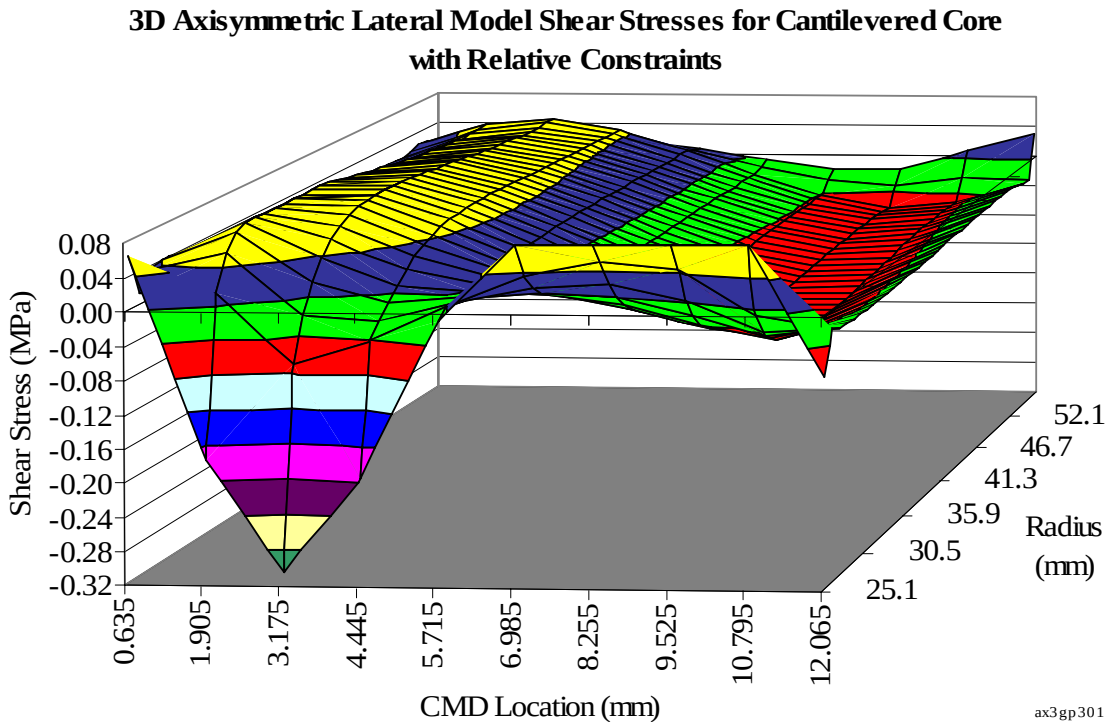

Figure #III-27: The relatively constrained layers shear away from the center perhaps as a response to each new layer spreading out over the ones below it.

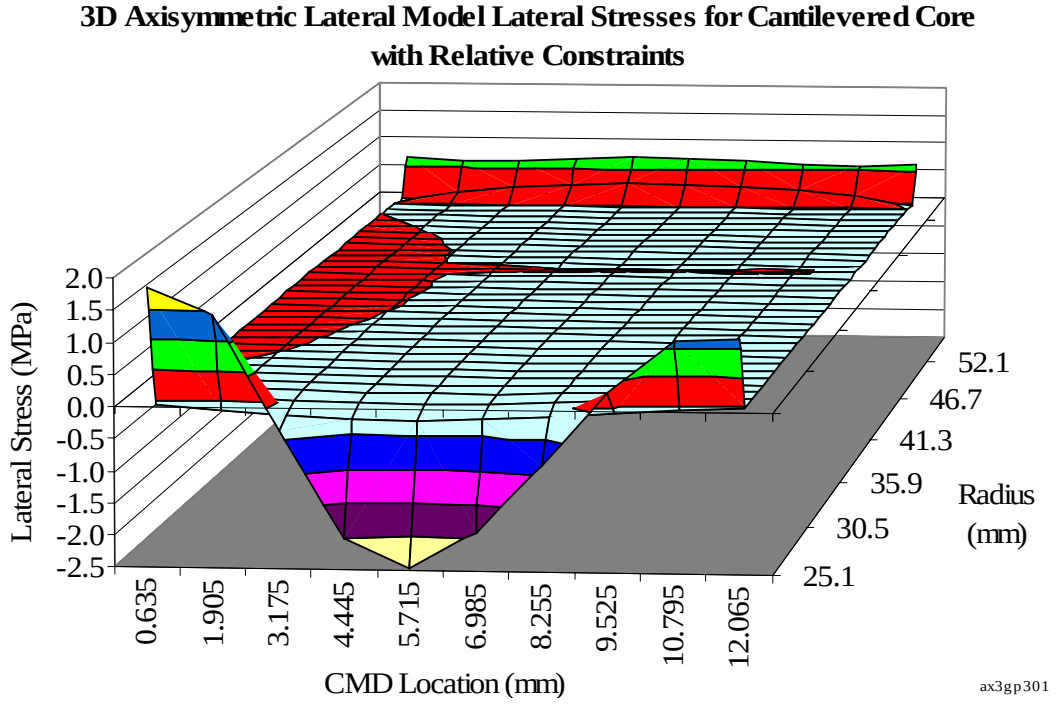

Figure #III-28: The lateral stresses are markedly improved as a result of the relative constraints, and demonstrate lateral compression throughout the roll except near the core and along the left edge.

The models' non-cantilevered core results also look promising. Figure #III-29 displays the predicted radial core stress, across the width, for the axisymmetric model, along with Cole and Hakiel's [4] coupled model, and their measured values.

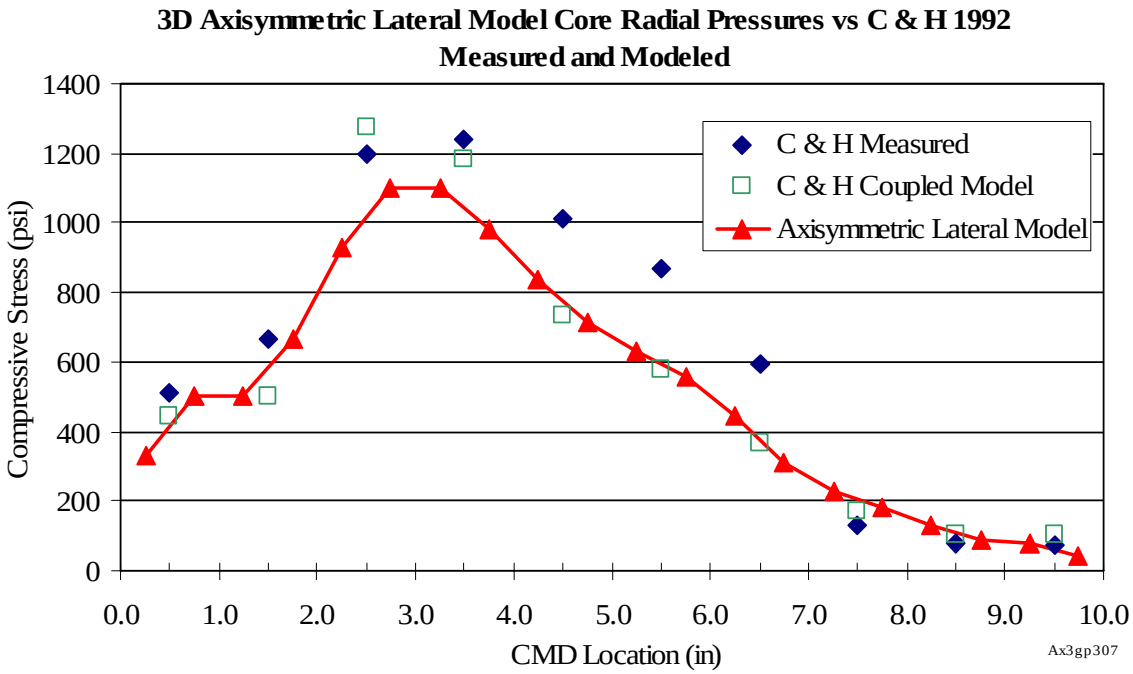

Figure #III-29: The radial pressures at the core follow the measured behavior, but fall short of the magnitudes in the peak regions.

As before, this is their PET, web A, but in this instance, the web line tension is 4 pli. The axisymmetric model behaves quite similarly to their measured results, but undershoots the radial stress magnitude throughout the center region. The model's accuracy could be suspect, because logically, if it was correctly predicting the pressures, they should average out to the measured values. Rather, this is mostly the result of inadequate resolution. As mentioned in the literature discussion of Hakiel [15], the pressure values came from a ten inch wide instrumented core, with one inch wide segments. This is sufficient cross-width resolution to show that the pressure varies in the CMD, but the mean pressures across the segment widths provide no insight into the pressure deviation.

The model cannot accurately represent the wound roll if the variation occurs at a higher frequency then the resolution. The radial profiles in Figure #III-30 provide some insight.

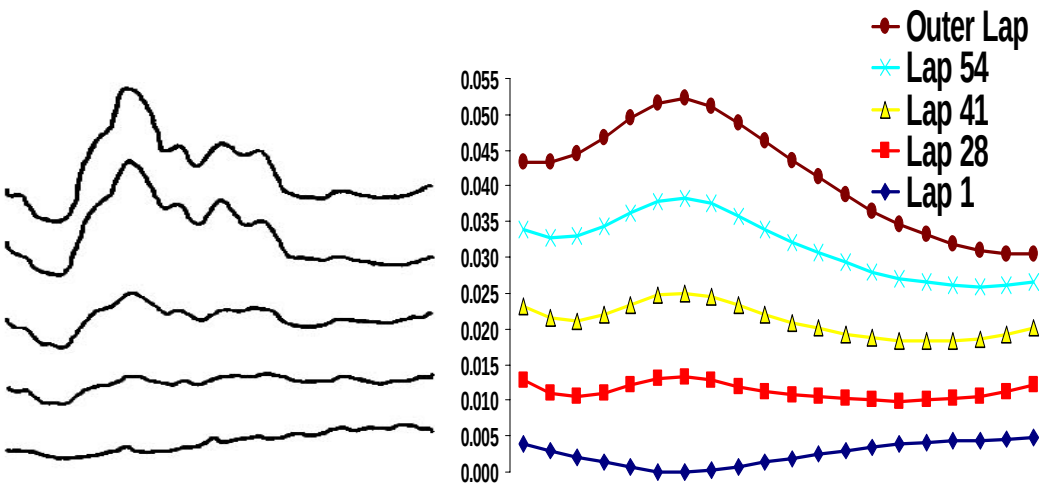

C & H '92 Measured Axisymmetric Lateral Model

Figure #III-30: The lateral axisymmetric model's radii, throughout the roll, compare quite well with the measured values, especially considering that only 20 segments were used across the width.

Both the general shape, and the radial distance between the highest and lowest points match nicely. The axisymmetric model uses twenty segment thicknesses across the width obtained directly from Cole & Hakiel, in order that the input values would be the same they used in their models. This is the source of the CMD thickness profile reported in Figure #I-6. Notice from the above figure though, that the measured radii show a much finer resolution than twenty equal segments can provide. For this reason, a new fifty segment version was obtained by taking direct measurements of the thickness profile plot in Hakiel [15]. As can be seen in Figure #III-31, it captures considerably more thickness variation detail then the twenty segment profile, and the segment widths are not uniform either. When the axisymmetric model ran at 4 pli using this profile, the results were improved as seen in Figure #III-32.

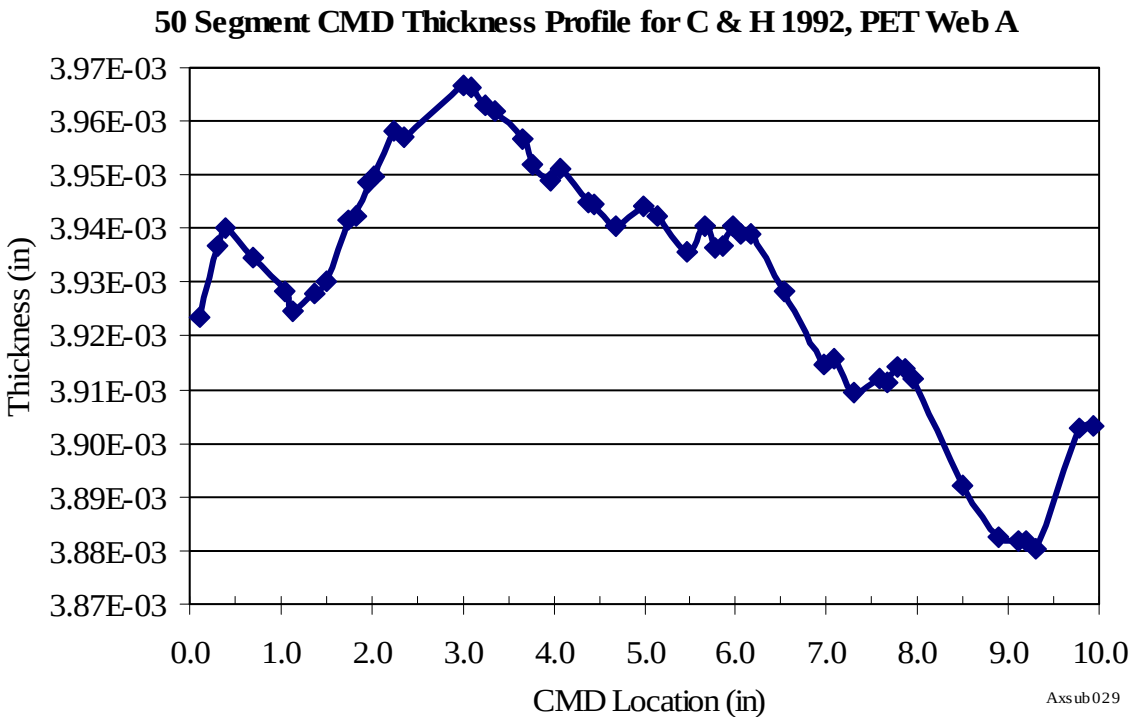

Figure #III-31: Fifty segments across the width provides a more accurate representation of the thickness variations in Cole and Hakiel [4]'s web A.

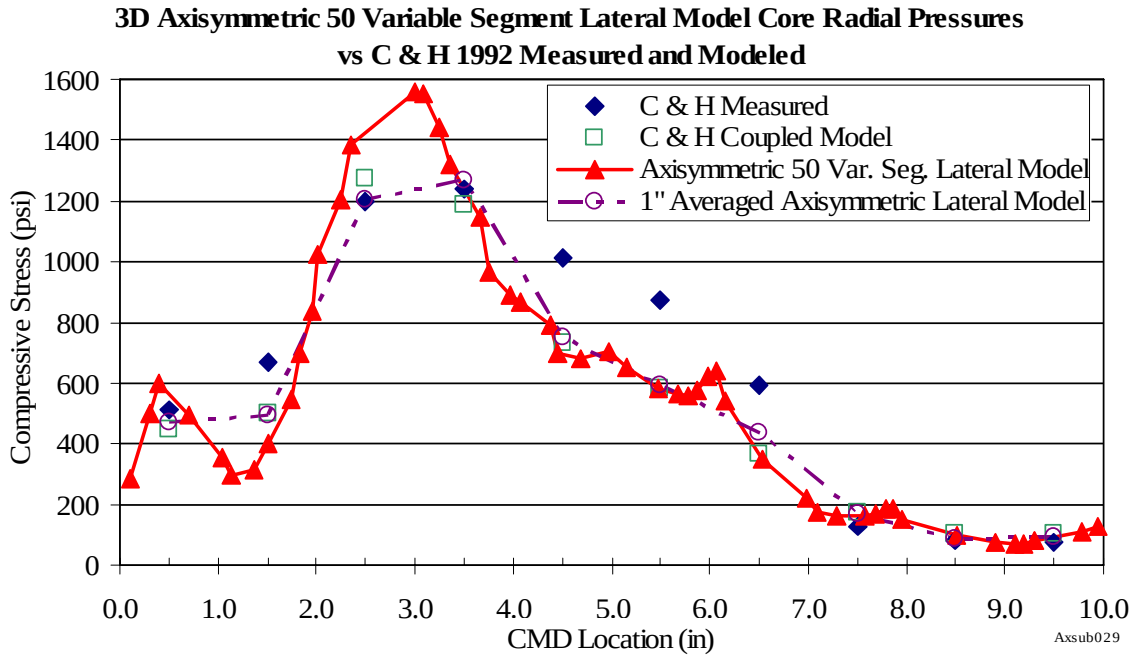

Figure #III-32: The fifty segment model reveals more is going on in the wound roll, and its average values compare quite nicely to those measured by Cole and Hakiel [4] at 4 pli.

The radial profiles for the fifty segment model compare very nicely to the values measured by Cole and Hakiel [4] as seen in Figure #III-33.

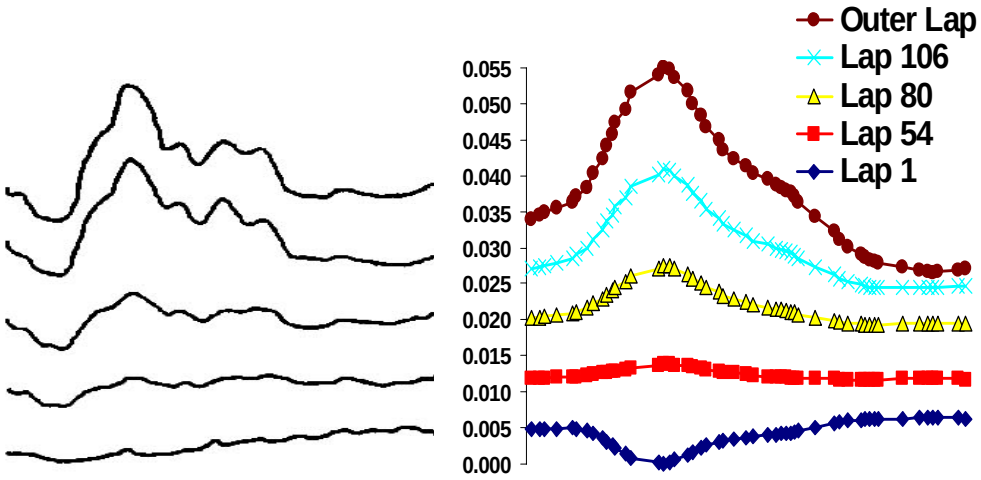

C & H '92 Measured Axisymmetric 50 Segment Lateral Model

Figure #III-33: Using fifty segments across the width helps the axisymmetric model closely match up to the experimental behavior, magnitude and inflections.

Figure #III-34 shows quite an interesting perspective on the lateral stresses in the 20 segment wound roll. As the web goes onto the roll, it stretches laterally over the high radius segments, but down in the roll, in what would be the radial stress' plateau region, the lateral stress relaxes. Near the core, the lateral stresses are higher then in the roll body. As the roll compresses the core radially, and circumferentially, the Poisson effect elongates the core laterally. The core's elongation frictionally draws the adjacent web layers with it, which generates their lateral stresses.

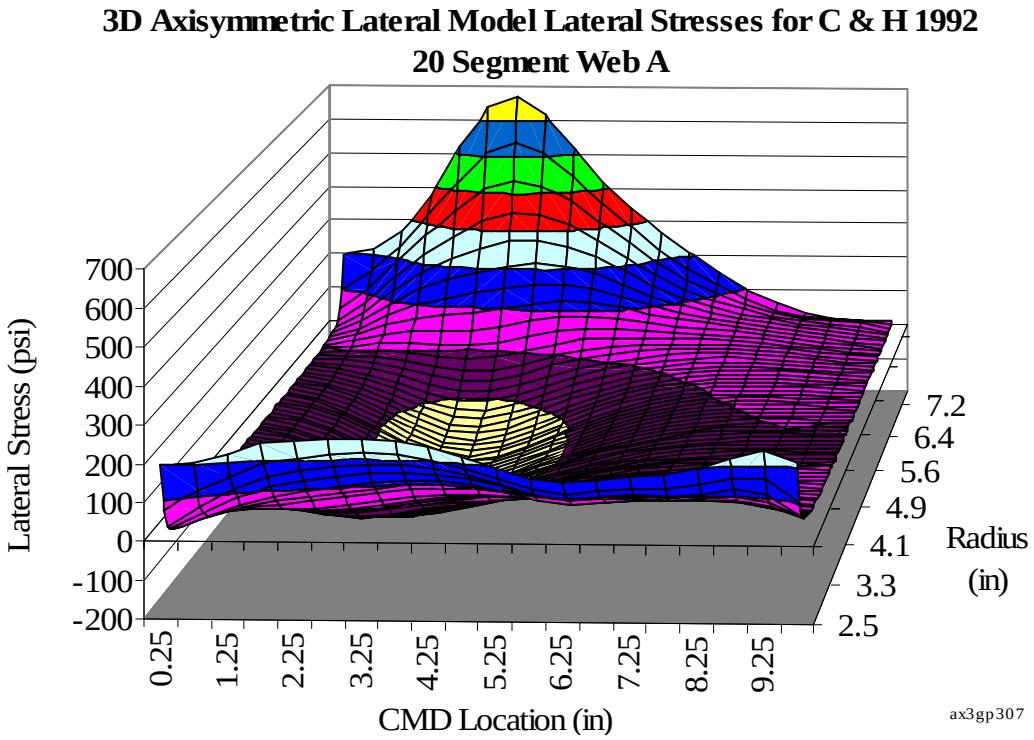

Figure #III-34: The lateral stresses for the Cole and Hakiel [4] 20 Segment web at 4 pli, vary considerably throughout the roll as they peak towards the outside, and relax in the middle.

Limitation

While the lateral movement version of the model accommodates CMD variations in the free span web line tension, its capability is limited. Simulations of a six inch wide PET web, and a twenty four inch wide News web, illuminated a stability threshold exists in the tension variation. The simulations had twenty four equally spaced elements across their widths, with twenty three of the segments kept at one pli in tension. Figure #III-35 displays the CMD thickness profile used for the two webs. The tension in the remaining segment (the thickest and fifth from the left) ranged from 1.5 to 80 pli as a step increase from the other segments. When the step increase reached 30 pli (3000 percent), the model became unstable. Figure #III-36 shows the next lowest step level of 20 pli.

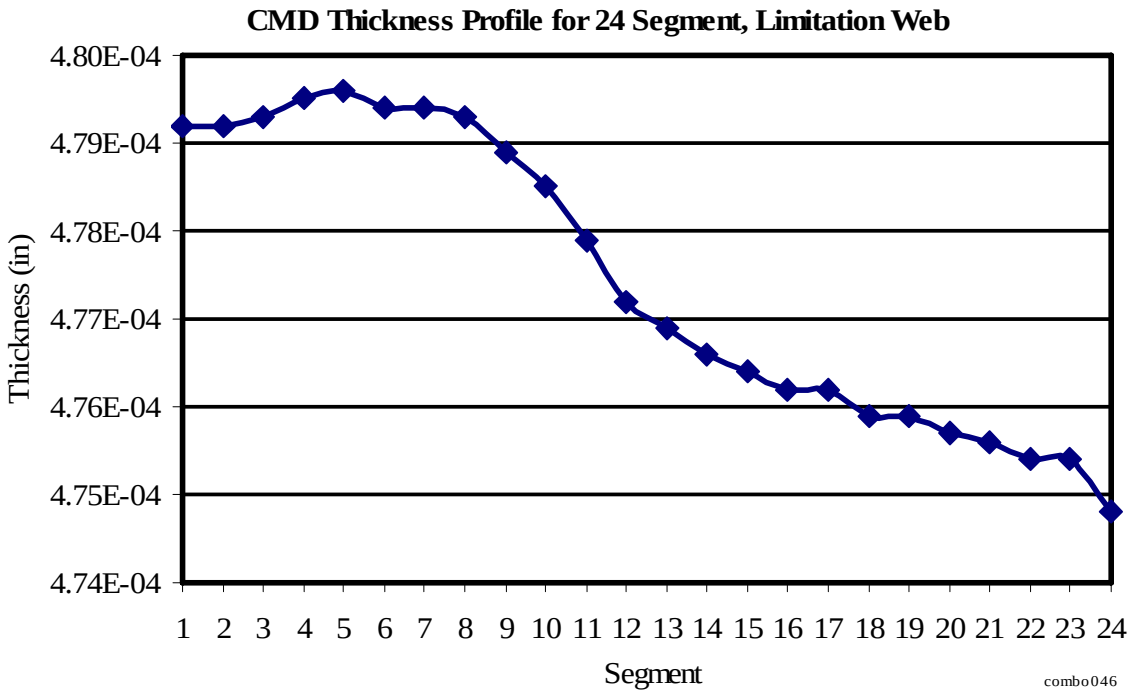

Figure #III-35: The thickness profile, for evaluating model limitations, peaks at CMD segment five, and diminishes off towards the right.

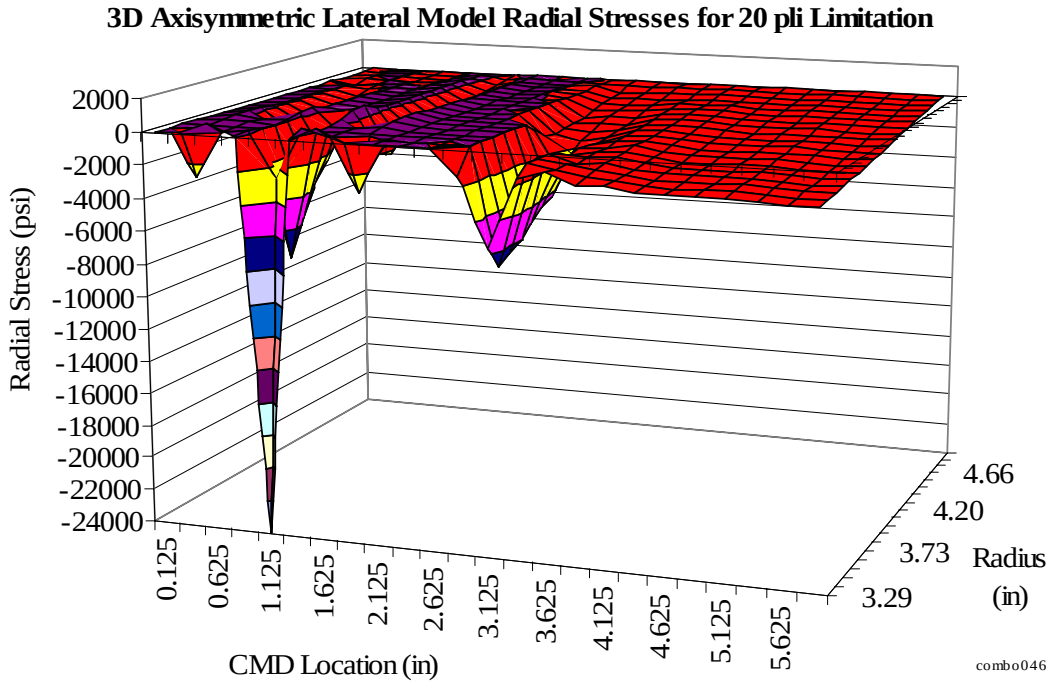

Figure #III-36: At 20 pli tension in segment five, the 6 inch wide PET model shows signs of on-setting instability in its radial stresses throughout the roll.

At the 20 pli tension step level, subordinate spikes in the radial stress near the core occurred across the width, away from the high tension segment. Additionally, some of the segments adjacent to the high tension segment, encountered tensile radial stresses. The roll was pulling apart and trying to gap.

It is unlikely that center wound rolls actually encounter the 3000 percent tension variation threshold. Such a local step increase would produce a large local shearing with respect to the adjacent segments. The layer drawing onto the roll, from the free span, can slip, and thus doesn't support much shear. It reacts instead by troughing, wrinkling, or at least redistributing the tension into adjacent segments. However, the model is to be used in conjunction with a nip, where the outer layer's ability to redistribute its tension is restricted. There is also an increased possibility of localized contact; on top of a hard steak for example. Thus, with a nip, larger CMD tension variations are more likely, and must be kept in mind during winding simulations.

CHAPTER FOUR

PERIPHERAL CONTACTING NIP MODEL

The nip model addresses the compression of the roll's exterior across the width and its ability to increase the tension wound into the roll. The nip's initial contact with the wound roll's periphery depends on its orientation to the roll and the roll's radial profile. As it presses down onto the roll, it will first contact the region with the smallest distance to the nip along the perpendicular to the roll's rotational axis. It will then respond depending on the rotational constraints of its supports. If the nip is free to rotate, it will rock around the first contact region until it rests on another region. From this point, or if no rotation is possible, the nip will progressively compress the initial contact regions adding more regions as needed until the nip load is fully countered by the roll. The resulting load across the width is important, because it feeds into the nip induced tension expression and increases the local tensions wound into the roll.

Nip Impingement

The peripheral nip model began as a work focused on understanding how a nip affects a stationary, uniform wound roll during impingement. As discussed in Hoffecker [17] (see chapter II), the wound roll was represented by an elastic foundation while the nip was a simple beam. Both were two dimensional cross sectional representations having a material modulus, moment of inertia, and a resulting bending stiffness.

This provided the means necessary to represent the roll's non-linear radial modulus and to investigate the role the nip's bending played.

A nip roller's CMD behavior is well represented by a finite element beam model. Just like the nip, beam elements are continuous along their length, they lie in a plane, they undergo rotations and displacements, and their bending depends on their material and moment of inertia. Figure IV-1 shows a generic beam finite element, e.

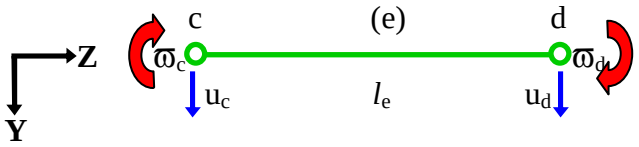

Figure #IV-1: A typical beam element contains two nodes with two degrees of freedom each.

It has elemental length l_e, two nodes c and d, and nodal displacements and rotations u and ϖ respectively. Each node's rotation is equivalent to its slope, as seen in Equation #IV-1.

$$\varpi = \frac{du}{dz} \qquad \text{(IV-1.}$$

The element lies in the YZ plane, with Z corresponding to the CMD, axial coordinate, and Y corresponding to the lateral direction. When representing a structure, such as a nip, the elements are placed axially end to end. Notice that in the representation in Figure #IV-1, the lateral direction is placed downward. This was done to simplify the expression when it was used in [17].

The derivation of finite element beams proceeds similarly to that of the axisymmetric elements. The beam's stress, Equation #IV-2, and strain, Equation #IV-3, substitute into the strain energy expression (Equation #III-1) to produce the beam's strain energy, Equation #IV-4.

$$\sigma_{ZZ} = -\frac{M_X}{I_{YY}} y \qquad \text{(IV-2.}$$

$$\varepsilon_{ZZ} = \frac{\sigma_{ZZ}}{E_Z} \qquad \text{(IV-3.}$$

$$U = \frac{1}{2} \int_V \frac{M_X^2}{E_Z I_{YY}^2} y^2 \, dV \qquad \text{(IV-4.}$$

The volume integral splits into integrals over the area and over the axial coordinate. The area integral combines with the y^2 to yield another moment of inertia. It cancels out one of the I_{YY} terms in the denominator, and leaves only the axial derivative. When this and the beam curvature relation (Equation #IV-5)

$$\frac{d^2u}{dz^2} = \frac{M_X}{E_Z I_{YY}} \qquad \text{(IV-5.}$$

are used in Equation #IV-4, it produces the strain energy in terms of the element's deformations, as shown in Equation #IV-6.

$$U = \frac{1}{2} E_Z I_{YY} \int_{l_e} \left(\frac{d^2u}{dz^2} \right)^2 dz \qquad \text{(IV-6.}$$

The integral is conducted over the element's CMD length, l_e.

The strain energy leads to the element stiffness matrix. One of the primary differences from the axisymmetric formulation is that the beam elements can be formulated with only one natural coordinate, ξ. In this formulation however, the slopes are added to the deformation vector as shown in Equation #IV-7.

$$\overline{\mathbf{q}} = \begin{bmatrix} u_c & \varpi_c & u_d & \varpi_d \end{bmatrix}^T = \begin{bmatrix} q_1 & q_2 & q_3 & q_4 \end{bmatrix}^T \qquad \text{(IV-7.}$$

Each degree of freedom requires a shape function that satisfies continuity requirements between the elements. The shape functions that work for the beam element are given, in terms of the natural coordinate, in Equation #IV-8.

$$\begin{aligned}\varphi_1 &= \tfrac{1}{4}(1-\xi)^2(2+\xi)\\ \varphi_2 &= \tfrac{1}{4}(1-\xi)^2(\xi+1)\frac{l_e}{2}\\ \varphi_3 &= \tfrac{1}{4}(1+\xi)^2(2-\xi)\\ \varphi_4 &= \tfrac{1}{4}(1+\xi)^2(\xi-1)\frac{l_e}{2}\end{aligned} \qquad \text{(IV-8.}$$

When the deflections and rotations are expressed in terms of the shape functions as $u = \overline{\varphi}\,\overline{\mathbf{q}}$, they can be substituted into the strain energy integral. To finish out the integral, $dz = \frac{l_e}{2}d\xi$, and the chain rule $\left(\frac{du}{d\xi} = \frac{l_e}{2}\frac{du}{dz}\right)$, aid in providing Equation #IV-9.

$$U = \sum_e \frac{1}{2} E_Z I_{YY} \int_{-1}^{1} \overline{\mathbf{q}}^T \frac{16}{l_e^4}\left(\frac{d^2\overline{\varphi}}{d\xi^2}\right)^T \left(\frac{d^2\overline{\varphi}}{d\xi^2}\right)\overline{\mathbf{q}}\, d\xi \qquad \text{(IV-9.}$$

When the $\overline{\mathbf{q}}$ are moved out, and the integration is performed, the result is the four by four element stiffness matrix shown in Equation #IV-10.

$$ESM_{beam} = \frac{EI}{l_e^3}\begin{bmatrix} 12 & 6l_e & -12 & 6l_e \\ 6l_e & 4l_e^2 & -6l_e & 2l_e^2 \\ -12 & -6l_e & 12 & -6l \\ 6l_e & 2l_e^2 & -6l_e & 4l_e^2 \end{bmatrix} \qquad \text{(IV-10.}$$

The elemental forces again result from the work potential expression. For the beam, the *WP* (see Equation #IV-11) is a combination of the distributed loads across the length, *p*, point loads, *L*, and applied moments, M_X.

$$WP = -\sum\left[\int_{l_e} pudz + Lu + M_X\varpi\right] \qquad \text{(IV-11.}$$

Each of these load types is enforced through the element's degrees of freedom, by applying the $u = \overline{\varphi}\,\overline{\mathbf{q}}$ equation to all three terms. The first term becomes another integral over ξ. In the second term, the shape functions are evaluated at the natural coordinate corresponding to element's node where the concentrated load is placed. All but one of the four shape functions will be zero at that point, so the product will be the magnitude of the load times the degree of freedom it acts on. Similarly, the third term multiplies the derivative of the shape functions evaluated at the node's natural coordinate where the moment is applied. Equation #IV-12 shows the final expression for the *WP*.

$$WP = -\sum\left[\int_{-1}^{1}\frac{pl_{\mathrm{e}}}{2}\overline{\varphi}\,d\xi\,\overline{\mathbf{q}} + L\,u(\xi) + M_{X}\,\varpi(\xi)\right] \qquad \text{(IV-12.}$$

A modified beam can also represent the wound roll as a foundation. Its formulation includes the compression of the roll, with a foundation stiffness per unit width, S. The Winkler foundation, as it is called, contributes to the strain energy through Equation #IV-13.

$$U = \frac{1}{2}\int_{l_{\mathrm{e}}} S u^{2}\,dz \qquad \text{(IV-13.}$$

When $\overline{\varphi}\,\overline{\mathbf{q}}$ again replaces u, and the integral is converted into the natural coordinate, the result is Equation #IV-14.

$$U = S\frac{l_{\mathrm{e}}}{2}\int_{-1}^{1}\overline{\varphi}^{T}\overline{\varphi}\,d\xi \qquad \text{(IV-14.}$$

Carrying out the integral produces the element stiffness matrix for the foundation as shown in Equation #IV-15.

$$ESM_{wink} = \frac{S l_e}{420}\begin{bmatrix} 156 & 22l_e & 54 & -13l_e \\ 22l_e & 4l_e^2 & 13l_e & -3l_e^2 \\ 54 & 13l_e & 156 & -22l_e \\ -13l_e & -3l_e^2 & -22l_e & 4l_e^2 \end{bmatrix} \qquad \text{(IV-15.}$$

Conceptually the Winkler element is a beam element on a spring foundation. For the roll, the foundation's stiffness is the non-linear radial modulus, thus the springs in Figure #IV-2 are shown to engage progressively when the beam is loaded.

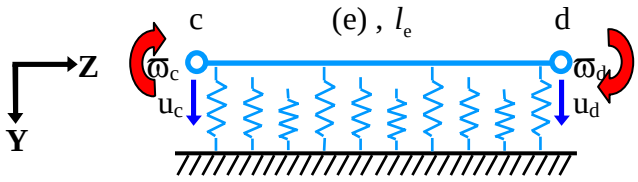

Figure #IV-2: The Winkler foundation element has an inherent stiffness which can be made to depend on compression.

The foundation's stiffness is determined using Hertzian contact (Johnson [18]), in a process similar to that used for rubber covered rollers in Good [12]. Hertz quantifies the critical role the geometries, of the contacting bodies, play during engagement. First, the curvatures of two bodies in contact, κ_1 and κ_2, can be combined to make one effective total curvature. The inverse produces an effective radius, R_{eff}, shown in Equation #IV-16.

$$R_{eff} = (\kappa_1 + \kappa_2)^{-1} \qquad \text{(IV-16.}$$

The effective radius provides a measure of the rate the contact will change under loading. For example, when a large diameter nip presses down onto a large roll, very little deformation is needed for more of their surfaces to engage. The large R_{eff}, resulting from their two small curvatures, indicates the contact region will change rapidly.

For two cylinders aligned along their length, the area of contact depends on their total deformation. At first contact, the area begins as a point in their cross sectional

plane. The out of plane dimension is equivalent to their mutual lengths. The cross dimension grows, as they press together, such that their contact area becomes a rectangle. As seen in the cross section in Figure #IV-3, the entire cross dimension is labeled 2a.

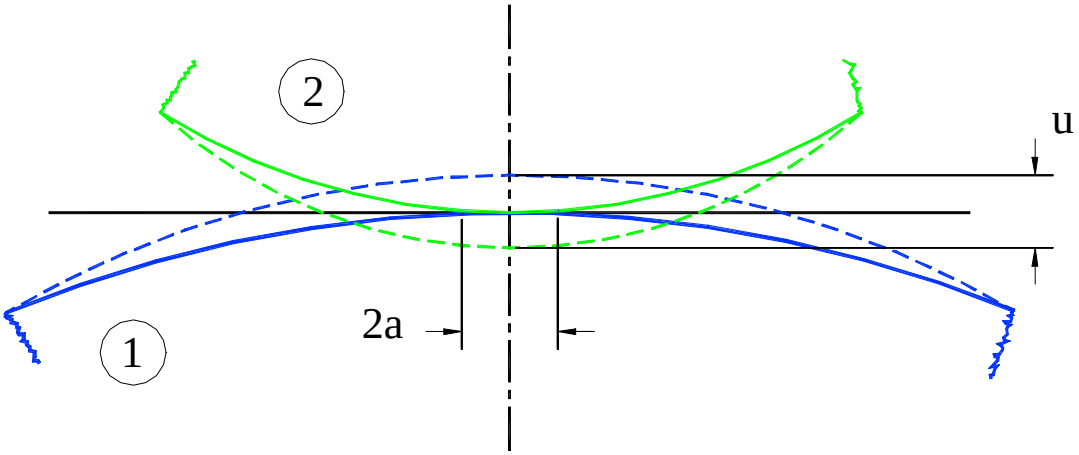

Figure #IV-3: The cross sectional view of two cylinders in contact shows the width of contact, and its inherent dependence on their radii, and deformation.

It is referred to as the width of contact, and *a* thus is called the half width of contact. Hertz defined the half width as dependent on the deformation, u, and the effective radius as given in Equation #IV-17.

$$a = \sqrt{2R_{eff}u} \qquad \text{(IV-17.}$$

In the event the radii, and deformations, remain constant along the length of the cylinders, the half width of contact will be invariant. However, for a three dimensional roll, the radii and deformations do vary, and *a* becomes a local variable.

The deformation in the contact region determines the foundation stiffness. Hertz established that the applied load distributes throughout the contact region as a Load Per unit CMD Width, as shown in Equation #IV-18.

$$\frac{load}{width} = LPW = \frac{\pi * a^2}{4R_{eff}\left(\frac{1-\nu_1^2}{E_1} + \frac{1-\nu_2^2}{E_2}\right)} \quad \text{(IV-18.}$$

In this expression, the Poisson's ratios, and the elastic moduli, are the in-plane values associated with cylinder 1 and 2. The Load Per Width directly depends on deformation, u. This can be seen by substituting Equation #IV-17 into LPW. The change in LPW, its derivative with respect to the deformation, is the Winkler foundation's stiffness. Equation #IV-19 expresses S for the nip impinged wound roll.

$$S = \frac{dLPW}{du} = \frac{\pi}{2}\left\{\frac{\left[\frac{1-\nu_{R\theta,roll}\nu_{\theta R,roll}}{E_{r,roll}} + \frac{1-\nu_{R\theta,nip}\nu_{\theta R,roll}}{E_{r,nip}}\right] + \left[\frac{u}{E_{r,roll}^2}\frac{dE_{r,roll}}{du}\right]}{\left[\frac{1-\nu_{R\theta,roll}\nu_{\theta R,roll}}{E_{r,roll}} + \frac{1-\nu_{R\theta,nip}\nu_{\theta R,roll}}{E_{r,nip}}\right]^2}\right\} \quad \text{(IV-19.}$$

Here, the orthotropic Poisson's ratios have been used for both the roll and the nip. $E_{r,roll}$ is the roll's radial modulus evaluated at the current deformation conditions. Its derivative also appears in the S equation, and must be evaluated at the current conditions.

The nip beam and the roll foundation make up a finite element system that is symbolically the same as for the axisymmetric element formulation. The nip is represented by multiple beam elements across the width. Each will have its own radius, associated moment of inertia, and elastic modulus. Likewise, the wound roll is made up of interconnected foundation elements with their own radii, moments of inertia, and deformation dependent stiffnesses. The CMD lengths, of the foundation elements, equal the CMD widths of the roll's sectors. The nip's beam elements, those that can contact the foundation elements, must have the same CMD length. This is shown graphically in Figure #IV-4.

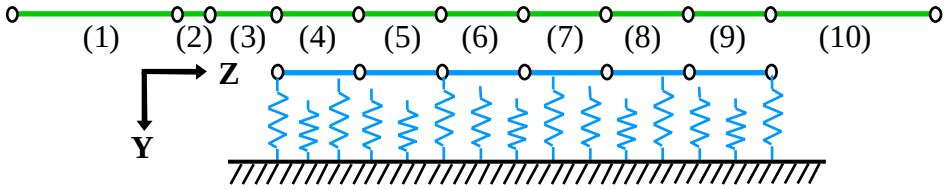

Figure #IV-4: The nip beam mesh must match up across the width to its corresponding roll foundation wherever contact is possible, as for elements four through nine.

The beam and foundation elements make up $\overline{\mathbf{K}}$, while the loads applied to the nip to press it into the roll produce $\overline{\mathbf{F}}$.

Usually, the beam and foundation elements sum together inside of the global stiffness matrix. However, when their respective ESMs are simply summed together, their behavior becomes indistinguishable. They share the same degrees of freedom, and thus have identical movement. This would be desirable as it would reduce the size of $\overline{\mathbf{K}}$, but, it assumes that the nip and roll maintain full contact across the width throughout the impingement. Even though this model is for a uniform thickness wound roll, such may not be the case. The nip's bending across the width could conceivably cause it to pull away from the roll somewhere across the width, like in the center for example.

The nip impingement model places the nip's beam elements, and the roll's foundation elements, separately into $\overline{\mathbf{K}}$, and then links them together. Like multipoint constraints, the links lock the motion of two corresponding degrees of freedom together. However in this method, known as Lagrange Multiplier Adjunction (Fellipa [7]), instead of modifying $\overline{\mathbf{F}}$ with a β_0 term, the reaction load pair ($\pm\lambda$) is brought over and adds onto the vector of unknowns, $\overline{\mathbf{Q}}$. The reaction parameter essentially becomes a newly created degree of freedom. Figure #IV-5 presents two elements linked at their left nodes.

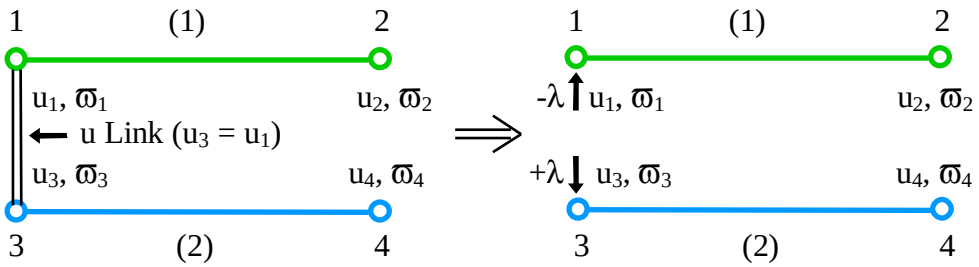

Figure #IV-5: Lagrange Multiplier links tie together individual degrees of freedom by inserting reaction load pairs.

In addition to modifying $\overline{\mathbf{Q}}$, enforcing the links requires modification to $\overline{\mathbf{K}}$. Positive unity values are placed into column vectors whose rows equal the number of degrees of freedom for the entire nip. Another column vector, with its rows equal to the number of degrees of freedom for the entire roll, holds negative unity values. The vectors are referred to as $\overline{\mathbf{A}}_{nip}$, and $\overline{\mathbf{A}}_{roll}$ respectively. They append onto $\overline{\mathbf{K}}$ as shown in Equation #IV-20.

$$\overline{\mathbf{K}}\overline{\mathbf{Q}} = \begin{bmatrix} ESMs_{\text{nip}} & \overline{\mathbf{0}} & \overline{\mathbf{A}}_{nip} \\ \overline{\mathbf{0}} & ESMs_{\text{roll}} & \overline{\mathbf{A}}_{roll} \\ \overline{\mathbf{A}}_{nip}^{T} & \overline{\mathbf{A}}_{roll}^{T} & 0 \end{bmatrix} \begin{bmatrix} \overline{\mathbf{Q}}_{nip} \\ \overline{\mathbf{Q}}_{roll} \\ \lambda \end{bmatrix} \qquad \text{(IV-20.}$$

Equation #IV-20 also shows the separation of the global deformation vector into sub vectors. The $\overline{\mathbf{Q}}_{nip}$ and $\overline{\mathbf{Q}}_{roll}$ correspond to the degrees of freedom for the entire nip and roll.

The links can be removed when contact is lost. If the nip does attempt to pull away from the roll, links will go into tension. The link with the most tension is removed. The nip and roll become independent at that degree of freedom, which is referred to as gapping. The model resolves to verify if any other links are in tension, and need to be removed. Later, if the nip moves back down onto the roll, the link can be re-established.

The nip impingement model flow is presented in Figure #IV-6.

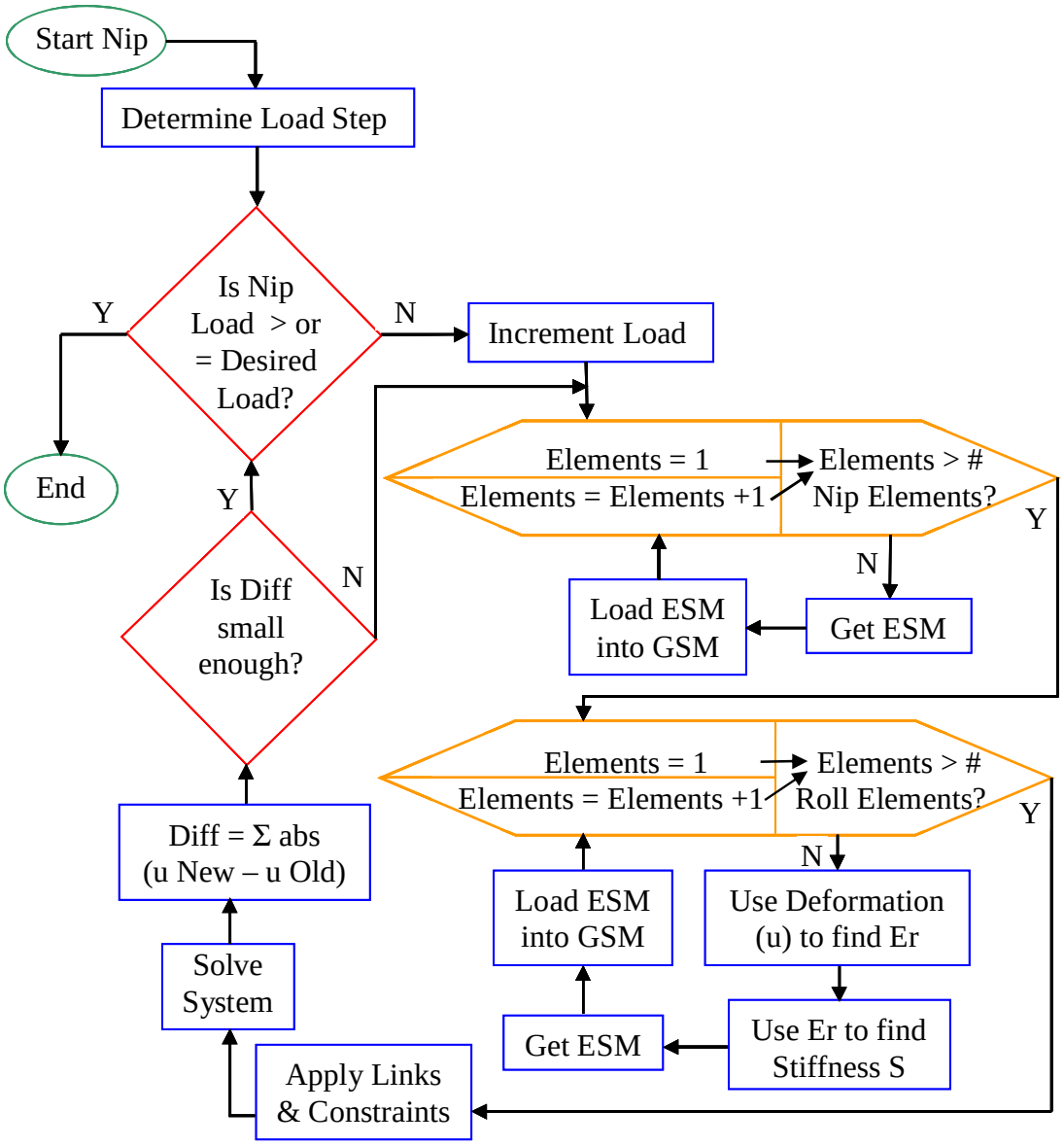

Figure #IV-6: The model iterates until the deformation resulting from the nip load is the same as the deformation that produced the foundation stiffness.

Because the wound roll foundation's stiffness is a function of the roll's deformation, and the nip's induced deformation depends on the stiffness, the nip model is iterative. It uses a bracketing scheme to close down on the unique deformation which both produces the stiffness, and results from the nip. In an effort to reduce the iterations

needed to converge, especially as the foundation approaches a knee in its radial modulus expression, the model loads the nip incrementally. The increment size is an input variable. During iteration, the model finds the ESM for each beam element, and places it into $\overline{\mathbf{K}}$. Then, for each element across the wound roll, it uses the current deformation in the half width of contact expression (#IV-17) to approximate the radial strain. This in turn produces E_r, yields the element's foundation stiffness, and its ESM. The foundation's ESM are also placed into $\overline{\mathbf{K}}$, and the model proceeds to set the links. Every nip node in contact with the foundation receives a link for both its lateral and rotational degrees of freedom. The constraints are then imposed, the finite element system solved, and the resulting deformations are analyzed for convergence. The process repeats by converging the deformations at each applied load, and stepping up the load until it equals the total applied. See page #II-30, and Hoffecker [17], for results and more details on this model.

Nip Engagement

The nip engagement version increases the model's functionality to match the axisymmetric model's complexity. As discussed in the axisymmetric chapter, the roll can have a core with inserts, stub shafts, and radii and widths that vary across the width. Similarly, the nip has shafts, inserts, and support locations. The Winkler foundation's radius is allowed to vary across the width, like a three dimensional roll. All of these together increase the interaction's complexity, when the nip contacts the roll. For this, the model's representations were upgraded to that shown in Figure #IV-7.

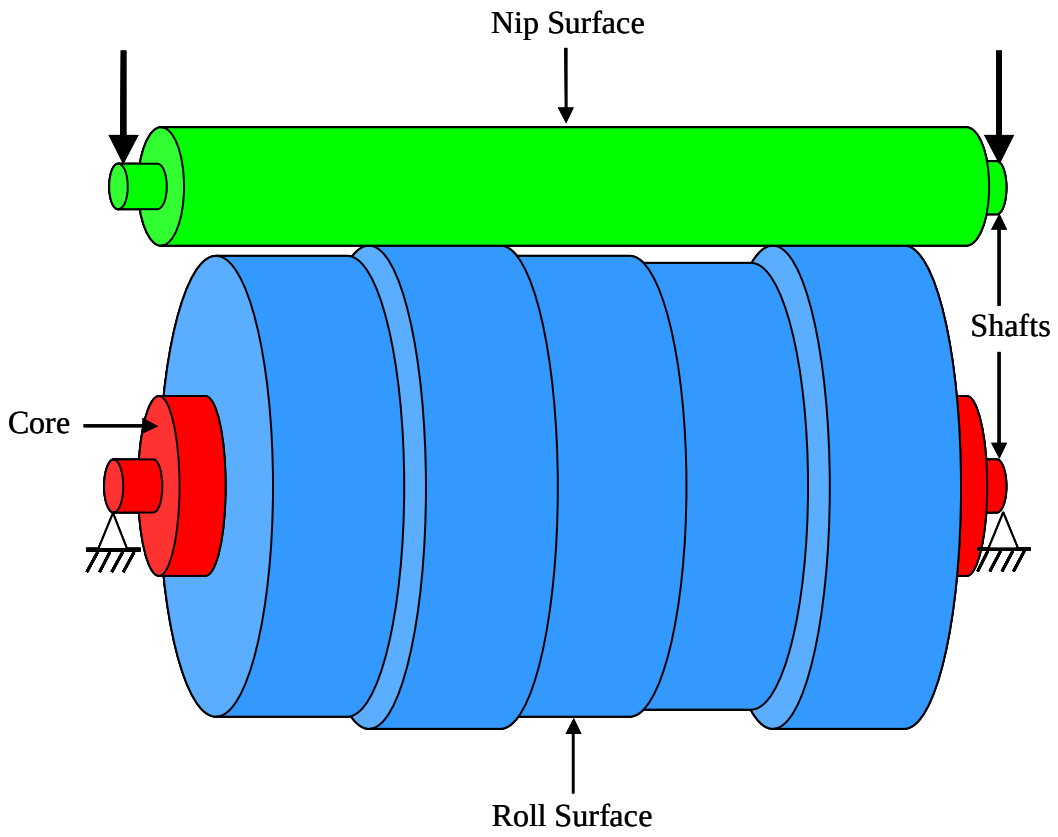

Figure #IV-7: The nip peripheral model includes a varying radius roll surface, a wound roll core with a center shaft, and a nip roller with a center shaft.

Not shown in the figure are the dimensions, which locate the nip and roll, from left to right. These are variable inputs which gives the model some flexibility, including allowing the nip to be placed offset of the roll (so it will contact only the right hand segments, for example), or a core that extends well out from the web.

Adding the core to the model requires an expansion of the finite element formulation. When the axisymmetric model was expanded for the core elements, their nodes were simply placed at the desired coordinates, and meshed together with the core cylinder that was already there. Their inherent spatial locations allowed them to have their own behavior, while contributing to the entire core. For the nip model though, the core elements are instead spatially superimposed over the wound roll elements. Their

degrees of freedom are all collinear. To allow them to behave independently, the elements must somehow be isolated inside $\overline{\mathbf{K}}$. With no gapping allowed between the foundation and the core, links should not be used to tie them together. Instead, the foundation elements become double sided. Their top sides link and move with the nip, while their bottom sides move with the core. Analogous to a spring with both ends free to move, the foundation's net compression becomes the top's deformation minus the bottom's deformation. Equation #IV-21 gives the new system formulation.

$$\overline{\mathbf{K}}\overline{\mathbf{Q}} = \begin{bmatrix} ESMs_{\text{nip}} & \overline{\mathbf{0}} & \overline{\mathbf{0}} & \overline{\mathbf{A}}_{nip} \\ \overline{\mathbf{0}} & ESMs_{\text{roll}} & -ESMs_{\text{roll}} & \overline{\mathbf{A}}_{roll} \\ \overline{\mathbf{0}} & -ESMs_{\text{roll}} & ESMs_{\text{roll}} + ESMs_{\text{core}} & \overline{\mathbf{0}} \\ \overline{\mathbf{A}}_{nip}^{T} & \overline{\mathbf{A}}_{roll}^{T} & \overline{\mathbf{0}} & 0 \end{bmatrix} \begin{bmatrix} \overline{\mathbf{Q}}_{nip} \\ \overline{\mathbf{Q}}_{roll} \\ \overline{\mathbf{Q}}_{core} \\ \lambda \end{bmatrix} \quad \text{(IV-21.}$$

The $\overline{\mathbf{Q}}_{core}$ and $ESMs_{\text{core}}$ above are the newly added degrees of freedom for the core, and its elemental stiffness matrices, respectively. The formulation is somewhat simplified in the fact that the number of degrees of freedom for the core, almost certainly will exceed the degrees of freedom for the bottom side of the roll. In this situation, the formulation would include ESMs for the core, that are not summed to the roll, and additional rows and columns to handle them. The expanded configuration is shown graphically, in Figure #IV-8, with the added core, and the double sided foundation.

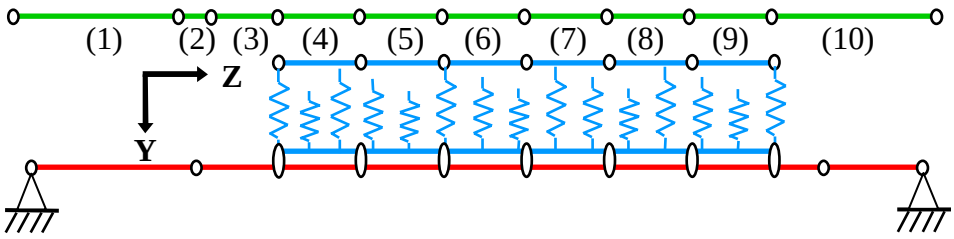

Figure #IV-8: The expanded version of the nip model includes core elements that can bend away from the impinging nip via a double sided roll foundation.

Each element must now be given a radius. It is essential to determining when the nip contacts the three dimensional foundation. In the previous version, none of the elements really had one. Instead, each element had an associated radius value used only to produce its moment of inertia, and effective radius. The elements actually were radially located on the Y = 0 line, and they deformed with respect to it. In the case of the foundation, the deformations then modified each element's associated radius value so the moment of inertia and effective radius could be recalculated. But, with the addition of the core, and particularly the foundation's CMD varying radius, the radial locations themselves become the desired result.

Strictly speaking, the finite element formulation will still perceive the nip, foundation, and core as collinear, but their radial coordinate will be maintained in CMD arrays. The axisymmetric representation has a distinct advantage in this endeavor, because it inherently tracks the radial locations of the element's nodes, and the radius can change over the length of the element. Not so for beam elements with one inherent dimension, length, and a radius that stays constant along it. This presents no problem, and is even desirable, for the nip and core whose radii usually are constant, or have discontinuous radial steps along their length. Their values are stored in two independent arrays. However, for the continually varying radius of the foundation, a nodal average is required to achieve a single, distinct, elemental radius. When the average radii of all the CMD foundation segments are found, they are saved in a third array. Collectively, the foundation's elemental array values portray the foundation's radius as discontinuous across the width. If the model ever needs the radius of a node lying on a discontinuity, then the larger of the two has to be assumed to be representative of the actual radius.

During the nip's engagement, the radius arrays are regularly updated, and used to produce position arrays. To update the nip, core, or foundation radii, their nodal deformations are averaged, but they do not subtract directly from the radial values. This is because the deformations do not correspond to their outer surfaces. They correspond instead to the bending movement of their respective element's centerline. Figure #IV-9 shows the surface that surrounds the element.

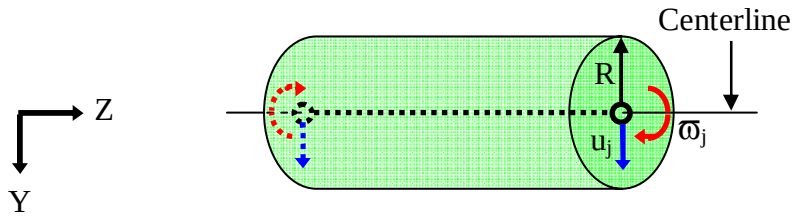

Figure # IV-9: The beam element defines the centerline of the nip, core, or roll it represents without regard to the surface or its radius.

For the core and nip, the model does not allow any surface compression. Thus, their actual radii remain unchanged throughout. To find the core's outer surface positions, the deformations simply subtract from the radii, because the core's centerline is collinear with the winding axis. The nip's centerline is offset from the winding axis, so the offset is first found, at the CMD center of each element, and then the elemental deformation is subtracted from that. The position of the surface results by further subtracting the nip's radius. In the case of the foundation, its centerline coincides with the winding axis, but it interacts with the core and the nip. The bottom side of the foundation bends with the outside surface of the core, while the top side compresses inward. So, the radius will be the initial elemental radius, minus the compression deformations of the element tops, plus the bending deformations of the core. The location of the foundation's top surface will be its initial radius minus the compression deformations only.

Initial Contact

The initial contact, between the nip and the three dimensional foundation, relies on the information in the position arrays. As the nip proceeds down onto the roll, it will contact the highest radius location first, unless the centerlines are not parallel. Some winders are misaligned so that one end contacts the roll before the other. For this reason, the model assesses the angle of incidence, and determines the perpendicular separation distance between the nip and each wound roll segment. No matter its radial height, the segment with the minimum separation will be contacted first. Figure #IV-10 shows the first contact schematically. This segment will be the first one to undergo compression. At this point, the model gives the rest of the segments a gapped status.

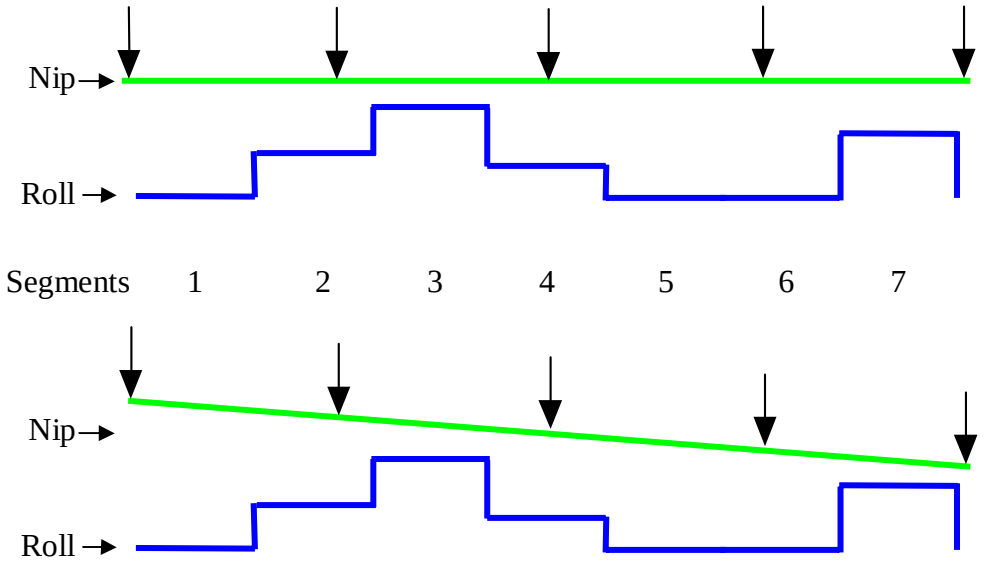

Figure #IV-10: In this example, the nip's angle of incidence can change which segment is contacted first (and therefore compressed first) from segment three to seven.

The nip may also be allowed to rotate as it first contacts the roll, depending on the winder's constraints. If so, the rotation will allow it to conform to the roll. In this case,

the initial contact point becomes a fulcrum as the nip transitions to contact a second point. The model determines which point receives the second contact by analyzing the moments about the fulcrum. If the nip load is distributed equally to the nip's two ends, it will be on the side with the largest moment arm from the fulcrum. An example of a nip rotating about a fulcrum, and forming two contact points, is shown in Figure #IV-11.

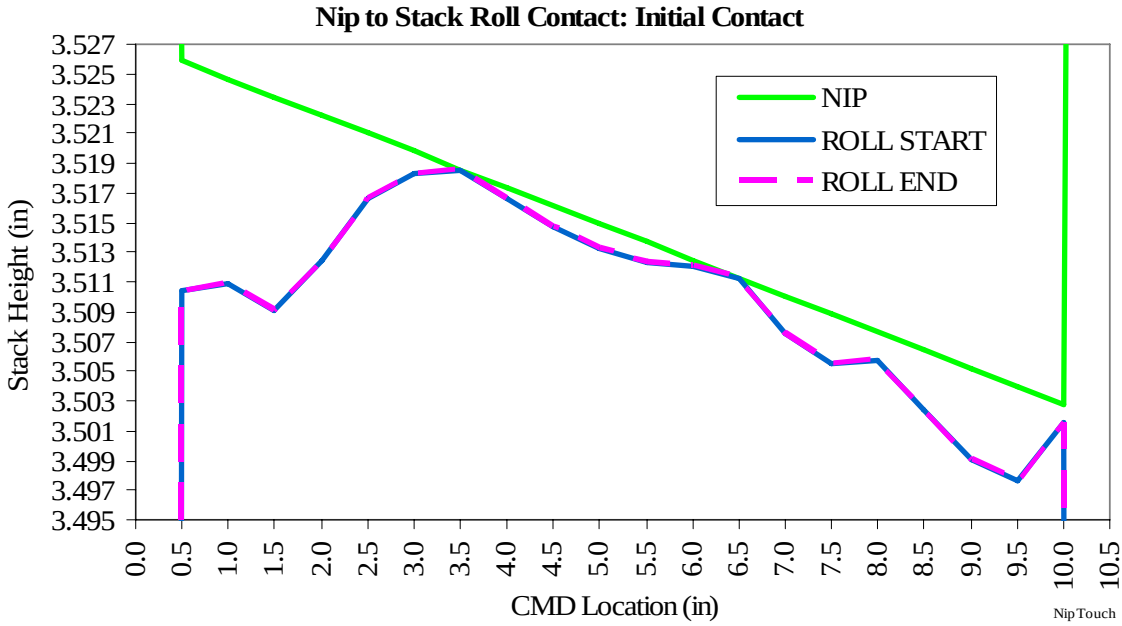

Figure #IV-11: In this simulated wound roll contact, the nip touched the stack at the 3.5 inch CMD location , and rotated over on the right to a second contact at 6.5 inch, because of the larger moment to the right side.

The example's roll foundation is represented continuously across the width. While this is not how the model perceives the foundation, it is more graphically intuitive. The values are not just conceptual however, they came from the model.

Nip Response

After the initial contact, there are a number of factors which will determine the final engagement. The first is the manner in which the nip is constrained. Also, the nip's rigidity will play a role. A third factor is the roll's configuration as determined by the moduli, and radial profile. Also, the core's stiffness affects the engagement.

The nip's rotational freedom may allow the angle of incidence to change during the wind, and ensuing engagement. Segments that received initial contact will compress as the load increases, and until the load is fully resisted by the roll. If the nip is free to rotate, shorter, softer, contacted segments could lead to additional nip rotation during the engagement. This is because the softer segments have a relatively low radial stiffness that can compress rapidly under their newly initiated nip loading. Those segments essentially drop away from the contact. At the same time a higher, stiffer contacted segment will undergo little, to no, compression. The segment drop out leaves the nip unbalanced, and it thus rotates to seek out equilibrium. This is demonstrated in Figure #IV-12, which is a continuation of the setup in Figure #IV-11.

As before, the nip initially contacted the high segment at a CMD position of 3.5 inches. It then rotated to contact the segment at 6.5 inches, but after a simulated drop out of that segment, the nip came to rest on the segment at 6.0 inches. If that segment too, were to drop out, the nip would again rotate, and this time end up contacting the far right segment at 10.0 inches. This is shown in Figure #IV-13.

A final example of elements dropping out is in Figure #IV-14, where contact moves to a fourth element, the one at 5.5 CMD inches.

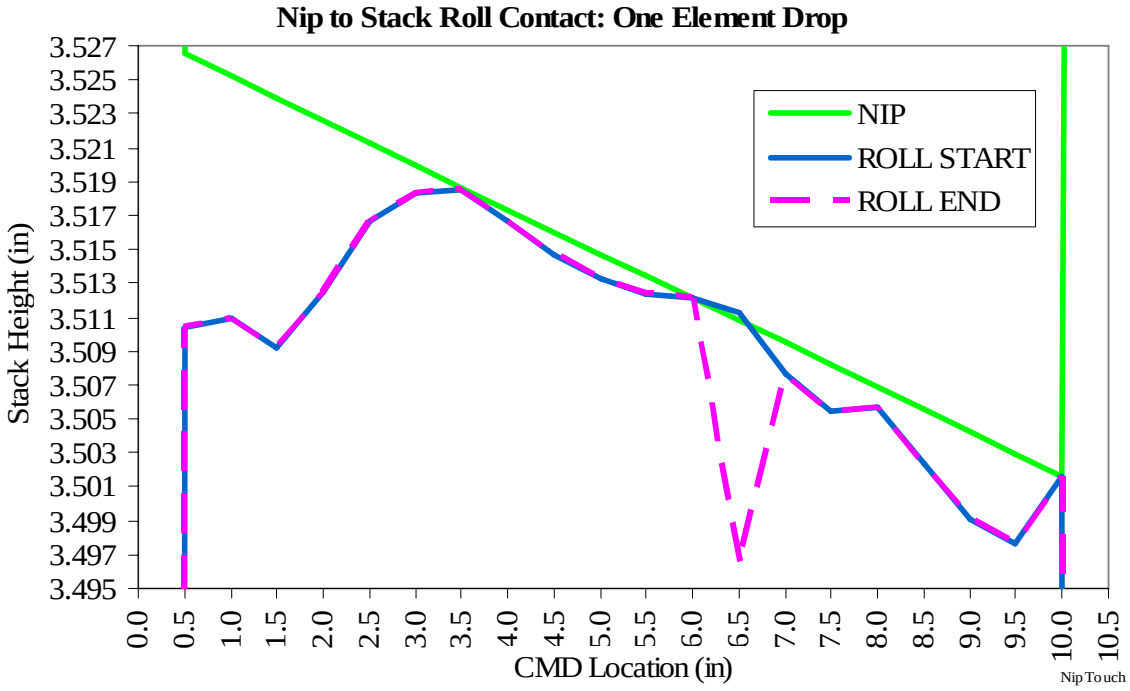

Figure #IV-12: As compression begins, a segment may drop away forcing the nip to find a new contact point, the segment at 6.0 in this example.

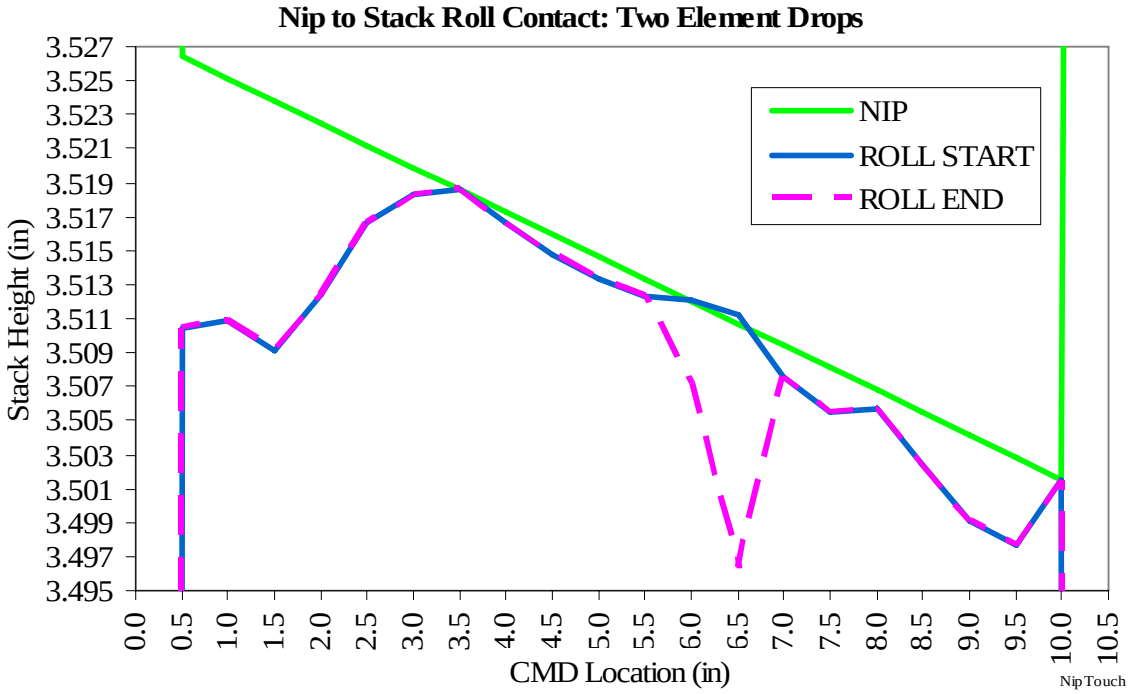

Figure #IV-13: If the two segments near 6.0 drop away, the nip will contact at 10.0.

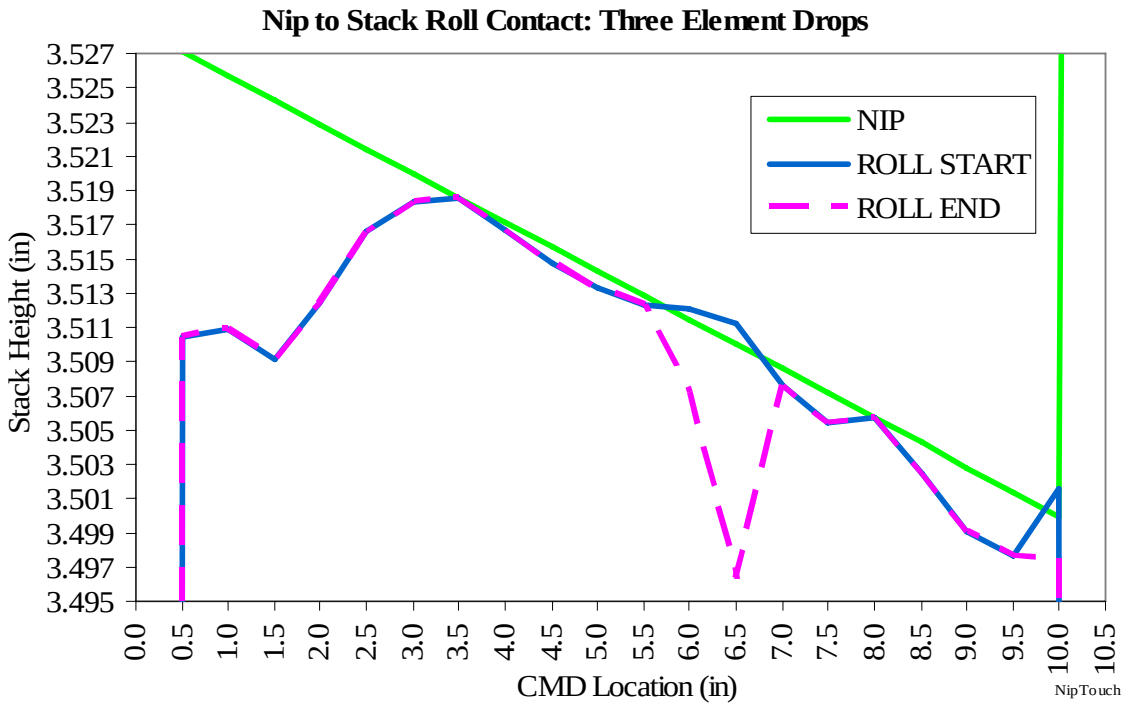

Figure #IV-14: After three elements drop away from the nip, it will rotate to contact the one at the 5.5 inch CMD location.

The model looks for these drop outs (by constantly analyzing the slope of the nip, and the slopes between the segments). If the slope between an already contacted segment, and a segment believed to have no contact, is less than that of the nip at the time, it is likely that the segment should receive contact as well. This is true in the absence of drop outs also. The compression of all the contacting segments could be sufficient to cause additional segments to contact the nip. In either case, when a segment engages the nip, the model must back the nip off to where the contact was initiated, and lock the segment to it, using a link. With the new segment thus engaged, the nip loading continues. Figure #IV-15 is an example where two contacting segments (at 3.5 and 6.5 inches) are compressed, and a third (at 6.0 inches) drops out as it is then engaged, so the segment at the CMD 4.0 location becomes linked. It will be the next segment to undergo compression, and counter the nip's load.

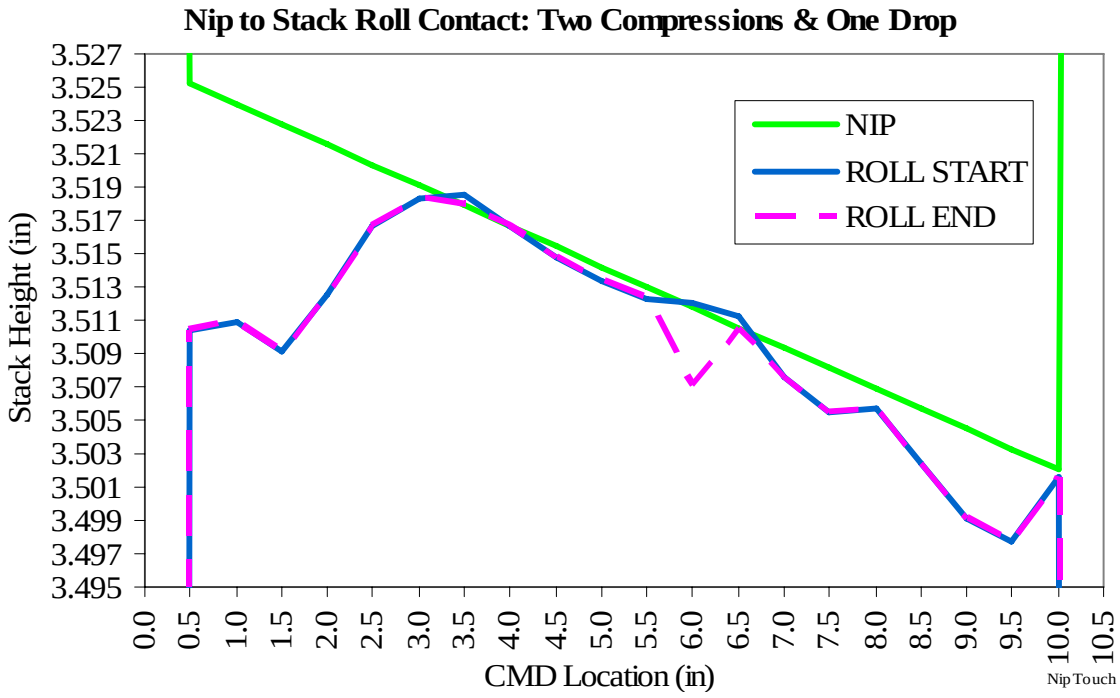

Figure #IV-15: As the elements at 3.5 and 6.5 inches are compressed by the nip, additional elements, like the one at 4.0 inches, will become engaged.

Of course, if the nip is not allowed to rotate, the analysis is simplified, but the nip still incrementally impinges the roll, and engages new segments, until its load is countered.

Whenever the nip's motion is resisted by contact with a segment, the nip will also bend. This is important, because the bending may bring the nip into contact with another segment. This is especially true if the nip is restrained from rotation. The nip's contact, under bending, is represented in figure #IV-16.

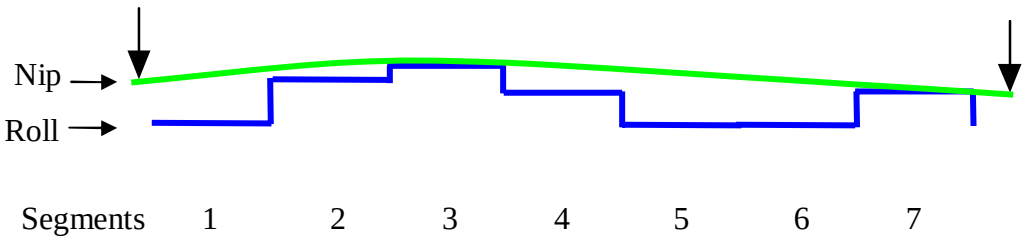

Figure #IV-16: As the nip engages the roll it bends around its contact points, possibly resulting in contact with segments before expected.

From a modeling standpoint, this is a complex variable, because the nip's centerline and radii off of that must be constantly rechecked and evaluated. The amount of bending will also change in response to the support received by the roll, and where across the nip's width that support occurs.

The wound roll's configuration determines the support it provides to the nip. Of course, the discussion in chapter III, already covered how the moduli and radial profile impact its configuration, but that was their axisymmetric impact. The change in modulus, which results from the nip compression, will instead be asymmetric. It is technically confined to the single RZ plane in common to both the roll and nip. Thus, it is located only at the circumferential coordinate corresponding to the impingement. This is because the Hertzian half width of contact in Equation #IV-17, assumes the contacting bodies are stationary. It does not include the rotation of the nip and roll. Properties, such as E_r, that are based on the half width of contact, are really only valid on that common RZ plane. Thus, when they are used here, they include some amount of error. Likewise, the radial profile will also be asymmetric around the circumference, because the beam bending of the nip, core, and foundation, lies only in that same RZ plane. In other words, the bending on the top of the roll, or core, will not be symmetric, with respect to the Z axis. It will have the opposite direction at the bottom. These are unavoidable consequences of the static nature of the contact model.

Ultimately, the nip engagement model is designed to simulate a nip impinging a wound roll. The nip, wound roll, and its core are represented by finite element beams. Each has its own radius, moment of inertia, and modulus of elasticity property that combines with its length to make up its bending stiffness. In addition, the wound roll is

also represented by an elastic Winkler foundation. It has a deformation dependent stiffness which resists the nip's impingement. Despite the beam elements' dimensions being limited to their length, the model tracks their associated radial magnitudes. This is essential to properly accommodating the initial, and ensuing, cross-width contact between the nip, and the radially varying wound roll. Figures #IV-17 and #IV-18 demonstrate the model's deformation and Load Per CMD Width on a uniform, 36 inch wide roll. The roll is a one inch stack of 3.26 mil thick News material (E_r = 3.524psi*24.4897 + 24.4897*P), on a 4.0 inch radius, 40 inch wide aluminum core. The applied nip load of 200 pounds clearly induces a varying compression across the roll's width, and causes the core to bend away. The Load Per Width has a corresponding variation across the width, and is quite significant to Equation #II-33's NIT, because it is the factor N/w.

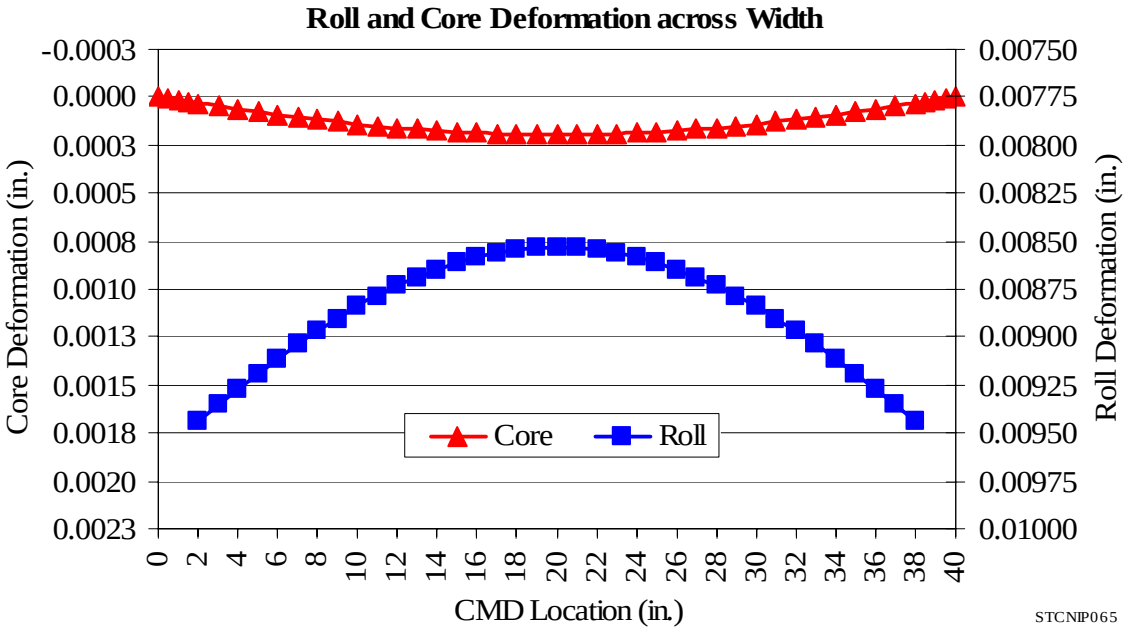

Figure #IV-17: The wound roll and core deform, across their widths, in proportion to their compressive and bending stiffnesses respectively, as they are loaded by the nip.

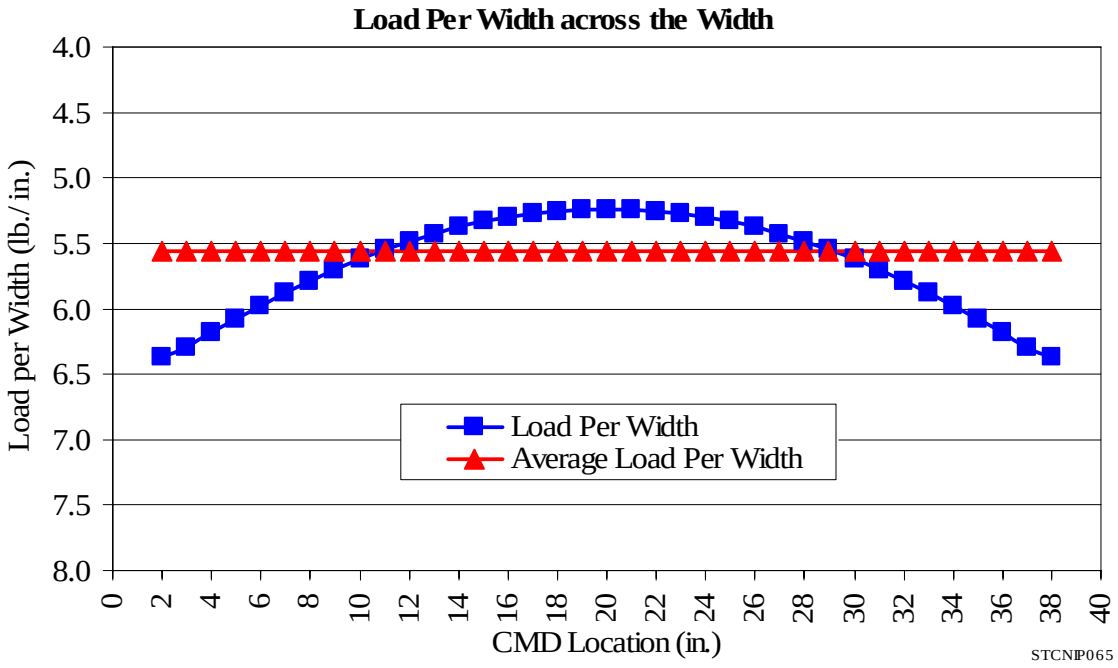

Figure #IV-18: The Load Per Width across the roll's width, varies in comparison to the average, and is the principal contributor to the NIT.

CHAPTER FIVE

NIP IMPINGED, THREE DIMENSIONAL WOUND ROLL MODEL

The nip impinged, three dimensional, roll model merges the nip and axisymmetric models into a recursive exchange. The axisymmetric, three dimensional, model first accretes some layers onto the core. As usual, the web line tension is allocated out across the width. This yields a preliminary foundation, and radial profile, to send over to the peripheral nip model. The nip is then brought down into contact with the roll's periphery. Regions across the width compress and become harder as the nip impinges fully down into the roll. The compressed roll goes back to the three dimensional model, but the web line tension now couples with an additional nip component. The model accretes more layers, and the process repeats until the roll reaches the desired radius. Finally, the resulting stresses throughout the roll, and its radial profile, are computed to complete the simulation.

The winding method drastically impacts how much web line tension makes it into the wound on tension. In center winding with no nip, and torque applied to the core draws the outer layer onto the roll. The layer's tension readily allocates out based on the radius variation across the roll's width. When center winding with an undriven nip roller, the roll is compressed, and the incoming layer must conform to the roll's shape, at points of contact. When the nip is driven instead of the core, the setup is referred to as surface winding. Here, the relative surface velocities control the final tension wound into the

layer. In another winding method called gap winding, the nip is instead backed off of the roll a short distance. This eliminates the roll compression associated with nip contact, and also restricts the layer's tension reallocation.

Wrap Angle

In all of the winding methods that utilize a nip roller, the amount the web wraps the nip affects the web's Wound On Tension. The amount of wrap is quantified as the angle subtended by the web to nip contact region extending around the nip's circumference. This "wrap angle", provides a mechanism for the tension to increase above the web line tension. As seen in Equation #V-1, the wrap angle ϕ combines with the incoming T_W, and the static coefficient of friction μ_s, to produce the maximum tension which can enter the nip to wound roll contact region, $T_{C.R.}$

$$T_{C.R.} = T_W * e^{\mu_s \phi} \qquad \text{(V-1.}$$

Figure #V-1 shows the variables in a cross sectional view of the nip roll.

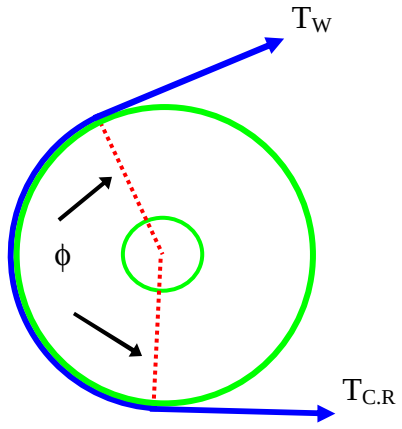

Figure #V-1: The angle the web layer wraps the nip impacts how much web line tension transmits to the roll.

The difference in tension, between T_W and $T_{C.R.,}$ is due to the capstan effect. The effect accommodates different tensions on each end of the web layer, because the friction throughout the interface holds bits of tension differential. Larger wrap angles have larger friction regions, and therefore support a greater increase in the tension. The maximum value obtainable by $T_{C.R.}$ is given by the WOT expression, Equation #II-33. But, if the wrap angle is insufficient, or there is slipping around the nip, the full value of NIT will be combined with a diminished T_W contribution.

The wrap angle also makes the web layer resist tension reallocation. The friction between the web and the nip, and the web's continuity across the width, tend to make the web travel as a unit over the nip. This is the case as the web exits the nip and enters the roll, where it is subjected to the roll's radius based tension allocation. To actually reallocate its tension to different segments, the segments would have to slip by each other locally. The friction prevents such slippage, and larger wrap angles produce greater resistance. Likewise, in the free span coming up to the nip, web tension variations that result from winding conditions tend not to disseminate. Even if the nip does not contact the roll, the web maintains its resistance to reallocation. This is how gap winding influences the wound roll without nip contact. Since the resistance diminishes with the distance from the roller, the separation between them is important.

The complexity associated with the wrap angle, and the winding methods which use it, are beyond the scope of this project. Thus, the combined model is not set up for surface, or gap winding. It does allow center winding with a nip, however, the treatment is simplified. When the combined model encounters a wrap angle, it just disengages the radius based tension allocation, and assumes the tension applies uniformly.

Gapping

With the introduction of gap winding, the definition of gapping may now appear inconsistent. Recall that models dealing in thickness variation effects, like Cole and Hakiel [4], defined a gap as any segment with a stack height equal to the relaxation radius, R_0. It was termed "gapped", because the segment supposedly carried no tension, and thus had no interlayer contact. For models with nip rollers, gaps were regions with no contact between the nip and the wound roll. Combining these two presents a possible definition for models with both thickness variations and a nip roller; a gapped segment is one with no tension and no physical contact. This contradicts gap winding's ability to impart tension to segments without nip contact, however. And, in the axisymmetric roll model which maintains continuity across the width, gapped segments can hold tension. Thus, a gap must be considered as any region which does not physically contact either a nip roller, or an adjacent layer. A gap indicates there is no local radial pressure, but there can still be circumferential stress, although inside the roll it will likely be diminished.

In addition to the impact they make separately on the sub-models, gaps affect the combined model as a whole. Most notably, a segment with a nip to roll gap does not directly produce a NIT component to the WOT. The segment may receive some NIT spillover if there is nip contact in an adjacent segment though. Also, gapped segments cause the nip load to redistribute across the remaining contacting segments. With fewer segments available to resist, the deformation and tension increases in those segments. This could cause gaps to close.

When a gap closes in the combined model, it might become an oscillating occurrence. If the closure is a result of new nip contact, the accompanying NIT increases

that segment's tension. This could cause the segment to momentarily track with the nip, and take up any circumferential slack. At the same time, the lack of outward pressure in the layers below allows the segment to cinch radially inward. This is especially true as new layers are wound on top of it, and may result in the gap reopening. The softer stack associated with the gap is susceptible to the nip's compression, and thus the gap can easily close again and start a repeating process.

While gapped sectors cinch in radially, they pull down and back on their contacting neighbors. Those neighbors are frictionally restrained by their nip contact, and thus resist. They pull the gapped segments radially outward, and their higher strain pulls the gapped segments forward. The result is that gapped segments lag behind the contacting ones, become more relaxed, and work to redistribute the wound roll tension. This is conceptually illustrated in Figure #V-2.

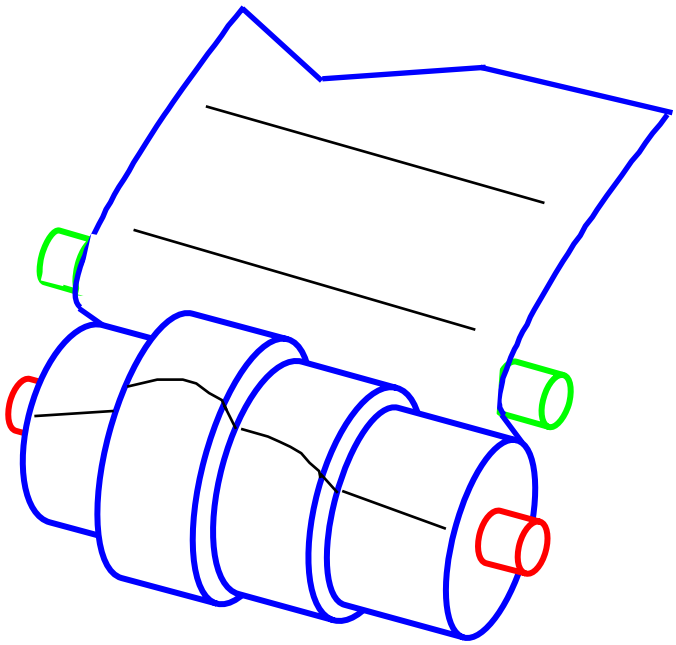

Figure #V-2: The web relaxes and lags behind in the low friction gapped regions, but can retain some tension as neighboring segments pull them up.

Wrinkling

Wrinkling in wound rolls results from one segment circumferentially shearing past another. The web's thickness, geometry, and its shear modulus all determine its shear limit. But, when one segment has considerably more wound on tension than the next, the nip roller compresses adjacent segments unevenly, or both, the tension differential (ΔWOT_j) along a segment boundary, can exceed the shear limit. Figure #V-3 illustrates shear wrinkles in a front view of a nip impinged, center wound roll with CMD thickness variations.

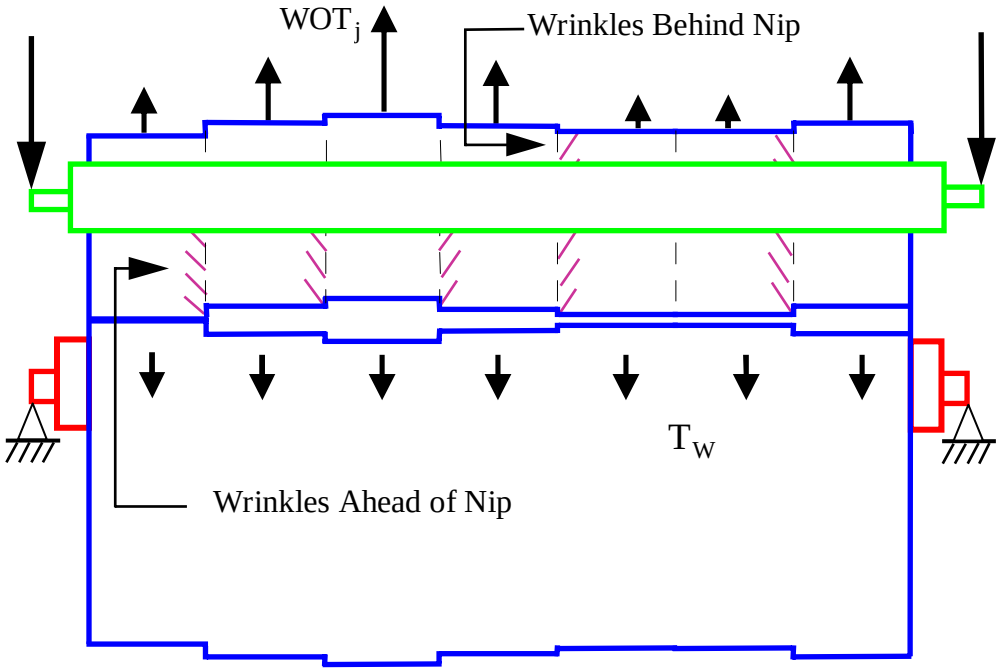

Figure #V-3: Gapped regions, or regions with no web wrap, may be unable to resolve larger tension differentials which can form shear wrinkles.

Wrinkles can also enter a wound roll by traveling over the nip roller, or through its contact region. If they exist in the span prior to the nip, the nip may not be able to adequately smooth them out before they enter the wound roll.

The combined model tracks every layer's circumferential stress across the width. When the winding simulation is complete, it determines the maximum tension differential inside the roll, and in the outer layer. The maximum differentials, and the boundaries on which they act, are identified. The user can then use this data, as they see fit, to determine if either differential will result in shear wrinkles.

Model Flow

Figure #V-4 depicts the combined model's overall flow. First, all the material properties, winding parameters, physical dimensions, friction coefficients, and material thicknesses are entered. The model then sets up the finite element meshes for the core, web, and the nip. Next, the roll accretes by adding web layers until a pre-specified trigger diverts the flow to impinge the nip. The nip load is progressively applied while adjustments are made to the contact across the width. After the nip is fully impinged, the accretion process resumes. The model continues accreting, and impinging the nip, until the roll exceeds the desired outer radius.

There are a number of events that can be used to trigger the nip impingement. The model could simply wind on a pre-specified number of layers, and then re-engage the nip. Similarly, a change in the roll's average radius across the width could be used. Another possibility would be to trigger the nip when a gap opens, or closes, between the nip and the roll. This could be done by monitoring the differences in the roll's radii across the width, and whether they become engaged or disengaged from the nip's surface. While this method would ensure the nip was readjusted at appropriate times, the model could go into the previously mentioned oscillating gap scenario.

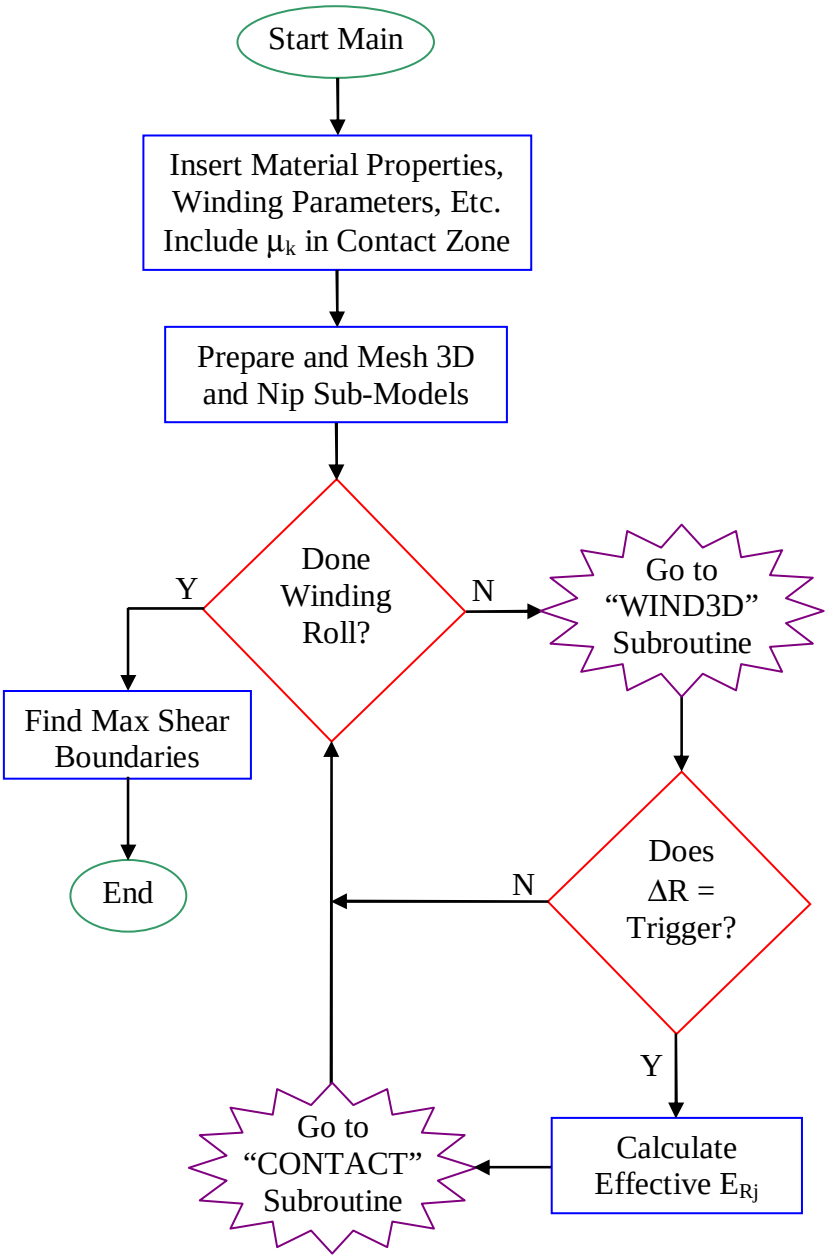

Figure #V-4: The combined model transfers control back and forth from the three dimensional, axisymmetric model to the nip impingement model in a recursive exchange.

Alternatively, the nip could be triggered anytime a preset radius variation, across the width, built up between the highest and lowest sectors. This would prevent excessive CMD radial variations. For the time being however, the combined model will trigger the

nip using the change in the average radius. This is simple to implement, and effective because it reoccurs regularly during the winding, is a readily available parameter, can be controlled by a single input, and keeps the model away from the oscillating gaps.

The combined model passes the axisymmetric roll's radial moduli to the nip's foundation. They are generated during accretion, and thus exist for each CMD segment, in every layer. To be compatible with the nip model's foundation stiffness, each segment's moduli must be converted into a single, representative value. Since they are essentially a stack of springs in series, the effective value is calculated in the same way. Spring deformations, x, are determined by Hooke's law, x = F/k. F is the applied force, and k is the spring's stiffness. In a series stack, the sum total of all the individual spring deformations is the stack's total deformation, x_{total}. The summation, over the stack's laps i, is shown as Equation #V-2.

$$x_{total} = \sum_i x_i = \sum_i \left(F/k\right)_i = F\sum_i 1/k_i \qquad \text{(V-2.}$$

Since F is the single load applied to the whole stack, it factors out of the expression. This leaves the effective stiffness as the inverse of the sum of the inverted stiffnesses. This is demonstrated in Equation #V-3, which gives the effective spring stiffness of the stack, k_{eff}. The radial modulus analog, $E_{r,eff}$, is in Equation #V-4.

$$k_{eff} = \frac{F}{x_{total}} = \left(\sum_i 1/k_i\right)^{-1} \qquad \text{(V-3.}$$

$$E_{r,eff} = \left(\sum_i 1/E_{r,i}\right)^{-1} \qquad \text{(V-4.}$$

Each segment's effective modulus produces an effective strain, via a strain-dependent version of the modulus expression. This is the segment's minimum strain during

impingement. When put back into the modulus expression, it establishes a baseline by shifting the expression into the proper stiffness region. When the effective strain is first combined with the strain induced by the nip, the result is $E_{r,net}$, shown in Equation #V-5.

$$E_{r,net} = E_r\left(\varepsilon_{r,nip} + \varepsilon_{r,eff}\left(E_{r,eff}\right)\right) \qquad \text{(V-5.}$$

The combined model must pass other information back and forth between the nip and axisymmetric sub-models. As the axisymmetric sub-model winds on layers, the core contact surface's inner and outer radii, its stub radii, and the outside radius of the roll, change. Since the radii are represented by nodal coordinates, and the nip sub-model uses elemental values for its moment of inertia calculations, and for determining nip to roll contact, the nodal radii are converted to elemental averages. Then they are sent to be used for the nip impingement. The nip sub-model returns the Load Per Width values discussed in chapter IV. The Loads Per Width are calculated as nodal values, so they are ready to be used directly in conjunction with the static friction coefficient, and layer thickness, to produce the NIT at each node across the web's width.

The combined model accesses the two sub-models by making them subroutines. The "CONTACT" subroutine is essentially the stand alone nip impingement model; it determines the NIT values. The roll accretion is performed by the "WIND3D" subroutine, which is a modified version of the axisymmetric, three dimensional winding model. While it still calculates and enforces the nodal interferences to impose the tension, it iterates to match the total WOT, (T_W + NIT), not just the T_W. Whenever there is a wrap angle, the radius based allocation turns off, and the web line tension component evenly divides across the CMD segments instead. Figure #V-5 shows the model's resulting $\sigma_{\theta\theta,j}$ (WOT_j), being summed, compared, and factored as needed in "WIND3D".

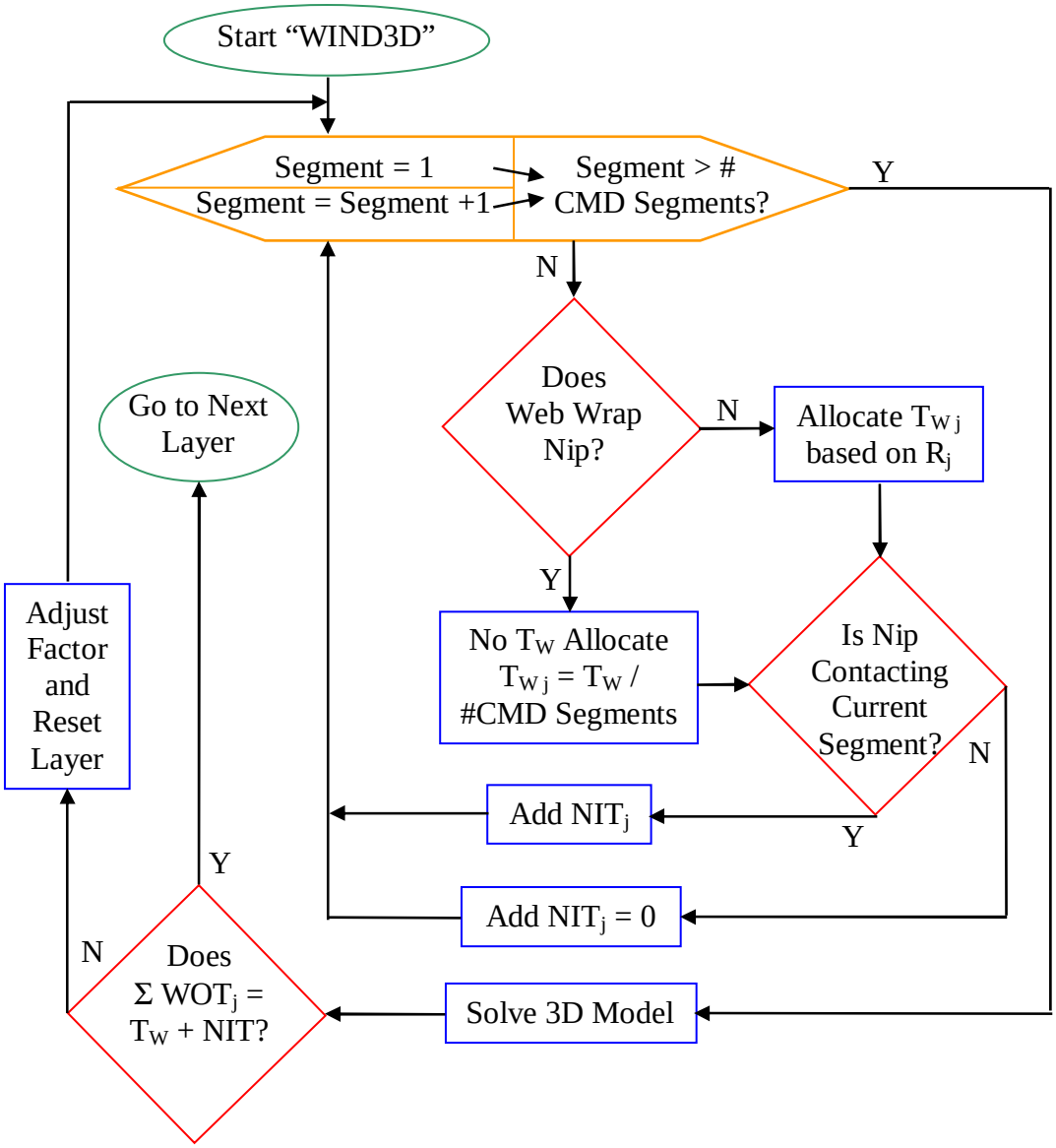

Figure #V-5: The axisymmetric sub-model incorporates the nip via a NIT component.

Combining the axisymmetric model, and the nip model invokes a noteworthy assumption. As discussed in chapter III, axisymmetric models do not accommodate variations in the circumferential direction. This includes all loadings. But, the impingement of a nip onto the wound roll's circumference is a localized occurrence that results in radial compression of the Winkler foundation elements. The impingement is not a load or deformation distributed over the entire circumference. Such a departure

from the conditions of the axisymmetric formulation most certainly will reduce its accuracy in modeling the actual wound roll. Fortunately, the error is mitigated. First, the nip's influence is converted from an axially directed impingement to a circumferentially directed NIT. Second, the roll rotates, so eventually the entire circumference undergoes the nip compression. Finally, the Hertzian contact formulas convert the generic Winkler foundation into an equivalent cylindrical roll. Even so, any discrepancies between the model and an actual wound roll will require further scrutiny of this assumption.

Another incompatibility between the sub-models is the meshing scheme of the quadrilateral axisymmetric elements, and the beam elements. More specifically, the CMD locations of their elements and nodes do not match each other. In order for the radii, Load Per Width, deformations, radial moduli, etc. to pass properly in the combined model, their locations have to do the same. The axisymmetric sub-model's meshing scheme is considerably more complex, so the nip sub-model's scheme was revised to use smaller CMD steps to place its nodes and elements at the same locations.

The model is written to be as efficient as possible in order to run on a personal computer. As the geometry of the core, the width of the web, and the radius of the desired roll are input by the user, the model estimates array dimensions. To reduce the necessary memory, many of the arrays are then dynamically allocated. Because of the potentially large number of layers, accurately estimating their number is particularly important to reducing the memory required. The model uses the desired outside radius, the core contact surface's radius, the number of actual layers to place in a model layer, the anticipated strain, and the winding tension to estimate the layers. When there is a nip load, it is also factored into this calculation.

For further reference, the appendices contain the computer input files, and combined model's source code. Appendix A has an example input file used for the comprehensive, three dimensional, axisymmetric model. A peripheral nip contact model example input file is in Appendix B. The information, from these two files, combines with the example file in Appendix C, to supply the inputs needed for the fully combined model. Appendix D is a line by line listing of the FORTRAN source code used for the combined model. Because of the confidential nature of the work, it is in a separate volume available on a restricted basis through the Web Handling Research Center at Oklahoma State University's Mechanical Engineering Department.

PET Experimental Verification

Ron Markum, of the WHRC, conducted experiments on center wound PET rolls, with and without a nip roller, so the combined model could be verified. After winding, he recorded each roll's CMD diameter with a diametral profiler. It uses Keyence LS-3060T edge sensors. Next, his Acoustic Roll Structure Gage (ARSG) provided an indirect way to determine each roll's CMD radial pressures. The ARSG sends radially directed sound pulses through the web and core, and measures how long the pulses take to travel. These measurements, referred to as the times of flight, can then be compared with radial pressure-dependent results calculated from the combined model simulation. Equation #V-6 gives the time of flight necessary to travel through a layer of thickness t.

$$t.o.f = \frac{t}{\sqrt{\frac{E_r(P)}{\rho}}} \qquad \text{(V-6.}$$

Here the radial modulus' dependence on radial pressure is shown explicitly, while ρ is the material's density in units of mass per volume. Summing a segment's calculated *t.o.f.* for all the model layers, and for the core, produces a total flight time for the segment. The segment flight times can then be compared to the experimental data across the width.

Other experimental methods were considered. Pull tabs provide a way to measure the interlayer pressure in a wound roll. They are thin brass strips inserted across the roll's width that are held in place by the interlayer friction. But, they are quite limited in their ability to portray pressure variations across the width. Strain gauge instrumented cores (like the one developed by Hakiel [15]) are another way to measure the radial pressures. When properly aligned, and calibrated, they can produce a radial pressure profile across the width. The profile is only at the core however, and they are difficult to space tightly in the CMD. Peeling off the outside layer and measuring its WOT is an indirect method that can infer the stresses throughout the roll's radius. Unfortunately, it is difficult to get cross width variations, and the measurement has been shown to interfere to some extent with the values. A type of hybrid between pull tabs and an instrumented core are Force Sensing Resistor (FSR) pads. The pads change resistance under loading and thereby can be used to measure radial pressure. More than one can be placed across the roll to provide a CMD profile, and they can be placed at any depth. Their resistance tends to wander over time, and the winder must be stopped in order to insert them. Also, they tend to add some bending stiffness across the width. Their stiffness could be especially significant for thin webs.

The web used in the experiments was a six inch wide PET. First, two rolls were wound without a nip roller, at a uniform tension across the width of 1 pli. Table #V-1 lists the core and web properties of those rolls.

Parameter	Web	Core
Thick	0.00048 in	0.289 in
Width	6 in	7 in
E_R	0.000232*372.8+372.8P psi	10000 ksi
E_T	678370 psi	10000 ksi
E_Z	678370 psi	10000 ksi
$\nu_{\theta z}$	0.3	0.3
$\nu_{\theta r}$, ν_{zr}	0.01	0.3
G_{RZ}	305300 psi	4000 ksi
Layers	20 / model layer	3
Radius	4.914 in	3.289 in

Table #V-1: The combination model's simulation was conducted on ½ mil thick PET film wound on an aluminum core.

The radial profiles of the finished rolls are displayed in Figure #V-6. They were used to determine the web layer's CMD thickness profile, by dividing the radii by the number of material layers in the roll. The resulting thickness profile is given Figure #V-7.

The error associated with this CMD thickness profile is different then for other methods. In most thickness measurement methods, multiple layers are stacked up, and directly measured, at multiple locations across the width. The stacks have little or no compression during the measurement. But, the finished roll's overall radii are for a compressed state, so when they are divided by the number of layers in the roll, the result is a single layer that is also compressed. The non-linearity of the radial modulus moreover makes that compression vary across the width. The profile is therefore not only diminished, but also contains a bias across the width.

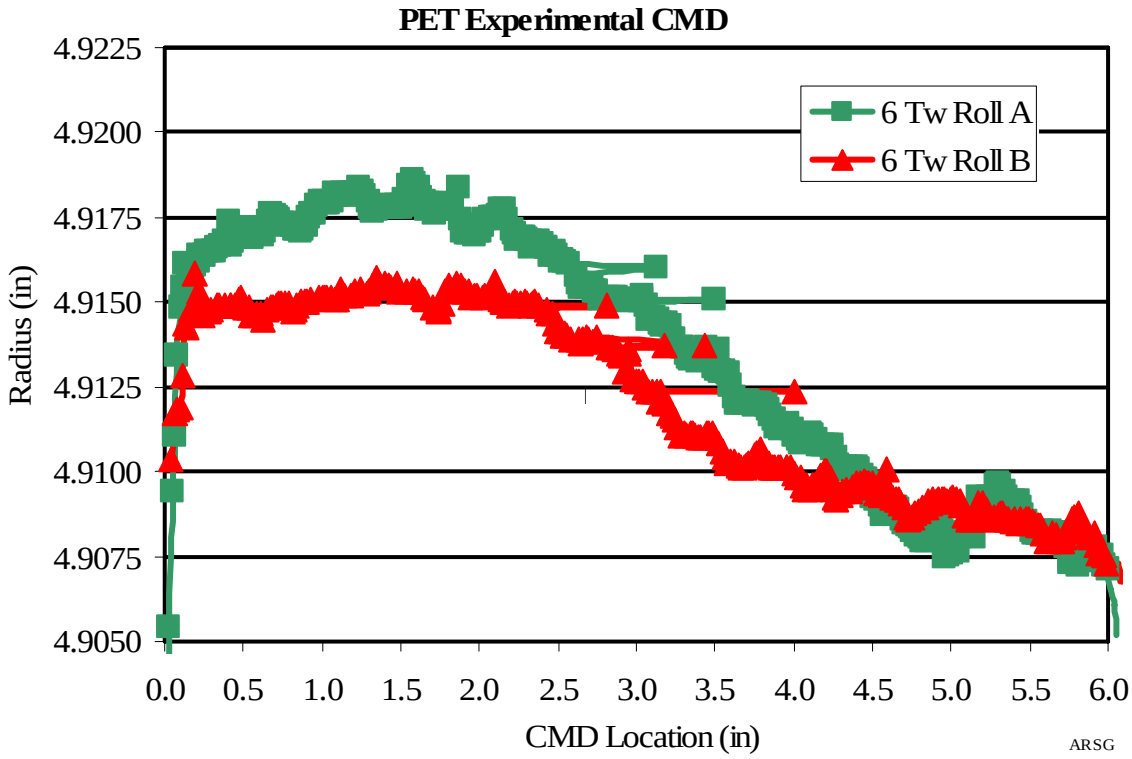

Figure #V-6: The experimental CMD radii are used to find the web's thickness profile.

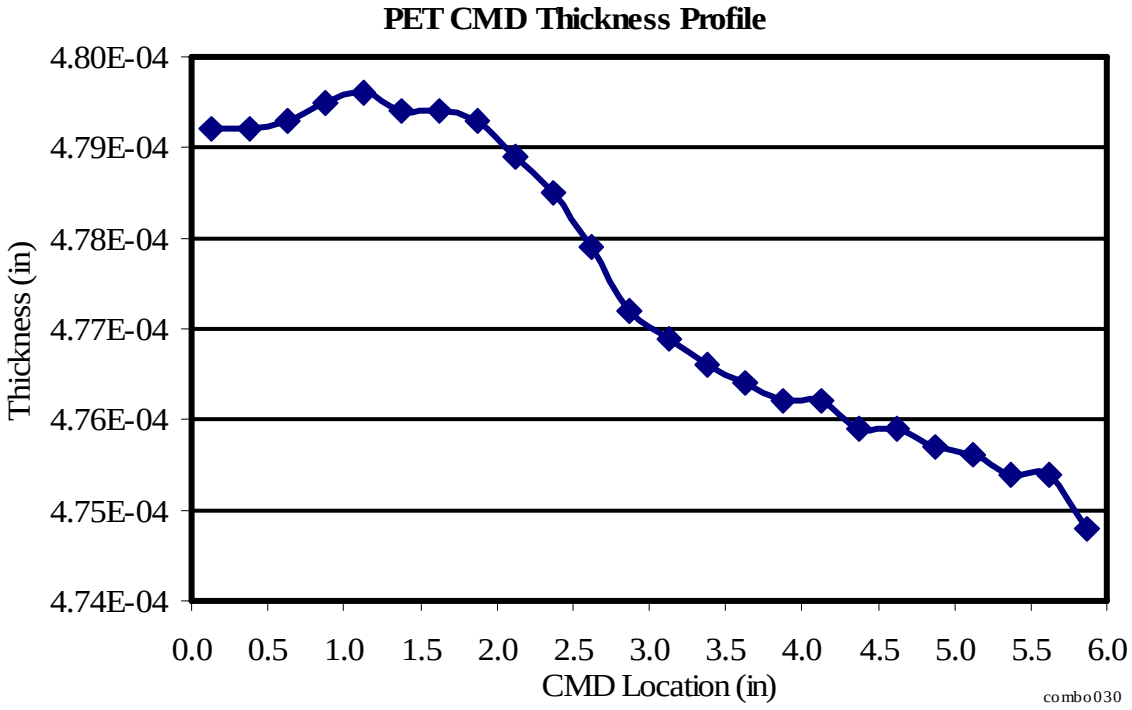

Figure #V-7: The PET web's thickness profile contains twenty four, CMD segments.

Combined Model PET Results

With the thickness profile now available, and with the other parameters listed in Table #V-1, the center wound PET rolls were simulated in the combined model. It wound 174 model layers, with 24 CMD segments across the web width, at zero pounds of nip force. Figure #V-8 plots the resulting outer layer's radii against the experimental values. (Note: the original, diametral profiler's experimental values were relative to a measured median. Thus, they must be, and have been, adjusted to match the simulation's median radius. The values in Figure #V-6 were adjusted to the desired radius of 4.914 inches, while for this plot, they were adjusted to 4.91502 inches.) The radii show excellent agreement, especially considering the aforementioned error possibilities. The CMD flight times were calculated next, for the combined model simulation. They are shown in Figure #V-9 along with the experimentally recorded data.

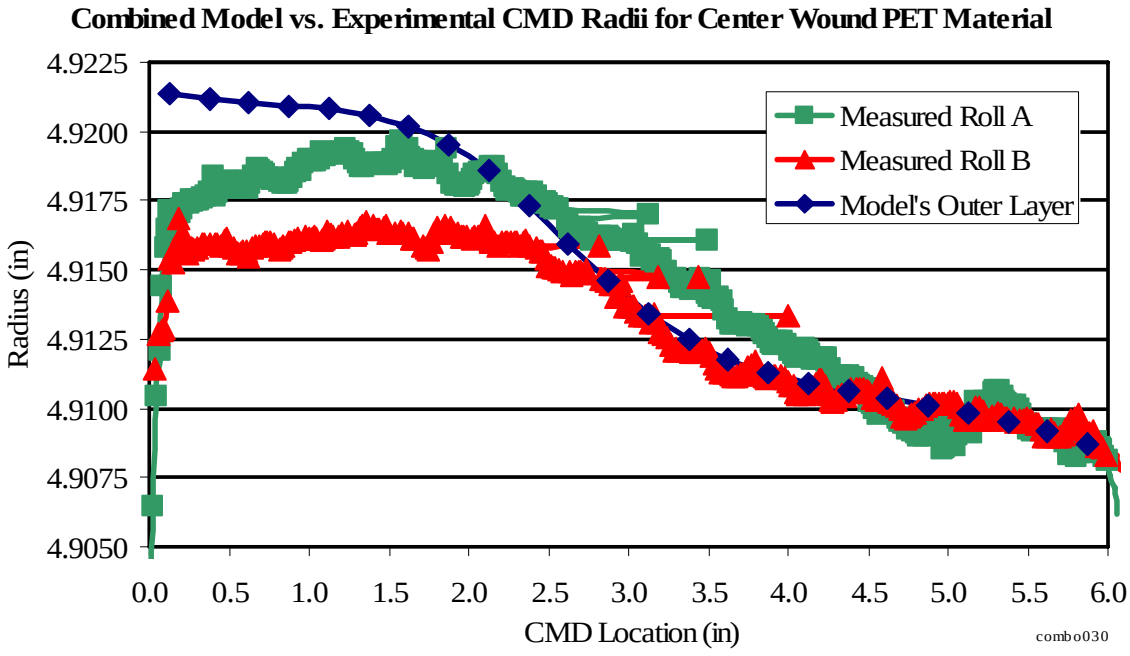

Figure #V-8: The model's radii match extremely well to the center wound data.

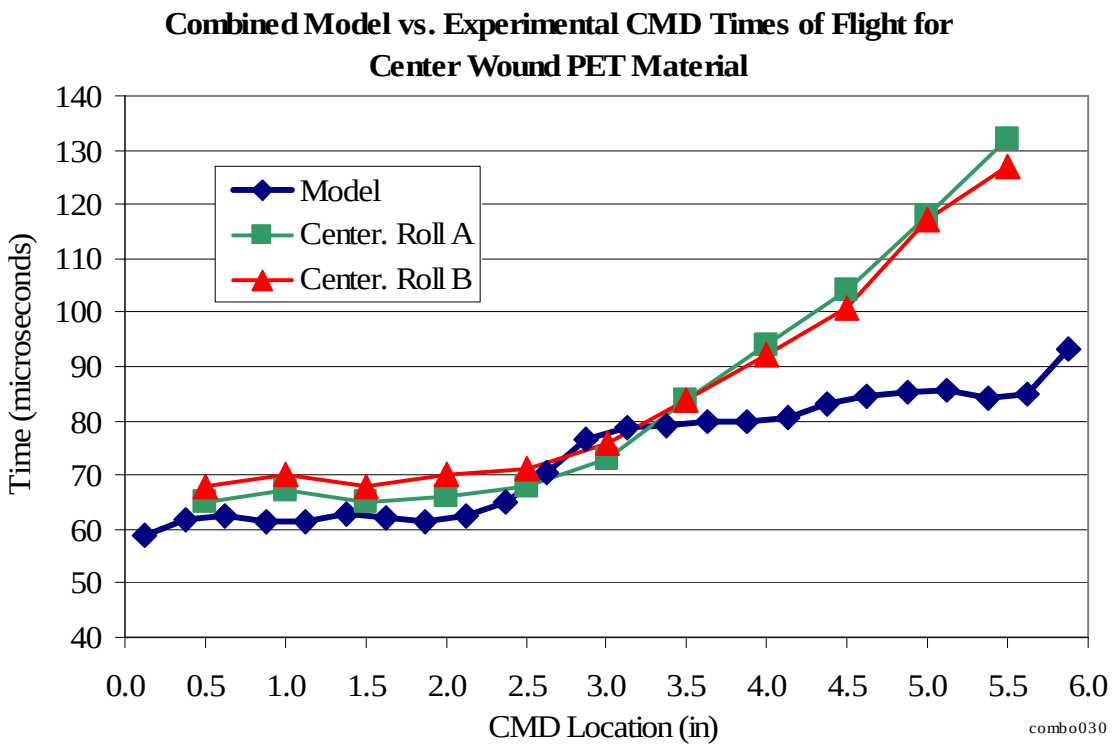

Figure #V-9: The times of flight across the width show good agreement to those determined experimentally for the center wound rolls.

Such good agreement between the *t.o.f.* values from the simulation, and the experiment, validate the combined model's results for the center winding case. While the axisymmetric model was already validated for center winding, this run ensures the combined model reduces to the sub-model when the nip load is set to zero. The corresponding radial and circumferential stresses, as determined by the model, are thus believed to be accurate representations of the wound roll. Figure #V-10 shows the radial stresses from the combined model. The circumferential stresses are displayed in Figure #V-11.

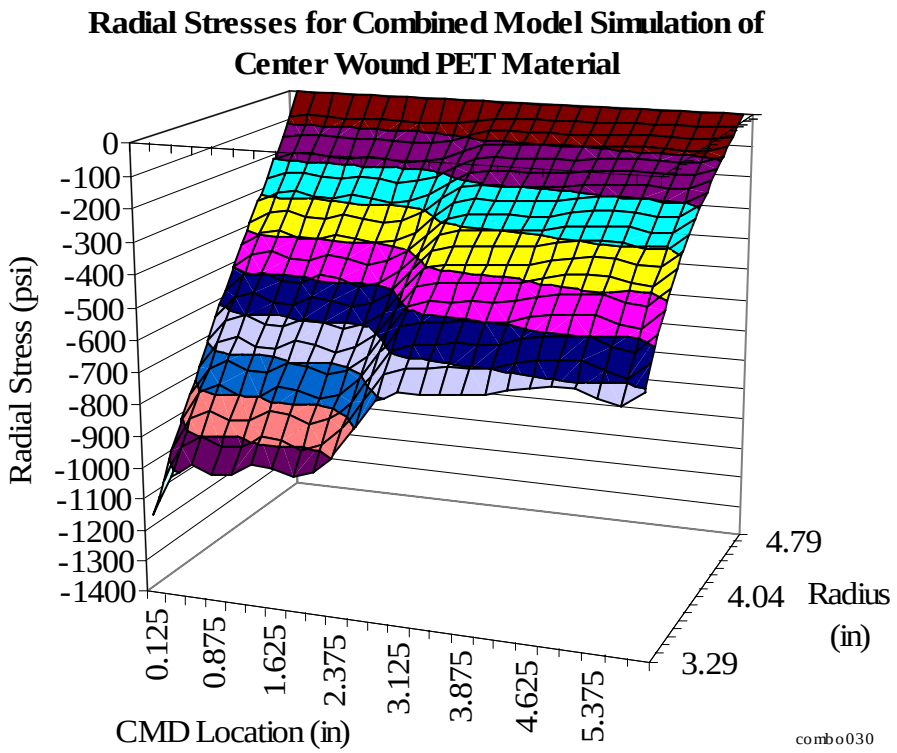

Figure #V-10: The radial stress throughout the center wound roll peaks at the core on the thicker left side.

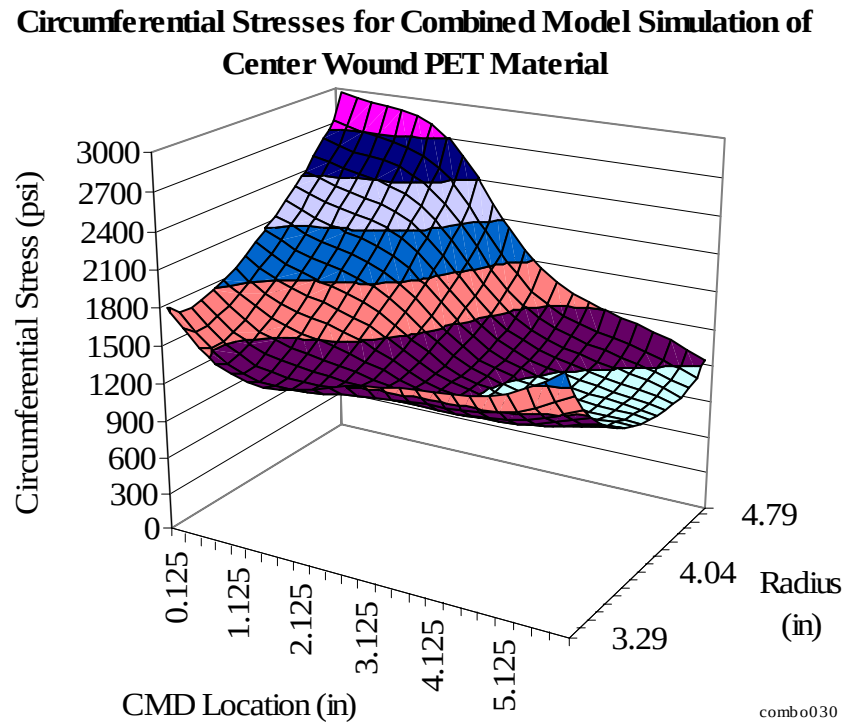

Figure #V-11: The center wound roll's circumferential stresses concentrate and saturate on the thicker left side, showing behavior typical of stiff webs like PET.

A mock nip run provided an intermediate test, before fully simulating the nip impinged rolls. The nip load was set to zero, technically making it a center winding run, but a CMD LPW vector was hard-coded in. The chosen mock load level was 14 pounds (the smallest of the 14, 30, and 40 pound experimental runs). It was distributed uniformly across the six inch width, producing 2.33 pli of tension. Inside the "WIND3D" subroutine, the LPW multiplied by μ_s (0.32), to make the NIT equal to 0.75 pli. This increased the WOT from the1.00 pli T_W, to 1.75 pli. Figure #V-12 plots the *t.o.f.* for the 14 lb experimental roll, the mock nip model, and the two center wound rolls for comparison sake.

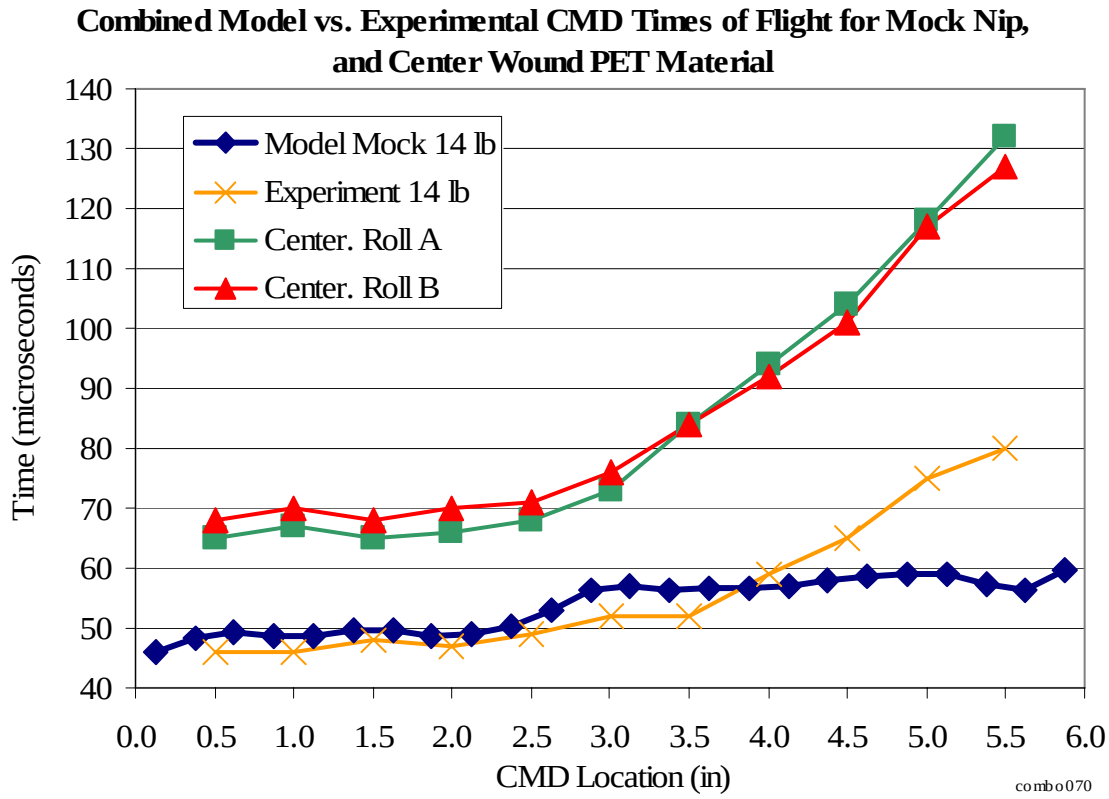

Figure #V-12: The mock nip run captures the influence of the nip as it matches the reduction in the times of flight across the width.

Note, in Equation #V-6, the *t.o.f.* relates inversely to the radial pressure, and thus decreases as the pressure increases. That is why increasing the WOT tension, by adding a nip induced tension component, dropped the times of flight down from the center winding results. Figure #V-13 re-plots the mock nip model against the 14 lb experimental results in a close-up plot. It shows the combined model follows the behavior seen in the 14 pound experimental data.

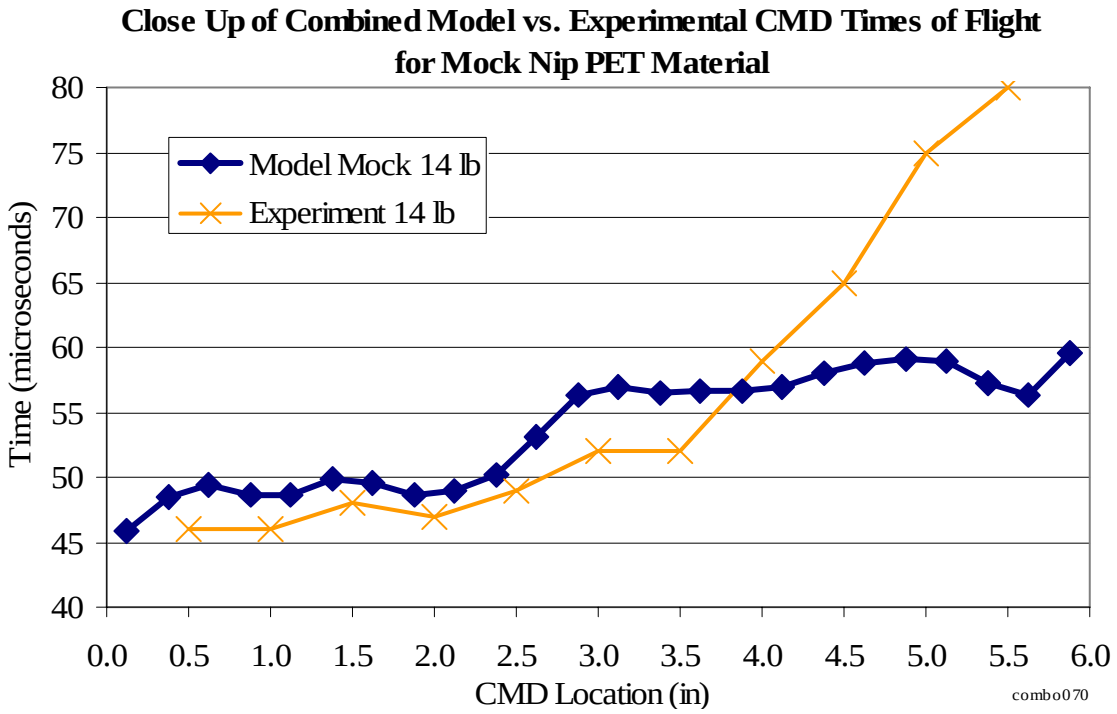

Figure #V-13: A close up of the 14 lb mock nip model, and the experimental data, show they agree well.

Figures #V-14 plots the radial stresses throughout the wound roll. Similarly Figure #V-15 displays the roll's circumferential stresses.

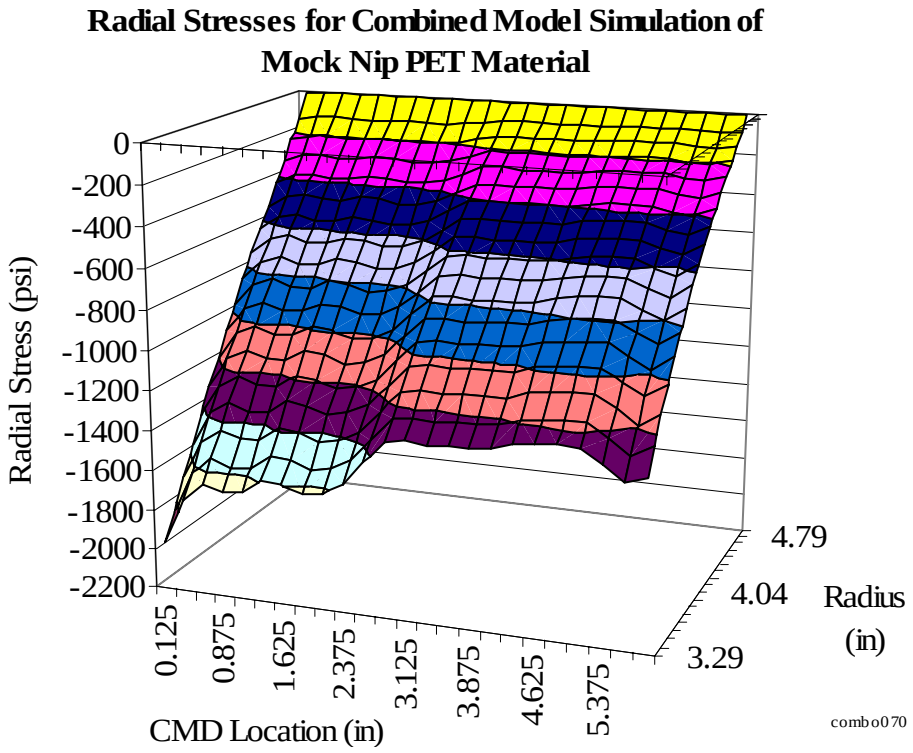

Figure #V-14: The radial stress in the mock simulation peaks at approximately 800 psi more than the center wound roll.

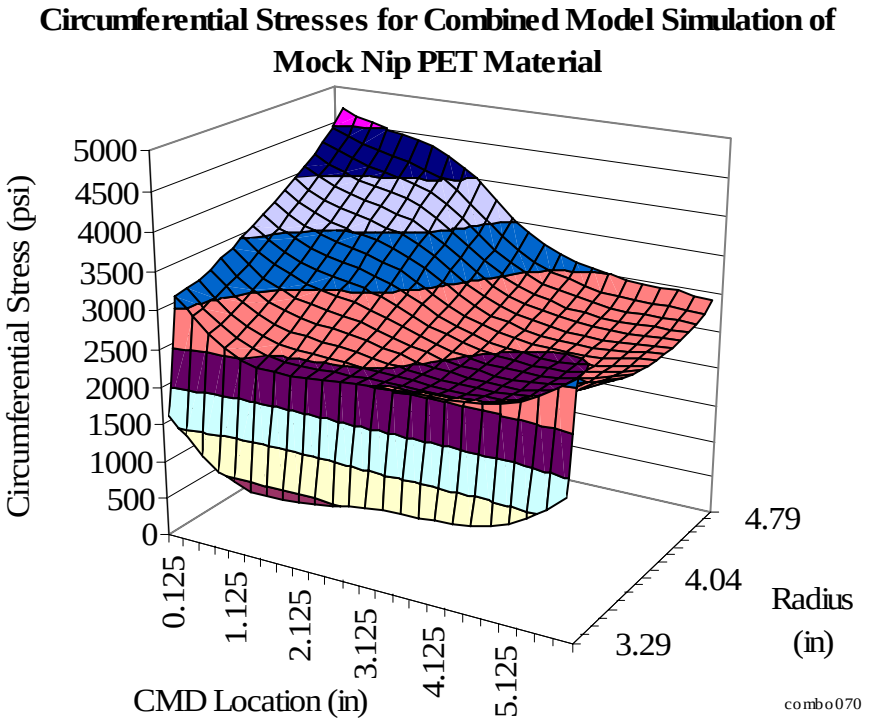

Figure #V-15: The mock nip's circumferential stresses behave similarly to the center wound values, except for a tension ramp up when the nip load was applied.

In general, the radial and circumferential stresses for the mock nip simulation look similar to those from the center wound simulation. This is, of course, to be expected since the mock simulation is a center winding case. The stresses in the mock simulation reflect its higher WOT. One notable difference between the two simulations is the rapid tension increase in the circumferential stresses near the core. Interestingly, this is due to the radius at which the model first placed the nip onto the roll. It is a separate variable, input by the user, referred to as the nip start radius. The model only loads the LPW values after the start radius is satisfied. During the mock run's first axisymmetric accretion, the "WIND3D" subroutine did not have the LPW vector loaded yet. Just like for an actual nip impingement, it wasn't added into the WOT until after the start radius.

The combined model's full nip impingement simulation proceeded as follows. At all three load levels, the nip start radius was set at 3.339 inches. The axisymmetric sub-model wound the roll to that radius, and then the nip-impingement sub-model set the nip on the roll's two highest sectors. The code pressed the nip into the roll, engaged the rest of the sectors, and determined the Load Per Width values across the width. While the algorithm, as expressed by the flow chart in Figure #V-4, implies the nip will be impinged multiple times during the wind, these values were instead maintained during the rest of the axisymmetric winding. This was accomplished by setting the nip trigger so that the desired second nip impingement was higher than the desired final radius.

Figure #V-16 presents the generic, model configuration. Many, of the model's required dimensions, are labeled. While only one side of the nip, and the roll, is labeled, both sides are necessary inputs, as the model permits left to right asymmetry. Table #V-2 lists the values used in the simulation.

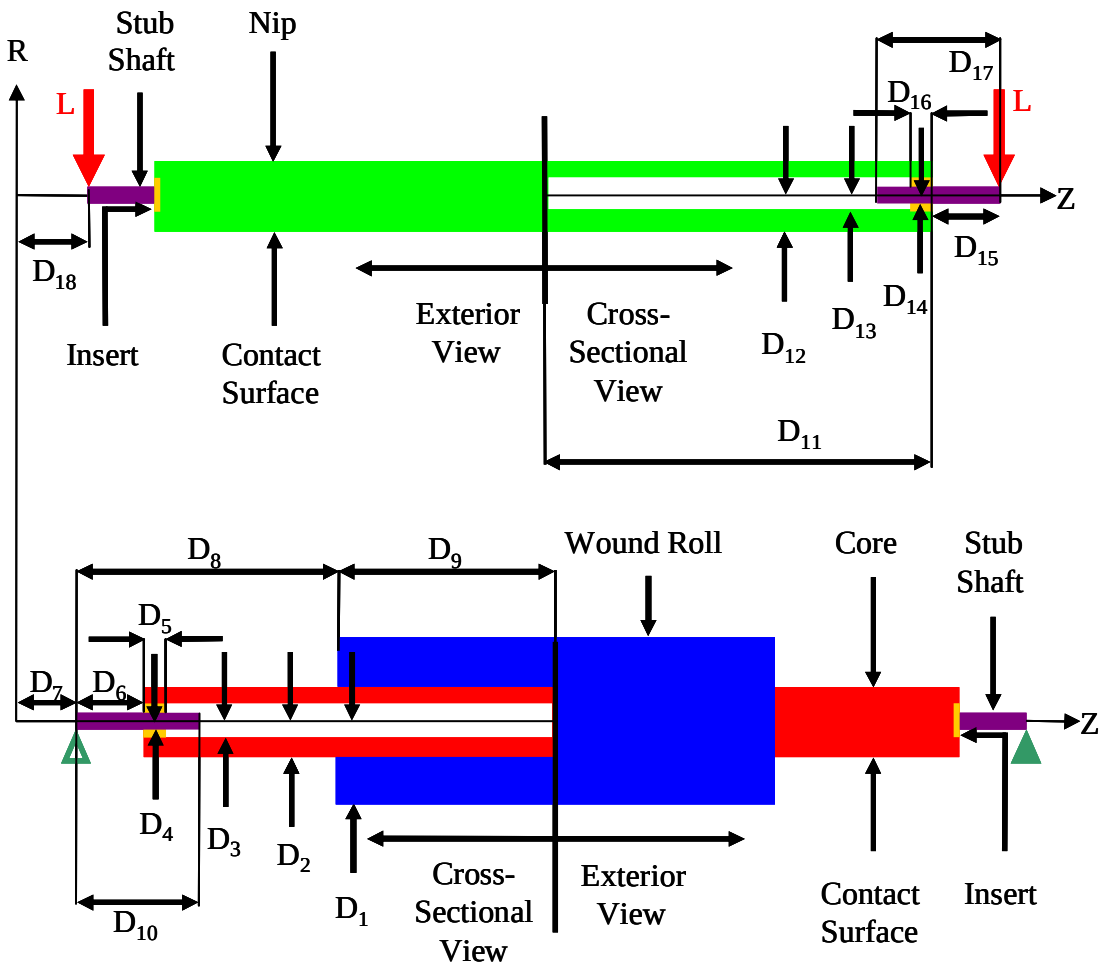

Figure #V-16: Many of the dimensions used in the combined model are shown here.

Dim.	Description	Value	Dim.	Description	Value
D_1	Wound Roll Radius	4.914 in	D_{11}	1/2 Nip C. S. width	4.000 in
D_2	Roll Inside Radius	3.289 in	D_{12}	Nip Contact Surface Radius	1.375 in
D_3	Core C. S. Radius In	3.000 in	D_{13}	Nip Insert Radius	1.0625 in
D_4	Core Stub Radius	0.938 in	D_{14}	Nip Stub Radius	0.500 in
D_5	Core Insert CMD Thickness	0.500 in	D_{15}	Nip Load to Insert Distance	1.625 in
D_6	Core Support to Insert Distance	0.000 in	D_{16}	Nip Insert CMD Thickness	0.500 in
D_7	Zero to Core Support Distance	2.125 in	D_{17}	Nip Stub CMD width	5.625 in
D_8	Core Support to Roll Distance	0.500 in	D_{18}	Zero to Nip Load Distance	0.000 in
D_9	1/2 Web/ Roll CMD width	3.000 in		Nip Load Sep. Distance	11.250 in
D_{10}	Core Stub CMD width	3.500 in		Core Support Sep. Distance	7.000 in

Table #V-2: The PET full simulation used the above dimensions to represent the rolls.

For the PET web, the combined model's agreement to the experimental results showed multiple impingements were unnecessary. In Figure #V-17, the model's *t.o.f.* values match well to the 14 pound nip load experimental values. On the right side there is some discrepancy, but this is similar to the behavior seen with the center winding cases. Thus, it is likely the result of error in the thickness on the right side (due to unequal CMD compression), or in the assumption of constant density across the width.

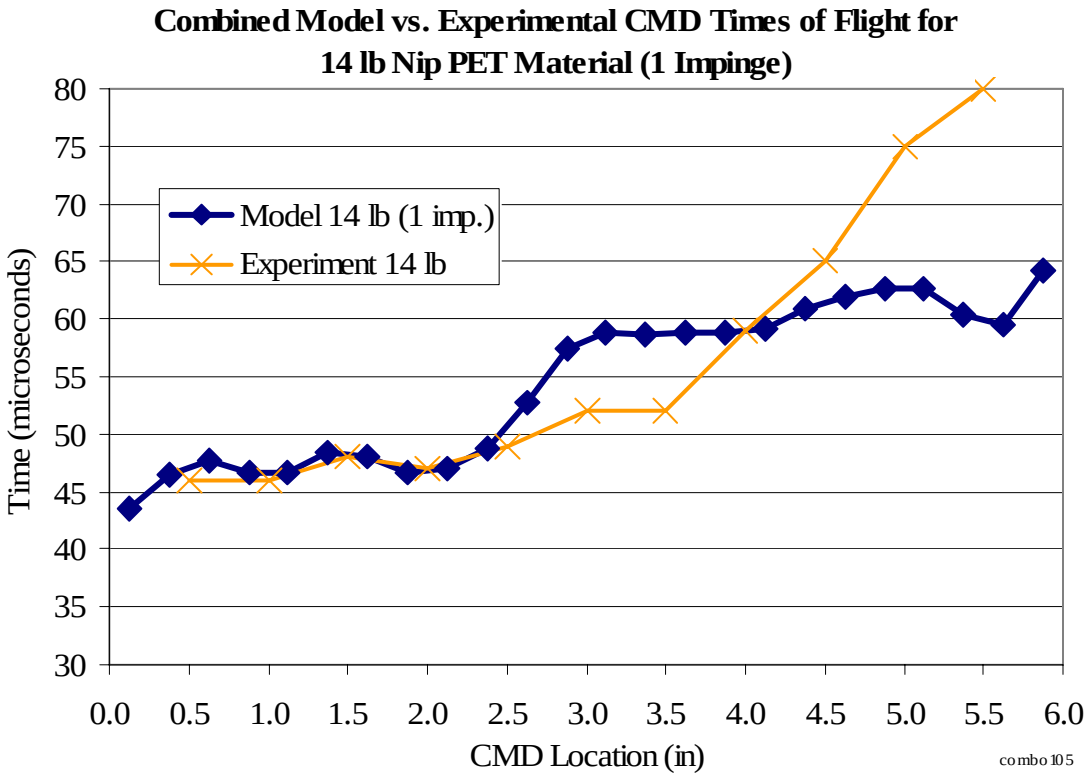

Figure #V-17: The combined model run's values match very well to the experimental times of flight for the 14 lb nip case, with CMD averages of 54 and 56 microseconds respectively.

When the simulation was rerun, with a greater number of impingements during the wind, the combined model produced tensile radial stresses. Their locations and magnitudes varied with the number of impingements throughout the wind, the web layers per model layer, and the radius of the first impingement. Without correction, the positive signed, tensile radial stresses would yield physically impossible, negative radial moduli.

This is because the radial modulus expressions (Equation #III-21) utilize a positive compressive pressure, so the usual, negative radial stresses are automatically converted through multiplication by negative one.

The axisymmetric sub-model prohibits the radial modulus of any quadrilateral element from going negative, by instead setting them to a very small positive value. This works in conjunction with inter-roll gapping, to keep those elements from holding layers together. When these small radial moduli convert to the effective segment moduli (and strain) via Equations #V-4, and #V-5, they remain small. This tends to ill-condition the nip impingement FEM matrix, because the small radial moduli produce small Winkler ESMs, compared to the much larger nip and core ESMs. The result is large, erratic variations in the LPW values across the width, or even complete failure of the simulation.

The source of the tensile radial stresses is the CMD variation in the nip's LPW values. When the combined model impinges the PET roll more than once, the LPW variations invoke the axisymmetric sub-model's limitation, as discussed in chapter III. A cascading effect then occurs. The LPW variations produce the tensile radial stresses, which successively yield the small E_R, the ill-conditioned matrix, and then even more erratic LPW. The ultimate result, for the PET roll simulation, is that increasing the number of impingements causes a growing instability due to the coupling of the two sub-models. It is important to note that despite this instability, when only one impingement is performed, the results match so well to the experimental data, additional impingements are not required. Also, this only happens for the radially stiff PET web.

Figures #V-18 and #V-19 show the radial and circumferential stresses in the roll. It had one, 14 pound impingement started and maintained from 3.339 inches in radius.

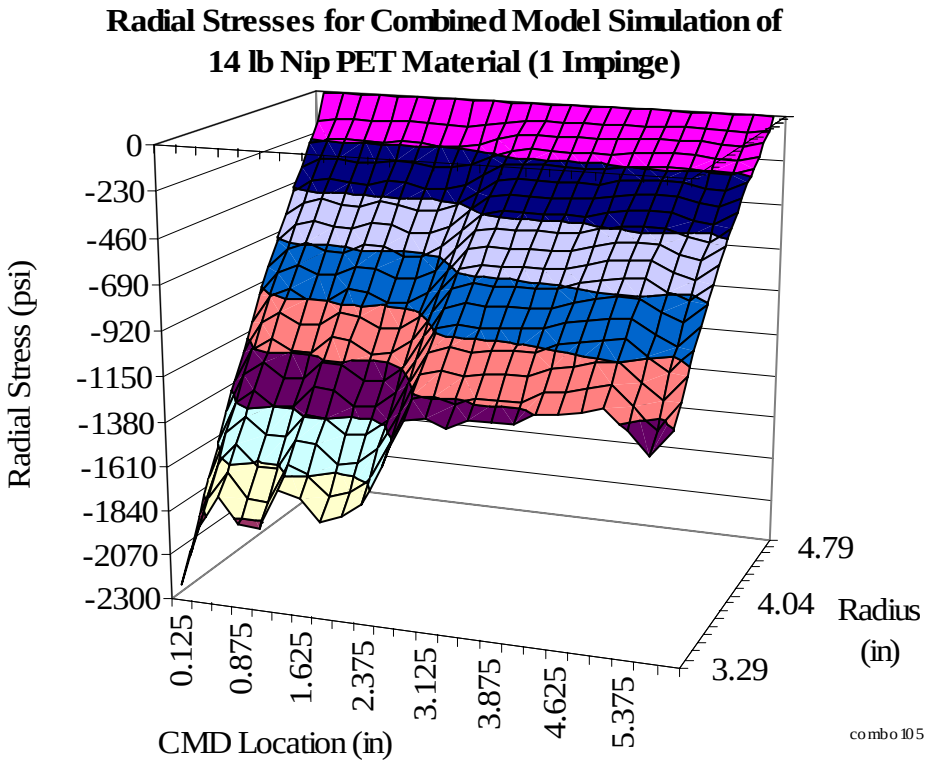

Figure #V-18: The combined model's radial stresses concentrate on the higher elements under the 14 lb nip load.

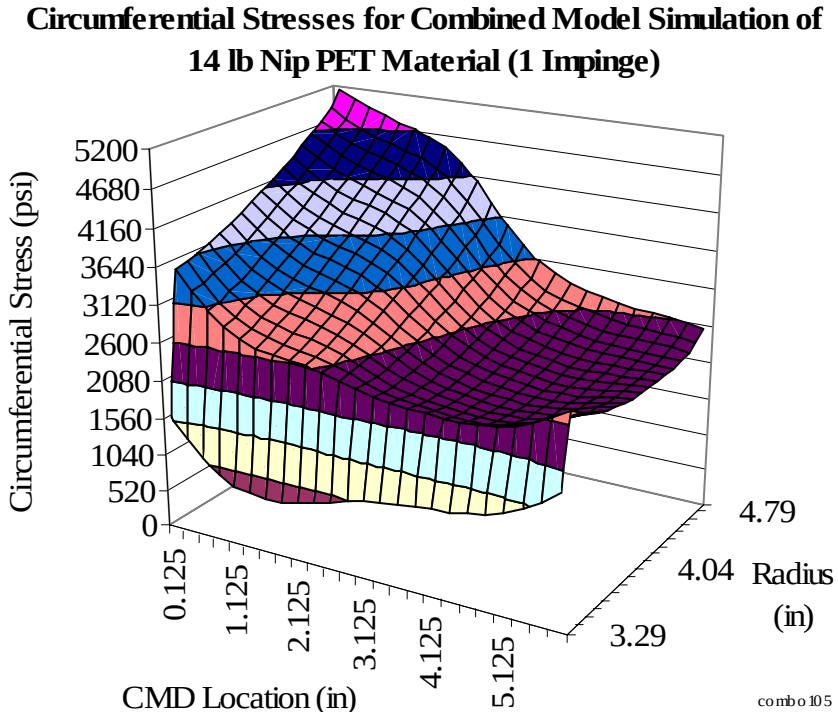

Figure #V-19: The 14 lb nip load ramps up the circumferential stress from the 1 pli web line tension near the core, and concentrates it on the web's thicker edge.

The simulation was repeated under the same conditions, and with the same web thickness profile, except the nip load was increased to 30 pounds. Figure #V-20 relates the *t.o.f.* values from the model with the experimental data. They both have shorter flight times, and are more uniform across the width, than for the 14 pound case. The model's average is 44 microseconds, while the experiment average is 54 microseconds.

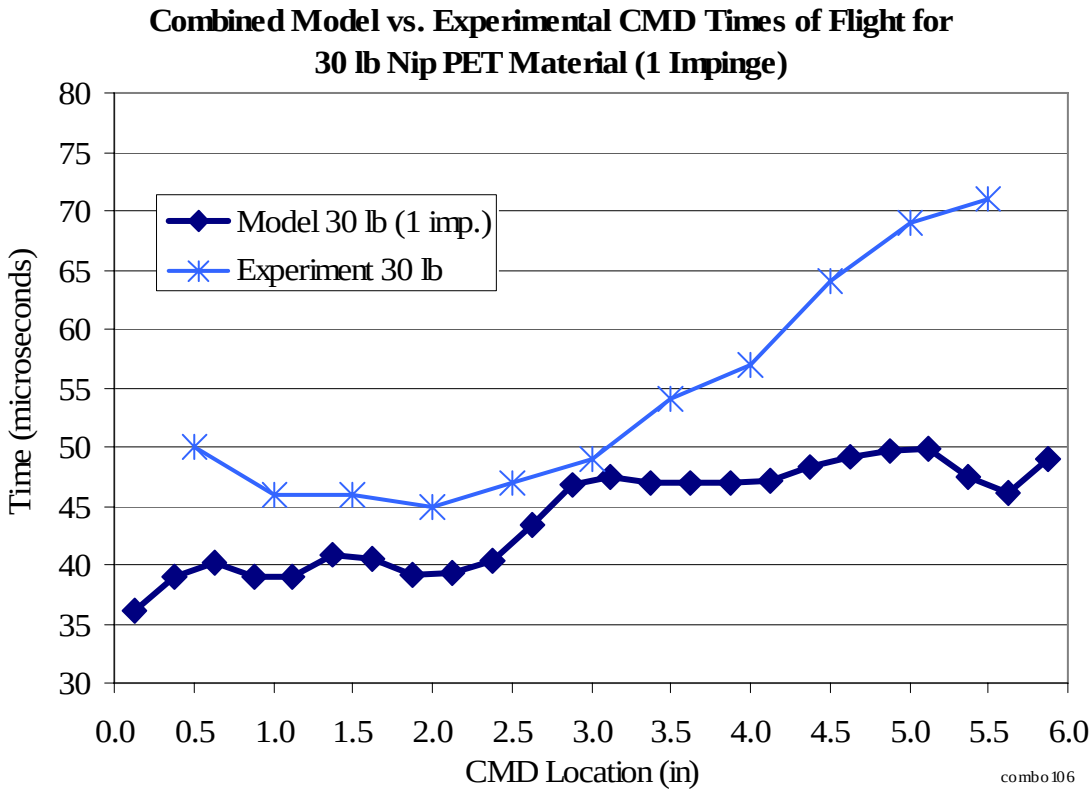

Figure #V-20: Both the combined model, and the experiment, had reduced times of flight when the nip load increased to 30 lb.

The roll stresses, throughout the 30 pound case, behave similarly to the 14 pound case. As seen in Figure #V-21, the radial stresses still concentrate on the thicker left side, and taper off to the right. For the 30 pound case, the peak magnitude is about 1200 psi greater. Also, they vary more severely across the width at the core. The circumferential stresses in Figure #V-22 show the expected increase in total stress. In contrast to the 14 pound case, their percentage of CMD variation is not as drastic, at the outer edge.

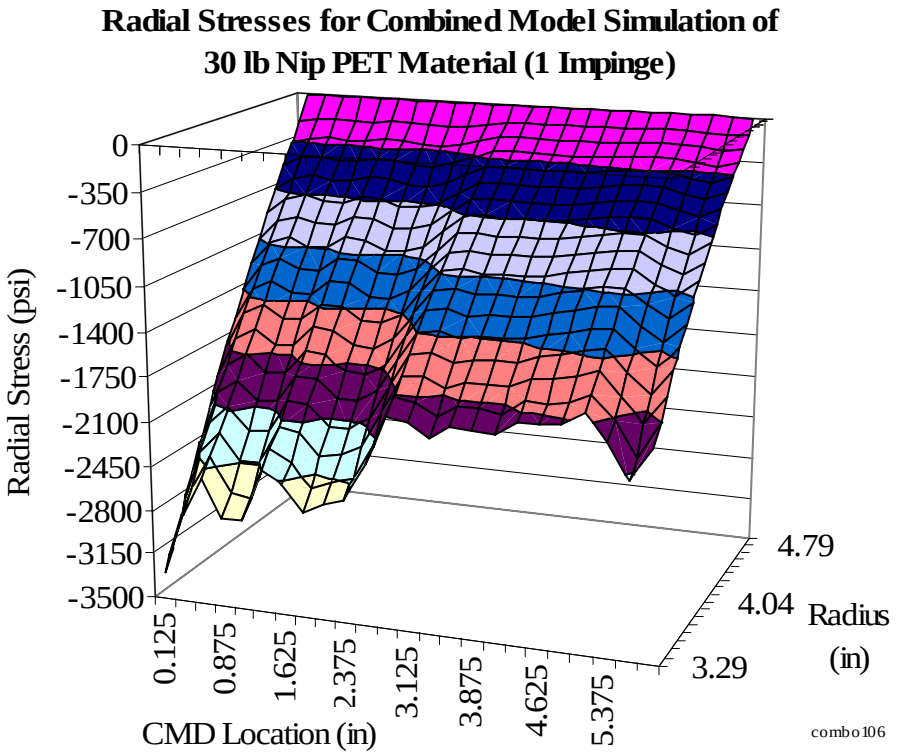

Figure #V-21: The combined model's radial stresses have a more pronounced variation across the width for the 30 lb nip load.

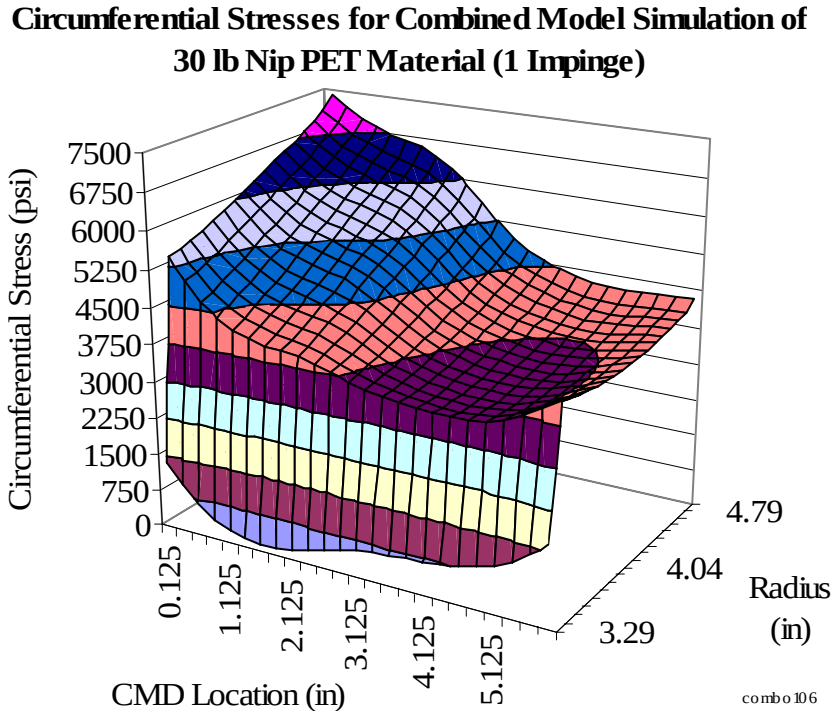

Figure #V-22: The shape of the circumferential stress plot for the 30 lb nip load is similar to the lower load case.

At the 40 pound load level, the trend continues. The flight times are again all reduced from the previous runs, as seen in Figure #V-23. The average across the width dropped to 40 microseconds for the model, and 49 microseconds for the experiment.

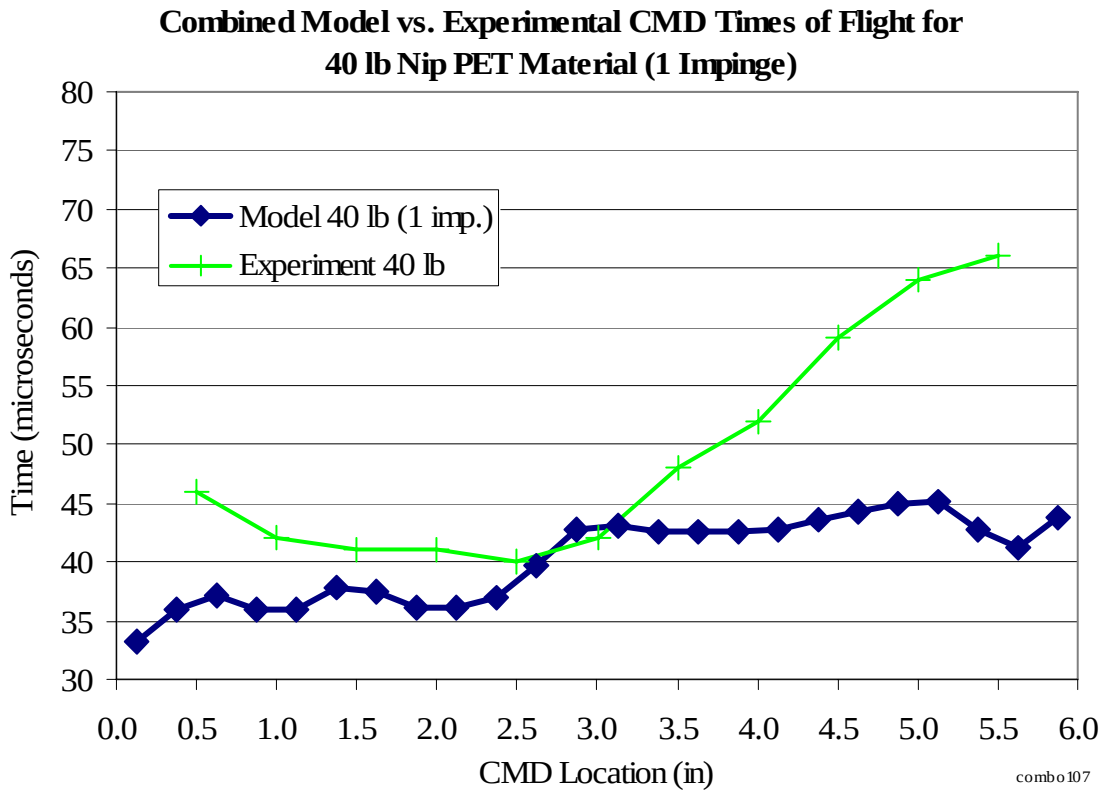

Figure #V-23: At some of the middle locations, the 40 lb nip load times of flight appear to agree better than for the 30 lb load.

While the model's times flatten out, and thus vary less across the width, the experimental times maintain their overall magnitude difference. But, this is mostly due to the third through seventh CMD experimental values (those from 1.5 to 3.5 inches) dropping relatively lower than the surrounding ones. They were comparatively higher at 14 and 30 pounds. This relative lowering produces a crossover between 2.5 and 3.5 inches CMD, and makes the model appear closer to the experiment than it was for the 30 pound simulation. But, the 9 microsecond difference between the model and experimental average times of flight is only one microsecond less than for the 30 pound case.

The fact that the 30 and 40 pound PET model flight times are less than their experimental times indicates the model's predicted pressures are higher than in the actual roll. The model has an excess of radial pressure. Since the web line tension, and the Nip Induced Tension, are the only load sources, one of them must be responsible for the excess. The web line tension is quickly ruled out, because the axisymmetric sub-model used it and repeatedly matched well to experiments. This means the calculated μN term for NIT was too high.

The 40 pound case's radial stresses in Figure #V-24, and the circumferential stresses in Figure #V-25, act similarly to the 14 pound case. They concentrate on the thicker left side. However, the radial stresses near the core fluctuate more, while the circumferential stresses at the outside fluctuate less.

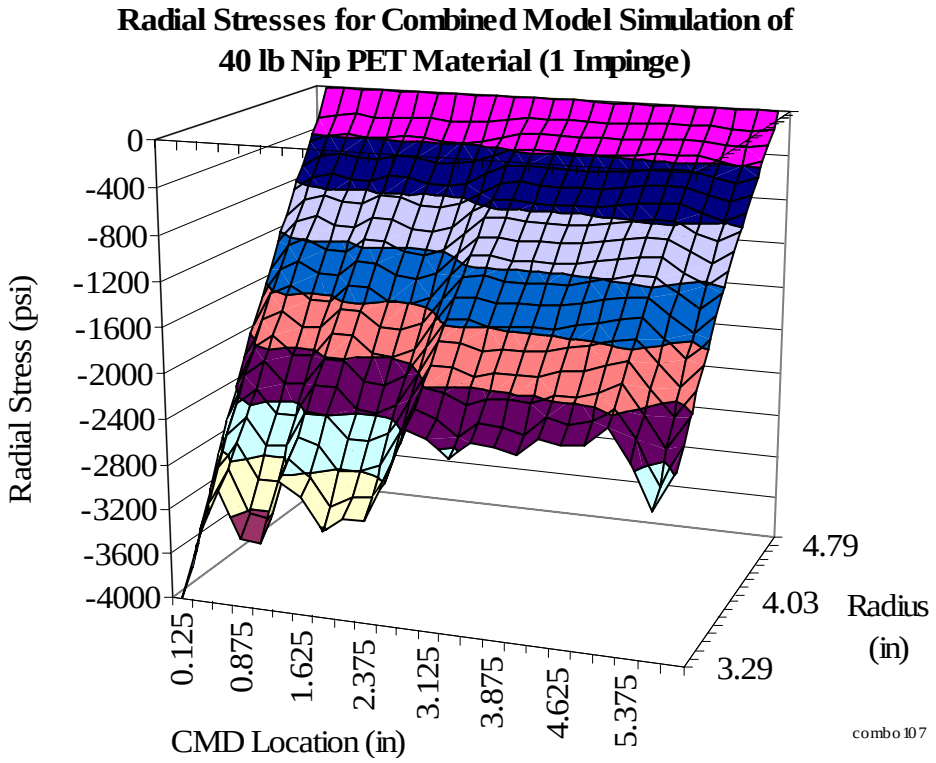

Figure #V-24: The combined model's radial stresses have a more pronounced variation across the width for the 40 lb nip load.

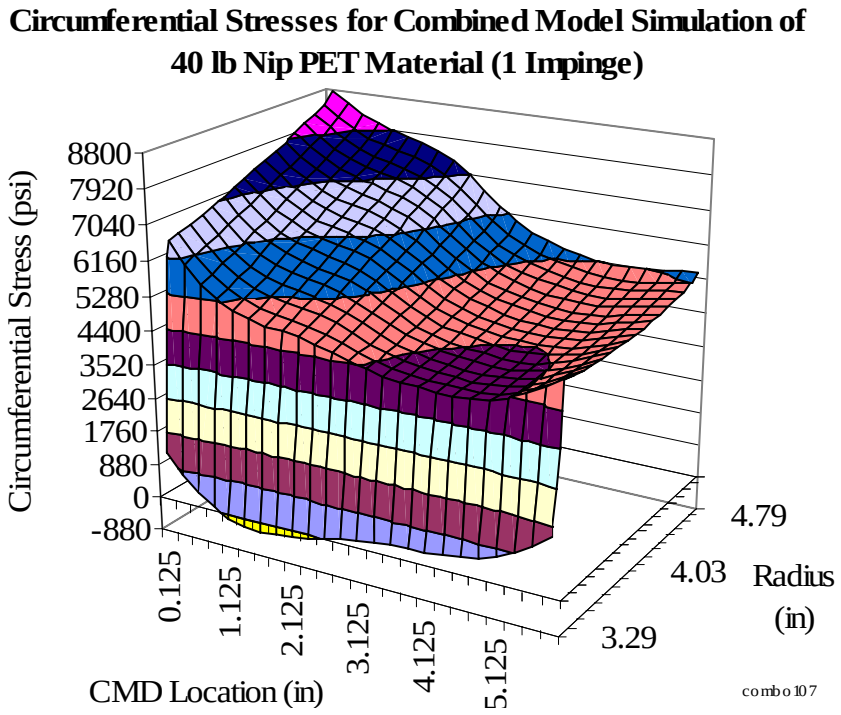

Figure #V-25: The shape of the circumferential stress plot for the 40 lb nip load is similar to the lower load cases.

All of the simulations up to this point were conducted without any lateral friction constraints. The 14 pound, PET case was rerun with the lateral friction turned on. Figure #V-26 plots the lateral friction dependent radial stresses throughout the roll. For the no-friction comparison, refer back to Figure #V-18. The friction dependent circumferential stresses are in Figure #V-27. They compare to Figure #V-19. Both the radial and circumferential stresses have perturbations near the core that are induced by the friction. They are most significant at 1.0 inches CMD, which is where the layers are laterally constrained to each other, to prevent a rigid body motion. When the friction is turned on, the lateral and shear RZ stresses become interesting, as they are no longer equal to zero. Figure #V-28 displays the lateral stresses throughout the PET roll. The shears are plotted in Figure #V-29. Both the lateral and shear stresses have magnitudes significant enough to warrant web handlers investigate their impact on the core, and on the web itself.

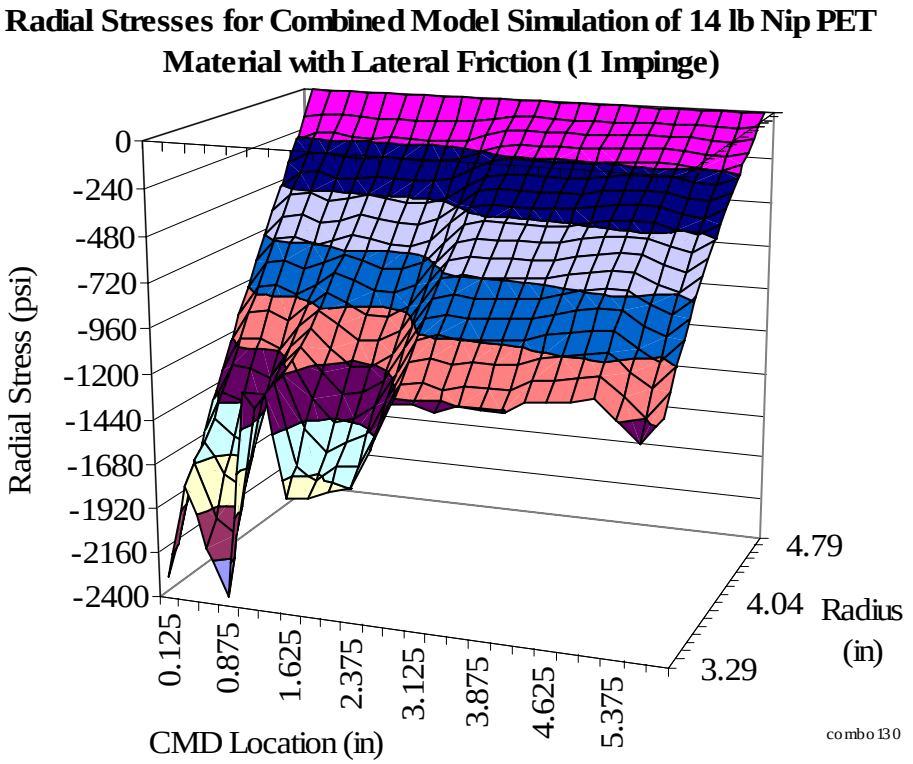

Figure #V-26: The radial stresses in the PET roll at 14 lb nip load, subject to lateral friction, are less uniform across the width at the core.

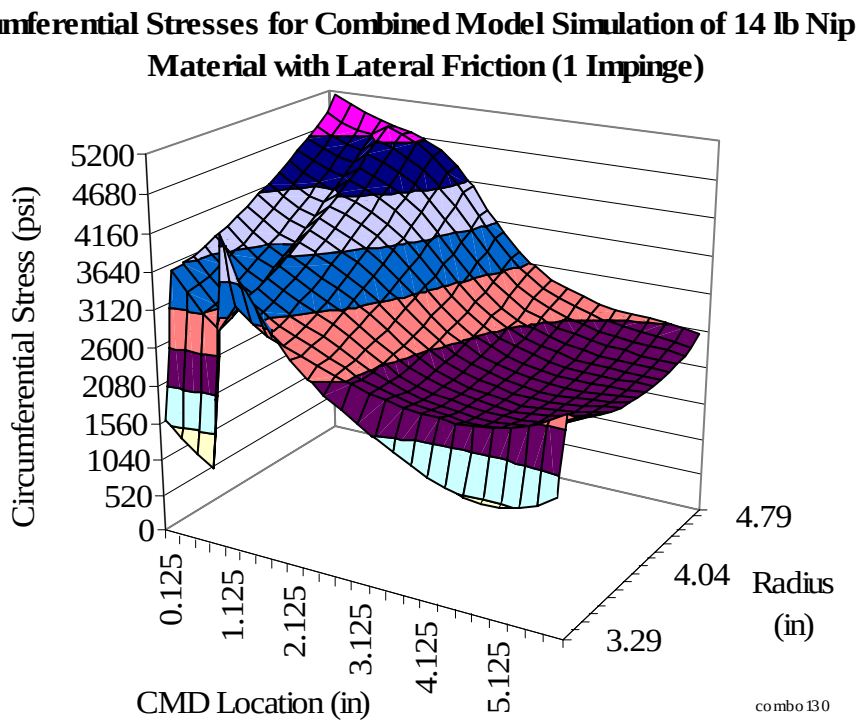

Figure #V-27: The core circumferential stresses spike upward at the 1 inch CMD location, for the 14 lb nip loaded PET roll, when lateral friction is engaged.

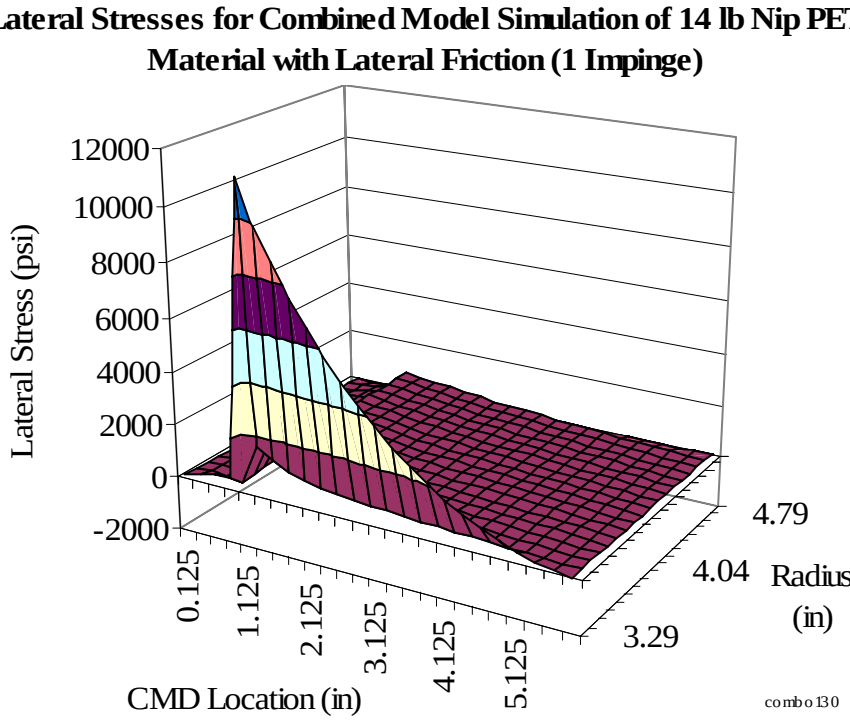

Figure #V-28: The 14 lb nip loaded PET roll has significant lateral stresses at the core, when the lateral friction is included in the simulation.

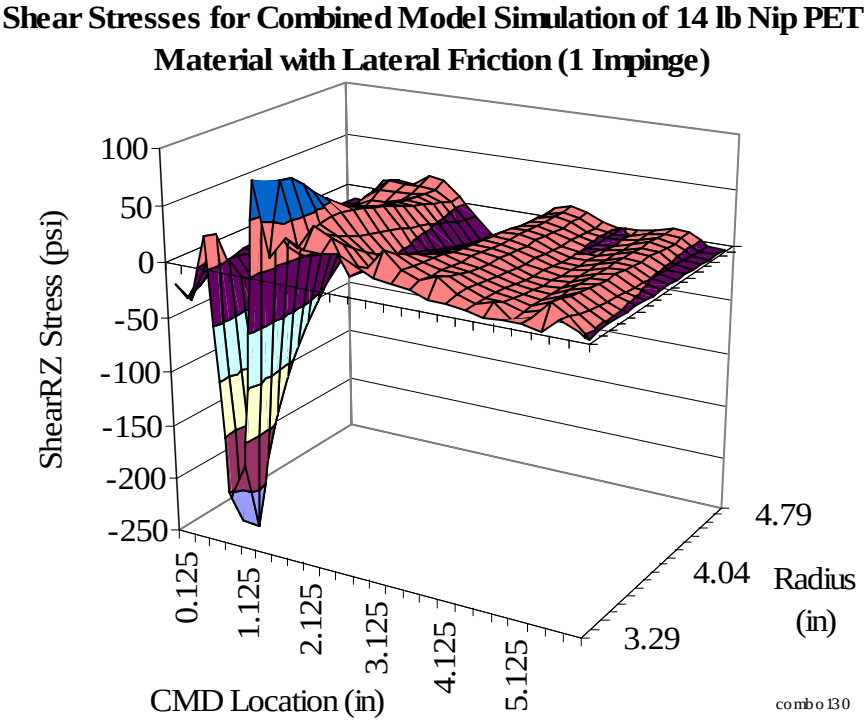

Figure #V-29: The lateral friction-induced shear stresses are uniform throughout the 14 lb nip loaded PET roll, except where the roll is laterally constrained in the cross machine direction.

The perturbations witnessed in the radial and circumferential stresses, as a result of the lateral friction constraints, change the times of flight as well. However, as seen in Figure #V-30, the *t.o.f.* are slightly higher from 1.125 inches CMD through 1.625 inches, then they were in the frictionless simulation shown in Figure #V-17. As expected, the changes are restricted to the CMD locations corresponding to the perturbations.

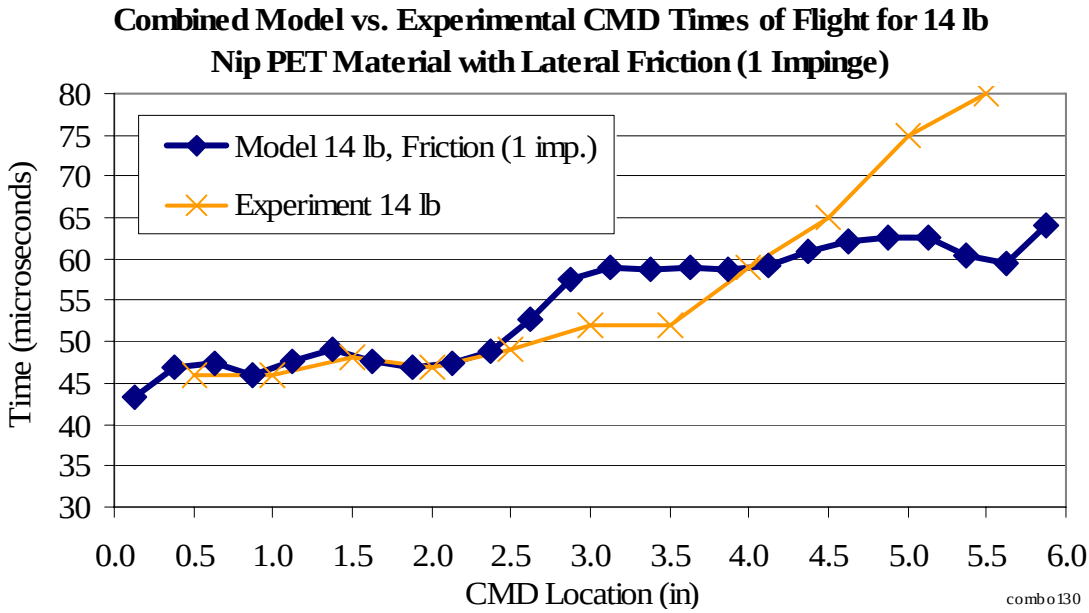

Figure #V-30: With the lateral friction included, the model's times of flight still match quite closely to the experimental values.

Combined Model NEWS Results

The combined model was next used to simulate a 14 pound, nip impinged NEWS paper. For simplicity and comparison, the web's dimensions, like width and relative CMD thickness variation, were chosen to match the PET. But, it was about six times thicker, and considerably softer in the radial direction. This mandated a reduction from 20 actual layers per model layer (20t) to 3t. The value of 3t was chosen because its results converged within 3% of a 5t test run. Table #V-3 lists its properties.

Parameter	Web
Thick	0.0028 in
Width	6 in
E_R	3.523*24.489+24.489*P psi
E_T	400000 psi
E_Z	400000 psi
$\nu_{\theta z}$	0.3
$\nu_{\theta r}$, ν_{zr}	0.01
G_{RZ}	697 psi
Layers	3 / model layer
Radius	4.914 in

Table #V-3: The NEWS material is thicker and softer than the PET.

In another test run, the shear modulus was set equal to half of E_Z, which produced radial pressures of approximately 25 psi. This yielded a new pressure dependent shear modulus of 697 psi (via Equation #III-14) to use in the actual runs. The NEWS friction values were all different from those for the PET. For example, μ_s went from 0.32 to 0.24. The machine setup however was assumed to be the same as for the PET, so all of the parameters listed previously in Table #V-2 still applied.

While it was not an actual web that could be experimentally verified, the stresses predicted throughout the roll exemplify behavior common to softer materials (compare to Hakiel [14, Figs. #2a, and #7]). As seen in Figure #V-31, the radial stress plateaus for much of the roll's radius. Because of the CMD thickness variation, the magnitude of the plateau varies across the width from about 20 psi on the left, to 16 psi on the right. Figure #V-32 presents the circumferential stresses in the NEWS roll. The region corresponding to the radial stress plateau contains compressive circumferential stresses. WOT was lost in the compression of the roll. The simulation performed four nip impingements during the wind.

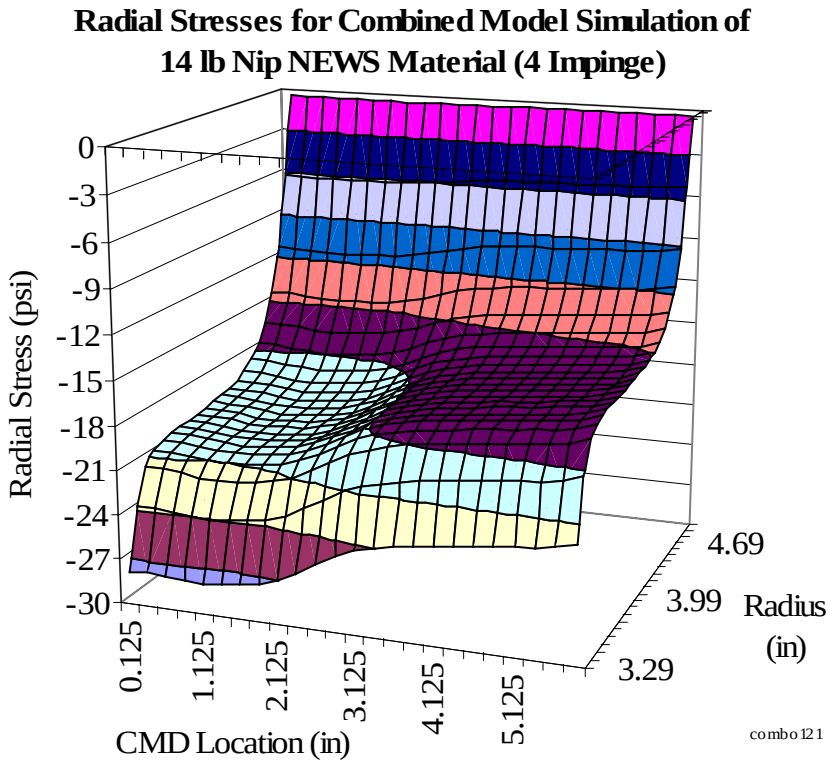

Figure #V-31: The radial stresses predicted by the combined model for 14 lb nip impinged NEWS roll, have a distinct plateau region, and CMD variation.

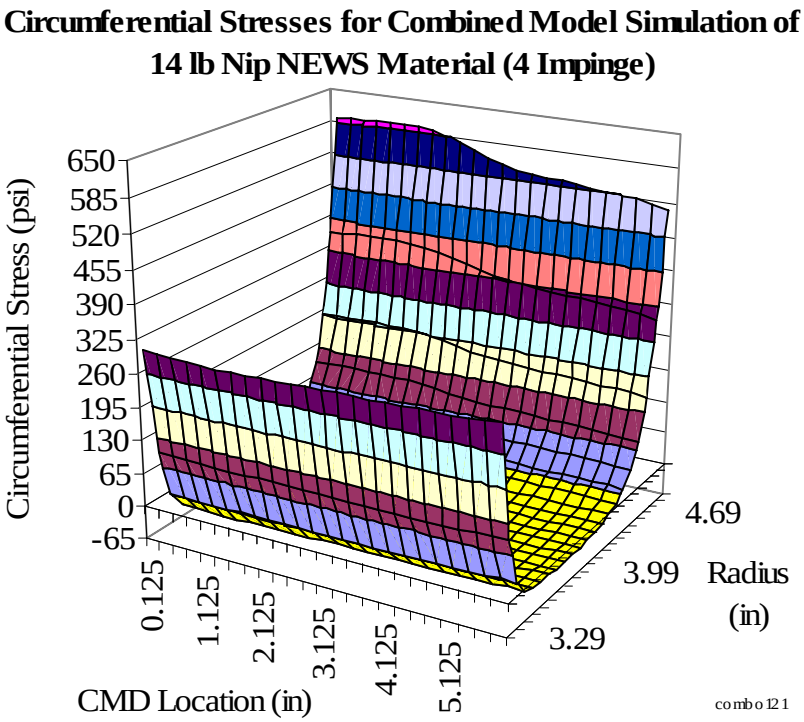

Figure #V-32: The 14 lb nip loaded NEWS roll's circumferential stresses are compressive for much of the radius.

The NEWS simulation was rerun with up to eight impingements during the wind, since the model encountered no multiple-impingement related instabilities. Each successive impingement responded to the roll's then-current configuration. Figure #V-33 displays the Load Per Width values across the width, at each impingement during the eight impingement run.

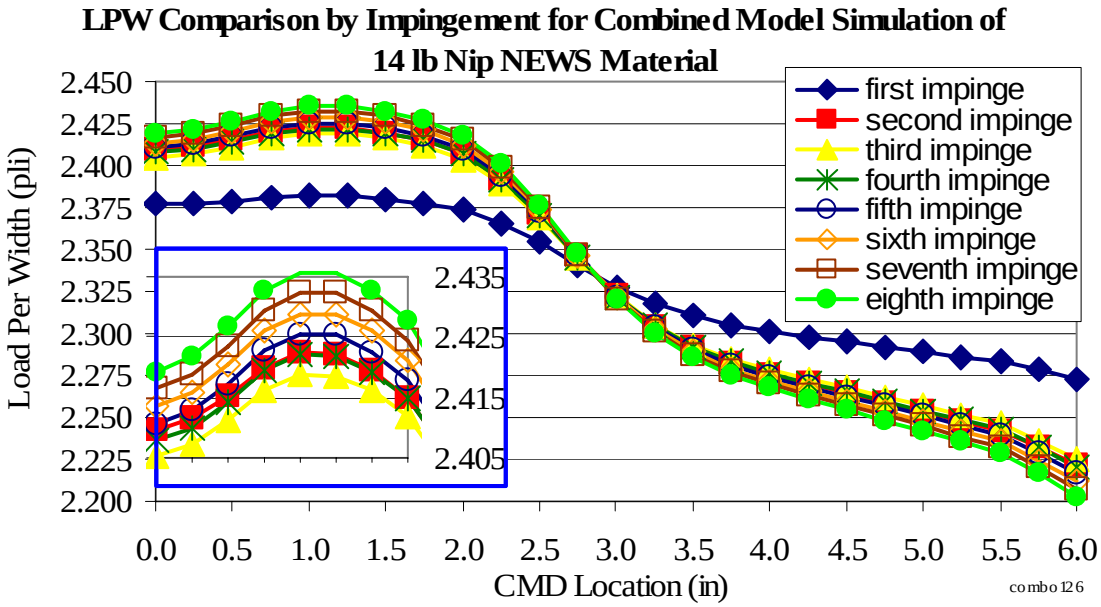

Figure #V-33: The CMD LPW values for the 8 impingement, 14 lb nip on NEWS change very little after the first impingement.

The first impingement's values are set apart from the rest, as the soft NEWS material undergoes its first compression by the increased nip tension. By the time the second impingement occurs, the Load Per Width values appear to settle to a consistent variation across the width. But, the "close-up" window in Figure #V-33 shows each impingement (with the exception of the second) progressively varies a little more across the width.

Next, the friction was turned on during the four, 14 lb nip impingement NEWS simulation. Figures #V-34, and #V-35, respectively display the resulting radial and circumferential stresses. They remain largely unchanged from the non-friction stresses.

Radial Stresses for Combined Model Simulation of 14 lb Nip NEWS Material with Lateral Friction (4 Impinge)

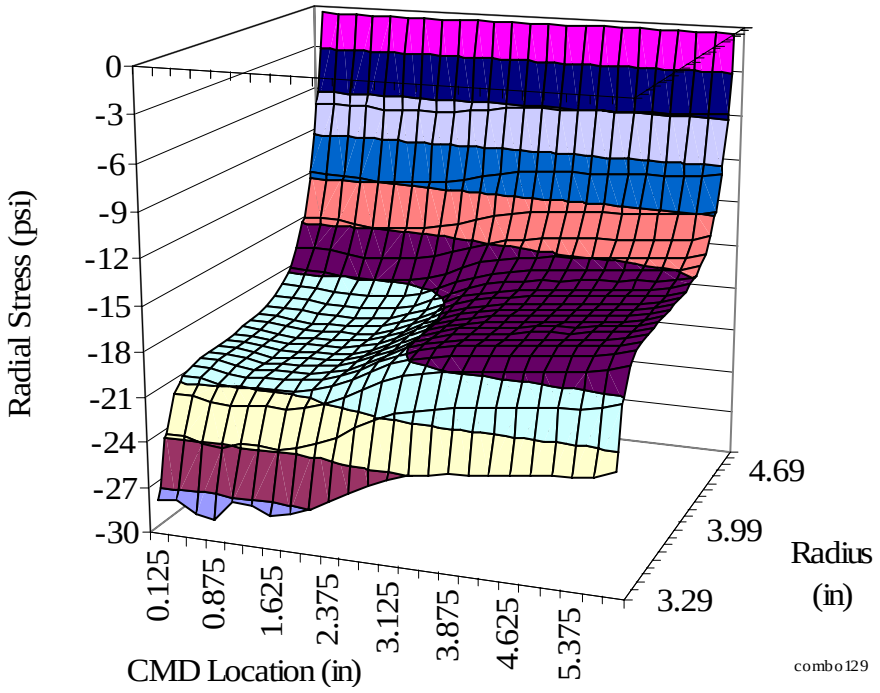

Figure #V-34: The radial stresses for the friction restrained,14 lb nip loaded NEWS roll show only a slight perturbation in the near-core values.

Circumferential Stresses for Combined Model Simulation of 14 lb Nip NEWS Material with Lateral Friction (4 Impinge)

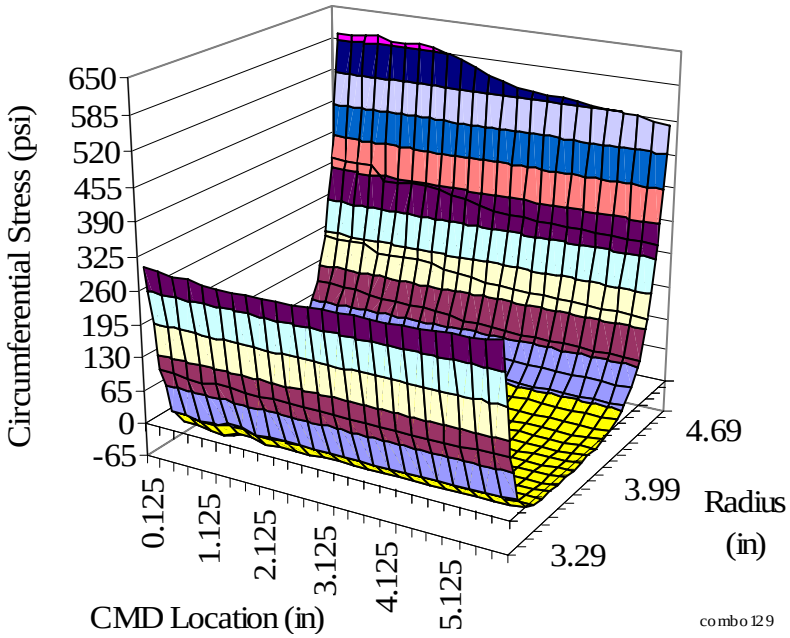

Figure #V-35: Turning on the lateral friction produced only minor changes in the 14 lb nip loaded NEWS roll's circumferential stresses in the outside layer.

Figures #V-36, and #V-37, give the lateral and shear stresses in the roll.

Lateral Stresses for Combined Model Simulation of 14 lb Nip NEWS Material with Lateral Friction (4 Impinge)

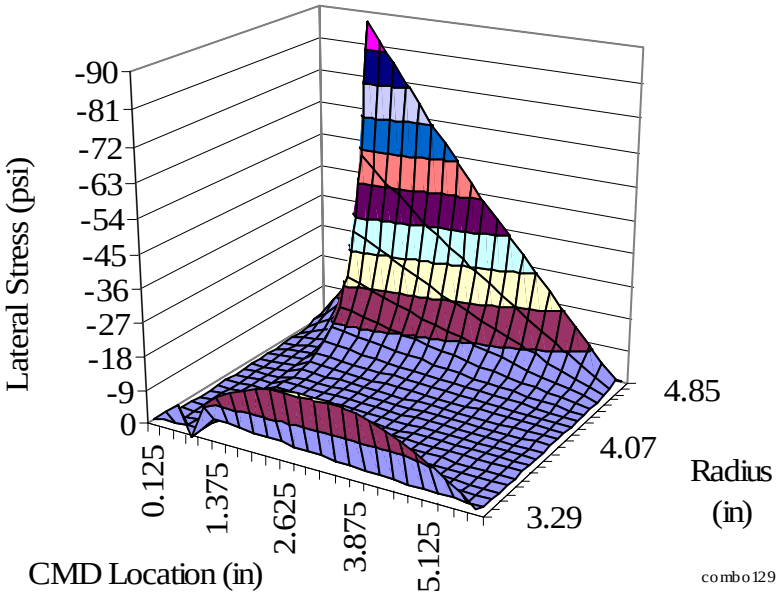

Figure #V-36: The lateral stresses in the friction restrained,14 lb, nip loaded NEWS roll, reach their minimum in the outside layer (note negative plotted up).

Shear Stresses for Combined Model Simulation of 14 lb Nip NEWS Material with Lateral Friction (4 Impinge)

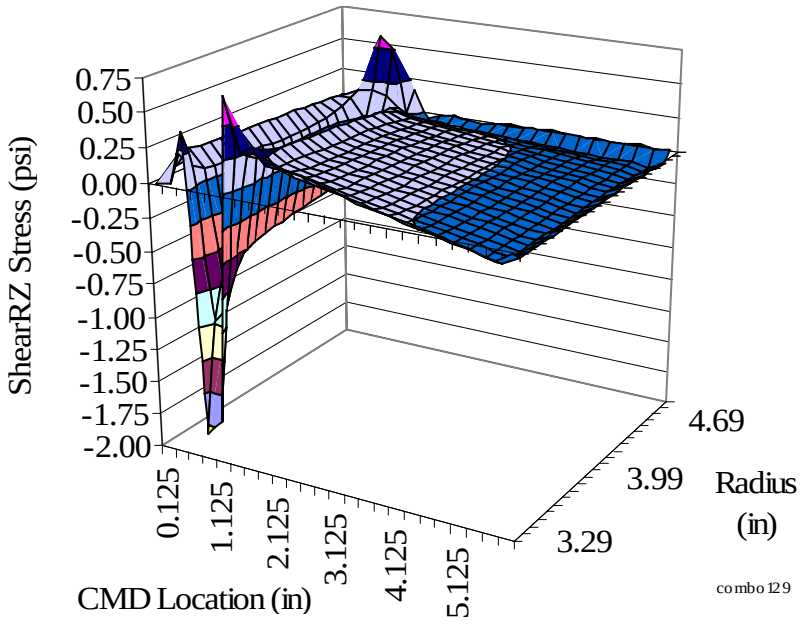

Figure #V-37: The shear stresses for the NEWS roll, subject to a 14 lb nip load, and lateral friction, concentrate along the laterally constrained CMD location, especially at the core.

The NEWS' lateral stress has a compressive peak in the outside layer, while the PET had a tensile peak next to the core. The friction coefficients primarily drive this behavior.

For further comparison's sake, the NEWS simulation was rerun with more layers per model layer, and also as a center winding equivalent. The first model rerun was with 20t, instead of the previous 3t, and thus required only 32 model layers to simulate the roll, down from 208. Its radii are plotted in Figure #V-38 as "4 Imp., 20t (adj)" against the one through four, and eight impingement simulations at 3t, and the four impingement, 3t, lateral friction simulation. As before, the "(adj)" notations in the Figure indicate the median CMD radii were adjusted to match the median radius of the "4 Imp., 3t" run. The radii across the width, for the 20t run, do not vary as much across the width as the 3t runs, and they hook downward at each edge. This indicates that the 20t model lacks the resolution through the roll's radius to adequately represent its behavior.

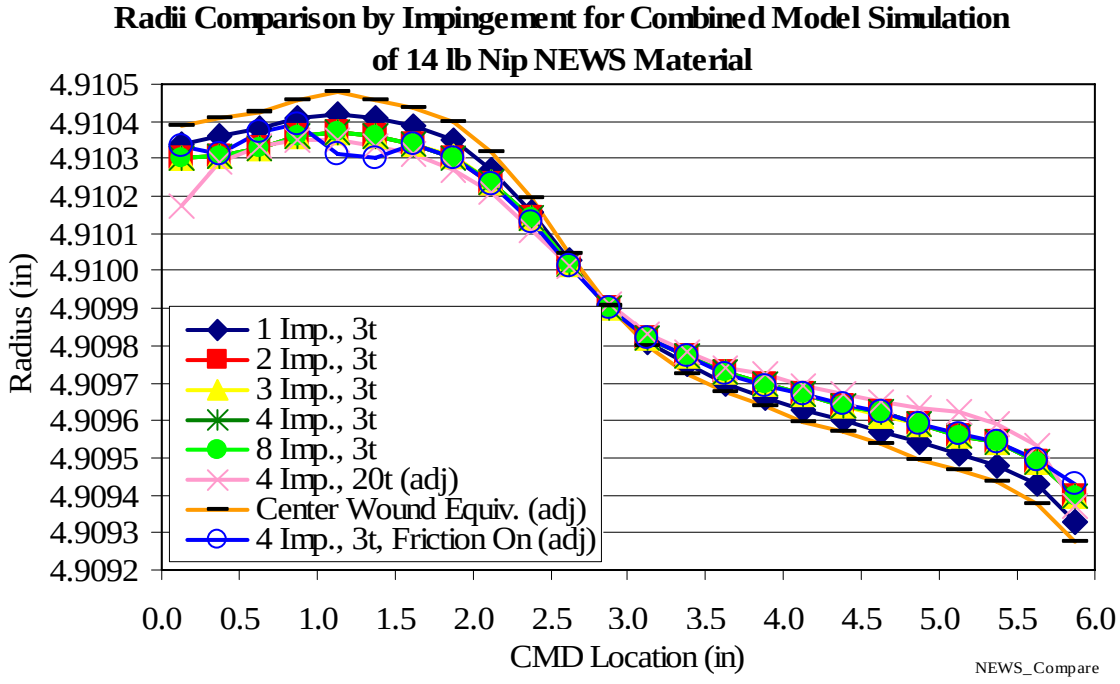

Figure #V-38: The cross width radii for the NEWS roll, under a 14 lb nip load, clearly show the nip roller reduces the radial variation across the roll's width, compared with an equivalently loaded center wound roll.

For the center wound equivalent run, the 14 lb nip load was converted from a net NIT of 0.56 pli, to web line tension. This brought the total tension equal to 1.56 pli. At this tension level, with 3 actual layers per model layer, the model wound 209 layers. When the center wound equivalent simulation's radii are also plotted in Figure #V-38, the nip's impact is clear. The radii are more uniform across the width when the nip is present.

The radial and circumferential stresses for each of the simulations have also been plotted against each other for comparison. Figure #V-39 contains the radial stresses.

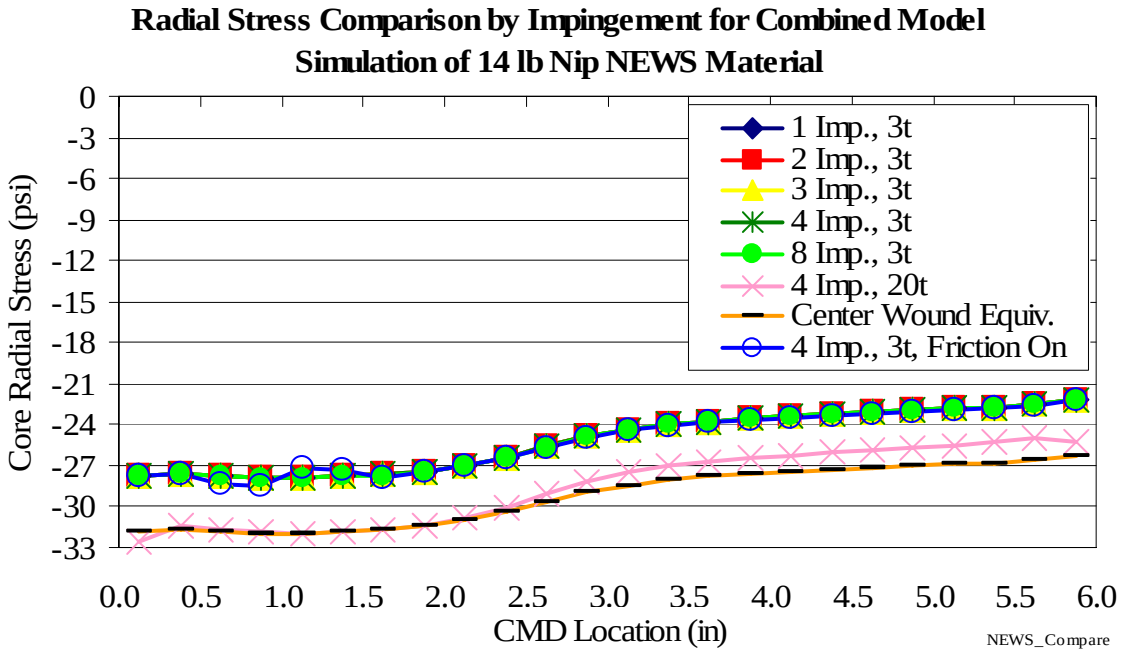

Figure #V-39: The radial stresses present at the core, for the center wound, and 20t simulations, are notably greater than the other 14 lb nip loaded NEWS runs.

All the 3t, 14 lb nip impingement simulations have similar core stresses. But, the 20t, and center winding equivalent runs, have about 10% more pressure across the width. Like the discrepancies found in the radii, the additional pressure in the 20t run is a result of the resolution used. The additional pressure in the center winding run is most likely due to the nip start radius of 3.339 inches used in the nip impingement runs. The center winding run had the 1.56 pli web line tension present from the onset of the simulation,

and therefore imparted more tension to the layers inboard of the nip start radius. Figure #V-40 plots the outer layer's circumferential stresses across the width for the various runs. Their close agreement indicates they are enforcing an equivalent amount of tension in each new layer as it winds on. The one exception is the 20t case. Its circumferential stress, and thus its tension allocation, varies more across the width than for the 3t simulations. Again, this is a by-product of the radial resolution associated with the number of actual layers per model layer.

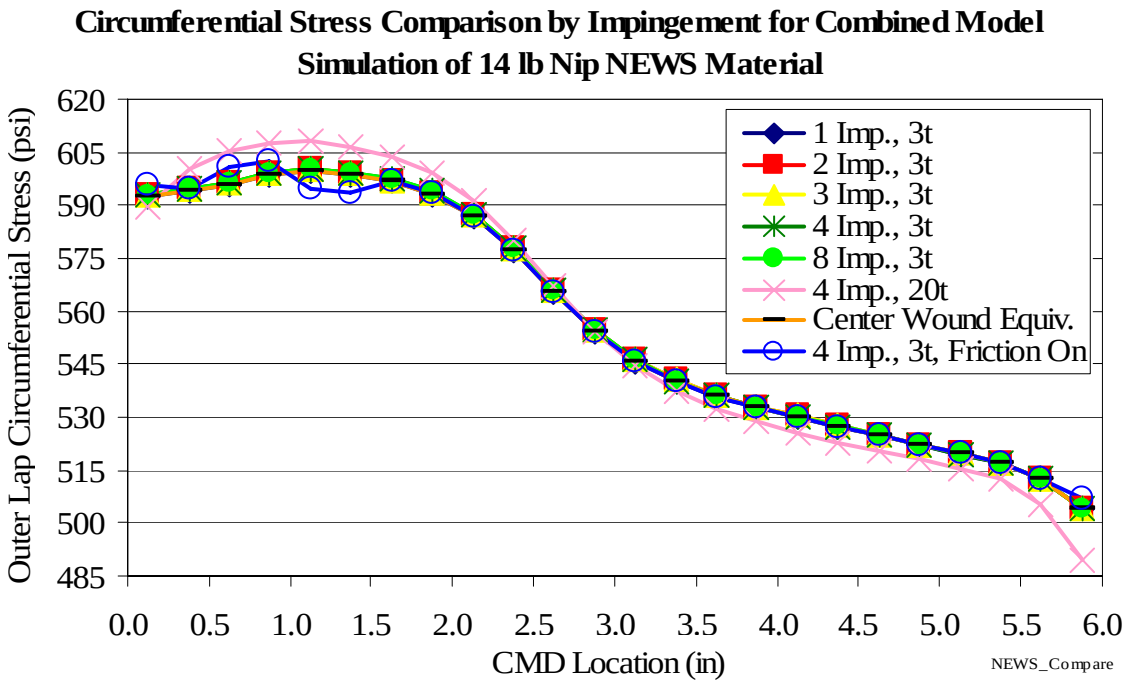

Figure #V-40: The circumferential stresses in the outer layer of the various 14 lb nip load, NEWS simulations, compare quite well, with the exception of the 20t run.

All three of the NEWS comparison plots show the lateral friction results falling away from the general trend, in the CMD region between 1.0 to 1.5 inches. During the combined model's development, the axisymmetric sub-model's lateral friction simulation instigated drastic, unbelievable fall-outs in the results. When the layers were instead allowed to freely slip by each other, by turning the lateral friction off, the results became

smooth and continuous. This, uncovered errors in the implementation of the nip impingement sub-model's convergence routine. When the errors were corrected, the combined model's convergence became significantly more robust in the presence of lateral friction. However, the presence of the lateral friction simulation still often produces regions which fall away, or have perturbations. Further study is necessary to determine if they are anomalies in the simulation, or actual phenomena present in the roll. But, it is interesting to note that the lateral friction results more closely resemble the general shape of the web layer's thickness profile, as seen back in Figure #V- 7.

Combined Model UCB Results

The combined model's dependence on the Load Per Width's CMD variation warrants further investigation into its cause. Both the PET, and NEWS, materials were based on the same thickness profile across the width, and its variation was the obvious source of the Load Per Width's variations in those simulations. However, the impact of the bending present in the winder's configuration has not been determined. For this, another roll simulation was conducted. The web was an intermediate stiffness material, Un-Coated Bond (UCB) paper, with a K_2 of 37.470. It was 48 inches in width, with a uniform thickness of 0.00416 inches. The web was wound onto a thick walled, 70 inch wide core made of Aluminum. Table #V-4 lists the web and core material properties.

The simulation was conducted twice, in order to compare two different nip rollers. While both had a 2 inch outer radius, and were 70 inches wide, their wall thicknesses and materials were chosen to give them different bending stiffnesses. The first was made of Aluminum, with a 1/16 inch wall, and thus its contact surface's inner radius equaled

Parameter	Web	Core
Thick	0.00416 in	0.375 in
Width	48 in	70 in
E_R	2.0196*37.470+37.470P psi	10000 ksi
E_T	926000 psi	10000 ksi
E_Z	926000 psi	10000 ksi
$\nu_{\theta z}$	0.3	0.3
$\nu_{\theta r}$, ν_{zr}	0.01	0.3
G_{RZ}	450 psi	4000 ksi
Layers	5 / model layer	3
Radius	6.00 in	4.00 in

Table #V-4: The simulations wound a UCB web with the above material properties.

1.9375 inches. The second was a considerably stiffer roller due to its steel material, thick 7/16 inch wall, and corresponding inner radius of 1.5625 inches. The simulations again used a 1.0 pli web tension. But, to amplify the bending across the width, the applied nip load was greatly increased to 384 pounds. The friction was: $\mu_s = 0.39$, $\mu_k = 0.37$. Table #V-5 gives the dimensions used for the simulations which refer back to Figure #V-16.

Dim.	Description	Value	Dim.	Description	Value
D_1	Wound Roll Radius	6.000 in	D_{11}	1/2 Nip C. S. width	30.00 in
D_2	Roll Inside Radius	4.000 in	D_{12}	Nip Contact Surface Radius	2.000 in
D_3	Core C. S. Radius In	3.625 in	D_{13}	Nip Insert Radius	var. in
D_4	Core Stub Radius	1.500 in	D_{14}	Nip Stub Radius	1.500 in
D_5	Core Insert CMD Thickness	3.000 in	D_{15}	Nip Load to Insert Distance	4.000 in
D_6	Core Support to Insert Distance	4.000 in	D_{16}	Nip Insert CMD Thickness	3.000 in
D_7	Zero to Core Support Distance	0.000 in	D_{17}	Nip Stub CMD width	7.000 in
D_8	Core Support to Roll Distance	11.00 in	D_{18}	Zero to Nip Load Distance	0.000 in
D_9	1/2 Web/ Roll CMD width	24.00 in		Nip Load Sep. Distance	70.00 in
D_{10}	Core Stub CMD width	7.000 in		Core Support Sep. Distance	70.00 in

Table #V-5: The UCB simulation's dimensions listed above include a 70 inch wide core and nip.

All of the output results clearly show the impact made by the nip's bending stiffness. As seen in Figure #V-41, the CMD Loads Per Width vary considerably more for the soft nip, than they do for the stiff nip.

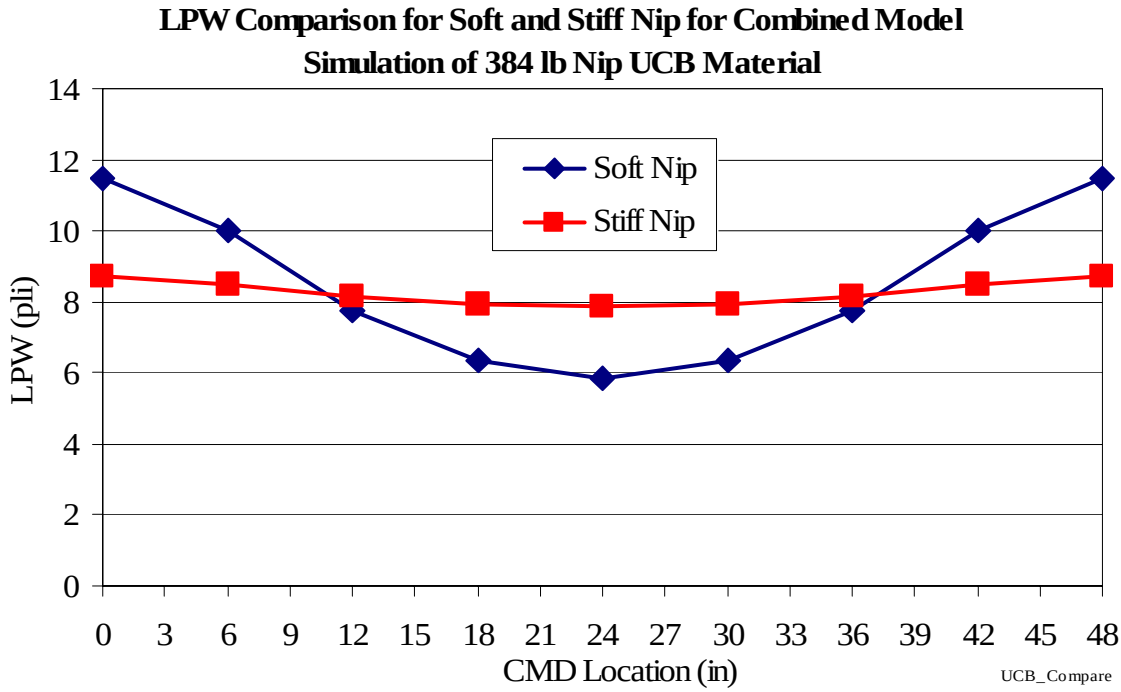

Figure #V-41: The 384 lb nip load produced an average LPW of about 8.4 pli, with the stiff nip varying 0.4 pli, and the soft nip varying 2.8 pli, from that average.

For both stiffnesses, the nip's bending causes it to distribute more of the applied load towards the UCB roll's ends. The result is higher NIT at the ends, and higher radial and circumferential stresses there too. This is evident in Figures #V-42 and #V-43.

But, the radial and circumferential stress variations across the width are smaller than expected. For example, Equation #II-33 leads us to believe the expected change in circumferential tension will be 489 psi, not the 6 psi witnessed. That is, with the LPW change of about 11.5 pli at the ends, to 6 pli at the center, the corresponding change in the NIT should be 2.035 pli (5.5 pli*0.37). Dividing by the web's thickness produces the expected 489 psi change in circumferential tension in the outer layer. Indeed, Figure #V-

44 shows the LPW, and the total WOT, do vary considerably across the soft roll, but this only occurs at 4.26 inches in radius.

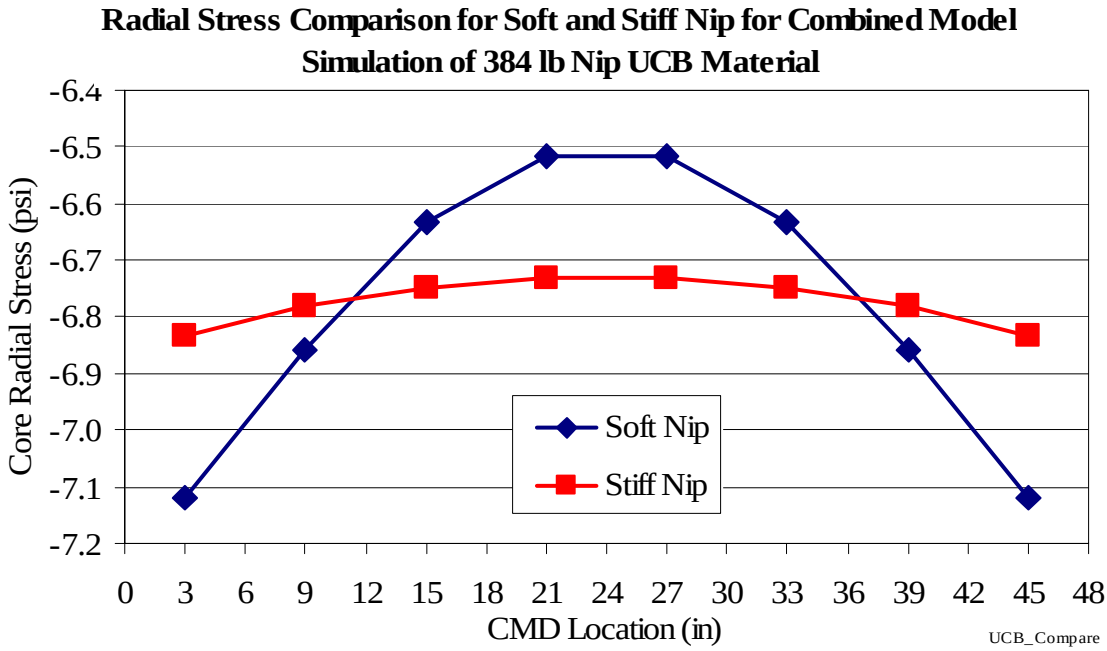

Figure #V-42: The core radial stresses produced by a soft nip, on a UCB roll, peak 4% higher than for a stiff nip, and vary over 9% across the width.

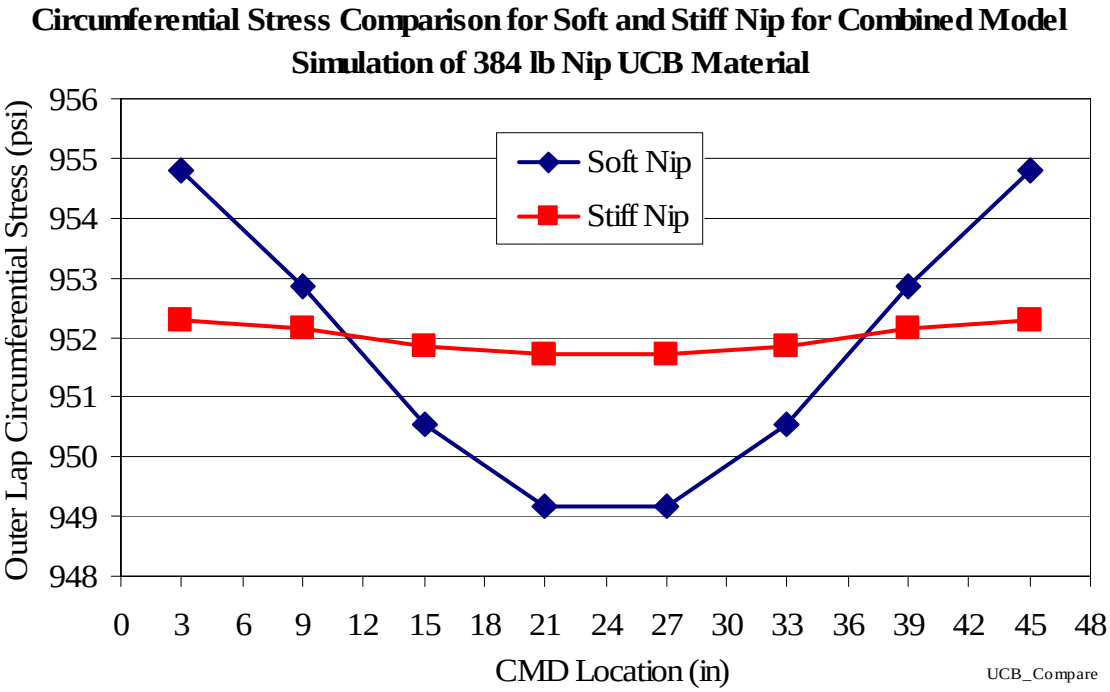

Figure #V-43: The CMD variations, in the circumferential stresses, are clearly affected by the stiffness of the nip.

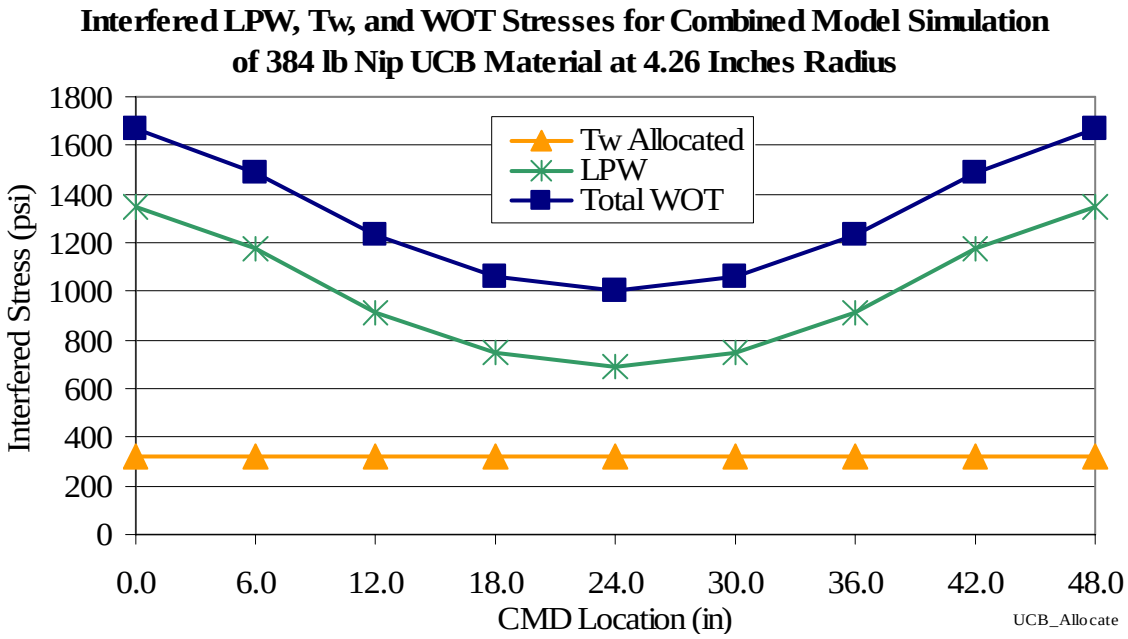

Figure #V-44: The LPW, and the resulting total WOT, vary considerably across the UCB roll's width, when the nip is first impinged at 4.26 inches in radius.

The reduced CMD stress variations are caused by a variation in the radii across the width. As the nip impinges the roll, its bending induces them. Figure #V-45 plots the radii at the outside of the UCB roll, for both simulations.

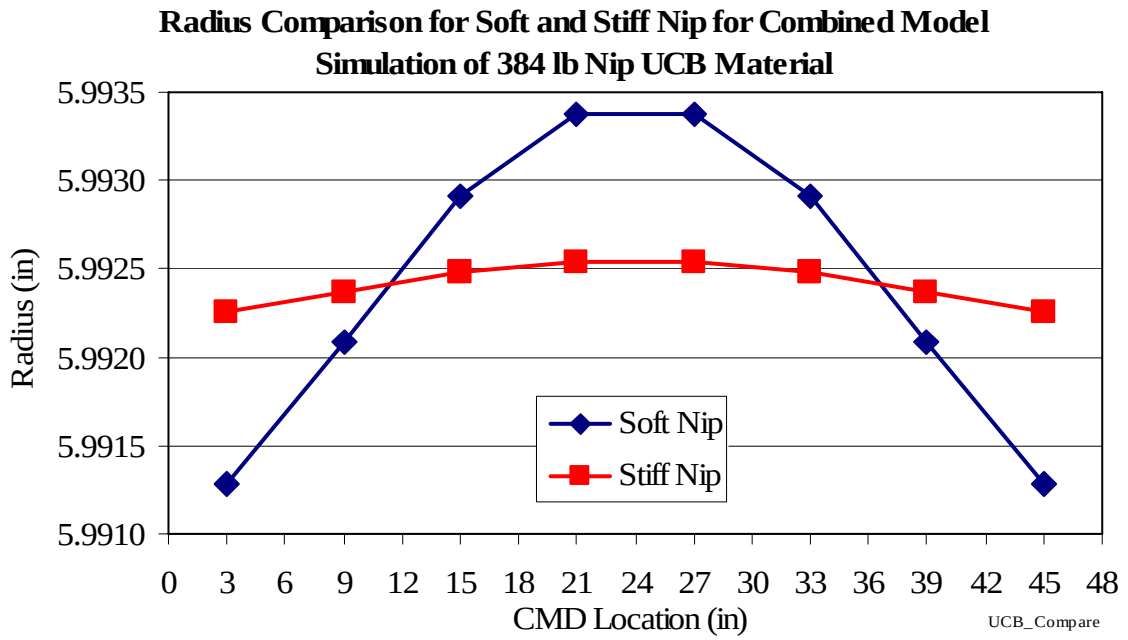

Figure #V-45: The radii across the width of the UCB roll are considerably different depending on the nip's stiffness.

Because the web line tension still allocates out in proportion to the roll's local radius, the radial variations result in a non-uniform T_W distribution. As the roll accretes, the radial variation across the width grows, as does the T_W non-uniformity. Figure #V-46 shows the allocated web line tension, for the soft roller, at 4.77 inches in radius, varies greatly across the width.

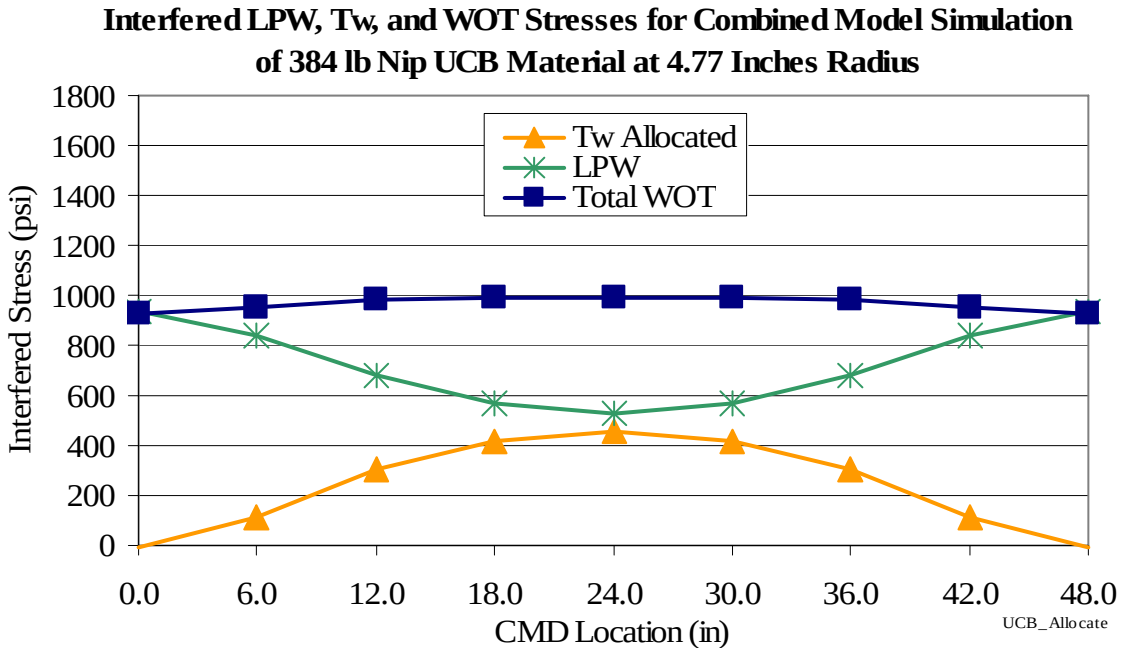

Figure #V-46: At 4.77 inches in radius, the UCB roll's T_W allocation has concentrated toward the center, and counteracts much of the LPW distribution.

Eventually, the LPW variation produces a radial variation, that itself produces a web line tension distribution, sufficient to totally counteract the LPW. This is true in the soft nipped UCB roll, at 5.77 inches in radius, as evidenced in Figure #V-47. By then, the net WOT in each new layer has only a small variation. All of this happens despite the web being perfectly uniform in thickness across the width.

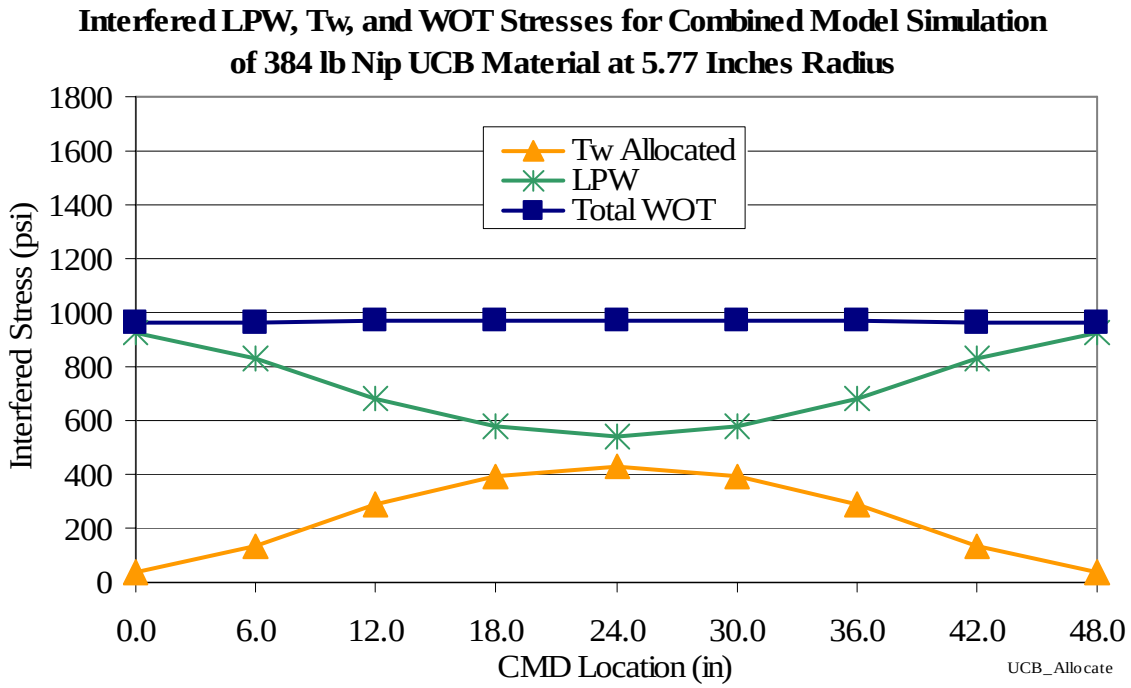

Figure #V-47: When the UCB roll reaches 5.77 inches in radius, the T_W allocation counteracts the LPW distribution resulting in a nearly uniform total WOT.

It is important to note a few things about the values plotted in Figure #V-44, #V-46, and #V-47. They are not the actual WOT stress, or its components. They are conversions of the strains, calculated as the values necessary to produce the desired circumferential stress, in the outer layer. Inside the axisymmetric model, they are further manipulated to compensate for the roll's compression, and used to determine the interference of the new outer layer into the roll. To this end, they are nodal values, not elemental, and they represent the inside surface of the outer layer, not the middle. Thus, they can not be compared directly to the circumferential stresses in the outside layer.

The effects of this changing WOT can be seen in Figure #V-48, which shows the completed roll's circumferential stresses. They retain a compressive spike, with a sharp CMD variation, at the radius where the nip was applied. Then they become uniform across the width for the remainder of the roll, and rise to be tensile toward the outside.

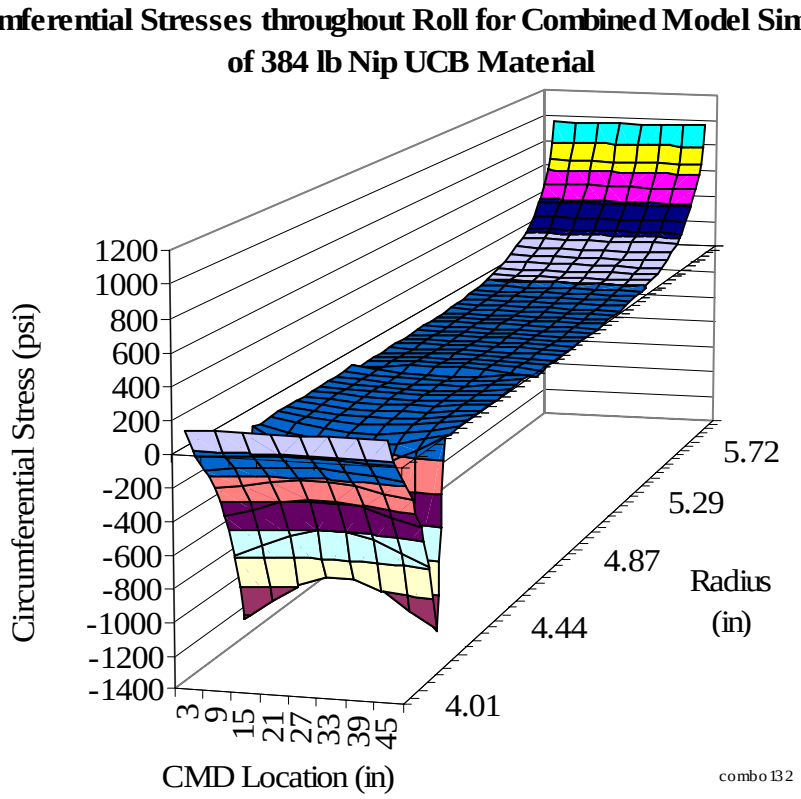

Figure #V-48: The UCB roll's circumferential stresses become quite uniform across the width as the wind proceeds past where the nip impinged.

Limitations

Both the axisymmetric and the combined models are sensitive to variations in the applied tension across the width. They can be induced to yield unexpected results. If the variations are too large, they generate tensile radial stresses in elements inside the roll. If these elements are instead allowed to gap, the axisymmetric sub-model often seems unable to converge the segment tensions to the WOT. While both models usually can handle the tension variations that result from thickness based, tension allocation, the tension variations of concern are the free-span web line tension, and the Load Per Width tensions calculated from the nip impingement. When these variations are large enough to

generate tensile radial stresses, the nip impingement sub-model's calculations become more erratic. This can lead to the whole simulation becoming unstable.

The model's sensitivity was discovered to be material dependent during the first simulations, which were on the PET web. Changing parameters such as the radius of first impingement, layers per model layer, minimum allowable E_R, and applied load, all proved ineffective to stabilize the model. The same was true for other convergence schemes. Whenever there was more than one impingement, the results were unbelievable. But, when simulations were performed with the NEWS, and UCB webs, the model showed no problems with multiple impingements.

To avoid tension variation sensitivity, the user must exercise some judgment during each simulation's set up. No matter the material used, they should select an initial impingement radius that is early in the wind; it should be fairly close to the core. Next, the user should pick a ΔR trigger that will initiate three or four more impingements during the wind. Then they should run the simulation. When it is finished, the user can inspect the output LPW values for any obvious irregularities including large variations in the LPW, or even negative values. If irregularities exist, the simulation should be rerun, but with only one impingement. (This is accomplished by using a ΔR trigger larger than the desired pile height.) Such requirements may seem to be a limitation of the combined model. But, the fact that the model compared well to experimental results shows that they are necessary and sufficient. There is no need to have additional impingements throughout the wind for sufficiently stiff webs.

In the event simulations conducted using the model don't accurately match experimental values, there are a few assumptions that can be investigated. One such

assumption relates to the accuracy of the bilinear thickness profile representation (discussed in chapter III). It can not perfectly represent an actual thickness profile, unless the actual thicknesses vary only linearly across the width. The difference between the representation, and the actual profile, can be minimized though. First, the thicknesses must be sufficiently sampled in the CMD. Second, the segments should be narrow wherever there are rapid thickness variations in the profile. Finally, a segment should be placed in the center of every peak or valley. This will help the mesh averaging to capture the extrema.

Similarly, the axisymmetric sub-model, and thus the combined model, assumes the CMD variations in thickness persist throughout the wind. There is no accommodation for the variation to change in the MD. The validity of this assumption depends on the manner in which the thickness profile was obtained. The profile presented in chapter I, from Cole and Hakiel [4], was an average of thickness values taken throughout the entire length of the web. Similarly, the PET profile used here was an average of the CMD radii of the finished wound roll. Both averaging methods should have effectively discarded minor fluctuations in the thicknesses. If however, the profile was measured at only one location along the length of the web, it has a high likelihood of error. With the combined model's dependence on the thickness profile, its accuracy (along with the radial moduli) is important to the success of the simulation.

Another assumption is inherent in the beam formulation. It utilizes a constant moment of inertia along the length. This is significant, because it requires that the y dimension must remain constant. Of course, since the beams are used to represent the cylindrical nip, core, and foundation, y is their radii. Thus, the formulation mandates their

radii can not vary along the element length, and is a single, distinct value for each element. This proved somewhat problematic in dealing with the three dimensional foundation, as it required numerous conversions between elemental and nodal values. The most significant was when a nodal deformation had to be disbursed to its two elements in common, when they had a discontinuous radius between them. This presented numerous instances of ambiguity, and required additional contingencies to resolve what the true behavior should be.

There are a few reasons this approximation was not changed for this work. First, finite elements are not exact representations of the structures they represent, but are by their very nature approximations. Whenever performing a simulation then, it is considered acceptable to simply decrease the mesh size, thus increasing the number of elements, and reducing the likely error. The corresponding average modulus and moment of inertia reasonably represent the actual behavior. And, in most structure simulations, the actual radius value is not important. Second, the original nip impingement model (Hoffecker [17]) served as the basis for the engagement model used here. It did not have a three dimensional roll foundation, and thus the beam elements were sufficient. Only when the radii could vary along the length due to roll accretion, and not to beam bending, did this become an issue. Thus to save effort, and utilize the earlier work, the original model served as the basis for the combined model. Third, the difficulties encountered were largely unforeseen. As the project progressed, the shortcomings slowly accumulated to a point that they are identifiable as worthy of further investigation, but were not thought unreasonable during development.

Two possible ways to improve the model's accuracy, and ease the roll simulation, change the type of beam element used during the nip sub-model. First, at least the foundation elements would likely benefit from the application of a tapered beam element. Instead of having a constant radius along the length of each element (as in chapter IV), it could vary linearly. Such would be derived by making y a variable in the strain energy expressions of chapter IV. The resulting tapered elements would have the same order as, and thus agree better with, the axisymmetric elements because they would both be linearly varying on the top edge. This would eliminate the ambiguity between nodal and elemental properties. The taper would also reduce the number of necessary CMD elements, and the corresponding simulation run times. A second approach would be to instead isolate each beam foundation element from its neighbors. More specifically, each element across the width would have its own nodes, which would not be shared, or in common, with the adjacent elements. The cross width continuity would instead be maintained through additional degree of freedom links. The advantage here would be to provide each element with the identical radius to each of its nodes (not an average of them). It would thus retain its own separation distance (nip to winkler), its own contact status, and a more independent radial deformation. One drawback would be the increased solution time required to solve the resulting larger stiffness matrix.

The foundation's mesh size is a user controllable assumption. Decreasing it usually is a viable way to improve accuracy. But, it requires more elements across the width, meaning more computation time. Plus, the beam elements in the nip impingement sub-model have to have the same widths as the axisymmetric elements. While the chosen

mesh size may work well for one sub-model, it may be insufficient for the other. The user must be cognizant of these considerations and balance out accuracy versus run time.

The error in the PET thickness profile, due to its measurement being performed while the roll was compressed (see page #V-16), is somewhat mitigated by an inadvertent coincidence. When a layer is meshed into the axisymmetric FEM, its assigned thickness is that of the profile. As the layer moves out radially, to resolve the interference, the resulting circumferential stress should neck the profile down via the Poisson effect. (The same is true for the web's width.) However, web handling literature states $\nu_{\theta R}$ is difficult to measure, and bears little consequence on model results, so it is usually set very small (see Good [9], and Hakiel [14]). This makes the resulting thickness change very small.

The axisymmetric, three dimensional wound roll model assumes the incoming web has negligible MD bending stiffness. But, many web handlers wind thicker webs made of higher modulus materials whose bending affects the winding outcome. The bending stiffness in the CMD influences how the roll's layers will shape themselves over radial variations across the width. This too, likely affects the web layers per model layer necessary to accurately simulate a wound roll, as discussed in chapter III. In the MD, the bending stiffness causes the flat, free-span web to resist bending into a coil as it enters the roll. According to Edwards [6], the process of coiling into the roll draws energy from the web line tension, and thus reduces the tension available inside the roll. He suggested an expression to adjust the incoming web line tension, which is modified for consistent nomenclature, and seen here as Equation #V-7.

$$T_W = m_{eff}\frac{V_A I_A}{V_0} - T_{fb} - T_{fI} \qquad \text{(V-7.}$$

In this expression, T_W, T_{fb}, and T_{fI} are the web's tension in the line, lost to bending, and that due to inertia, respectively. They are all in force units. (For the expressions used to determine T_{fb}, and T_{fI} , see Edwards[6].) The other variables are the drive motor to the mandrel shaft's electrical energy conversion efficiency, m_{eff}, the armature voltage and current, V_A and I_A, and the web's velocity, V_0. Edwards' tension force lost to bending is given (in modified form) as Equation #V-8.

$$T_{fb} = \sigma_y w \left[\frac{t^2}{L_{MD}} - \frac{R^2}{3E} \right] \qquad \text{(V-8.}$$

The expression uses the material's yield stress, σ_y, and its free-span, unsupported MD length, L_{MD}. Adding these two equations to the model, would help it accommodate thicker webs.

Meshing multiple axisymmetric elements through the web's thickness would improve the model's bending stiffness simulation. As mentioned in chapter III, this is already done for the core, because it is often at least a quarter of an inch thick. But, the thinness of most webs required a maximum of one quadrilateral finite element be used for the web's thickness. Additional elements in their thickness direction could have produced a thickness to width aspect ratio beneath the limits necessary to maintain a proper representation of linear elastic behavior. For thicker webs (with a correspondingly larger aspect ratio), multiple elements through the thickness would better capture the CMD circumferential stress variations that result from bending. Both the web line tension adjustment, and the multiple radial element mesh, could be implemented to expand the model's capabilities.

Another limitation is that the nip's angle of incidence to the wound roll, coupled with its bending, may inadvertently produce axially directed loadings. However, during

the nip sub-model's development in chapter IV, the angle and bending necessary to produce a significant horizontal, axial component were believed greater than would be usually encountered. If an investigation revealed their magnitudes are significant, the nip elements could be modified to contain an additional axial formulation. It would convert the beam elements into frame elements with three degrees of freedom per node.

CHAPTER SIX

CONCLUSIONS

Project Objective

The Project Goal section of Chapter I, and the Project Method discussion in Chapter II, defined this work's research objective to be the development of an accurate, three dimensional, nip contacting, wound roll model. To reach this objective it was thus necessary to first develop separate three dimensional, and nip impingement roll models. These separate models required investigations into equilibrium, thickness variations, and dominating mechanisms such as tension allocation, wrap angle, gapping, and wrinkling. Then, they had to be combined together into a versatile model capable of various roll, core, and nip configurations. Finally, the model had to match experimental results. Only then could the model be considered to be a tool for predicting, and improving the quality of wound rolls in industry.

Project Conclusions

- The three dimensional wound roll model developed as part of this work, is one of the most extensive, and accurate, known to exist. As discussed in chapter III, it utilizes axisymmetric finite element shells to maintain equilibrium, allocate tension, and incorporate thickness and stiffness variations, all in the CMD. Additionally, its versatility was proven, and its accuracy verified, in multiple close comparisons against two and three dimensional experimental data.

- The combined nip impinged, three dimensional, wound roll model is a significant step forward in wound roll simulations. This is true because it is the first, and only, model known to incorporate the CMD compression, and load distribution, effects resulting from nip impingement. And, this is true because its comparison to the 14 pound, PET experimental data in chapter V wasn't just close, it was excellent.

- The combined model can be a valuable industry tool when used to improve the quality of webs, or their wound rolls. As done throughout chapter V, individual parameters up through multiple configurations can be altered, and compared, making it both usable, and versatile. It is accurate, yet expandable to accommodate future research. And, it runs on a personal computer, which makes it readily accessible to web handlers, without interrupting actual web production lines.

Future Work

In chapter V, the combined model's validation compared it against experimental data for the six inch wide PET web only. This is sufficient to show its relevance, and verify its methodology, but it does not guarantee the model's universality. Before industry web handlers can rely exclusively on the model's results, additional materials, CMD thickness profiles, and nip load levels, should be assembled and conducted experimentally. They must then be simulated, and compared against the experiments. The similarities, and the discrepancies, will characterize the model's application.

Not much attention has been given here to the CMD displacements or stresses. This is because radial and circumferential results make up the bulk of the literature available for comparison. Only now, with the combined model, can the CMD effects be investigated practically. The user can try different materials, properties, and thickness variations, and then scrutinize the resulting stresses to verify they don't exceed known limits. For example, the CMD shear between layers is especially useful for web handlers who apply adhesive to their webs. It tells them if the adhesive will flow out of the ends.

Dr. Keith Good, Director of the WHRC, has already used a modified version of the axisymmetric, three dimensional model to explore CMD stress effects. The first modification eliminated the lateral constraints beneath the outer layer as it came onto the roll. As a result, the web contracted laterally as it necked from the web line tension. The second modification stuck the rest of the roll body together throughout the wind. This made it possible to examine the lateral stress interaction between layers, as a function of web width. (Both modifications would prove useful as future, user-selectable options.) Using the modified model, Dr. Good compared the stresses in four different width webs

against those from a two dimensional roll model, “WINDER 6.3”. Figure #VI-1 shows the radial pressure at all widths compared closely to the two dimensional results. For the webs 18 inches and greater in width, the plateau pressure drops about two psi below the 6 inch web’s pressure, and converges at 30 psi. At the same time, the core pressure rises about 5 psi and converges around 50 psi.

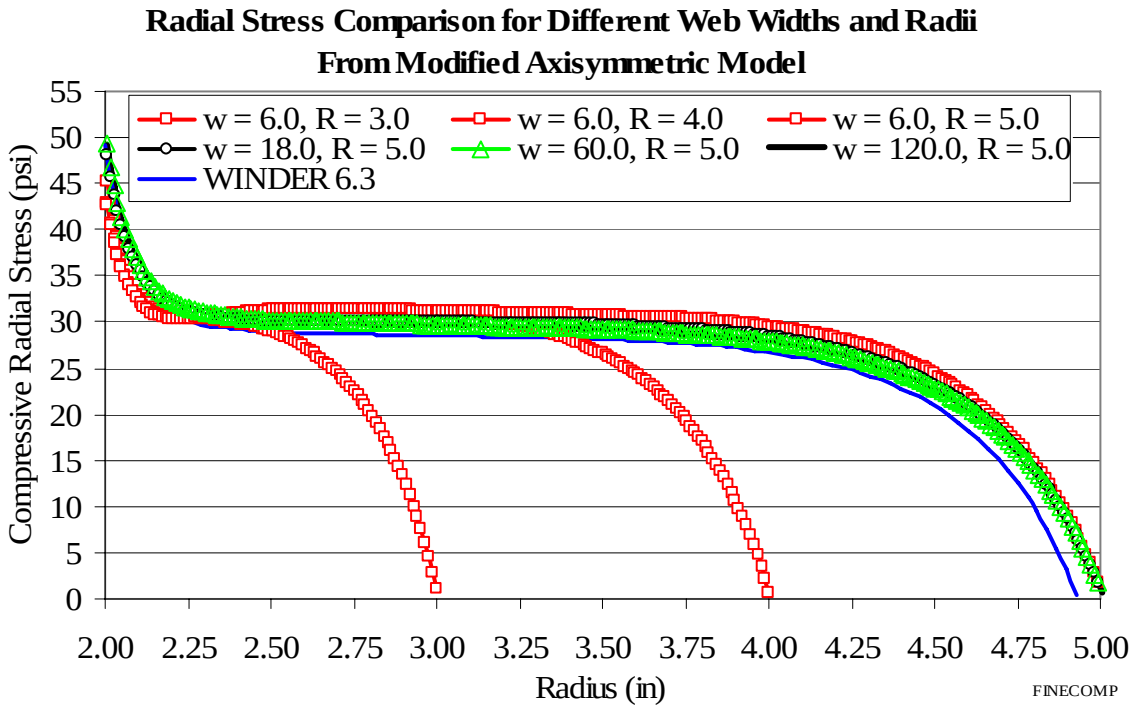

Figure #VI-1: The radial pressure plateau is nearly independent of web width and the wound roll’s final radius.

Figure #VI-2 displays similar behavior for the circumferential stresses. The 18 inch wide web has not quite converged to the two wider ones, but it is much closer than the 6 inch web. In fact, the 6 inch web remains in tension throughout the roll, while all the other webs experience compression for much of their radii. The wider webs are actually converging to two dimensional behavior. They have less edge related effects, and thus behave closer to a plain strain idealization. The roll’s radius is shown to make little difference on the circumferential stress results.

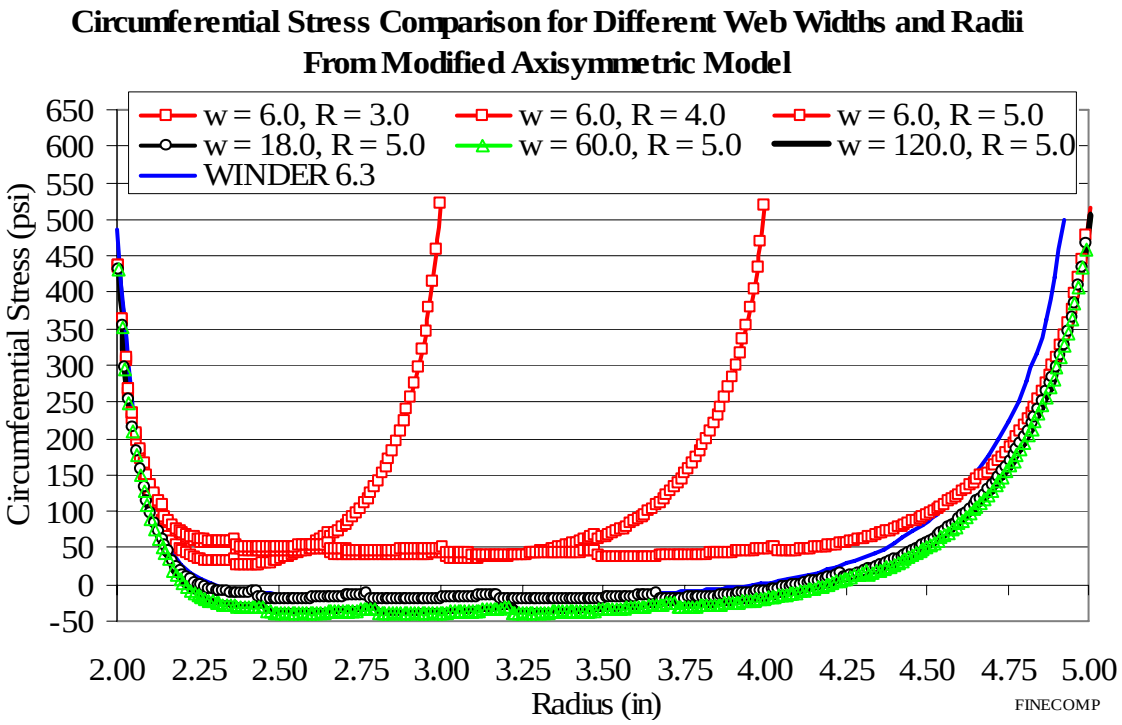

Figure #VI-2: Wider webs relax their circumferential stresses more.

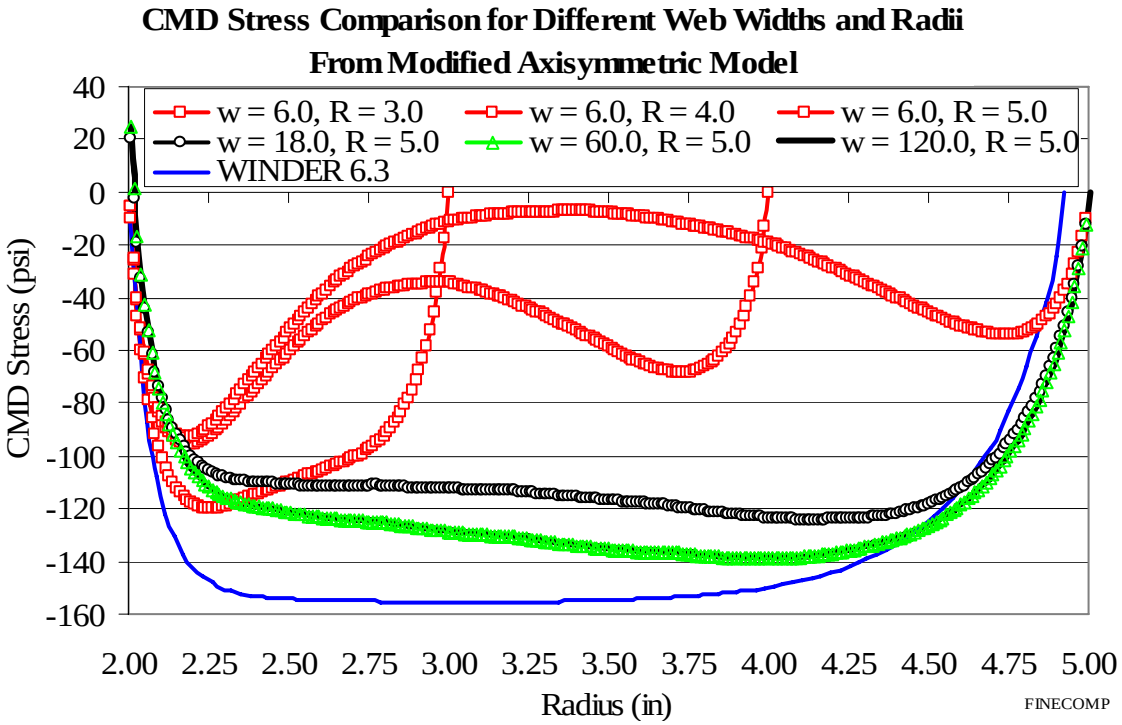

Figure #VI-3: Wider webs approach plain strain behavior and can develop significant CMD Stresses.

Figure #VI-3 plots the CMD stresses in the various width rolls against the results from the two dimensional model, WINDER 6.3. Because the two dimensional roll model does not even address lateral stresses, they must be calculated afterwards from the Equation #VI-1.

$$\sigma_{ZZ} = \frac{\nu(\sigma_{\theta\theta} + \sigma_{RR})}{E} \qquad \text{(VI-1.}$$

There is much more independence between the lateral stress results, then for the radial and circumferential. It isn't until 60 inches in width that they converge. It is also interesting to note that the axisymmetric, wide web results achieve about 25 psi tension at the core, whereas the two dimensional results only reach zero psi. This shows that there are tensile, CMD stresses, previously unaccounted for, that can rip the core apart. Also evident is that wider webs develop significant compressive CMD stresses in the roll body. They have more lateral traction capability.

Many of the imbedded algorithms can be easily updated in the future to accommodate new research as it becomes available. The NIT allocation can be made to be torque dependent. Surface winding can be discriminated from center winding. And, combinations of the effects on WOT from wrap angle, sub-regions of stick and slip, and gapping can be included. The WHRC is currently investigated these concepts, and has determined that there is a traction capacity beneath the nip that controls how much NIT can be built up. In fact, the NIT saturates and becomes independent of the applied nip load. This begins to explain why the *t.o.f.* data matched so well to the experimental values for the 14 pound impinged PET in chapter V, but not so well for the 30 and 40 pound cases. The combined model utilizes the simplistic μN term for NIT, from

Equation #II-33. When more sophisticated versions are available, the model should capture the behavior at the higher loads even better.

Further investigation would be necessary to determine the definite cause, and to find a solution, to the occasional stability limitations expressed in chapters III, and V. A primary suspect is the interference of the outer layer into the simulated roll, to impose the desired tension. It constricts the roll, and simultaneously produces a varying expansion across the width of the outer layer. In contrast, an actual roll's outer layer does not expand outward. It is wound on at its maximum radius, and only cinches inward during the rest of the wind. The interference may create the instability, because a large variation, across the width of the thin shelled outer layer, may exceed linear continuity limits between adjacent four node quadrilaterals. If so, one option would be to simply refine the mesh in the instable locations, and rerun the model. This would likely stabilize one simulation, but each subsequent simulation would require different refinements. Another approach would be to utilize a more advanced axisymmetric element that allows strain to vary non-linearly across the element. The additional degrees of freedom would require adjustments to the gapping criteria, and would slow down computation time however. If linear continuity limits aren't the source of the instabilities, the interference method of tension enforcement could be replaced. An initial strain method alters the stress formulation by subtracting off a value from the strain expression, Equation #III-10 (temperature fluctuations are often handled in this manner). Because the initial strain is in the circumferential direction, its value would be in the fourth row of the $\bar{\boldsymbol{\varepsilon}}$ vector, as discussed in conjunction with Equation #III-13. The result would be a constant term that adjusts the value of the strain energy expressions (Equations #III-11, #III-12, and #III-

15). And, for all intents and purposes, it ends up becoming an adjustment to $\overline{\mathbf{F}}$ in the linear system of Equation #III-19. With the fewer degrees of freedom required, an added benefit to this method should be a reduced computation time.

A separate effort underway at the WHRC, is to validate the model's lateral stresses. First, webs are center wound without a nip roller, and their lateral stresses are measured experimentally. Then the properties and roll configuration are input to the model. The model's results are then compared back against the measured values. The comparison will aid in improving the model, and better characterizing roll behavior.

Another future improvement would be a more accurate determination of G_{RZ}, during each simulation. It is a material dependent parameter originally treated as a material constant, because its isotropic form, $G = E/2(1+\nu)$ [5, Eq. #ζ.8], uses constants. It was thus coded into the axisymmetric sub-model as an input. But, since its experimental values were not available during the simulations in chapter III (nor for the PET in chapter V), and since ν is very small, it was often approximated around $E_T/2$. Then Equation #III-14 was discovered; it portrays G_{RZ} as a radial-pressure dependent variable. This changed the approach used for the remaining two simulations in chapter V. The model was run with an initial value, and the radial pressures were then used to determine G_{RZ} in a rerun. If it indeed is a pressure dependent parameter, it may be more accurate and efficient in the future to insert the G_{RZ} expression directly into the combined model, and allow it to be determined during the simulation.

In fact, the nature of webs makes G_{RZ} an elusive parameter. Their cross section is so thin that there is no practical way to apply loads to it, or to measure the shear, to determine its experimental value. When inside of a roll, its thinness may actually keep its

lateral load differential, from top to bottom, too small to shear it. Thus, it may be valid when simulating wound rolls, to assign it a large value, so the model doesn't shear it. Another possibility might be to instead measure a stack shear modulus value, in a manner similar to the radial modulus. Its pressure dependence could thus be verified. Then, as was done for Dr. Good's extended research discussed above, the model could be laterally linked throughout the roll, and the stack shear modulus would determine the whole roll's shear.

One great advantage to the combined model's formulation is its expandability. First, the axisymmetric finite elements of chapter III can accommodate body forces, and thermal loadings. For the body force vector, any forces acting axisymmetrically through the roll's volume can be included, like rotational effects. Thermal loadings in the roll often occur as a result of heating the roll, or web, and allowing it to cool. This produces tension changes that can be investigated with the model. Similarly, the viscoelastic web properties can be applied to the completed wound roll, to determine the stresses remaining after time. Another possibility is to allow the web's thickness profile to change during the wind in proportion to the radius, or the length of material wound onto the roll. The material properties can also be allowed to change across the web's width, its depth, or through the core, for example. This would accommodate strips of dissimilar material being combined into a complete web across the width, multi-material laminated webs, and paper cores on mandrels, respectively. Two other possible expansions address the nip's formulation from chapter IV. Its applied load can be adjusted to be uneven between its points of application. Or, a rubber cover could be put onto it, and modeled as another Winkler foundation.

BIBLIOGRAPHY

[1] Altmann, Heinz C., "Formulas for Computing the Stresses in Center-Wound Rolls.", TAPPI Journal, Vol. 51, No. 4, pp. 176-179, April 1968

[2] Chandrupatla, T. R., Belegundu, A. D., Introduction to Finite Elements in Engineering, 2nd Edition, Prentice-Hall, Inc., 1997

[3] Cheng, S., and Cheng, C. C., "Relation Between E, ν, G and Invariants of the Elastic Coefficients for an Orthotropic Body.", ASME, Mechanics of Wood and Paper Materials, AMD Vol. 112, MD Vol. 23, pp. 53-65, 1990

[4] Cole, K., and Hakiel, Z., "A Nonlinear Wound Roll Stress Model Accounting for Widthwise Web Thickness Nonuniformities.", ASME, Applied Mechanics Division, Vol. 149, ASME 1992

[5] Donaldson, Bruce K., Analysis of Aircraft Structures, An Introduction, McGraw-Hill, Inc., 1993

[6] Edwards, W. J., and Boulton, G., "The Mystery of Coil Winding.", Association of Iron and Steel Engineers, 2001

[7] Felippa, C.A. "Lecture Notes in Introduction to Linear Finite Element Methods", Vol. 1, pp. 10-8, pp. 7-6, 1989

[8] Giachetto, R. Matthew, “Tension Losses Encountered in Centerwound Rolls”, Masters Thesis, Oklahoma State University, December 1991

[9] Good, J. K., and Fikes, M.W.R., "Predicting Internal Stresses in Center-Wound Rolls with an Undriven Nip Roller.", TAPPI Journal, Vol. 74, No. 6, pp. 101-109, June 1991

[10] Good, J. K., and Pfeiffer, J. D., "Tension Losses during Centerwinding.", Proceedings of the 1992 TAPPI Finishing and Converting Conference, pp. 297-306

[11] Good, J. K., Wu, Z., and Fikes, M.W.R., "The Internal Stresses in Wound Rolls with the Presence of a Nip Roller.", Transactions of the ASME, Journal of Applied Mechanics, Vol. 61, pp. 182-185, 1992

[12] Good, J. K., "Modeling Rubber Covered Nip Rollers in Web Lines.", Proceedings of the Sixth International Conference on Web Handling, Oklahoma State University, 2001, pp. 159-180

[13] Gutterman, R. P., "Theoretical and Practical Studies of Magnetic Tape Winding Tensions and of Environmental Roll Stability.", Contract # DA18-119-SC-42, General Kinetics, Inc., Arlington, Virginia, 1959

[14] Hakiel, Z., "Nonlinear Model for Wound Roll Stresses.", TAPPI Journal, Vol. 70, No. 5, pp. 113-117, May 1987

[15] Hakiel, Z., "On the Effect of Width Direction Thickness Variations in Wound Rolls.", Proceedings of the First International Conference on Web Handling, Oklahoma State University, 1991, pp. 79-98

[16] Higdon, A., Ohlsen, E. H., Stiles, W. B., Weese, J., Riley, W. F., Mechanics of Materials, 4th edition, John Wiley & Sons, Inc., 1985

[17] Hoffecker, P., "Characterization of a Nip Impinged Wound Roll.", Masters Thesis, Oklahoma State University, May 1997

[18] Johnson, K.L., Contact Mechanics, Cambridge: Cambridge University Press, 1985

[19] Kedl, D. M., "Using A Two Dimensional Winding Model to Predict Wound Roll Stresses that Occur Due to Circumferential Steps in Core Diameter or to Cross-Web Caliper Variation.", Proceedings of the First International Conference on Web Handling, Oklahoma State University, 1991, pp. 99-112

[20] Lee, Y.M., and Wickert, J.A., "Stress Field in Finite Width Axisymmetric Wound Rolls.", Submitted for Publication in Transactions of the ASME, Journal of Applied Mechanics, 2002

[21] Lee, Y.M., and Wickert, J.A., "Width-Wise Variation of Magnetic Tape Pack Stresses.", Transactions of the ASME, Journal of Applied Mechanics, Proof Copy, Vol.69, pp.1-12, May 2002

[22] Lekhnitskii, S. G., Anisotropic Plates, Gordon and Breach, Science Publishers, Inc., pp. 106-110, 1968

[23] Matthews, John H., Numerical Methods for Mathematics, Science, and Engineering, 2nd Edition, Prentice-Hall, Inc., 1992

[24] Pfeiffer, J. David, "Internal Pressures in a Wound Roll of Paper.", TAPPI Journal, Vol. 49, No. 8, pp. 342-347, August 1966

[25] Pfeiffer, J. David, "Mechanics of a Rolling Nip on Paper Rolls.", TAPPI Journal, Vol. 51, No. 8, pp. 77A-85A, August 1968

[26] Pfeiffer, J. D., "Nip Forces and Their Effect on Wound In Tension.", TAPPI Journal, Vol. 60, No. 3, pp. 115-117, March 1977

[27] Pfeiffer, J. David, "Prediction of Roll Defects from Roll Structure Formulas.", TAPPI Journal, Vol. 62, No. 10, pp. 83-85, October 1979

[28] Pfeiffer, J.D., "Surface Winding to Overcome the Strain Deficiency.", Proceedings of the 1990 TAPPI Finishing and Converting Conference, pp. 233-236

[29] Press, W.H., Teukolsky, S.A., Vetterling, W.T., and Flannery, B.P., Numerical Recipes, Cambridge University Press, 1992

[30] Qualls, William R., "Hyrgothermomechanical Characterization of Viscoelastic Centerwound Rolls.", Doctoral Thesis, Oklahoma State University, May 1995

[31] Roisum, David R., "The Measurement of Web Stresses During Roll Winding.", Doctoral Thesis, Oklahoma State University, May 1990

[32] Tsai, Yi-Cheng, "Development of Three Dimensional Roll Models.", Masters Thesis, Oklahoma State University, July 1995

[33] Yagoda, H. P., "Resolution of a Core Problem in Wound Rolls.", Transactions of the ASME, Journal of Applied Mechanics, vol. 47, pp. 847-854, 1980

APPENDIX A

INPUT FILE FOR COMPREHENSIVE, THREE DIMENSIONAL, AXISYMMETRIC MODEL

1) DESCRIPTIVE TITLE OF THE PROGRAM RUN
Final Combined Model run, NEWS, 14# nip
2) NAMES FOR THE THREE OUTPUT FILES
AXOR_CMB.121
AXSM_CMB.121
CORE_CMB.121
3) YES OR NO TO ACCRETE/ WIND
Y
4) YES OR NO TO ITERATE ON OUTER LAP TENSIONS TO EQUAL TW
Y
5) YES OR NO TO ALLOW GAPPING IN THE ROLL
N
6) YES OR NO TO FRICTIONALLY LINK ROLL
N
7) NUMBER OF LAYERS TO COMBINE AS ONE MODEL LAYER
3
8) NUMBER OF DIFFERENT CMD, WEB THICKNESSES
24
9) INITIAL SINGLE LAYER WEB SEGMENT THICKNESSES
2.81051D-03
2.81051D-03
2.81109D-03
2.81227D-03
2.81285D-03
2.81168D-03
2.81168D-03
2.81109D-03
2.80875D-03
2.80640D-03
2.80288D-03
2.79878D-03
2.79702D-03
2.79526D-03
2.79409D-03
2.79291D-03
2.79291D-03
2.79115D-03
2.79115D-03
2.78998D-03
2.78939D-03
2.78822D-03
2.78822D-03
2.78470D-03
10) WEB CMD WIDTH; INSIDE ROLL RADIUS; OUTSIDE ROLL RADIUS
6.0D+00 3.289D+00 4.914D+00
11) CMD WIDTHS OF SINGLE LAYER WEB SEGMENTS
0.25D+00
0.25D+00
0.25D+00
0.25D+00
0.25D+00
0.25D+00
0.25D+00
0.25D+00
0.25D+00
0.25D+00

0.25D+00
0.25D+00
0.25D+00
0.25D+00
0.25D+00
0.25D+00
0.25D+00
0.25D+00
0.25D+00
0.25D+00
0.25D+00
0.25D+00
0.25D+00
12) YES OR NO TO INCLUDE CORE; # OF CORE MODEL RADIAL LAYERS; CORE ENDS CMD STEP SIZE
Y 3 0.16666667D+00
13) CORE CONTACT SURFACE MATERIAL PROPERTIES: ER, ET, EZ, NUTR, NUZR, NUTZ, GRZ
1.00D+07 1.00D+07 1.00D+07 0.3D+00 0.3D+00 0.3D+00 4.00D+06
14) CORE CONTACT SURFACE INSIDE RADIUS (A)
3.0D+00
15) CORE INSERTS MATERIAL PROPERTIES: ER, ET, EZ, NUTR, NUZR, NUTZ, GRZ
1.00D+07 1.00D+07 1.00D+07 0.3D+00 0.3D+00 0.3D+00 4.00D+06
16) CORE STUB SHAFTS PROPERTIES: ER, ET, EZ, NUTR, NUZR, NUTZ, GRZ
3.00D+07 3.00D+07 3.00D+07 0.3D+00 0.3D+00 0.3D+00 1.16D+07
17) CORE STUB SHAFT RADIUS
0.9375D+00
18) OVERALL CMD DISTANCE BETWEEN CORE SUPPORTS; DISTANCE FROM CMD ZERO TO LEFT SUPPORT (B)
7.0D+00 2.125D+00
19) CMD DISTANCE FROM LEFT SUPPORT TO INSERT (C); LEFT INSERT THICKNESS (D)
0.0D+00 0.5D+00
20) CMD DISTANCE FROM LEFT SUPPORT TO CONTACT SURFACE; CMD CONTACT SURFACE WIDTH
0.0D+00 7.0D+00
21) CMD DISTANCE FROM RIGHT SUPPORT TO INSERT; RIGHT INSERT THICKNESS
0.0D+00 0.5D+00
22) CMD DISTANCE FROM LEFT SUPPORT TO WOUND ROLL (E)
0.5D+00
23) EXTERNAL CORE PRESSURE; INTERNAL CORE PRESSURE
0.00D+00 0.00D+00
24) YES OR NO TO ADJUST PRESSURE INDUCED CORE LOADING DURING ACCRETION
N
25) IS THE WINDING TENSION 1)PSI OR 2)PLI?
2
26) SINGLE LAYER WINDING TENSION
1.00D+00
1.00D+00
1.00D+00
1.00D+00
1.00D+00
1.00D+00
1.00D+00
1.00D+00
1.00D+00
1.00D+00

1.00D+00
1.00D+00
1.00D+00
1.00D+00
1.00D+00
1.00D+00
1.00D+00
1.00D+00
1.00D+00
1.00D+00
1.00D+00
1.00D+00
1.00D+00
1.00D+00
27) ER MODEL CHOICE: 1) = K1*K2 +K2*P, 2) = C1 + C2*P + C3*P^2 + C4*P^3,
3) = C0(1-exp(-P/C1)), 4) = (A + B*P)^C
1
28) ER MATERIAL PROPERTY COEFFICIENTS: K1, K2; C1, C2, C3, C4; C0, C1; A, B, C
3.52339961D+00 2.44896923D+01
29) WEB MATERIAL PROPERTIES: ET, EZ, NUTR, NUZR, NUTZ, GRZ
4.00D+05 4.00D+05 1.0D-02 1.0D-02 0.3D+00 6.97D+02
30) FRICTION COEFFICIENTS, WEB TO CORE: STATIC AND KINETIC; WEB TO WEB: S & K
0.4D+00 0.2D+00 0.336D+00 0.24D+00
31) MAXIMUM RADIAL STRAIN USED IN Er DETERMINATION (RECOMMEND 0.15D+00)
0.1D+00
32) LATERAL WEB CONSTRAINT TYPE: 1) = ABSOLUTE RIGID, 2) = RELATIVE TO LAYER BELOW
2
33) WISH TO PRINT IN OUTPUT FILE EXTENSIVE NODE LOCATIONS AND DISPS?
N

APPENDIX B

INPUT FILE FOR PERIPHERAL NIP CONTACT MODEL

1) DESCRIPTIVE TITLE OF THE PROGRAM RUN
Final Combined Model run, NEWS, 14# nip
2) SIX OUTPUT FILE NAMES
CMB_RAD.121
CMB_SUM.121
CMB_INC.121
CMB_DEF.121
CMB_PRO.121
CMB_MAS.121
3) UNIT SYSTEM: first three letters of ENGlish or METric
eng
4) CMD DIS. BTWN APPLIED NIP LOAD LOC.; FROM ZERO TO LEFT NIP LOAD LOCATION
11.25D+00 0.0D+00
5) CMD DIS. BTWN CORE SUPPORTS; CMD DIS. FROM ZERO TO LEFT CORE SUPPORT
7.0D+00 2.125D+00
6) NIP LEFT STUB SHAFT CMD TOTAL WIDTH (FROM LEFT LOAD TO RIGHT)
5.625D+00
6B) NIP RIGHT STUB SHAFT CMD TOTAL WIDTH (FROM RIGHT LOAD TO LEFT)
5.625D+00
7) CMD DIS. FROM LEFT NIP LOAD TO LEFT INSERT; LEFT NIP INSERT THICKNESS
1.625D+00 0.5D+00
7.5) CMD DIS. FROM RIGHT NIP LOAD TO RIGHT INSERT; RIGHT NIP INSERT THICKNESS
1.625D+00 0.5D+00
8) CMD DIS. FROM LEFT NIP LOAD TO NIP CONTACT SURFACE; NIP C.S. CMD THICKNESS
1.625D+00 8.0D+00
9) NIP STUB, INSERT, AND CONTACT SURFACE RADII
0.50D+00 1.0625D+00 1.375D+00
10) CORE LEFT STUB SHAFT CMD TOTAL WIDTH, CORE ENDS CMD STEP SIZE
3.5D+00 0.16666667D+00
10B) CORE RIGHT STUB SHAFT CMD TOTAL WIDTH
3.5D+00
11) CMD DIS. FROM LEFT CORE SUPPORT TO LEFT INSERT; LEFT CORE INSERT THICKNESS
0.0D+00 0.5D+00
11B) CMD DIS. FROM RIGHT CORE SUP. TO RIGHT INSERT; RIGHT CORE INSERT THICKNESS
0.0D+00 0.5D+00
12) CMD DIS. FROM LEFT CORE SUPPORT TO C.S.; CORE C.S. CMD THICKNESS
0.0D+00 7.0D+00
13) CORE STUB, INSIDE CONTACT SURFACE, AND INSIDE ROLL RADII
0.9375D+00 3.0D+00 3.289D+00
14) CMD DISTANCE FROM LEFT SUPPORT TO WOUND ROLL
0.5D+00
15) WEB CMD WIDTH; DESIRED OUTSIDE WOUND ROLL RADIUS
6.0D+00 4.914d+00
16) NIP MATERIAL DATA: STUB EZ, NUTR
3.0D+07 0.3D+00
17) NIP MATERIAL DATA: INSERT EZ, NUTR
1.0D+07 0.3D+00
18) NIP MATERIAL DATA: CONTACT SURFACE EZ, NUTR
1.0D+07 0.3D+00
19) CORE MATERIAL DATA: STUB EZ, NUTR
3.0D+07 0.3D+00
20) CORE MATERIAL DATA: INSERT EZ, NUTR
1.0D+07 0.3D+00
21) CORE MATERIAL DATA: CONTACT SURFACE EZ, NUTR
1.0D+07 0.3D+00

22) WEB MATERIAL PROPERTIES: EZ, NUTR, ET
4.00D+05 1.0D-02 4.00D+05
23) COEFFICIENT OF KINETIC FRICTION
0.24D+00
24) ER MATERIAL PROPERTY COEFFICIENTS: K1, K2, K3
3.52339961D+00 2.44896923D+01 0.00D+00
25) TOTAL APPLIED NIP FORCE LOAD; NIP FORCE STEP SIZE
14.0D+00 2.0D+00
26) DECISION: WANT OUTPUT FILE TO INCLUDE ROTATIONS?
N
27) IS NIP'S LEFT END CONSTRAINED FROM ROTATING?
Y
28) IS NIP'S RIGHT END CONSTRAINED FROM ROTATING?
Y
29) IS CORE'S LEFT END CONSTRAINED FROM ROTATING?
Y
30) IS CORE'S RIGHT END CONSTRAINED FROM ROTATING?
Y
31) WILL NIP AXIS REMAIN PARALLEL TO CORE AXIS IN PLANE?
N
32) NUMBER OF DIFFERENT CMD, WEB THICKNESSES
24
33) INITIAL SINGLE LAYER WEB SEGMENT THICKNESSES
2.81051D-03
2.81051D-03
2.81109D-03
2.81227D-03
2.81285D-03
2.81168D-03
2.81168D-03
2.81109D-03
2.80875D-03
2.80640D-03
2.80288D-03
2.79878D-03
2.79702D-03
2.79526D-03
2.79409D-03
2.79291D-03
2.79291D-03
2.79115D-03
2.79115D-03
2.78998D-03
2.78939D-03
2.78822D-03
2.78822D-03
2.78470D-03
34) CMD WIDTHS OF SINGLE LAYER WEB SEGMENTS
0.25D+00
0.25D+00
0.25D+00
0.25D+00
0.25D+00
0.25D+00
0.25D+00
0.25D+00

0.25D+00
0.25D+00
0.25D+00
0.25D+00
0.25D+00
0.25D+00
0.25D+00
0.25D+00
0.25D+00
0.25D+00
0.25D+00
0.25D+00
0.25D+00
0.25D+00
0.25D+00
0.25D+00

APPENDIX C

ADDITIONAL INPUT FILE FOR NIP IMPINGED, THREE DIMENSIONAL WOUND ROLL MODEL

THIS FILE IS FOR THE ADDITIONAL VARIABLES NEEDED FOR THE COMBINED CODE
1) AMOUNT OF WOUND ROLL TO ACCUMULATE BETWEEN NIP IMPINGEMENTS
0.46D+00
2) AMOUNT WEB WRAPS NIP TO WIND
0.0D+00
3) NIP TO WEB COEFFICIENT OF STATIC FRICTION
0.4D+00
4) YES OR NO TO RADIALLY COMPRESS ROLL WITH NIP...YES = NON-AXISYMMETRIC!
N
5) WEB TO WEB COEFFICIENT OF KINETIC FRICTION
0.24D+00
6) RADIUS AT WHICH TO START IMPINGING NIP
3.339D+00

APPENDIX D

NIP IMPINGED, THREE DIMENSIONAL WOUND ROLL

MODEL FORTRAN SOURCE CODE

Please contact Dr. J. Keith Good at the Web Handling Research Center to request access to the model's source code. The Center is part of the Mechanical and Aerospace Department at Oklahoma State University, in Stillwater, Oklahoma.

VITA

Paul Hoffecker

Candidate for the Degree of

Doctor of Philosophy

Thesis: THE ANALYSIS OF A NIP IMPINGED, THREE DIMENSIONAL WOUND ROLL

Major Field of Study: Mechanical Engineering

Biographical:

Education: Graduated from Berthoud High School, Berthoud, Colorado in May 1989; received Bachelor of Science degree in Aerospace Engineering from University of Colorado at Boulder, Boulder, Colorado in May 1994; received Master of Science degree in Mechanical Engineering from Oklahoma State University, Stillwater, Oklahoma in May 1997. Completed the requirements for the Doctor of Philosophy degree, with a major in Mechanical Engineering at Oklahoma State University in May, 2006.

Experience: Interned and Contracted as space science researcher for the National Air and Space Museum, Smithsonian, May 1992- August 1992, and May 1993- August 1993 respectively. Employed with Colorado Space Grant Consortium (September, 1993 -January, 1996) in numerous capacities from design team member to lead of sounding rocket structure team. Also shared structures team lead responsibilities on NASA student satellite proposal. Employed by Oklahoma State University, Department of Mechanical and Aerospace Engineering as a graduate research assistant, 1996 to June 2006.

Memberships: American Institute of Aeronautics and Astronautics

Name: Paul Hoffecker Date of Degree: May, 2006

Institution: Oklahoma State University Location: Stillwater, Oklahoma

Title of Study: THE ANALYSIS OF A NIP IMPINGED, THREE DIMENSIONAL WOUND ROLL

Pages in Study: 210

Candidate for the Degree of Doctor of Philosophy

Major Field: Mechanical Engineering

Scope and Method of Study: An accurate, nip impinged, three dimensional wound roll model can improve the quality of numerous consumer products. This is because the products use webs that were once wound into a roll. The model identifies potentially destructive stress levels without actually winding, thereby reducing waste, and boosting efficiency. To this end, it integrates a three dimensional roll sub-model, with a peripheral nip contact sub-model, in a recursive exchange. The three dimensional sub-model is an orthotropic, axisymmetric-quadrilateral finite element model that accretes by interfering layers onto each other. It incorporates thickness variations in the web profile in the CMD, variable core configurations, and wound on tension iteration. The peripheral nip sub-model is a linked system of beam finite elements. A winkler elastic foundation, with a non-linear radial stiffness, represents the wound roll, which is radiatively coupled to both the impinging nip, and the core. Control passes back and forth between the sub-models as each contributes to the final nip impinged, three dimensional roll.

Findings and Conclusions: The combined model is a significant step forward in wound roll simulations. The underlying axisymmetric sub-model is one of the most extensive, and accurate, known to exist. Its CMD radii, and stresses, compared well to experimental data. It captured the tension concentration, and radius buildup, recognized to correspond with thicker CMD locations. When combined with the nip sub-model, the result is the first, and only, model known to also incorporate the CMD compression, and load distribution, effects of nip impingement. Its results show the nip load concentrates at higher locations to reduce their radii. And, its comparison to the 14 pound, six inch wide PET web experimental data was good. Ultimately, the combined model promises versatility, and utility, in its application to improve the quality of wound rolls in industry.

ADVISOR'S APPROVAL: Dr. J. Keith Good